

THE ATTENUATION OF SEISMIC WAVES  
IN DRY AND SATURATED ROCKS

by


DAVID H. JOHNSTON


S.B., Massachusetts Institute of Technology (1973)

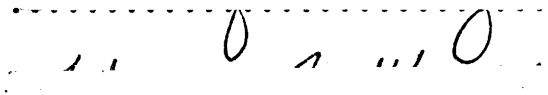
SUBMITTED IN PARTIAL FULFILLMENT  
OF THE REQUIREMENTS FOR THE  
DEGREE OF  
DOCTOR OF PHILOSOPHY  
at the

© MASSACHUSETTS INSTITUTE OF TECHNOLOGY

October 19, 1978

  
Signature of Author.....  
Department of Earth and Planetary Sciences, October 19, 1978

  
Certified by..... Thesis Supervisor

  
Accepted by.....  
Chairman, Departmental Committee on Graduate Students

WITHDRAWN  
MASSACHUSETTS INSTITUTE  
OF TECHNOLOGY  
FROM  
DEC 7 1978  
MIT LIBRARIES  
LIBRARIES

THE ATTENUATION OF SEISMIC WAVES  
IN DRY AND SATURATED ROCKS

by

David H. Johnston

Submitted to the Department of Earth and Planetary Sciences  
on October 19, 1978, in partial fulfillment of the requirements  
for the degree of Doctor of Philosophy.

ABSTRACT

The attenuation of seismic waves in upper crustal rocks is studied from both experimental data and theoretical models of specific attenuation mechanisms. The attenuation, or anelasticity may be used in conjunction with the compressional (P) and shear (S) wave velocities to infer the microstructure of the rock and the physical conditions encountered in the subsurface environment. Generally, the attenuation varies much more than velocity with accompanying changes in the physical state making this measurement a particularly valuable tool. Unfortunately, systematic studies of the behavior of attenuation with parameters such as pressure and saturation conditions are deficient. Nor has the development of new experimental techniques and theoretical models kept pace with the methods for elastic properties.

It is shown in this thesis that previous experimental data suggest one or more of several proposed mechanisms may be contributing to the overall attenuation observed in crustal rocks. These include crack and grain boundary sliding friction; fluid associated mechanisms such as crack lubrication, fluid flow through porous and permeable rock, squirting flow from thin cracks to larger pores, and viscous shear relaxation in the void spaces; losses associated with gas bubble resonances; and a host of geometrical effects with scattering from pores in the rock being most important from an experimental point of view. Mathematical models of all these mechanisms in terms of their frequency and pressure dependences are developed.

The attenuation or  $Q$  values (inverse proportional to



the energy loss) for P and S waves are determined for a suite of upper crustal rocks as functions of pressure and saturation using an ultrasonic pulse transmission technique with the goal of interpreting these results in terms of the theoretical models of the mechanisms. In general, it is found that  $Q$  for both P and S waves increases (attenuation decreases) as a function of pressure for dry and water saturated rocks.  $Q$  values for saturated and partially saturated rocks are less than for dry rocks and while not conclusive, the experiments suggest that  $Q_p$  for low gas saturations is slightly lower compared to the fully water saturated case. The major controlling factor in determining the differences in  $Q$  for individual rocks is the nature and concentration of thin cracks - the exceptions studied being shales and tuffs. Rocks with a higher density of fine cracks exhibit lower  $Q$  values and the rate of change of  $Q$  with pressure may be correlated with the crack width distribution inferred from static stress-strain measurements.

Modeling of the  $Q$  data obtained for dry and water saturated samples of Berea sandstone imply that friction is the dominant mechanism for attenuation. Increasing pressure decreases the number of sliding surfaces and thus  $Q$  increases. The major effect of fluid is to lubricate these surfaces thus facilitating sliding. Attenuation due to fluid flow plays a secondary role. At ultrasonic frequencies and moderate pressures, flow is, however, important in porous and permeable rock like the sandstone. Scattering is dominant only at very high frequency or, as with the tuffs, when the grain or pore sizes are large compared to the wavelength. Attenuation in shales may be due to relative shear motion between the rock matrix and clay or kerogen. Bubble associated losses in partially saturated rocks may be important only in limited cases.

The phenomenon of frictional attenuation is further examined using a resonance bar experimental technique. It is found that  $Q$  in dry rocks is dependent on amplitude, constant at low strains but decreasing rapidly at strains greater than about  $10^{-6}$ , explaining differences in  $Q$  observed between resonance and ultrasonic methods. The amplitude dependence is also a function of the types of cracks existing in the rock. This is investigated for samples that have been thermally cycled in order to induce cracking. It is found that rocks cycled at low heating rates show an increase in  $Q$  up to a cycled temperature of about  $400^{\circ}\text{C}$  which is accompanied by a migration of the amplitude transition to lower strains. These data are interpreted in terms of the widening of thin cracks thus reducing the contact area of frictional sliding - both

increasing  $Q$  and allowing the surfaces to slide at lower amplitudes. Some of the effect observed may also be due to outgassing of volatiles from the crack surfaces.

The results obtained in this thesis may be used to evaluate the difficulties involved in extrapolating laboratory data to insitu measurements of attenuation. Theoretical models such as those used to describe the anelastic behavior of the Berea sandstone, provide the best method at the present time. However, field measurements must be corrected for other factors that affect seismic wave amplitude. Furthermore, the contributions of mechanisms that may be important at low frequencies and not easily established from ultrasonic data plus the amplitude dependence of attenuation must be considered before any meaningful comparisons can be made.

Thesis Supervisor: M. Nafi Toksöz  
Title: Professor of Geophysics

## ACKNOWLEDGEMENTS

It is difficult to complete a thesis without the help of a great many people. The most important of these must be my advisor, Nafi Toksöz, who has the uncanny ability to recognize the important topics of research. He has supported my work for eight years and I will always be grateful for his help. I am also deeply indebted to Bill Brace who, for all practical purposes, was a second advisor. He let me take over a good size part of his lab and when it came down to the nitty-gritty of experimental work, was always there to lend advice and instruction.

Of all the other people at MIT, I probably received the most help and encouragement from my fellow student, Arthur Cheng. Although I will never forgive him for getting his degree before me, I look forward to working with him in the future.

Thanks must also go to Joe Walsh for his interest in my work and for the discussions we had concerning the interpretations of my data. Gene Simmons was kind enough to loan me many pieces of equipment which I hope have all been returned.

Special appreciation goes to the Chevron Oil Field Research Company and in particular, Turk Timur, for getting me started in the field of attenuation and releasing

the Q data presented in this thesis. Jim Spencer, also at COFRC, provided many useful comments on my work, not to mention the sample of Berea sandstone.

Several other students provided invaluable assistance during the course of my thesis work. Jim Scheimer found a way to get all the ultrasonic data into some usable form on the computer. Ray Harpin did some of the static measurements and his help with the gas release experiment is appreciated. I also thank all the other occupants of the rock mechanics lab for putting up with me for the past few years and for their help when needed.

I am indebted to Emeka Okoli for his work on the interactive graphics program for waveform processing. Without it the thesis would have taken far longer. My thanks also go to Joan Gomberg who was in on my early strugglings with the ultrasonic work and to Tom Rhodes who attempted (but unfortunately did not succeed) to build me a digital waveform acquisition device. At least I learned a few things about digital electronics and management decisions from the experience.

Nothing would have ever been done properly in the lab without the work of our machinist, Jock Hirst. I also received help in the electronics from Frank Miller and Paul Mattaboni. Dorothy Frank did a lot of the typing and Mary Roden assisted in drafting many of the figures. Sara Brydges made the final corrections to the manuscript.

I am also obliged to Brian Bonner of the Lawrence Livermore Laboratory for several useful discussions and the sample of oil shale. Frank Byers of the USGS provided information on the Tunnel Beds tuff. Thanks also go to the Atlantic Cement Company of Ravena, NY for allowing me into their quarry to collect the Esopus shale. Group 22 at the MIT Lincoln Laboratory kindly let me use their digitizer.

Finally, my greatest thanks go to Linda, who somehow put up with being a graduate student's wife far longer than anyone should have to. Her understanding and encouragement made it possible for me to complete this work.

This research was supported in part by a Chevron Fellowship and the Advanced Research Projects Agency, monitored by the Air Force Office of Scientific Research under contract F44620-75-C-0064.

## TABLE OF CONTENTS

	PAGE
TITLE PAGE	1
ABSTRACT	2
ACKNOWLEDGEMENTS	5
TABLE OF CONTENTS	8
CHAPTER 1: INTRODUCTION	13
CHAPTER 2: REVIEW OF ATTENUATION MEASUREMENTS	19
2.1 Laboratory Measurement of Attenuation	19
2.1a Free Vibration Method	22
2.1b Forced Vibration Method	24
2.1c Wave Propagation	29
2.1d Observation of Stress-Strain Curves	37
2.2 Previous Experimental Work	38
2.2a Individual Measurements of Attenuation	39
2.2b Correlation of Q With Simple Rock Properties	41
2.2c Attenuation as a Function of Saturation Conditions	43
2.2d Attenuation as a Function of Pressure	47
Table	51
Figure Captions	52
Figures	54

	PAGE
CHAPTER 3: ATTENUATION MECHANISMS	64
3.1 Phenomenological Models of Attenuation	66
3.1a Linear Models	67
3.1b Nonlinear Models	70
3.2 Attenuation Due to Matrix Anelasticity	71
3.3 Attenuation Due to Viscosity and Flow of Saturating Fluids	82
3.3a Biot Fluid Flow	83
3.3b Squirting Flow	91
3.4 Gas Bubbles	94
3.4a The Occurrence of Gas in Nature	95
3.4b Bubble Resonances	97
3.4c Bubble Losses	100
3.4d Attenuation Formulations	102
3.5 Other Sources of Attenuation	104
Figure Captions	108
Figures	109
CHAPTER 4: EXPERIMENTAL TECHNIQUES	114
4.1 Pulse Transmission - Amplitude Ratios	114
4.2 Ultrasonic Measurement System	118
4.2a Determination of Velocity	124
4.2b Data Processing	125
4.2c Sources of Error	127
4.3 Forced Vibration - Resonance	135

	10
	PAGE
4.4 Static Measurements	141
4.5 Sample Preparation	143
4.5a Pulse Experiment	143
4.5b Resonance Experiment	144
4.6 Description of Samples	146
Table	161
Figure Captions	162
Figures	165
CHAPTER 5: THE EFFECT OF PRESSURE AND SATURATION ON Q	188
5.1 Experimental Data	189
5.1a Berea Sandstone	190
5.1b Navajo Sandstone	202
5.1c Bedford Limestone	204
5.1d Shales	207
5.1e Tuffs	211
5.2 Interpretation of Laboratory Data	216
5.2a Sandstone Model of Attenuation	217
5.2b Comments on the Other Samples	226
Tables	230
Figure Captions	233
Figures	243
CHAPTER 6: CRACKS AND AMPLITUDE DEPENDENT ATTENUATION	299
6.1 Experimental Results	300



	PAGE
6.1a Strain Amplitude Dependent Q	302
6.1b Thermal Cracking and Amplitude Dependent Q	306
6.2 Mechanisms	314
6.2a Amplitude Dependent Attenuation	314
6.2b Volatile Loss	317
6.2c Thermal Cracking	319
6.3 Discussion	325
Tables	333
Figure Captions	334
Figures	339
CHAPTER 7: SUMMARY AND CONCLUSIONS	369
REFERENCES	378
APPENDIX A: DEFINITIONS	400
APPENDIX B: ELASTIC MODULI FOR CALCULATING ATTENUATION	408
APPENDIX C: FLUID FLOW FROM CRACKS, FORMULATION AND ESTIMATION OF RELAXATION TIME	412
APPENDIX D: HOMOMORPHIC DECONVOLUTION	417
Figure Captions	425
Figures	426
BIOGRAPHY	430

What ineffable twaddle! I never read such rubbish in my life.

- Dr. Watson, A Study in Scarlet

Sir Arthur Conan Doyle

## CHAPTER 1

### INTRODUCTION

Most of our knowledge of the structure and composition of the Earth's interior is based on data obtained from seismic waves. In particular, compressional and shear wave velocities, combined with density, provide the most direct information on the elastic moduli at great depths in the Earth. These, combined with controlled laboratory studies of rock properties under simulated subsurface conditions have provided a most valuable tool for determining lithology and structure not only for global seismology but for exploration geophysics as well.

Yet, knowledge of the elastic properties alone presents an incomplete picture. The interpretation of seismic data in terms of rock properties must also include the anelastic characteristics or attenuation. In fact, the attenuation generally varies much more than the seismic velocities as a result of changes in the physical state of rocks and their constituents. However, the development of experimental techniques for measuring attenuation in the laboratory and theoretical models of attenuation mechanisms has lagged far behind the methods for elastic properties.

The emphasis of this thesis will be on the anelastic properties of rocks in the upper crust - to depths of 5-10 km and at relatively low temperatures. Much of the application of this work may eventually be found in exploration geophysics. Attenuation combined with both P and S wave velocities may help in the identification of rock type, the characterization of pore spaces including porosity and permeability, and perhaps most importantly, the direct determination of pore fluid.

In order to understand the effect of the conditions commonly found in the upper crust on attenuation, one must start from empirical observations from the laboratory and field. Field data on attenuation, however, is nearly nonexistent and as we will see, laboratory data is fraught with interpretational difficulties. While the laboratory is practical for controlled experiments in terms of pressure and temperature, many times the frequency and/or amplitude of the seismic waves are quite different from those obtained in the field. In this case, theory provides a useful tool for the extrapolation of laboratory data to field conditions.

The theory of attenuation in rock may be approached two ways. From a phenomenological point of view, one may arrive at a differential equation relating attenuation with phase velocity and frequency,

establishing the behavior of seismic wave propagation. This kind of method, however, does not lead to a greater understanding of the physics of attenuation and does not relate the anelastic properties of seismic waves to rock properties. The mechanistic approach, used in this thesis, attempts to determine the specific physical mechanisms by which seismic energy is lost. A precise definition of each mechanism involved in attenuation, along with its pressure and frequency dependence is required.

Numerous mechanisms have been proposed and each may be considered to have a greater degree of importance to the overall attenuation under certain physical conditions. These mechanisms include: matrix anelasticity including frictional dissipation due to relative motions at the grain boundaries and across crack surfaces (Walsh, 1966); attenuation due to fluid flow including relaxation due to shear motions at pore-fluid boundaries (Walsh, 1968, 1969; Solomon, 1973); dissipation due to the relative motion of the rock frame with respect to fluid inclusions (Biot, 1956a,b and 1962a,b; Stoll and Bryan, 1970); "squirting" of fluid from cracks to pores (Mavko and Nur, 1975; O'Connell and Budianski, 1977); partial saturation effects such as gas pocket squeezing (White, 1975) and gas bubble resonance; energy absorbed in

systems undergoing phase changes (Spetzler and Anderson, 1968); and a large category of geometrical effects including scattering off small pores (Yamakawa, 1962; Kuster and Toksöz, 1974) and large irregularities and selective reflection from thin beds (O'Doherty and Anstey, 1971; Spencer et al., 1976). All the above mechanisms except large scale geometrical effects, are dependent upon intrinsic rock properties. Thus, the interpretation of data in terms of these mechanisms may provide information on the microstructure of rock.

The objectives of this thesis are as follows:

1. To investigate the variation of seismic body wave attenuation with pressure and fluid saturation. P and S wave attenuation ( $Q$  values) are found from an ultrasonic pulse transmission technique using spectral ratios (Toksöz et al., 1978).

2. To develop and use theoretical formulations of attenuation mechanisms to model the  $Q$  data. By doing this, we may discover under what conditions one or more mechanisms may be dominant in causing the overall attenuations of both P and S waves and determine to what features or rock structure attenuation is most sensitive. Another important aspect of theoretical modeling is addressing the question of the extension of laboratory data to other frequencies.

3. To further examine the dominant mechanism of attenuation in the upper crust - friction. Here, longitudinal bar attenuation is determined by a dynamic resonance technique for uncracked and thermally cracked rocks. The phenomenon of strain amplitude dependent attenuation is investigated. From the discussion, it will be seen that this presents a further complication in comparing laboratory to field data.

4. To synthesize the ultrasonic data and models and the information gleaned from the further study of the friction mechanism. New directions to be taken in the future for both experimental and theoretical work will be suggested.

In the next chapter the various techniques for measuring attenuation and the published data for rocks under varying physical conditions, highlighting important features that contribute to the understanding of the mechanisms involved will be reviewed. In the third chapter attenuation mechanisms along with their theoretical formulations are presented. Next, a detailed description of the experimental techniques and rock samples used in this thesis is given. In the fifth chapter, attenuation data as functions of pressure and saturation conditions are presented along with theoretical modelling and discussion of important

mechanisms. This is followed in the next chapter by a more thorough investigation of the friction mechanism. Finally, in the last chapter, a discussion and conclusions are presented. Again, the main emphasis throughout the thesis is to determine the relative importance of the mechanisms in contributing to the overall attenuation of seismic body waves in the upper crust and to what extent laboratory data may be used to infer rock properties from seismic data obtained in the field.



## CHAPTER 2

### REVIEW OF ATTENUATION MEASUREMENTS

In this chapter, previous experimental measurements of attenuation are discussed. In order to interpret these results and to appreciate the difficulties and weaknesses in attenuation measurements, a section describing common laboratory techniques is included. While a knowledge of common measures of attenuation is assumed, the definitions of these and derivations of their interrelationships are included in Appendix A.

#### 2.1 Laboratory Measurement of Attenuation

The accurate measurement of intrinsic attenuation is a difficult task and seriously limits the utilization of anelastic rock properties. Both in the laboratory and field, seismic wave amplitudes are strongly affected by geometrical spreading, reflections and scattering in addition to intrinsic damping. Thus, in many cases, to obtain the true attenuation it is necessary to correct for these other effects. This can be a formidable task.

Generally the methods for measuring attenuation in the laboratory can be separated into the following categories (Zener, 1948; Kolsky, 1953; Schreiber et al.,

1973):

1. Free vibration method
2. Forced vibration method
3. Wave propagation
4. Observation of stress-strain curves

Each method can be further split into subgroups.

The choice of an experimental method is based largely on the frequency range of interest, the actual values of attenuation, and the physical conditions under which the sample will be studied. For example, the use of stress-strain curves will provide information at frequencies below 1 Hz while resonance vibrations measure the attenuative properties in the range of 100 Hz-100 KHz and wave propagation experiments are commonly restricted to the ultrasonic range of 100 KHz or higher. And, while perhaps a more difficult technique to employ, the wave propagation method is most suited for jacketed samples in pressure vessels. Furthermore, each method determines a different attenuation or loss parameter. Their definitions and relationships must be specified if any meaningful comparison may be made among various laboratory measurements.

Of the four methods listed above, forced vibration (bar resonance) and wave propagation are utilized in this thesis. Descriptions of other common techniques will be presented for completeness and comparison while a detailed discussion of the specific techniques employed here are deferred until Chapter 3.

The most common measures of attenuation found in the literature are attenuation coefficient,  $\alpha$ , the "quality factor",  $Q$ , and its inverse,  $Q^{-1}$ , sometimes called the "internal friction". To avoid conflict in the name of an important attenuation mechanism,  $Q^{-1}$  will be referred to as the "dissipation factor" and may be defined as

$$Q^{-1} = \frac{\Delta W}{2\pi W} \quad (2-1)$$

where  $\Delta W/W$  is the fraction of strain energy lost per stress cycle. The relationship between  $Q$  and  $\alpha$  (derived in Appendix A) is given by:

$$Q = \frac{\pi f}{\alpha v} \quad (2-2)$$

where  $f$  is the frequency and  $v$  is velocity. The usefulness of the quantity  $Q$  is that it is related only

to the rate at which mechanical energy is converted into heat and is not dependent on any specific attenuation mechanism. Thus, for noncoupled mechanisms, the total  $Q^{-1}$  may be found by the sum of each individual contribution.

### 2.1a Free Vibration Method

In this technique the attenuation is found by the amplitude decay of successive cycles of free vibrations. In general, we may define the logarithmic decrement as:

$$\delta = \frac{\ln(A_1/A_2)}{(t_1-t_2)f} = \ln(A_\lambda/A_0) \quad (2-3)$$

where  $A_1$  and  $A_2$  are the amplitudes at times  $t_1$  and  $t_2$  and  $f$  is the natural free vibration frequency of the system. The alternative definition is in terms of the amplitude  $A_\lambda$ , one wavelength from a starting amplitude,  $A_0$ . For small attenuation:

$$Q^{-1} = \frac{\delta}{\pi} \quad (2-4)$$

where  $\delta$  is given in equation 2-3. This is approximately true provided that  $Q > 10$  (McSkimin, 1964).

This method has been implemented in several ways. The first is a torsion pendulum (Peselnick and Outerbridge,

1961) in which a rod of rock is clamped at the top and attached to a mass with a large moment of inertia at the bottom. If the mass is given a "kick" and the system is allowed to vibrate freely, the frequency is a function of the rock properties and the moment of inertia of the mass. The rate of decay of the amplitude of these oscillations is due to losses in the rock if other losses can be made small. One important application of this method is the study of elastic constraints and attenuation of metals and composite materials at high temperatures and very low frequencies on the order of 1 Hz (Kê, 1947; Kingery, 1959; Jackson, 1969). However, it is difficult to fabricate long cylindrical rock samples with uniform cross section needed for this type of experiment. Furthermore, the initial applied stress must be low so that: the sample does not fracture,  $Q$  and the elastic moduli are independent of amplitude and stress inhomogeneities in the sample are minimized.

Vibration may also be excited by piezoelectric, electromagnetic and electrostatic effects. These methods become necessary for short samples which have resonant frequencies in the KHz range. In each case, for rocks, one must apply a conductive coating or a transducer and thus corrections to the resonant frequency

must be made. While the effect of these corrections is minimal for attenuation measurements, they are crucial for the determination of elastic parameters. As with all resonant techniques the specific loss parameter determined depends on the type of vibration excited (White, 1965).

### 2.1b Forced Vibration Method

One of the more common methods for measuring attenuation is the forced longitudinal, flexural or torsional vibration of long bars. This is based on the phenomenon of standing waves. Under this condition for longitudinal and torsional waves the velocity of the wave is given by

$$v = \lambda f = \frac{2\ell f}{n} \quad n = 1, 2, 3, \dots \quad (2-5)$$

where  $f$  is the resonant frequency of mode  $n$  and  $\ell$  is the length of the sample. The expression for flexural waves is more complicated because the nodes do not occur at the quarter points.

Reasonably exact solutions of the three-dimensional wave equation exist for cylindrical and rectangular geometries, therefore these shaped bars are most suited for resonance experiments. Based on these solutions, Spinner and Tefft (1961) derived

relationships between the Young's modulus  $E$ , the shear modulus,  $\mu$ , and the resonant frequency,  $f$ . For longitudinal vibrations in a cylindrical rod:

$$E = \frac{\rho}{K_n} \left\{ \frac{2\ell f_n}{n} \right\}^2 \quad (2-6)$$

where  $K_n$  is the correction factor for the  $n^{\text{th}}$  mode,  $\rho$  the density and  $\ell$  is the length. In the case  $d/\lambda < 1$   $K_n$  as defined by Rayleigh (1945) is

$$K_n \approx 1 - \frac{1}{2} \{ \pi n \sigma d / 2\ell \}^2 \quad (2-7)$$

where  $d$  is the diameter and  $\sigma$  is the Poisson's ratio. A numerical solution of the same problem may be obtained for shorter rods. Note that except for very long and thin rods where  $K_n \approx 1$ , independent information on the Poisson's ratio must be obtained.

For torsional resonance, the shear modulus is given by:

$$\mu = \rho \{ 2\ell f_n / n \}^2 R \quad (2-8)$$

where  $R$  depends on the geometry and is equal to 1 for cylinders.

Equations for longitudinal vibrations in bars with rectangular cross sections have not been determined. The relationships for flexural vibration are more complicated and will not be presented here but may be found in Spinner and Tefft (1961) or Schreiber et al. (1973).

For a continuously driven system,  $Q$  may be found from the width of the resonance amplitude peak (Appendix A). Defining  $\Delta f$  to be the frequency range between those values for which amplitude is 3 db down from resonance, then:

$$Q = \frac{f_n}{\Delta f} \quad (2-9)$$

If the system can be driven easily, this method may be used for low  $Q$  materials with an accuracy of about 5-10% (Bozorth et al., 1951).

Again, the sample may be driven by electrostatic, electromagnetic or piezoelectric methods. Because of its weakness, electrostatic drives are more suited for high  $Q$  materials. Electromagnetic drives are useful if the sample is electrically conducting. Operation over a wide range of frequency is obtainable. Piezoelectric excitation (Quimby, 1925) is particularly simple to set up and will be used in this thesis. Very simply, piezoelectric transducers are cemented to the specimen and the combination is made to resonate. Corrections must be



made for the impedance and mechanical  $Q$  of the transducer (Chapter 4) but highly efficient, low loss ceramic transducers are available making this method attractive for both low and relatively high  $Q$  samples.

While the resonance methods are easily implemented and the  $Q$  values determined over a wide frequency range, the physical conditions in which these types of experiments may be performed without concern for extraneous losses are limited. In particular, it is necessary to consider radiation losses into the surrounding medium.

In torsional vibration only shear waves are leaked to the surrounding medium (e.g. air, gas). Since coupling is poor, this results in little energy loss. For longitudinally waves, however, damping along the cylindrical surface and radiation from the ends can be substantial. Browne and Pattison (1957) analyzed this problem in great detail and found the contribution to the logarithmic decrement due to radiation from the sample sides to be:

$$\delta_1 = \frac{\rho'}{\rho} \left\{ \pi d \sigma / \ell \right\}^2 \quad (2-10)$$

where  $d$  is the diameter,  $\ell$  is the length,  $\sigma$  is the Poisson's ratio,  $\rho$  is the density of the sample and  $\rho'$  is the

density of the surrounding medium. Treating the ends of the sample to be piston radiators, they found that the portion of the decrement due to this loss to be:

$$\delta_2 = \frac{2\rho'c}{\lambda f \rho} \left\{ 1 - \frac{J_1(2kr)}{kr} \right\} \quad (2-11)$$

where  $c$  is the sound velocity in the medium,  $f$  is the frequency,  $k$  is the wavenumber and  $r$  is the radius of the sample. These types of corrections are negligible for low  $Q$  materials in ambient air conditions. For high  $Q$  materials such as metals it would be advised to perform resonance experiments under vacuum. However, even for rocks, losses when the sample is subjected to pressure can be high compared to the intrinsic attenuation. For these types of experiments to be performed successfully it is imperative from equations 2-10 and 2-11 that the density and sound speed of the pressure medium be as low as possible. For this reason, hydrogen or helium is commonly used.

A further consideration is the effect of a jacket on the sample which will alter the resonant frequency and the apparent attenuation. These changes can be calculated using Rayleigh's principle (Gardner et al., 1964) and are generally small. For some porous rocks, though, the jacket will penetrate the sample and thus the results obtained represent an average of the sample and jacket

(Gardner et al., 1964).

### 2.1c Wave Propagation

The use of wave propagation experiments in the lower ultrasonic frequency range to determine attenuation in the laboratory is of particular interest since the loss parameters involved closely parallel those observed in the field. However, these types of techniques are fraught with experimental and interpretational difficulties. These methods assume that the amplitude of the seismic wave (generally considered to be a plane wave) decays exponentially with distance or time or that losses other than the intrinsic attenuation can be corrected for. This can be a formidable task. The extraneous losses include beam spreading, coupling losses, diffraction losses and wedging effects. It is not the purpose of this section to detail the causes and remedies of these difficulties but a brief description of each will be given.

At low frequencies ( $<1$  MHz) the effect of beam spreading can become significant. While direct corrections can be made, their validity is based on the assumption of plane or spherical waves. The extent of the plane wave region, dependent on the size of the transducer and wavelength of the seismic wave, must be determined. It is easier, in most cases, to design the

experiment so that spreading losses are minimal compared to the intrinsic attenuation.

At low frequencies, relative to the transducer diameter, diffraction losses may become important. Because of beam spreading, sidewall reflections and mode conversions may occur, interfering with the directly propagating wave. This interference can be readily observed in the pulse-echo technique as a non-exponential decay in amplitude. While it is possible in many cases to design the experiment so that the sample diameter to transducer diameter ratio is large, this is not always possible and diffraction may cause problems even with pulse transmission techniques. Turell et al. (1969) have treated diffraction theoretically but generally this problem must be tackled empirically.

Energy loss can occur due to the transducer itself, transducer coupling to the sample (bond) and the electrical measurement system. The transducer properties are known and one can choose a material with a much higher mechanical  $Q$  than the sample. However the other losses are impossible to calculate theoretically and must be determined empirically (Truell et al., 1969) or eliminated by the experimental method.

Finally, if the ends of the sample are not exactly parallel, non-exponential losses due to phase variations over the surface of the transducer may result. That is, a plane wave is not reflected or transmitted in phase by a non-parallel or "wedged" boundary. Again, this effect is a most important consideration for the pulse echo technique but unlike diffraction, is more pronounced at higher frequencies. Similar errors can occur if the transducer bond thickness is nonuniform or if, in the case of single crystals, elastic constants vary slightly within the ultrasonic beam. This problem has been analyzed by Truell and Oates (1963) and it is shown that in order to reduce the non-parallelism effects, the allowed deviation is inversely dependent on the  $Q$  of the material and the frequency.

All of the above corrections must be considered in terms of the problem to be solved. For low  $Q$  samples such as rocks, measured at low ultrasonic frequencies, nonparallelism is unimportant while diffraction may alter the result one wants to obtain. Furthermore, in designing an experiment to eliminate one of the effects, another might be enhanced. For example, it would be desirable to have the sample diameter several times larger than the transducer diameter to reduce sidewall reflections but at the lower frequencies, large diameter

transducers result in less beam spreading. Clearly compromises must be reached for each experiment.

In general, wave propagation experiments can be classified by pulse-echo or through-transmission methods. Also the type of excitation may either be a pulse, which provides an attenuation value averaged over a relatively broad frequency band, or a tone burst which is strictly band limited.

In the pulse-echo technique, the attenuation is found by observing the amplitude decay of multiple reflections from a free surface. Of course, exponential decay must be assumed. If the electronic measuring system is linear and the amplitudes can be directly determined then the attenuation coefficient can be calculated by:

$$\alpha = \frac{1}{(x_2 - x_1)} \ln\{A(x_1)/A(x_2)\} \quad (2-12)$$

where  $x_2 - x_1$  would be twice the sample length and  $A(x_1)$  is the amplitude at one echo while  $A(x_2)$  is the amplitude at the next echo.

Most times, however, the attenuation coefficient is found by a calibrated exponential decay curve superimposed on the echo images on an oscilloscope. The curve is generated by allowing a capacitor

discharge through a known resistor so that the R-C time constant can be evaluated. Measurements obtained in this way are in terms of inverse time. The essential advantage of this method over using the absolute amplitudes is that non-exponential behavior, if present, is easily seen. However, the technique does not work well for high attenuation. In this case, the pulse comparator method must be employed where a pulse of the same frequency as that applied to the transducer is sent through the same electronics. If this comparator pulse can be accurately attenuated then the relative amplitude loss between two echos can be determined.

The pulse echo techniques are generally used for high Q samples and are popular for determining the Q of single crystals. An important consideration of this method, however, is that the reflection at the free boundary is loss free. This assumption limits the method's usefulness in high pressure studies where energy will be lost into the pressure medium. The technique has, though, been used successfully on some fine-grained limestones at atmospheric pressure (Peselnick and Zietz, 1959). In this study, beam spreading, diffraction losses and incomplete reflection at the free surface were deduced to be negligible compared to the intrinsic attenuation.

The method for measuring attenuation that is most suited for use with jacketed samples in pressure vessels is through-transmission. And, in the use of spectral ratios, many of the problems that plague the pulse echo method can be, at least conceptually and mathematically, eliminated.

Transmission experiments can be categorized in terms of the transmitter and receiver transducer locations and sample size. In most cases the transducers are located at opposite ends of the sample. If the sample diameter is larger than the length, sidewall reflections are minimized. Alternatively, the guided wave method may be used using a cylindrical rod as a wave guide (McSkimin, 1956). The primary distinction is in the types of corrections that must be made. A further arrangement involves large blocks of material on which the transmitter and receiver are moved to measure the amplitude loss as a function of distance (Watson and Wuenschel, 1973). In this case, if the transducer diameters are small and the distances large with respect to the wavelength, simple inverse length beam spreading may be assumed.

The data for the first two arrangements may be analyzed in terms of echoes as before. While neither arrangement provides greater accuracy, the guided wave



method requires extensive sample preparation and calculations to determine the effect of mode conversions at the sidewall. These calculations not only depend on the sample's elastic properties but also on the attenuation. Short sample lengths compared to the diameter minimize mode conversions but the diffraction fields must be accounted for.

For large samples the attenuation may be found with some uncertainty from the amplitude decay of a particular peak in the wave train as a function of transmitter receiver separation. Of course it is assumed in this case that the coupling between the transducer and sample is the same in each case and that spreading has been accurately accounted for.

Attenuation may also be found from pulse type waveforms using a predictive waveform. If the input pulse is known or the waveforms at greater distances are normalized to a starting point, then the match of a synthetic waveform for a variable  $Q$  material with the actual waveform will yield an attenuation value (Watson and Wuenschell, 1973).

Spectral ratios is by far the most common technique used in seismology and allows for the elimination of many of the problems associated with wave propagation methods. This technique relies on the fact that high

frequencies are preferentially attenuated relative to low frequencies. In general, the spectral amplitude of the propagating wave may be expressed as (Ward and Toksöz, 1971):

$$A(f,x) = GA_r(f)\exp(-t^*f) \quad (2-13)$$

where G includes geometrical spreading, and transmission or reflection coefficients,  $A_r$  is the receiver response and

$$t^* = \pi \int_{\text{path}} \frac{dx}{QV} \quad (2-14)$$

for frequency independent Q. This expression is also valid for slowly varying Q in the frequency band of interest. For spectral amplitudes obtained at two points for a common source then:

$$\ln \frac{A_1(f)}{A_2(f)} = (t_2^* - t_1^*)f + \ln \frac{G_1}{G_2} + \ln \frac{A_{r1}(f)}{A_{r2}(f)} \quad (2-15)$$

If the receiver responses are known or are equal, equation 2-15 may be reduced so that the slope of a straight line fitted to the log of the spectral ratios versus frequency will yield the differential attenuation,  $t_2^* - t_1^*$ , between the two receivers.

A modification of this technique has been successfully applied to laboratory samples (Toksöz et al., 1978). Used in this thesis, this method allows the determination of attenuation in a rock sample relative to a high  $Q$  standard. This turns out to be a convenient method to measure  $Q$  over a variety of physical conditions. It is, however, for relatively narrow bandwidth signals as obtained in the lab, limited to samples with  $Q < 100$ . This is due to the difficulty in obtaining a good correlation coefficient for a linear regression analysis of data with a low slope (high  $Q$ ). A more complete discussion of this method is deferred until the next chapter where details of data reduction and analysis are presented.

#### 2.1d Observation of Stress-strain Curves

Energy loss may be measured graphically from stress-strain curves in loading-unloading cycles at very low frequency. Attenuation occurs during both hydrostatic and deviatoric loading (Walsh et al., 1970) and is reflected in nonrecoverable volume change. Specifically, the area between the loading and unloading paths on a stress-strain curve is the energy lost,  $\Delta W$ , in that cycle. The relative attenuation may be found by dividing  $\Delta W$  by the maximum work done during loading,  $W$ , i.e., the area under the loading path.

A direct comparison of results obtained by this method with those obtained by ultrasonics or resonant bars is difficult primarily because strain amplitudes involved are much higher than would be found in seismic or ultrasonic waves. Perhaps the method's greatest applicability is in the study of the properties of attenuation near an earthquake or underground explosion source. However, recent advances in servo feedback controls and strain gage technology may make this technique attractive for future experimental work at low strain amplitudes.

## 2.2 Previous Experimental Work

A variety of individual attenuation measurements have been obtained for many rock types over wide ranges of physical conditions and frequencies, and by many techniques. Unfortunately seldom are the variations in attenuation with respect to changes in physical state systematically examined. At best, one may deduce several qualitative generalizations concerning attenuation and its behavior with varying rock type, porosity, frequency, pressure, strain amplitude and temperature. In this section individual determinations of attenuation will be briefly summarized, followed by a more extensive review of data that is pertinent to this thesis.

## 2.2a Individual Measurements of Attenuation

A representative sample of individual attenuation measurements is listed in Table 2.1 along with other pertinent parameters. Another summary taken from the compilation of Bradley and Fort (1966) is shown graphically in Figure 2-1, where  $Q$  is a function of rock type and porosity is plotted. The values taken are generally at surface pressure although they cover a wide frequency range. Figure 2-1 shows the wide variability of attenuation in rocks and a general trend of  $Q$  inversely proportional to porosity. As noted by many investigators (Wyllie, et al., 1962; Knopoff, 1964, Bradley and Fort, 1966; and others), the accumulation of individual attenuation measurements has led to a series of generalities that may be applied to the nature of  $Q$  in crustal rocks. These are summarized below, with references to later sections of this paper where certain effects are discussed in more detail.

1. Frequency Dependence. Laboratory experiments show that  $Q$  may be independent of frequency ( $\alpha$  proportional to  $f$ ) over a broad frequency range ( $10^{-2}$ - $10^7$ Hz) especially for some dry rocks (Birch and Bancroft, 1938; Born, 1941; McDonal et al., 1958; Peselnick and Outerbridge, 1961; Attwell and Ramana, 1966; Pandit and Savage, 1973; and others).  $Q^{-1}$  in liquids, however, is proportional to frequency (Pinkerton, 1947) so that in some highly porous

and permeable rocks the total  $Q^{-1}$  may contain a frequency dependent component (Born, 1941; Wyllie et al., 1962). This component may be negligible at seismic frequencies even in unconsolidated marine sediments (Hamilton, 1972a).

2. Strain Amplitude. Attenuation appears to be independent of strain amplitude for low strains such as those associated with seismic waves (Mason, 1958; Gordon and Davis, 1968). Both the measurements carried out for this thesis and the studies of Winkler et al. (1977) suggest that attenuation may rapidly increase above some strain amplitude threshold. This will be discussed in detail in Chapter 6.

3. Fluid Saturation. Attenuation for fluid saturated rocks is higher than for dry rocks and depends on the degree of saturation, fluid type, and frequency in a complicated way. For rocks fully saturated with a low viscosity fluid (water, oil) it is generally found that at ultrasonic frequencies  $Q_p \geq Q_s$ . This topic will be further discussed in the next section.

4. Pressure and Stress Dependence. Observations show that attenuation decreases with increasing confining pressure. This is usually considered to be due to the closing of cracks in the rock matrix. Data supporting this and theoretical models of the pressure effects will be discussed in later sections of this paper. For applied

non-hydrostatic stress, the attenuation appears to be anisotropic (Merkulova, et al., 1972; Walsh et al., 1970). For shear waves polarized normal to the axis of maximum compression, attenuation is lowest due to the closure of cracks with faces normal to the axis (Lockner et al., 1977). At high differential stresses, the onset of dilatancy increases the attenuation (Lockner et al., 1977).

5. Temperature Dependence. The small amount of data on this topic (Volarovich and Gurevich, 1957; Gordon and Davis, 1968) indicate that  $Q$  is generally independent of temperature at temperatures low relative to the melting point. An increase of attenuation in quartzite with temperatures above 150°C noted by Gordon and Davis (1968) may be due to thermal cracking of the rock. Near the boiling temperatures of pore fluids, attenuation may be affected strongly by temperature.

#### 2.2b Correlation of $Q$ With Simple Rock Properties

In addition to the generalizations listed above, several investigators have attempted, with limited success, to correlate attenuation with simple rock properties such as the porosity, permeability, grain size, or shear modulus. This at first seems to be an attractive approach since, if successful it would provide an important diagnostic for determining rock lithology and reservoir

characteristics directly from seismic data. However, as will be seen later, the attenuation in rock depends not so much on the bulk properties but rather on micro-properties such as crack density, distribution and structure, and pore fluid-grain interaction.

The dependence of attenuation on porosity has been alluded to in Figure 2-1. Experiments by Toksöz et al. (1978) show for a very limited sample of sandstones that  $Q$  is inversely proportional to porosity. This effect probably reflects the fact that higher crack densities and permeability generally accompany high porosity. Attenuation measurements on fine-grained low porosity limestones (Peselnick and Zietz, 1959) indicate that higher porosity may be associated with higher attenuation but the authors prefer a correlation with grain size. In this case, attenuation is higher for samples with smaller grain sizes supporting the conclusion that the major contribution to attenuation is at the grain boundaries.

Any correlation with porosity is apparently not valid between different rock types.  $Q$  values of the Spergen limestone with a 14.8% porosity obtained by Toksöz et al. (1978) are nearly twice those obtained for a Navajo sandstone with a porosity of 12.5%. It is clear from the above discussion that porosity, by itself, is not a good



diagnostic. High porosity does not insure high attenuation.

Attenuation may be correlated with velocities (i.e., elastic moduli). This may be due, in part, to the possibility that conditions that determine elastic properties also effect anelastic properties. In particular, since in most cases in the earth, attenuation is associated with shear, rather than bulk, loss, it is not surprising that  $Q$  can be correlated with the shear modulus,  $\mu$  (Hamilton, 1972b). As would be expected, the strongest correlation is between  $Q_s$  and  $\mu$ . While, in the broadest sense,  $Q_s$  increases with increasing  $\mu$  (Hamilton, 1972), there is much scatter to the data and again, large differences exist among differing rock types.

### 2.2c Attenuation as a Function of Saturation Conditions

Although of great interest to the exploration community, relatively little experimental work has been done on the nature of attenuation as a function of saturation conditions. Even the published data must be examined critically due to the inherent difficulties involved in partial saturation work. Unfortunately, little or no detailed description is given in the experimental literature about the techniques of fluid saturation. An important, yet experimentally difficult, aspect is maintaining a homogeneous distribution of the saturant in the bulk of the rock. One must also address the

question as to what constitutes a "dry" rock. In most cases, samples are oven-dried prior to fluid injection. Heating the sample will cause some alterations of the matrix structure. In any event, it is nearly impossible to remove the fluid completely; at least a monomolecular layer of fluid will probably remain in the thinnest cracks.

In this and the next section the data are generally presented in terms of the relative change in  $\alpha$  or  $Q^{-1}$ . In many cases, the absolute determinations of attenuation are unreliable, yielding unreasonable values.

The degree of saturation and the type of saturant, characterized primarily by viscosity, appear to play an important role in attenuation. Studies of the effect of partial saturation by various fluids have been reported in Born (1941), Obert et al. (1946), Collins and Lee (1956), Wyllie et al., (1962), and Gardner et al. (1964). A summary of these results is shown in Figures 2-2 to 2-5, where  $Q$  or the fractional change in  $Q$  is plotted as a function of percent saturation. As pointed out in the preceding section, the overall  $Q$  of the rock may be considered to contain a frequency independent component plus a frequency dependent component due to the fluid inclusions. Thus the effect of partial saturation may

be frequency dependent (Born, 1941). However, since the curves shown here were taken over a wide range of frequencies but exhibit similar behavior, fluid losses may not dominate frequency independent losses in most rocks at surface pressures.

Most of the rocks shown in Figures 2-2 to 2-5 are saturated with water, chemically active with intergranular material. The exception is the alundum ( $\text{Al}_2\text{O}_3$ ) saturated with soltrol, a relatively inert petroleum naphtha, shown in Figure 2-3. The behavior of attenuation as a function of water saturation is similar for all rocks.  $Q$  is sharply reduced at low saturations presumably due to the wetting effect of water entering the fine cracks, possibly reacting with intergranular material and softening the rock. Also note that the effect of pressure is to reduce the effect of saturation for both P and S waves as shown in Figures 2-4 and 2-5 since the finer cracks are closed. In the case of soltrol saturation (Figure 2-3) the change in  $Q$  observed for water saturation is not seen. This implies that the effect observed for water saturation is primarily due to either chemical alteration of the intergranular material or a wetting phenomenon. Since it is unlikely that water reacts strongly with alundum, we favor the explanation that different wetting properties cause the different

saturation effects observed. In real rocks, of course, a combination of the two mechanisms is likely.

Of particular interest are the relative contributions of shear,  $Q_{\mu}$  and bulk,  $Q_K$ , loss as functions of saturation. The decomposition of the  $Q_E$  and  $Q_S$  measurements of Gardner et al. (1964) into these components is shown in Figure 2-6 for a differential pressure of 500 psi (35 bars). The results are similar for other pressures. It is evident that for dry rocks, shear losses dominate bulk losses ( $Q_{\mu} < Q_K$ ) while for partial saturation, a reversal occurs and  $Q_K < Q_{\mu}$ . For full saturation it appears from the data of Toksöz et al. (1978) for a similar Berea sandstone,  $Q_{\mu} < Q_K$  as in the dry rock. If high bulk attenuation really exists, this may require a mechanism in the partially saturated case that is not operative in dry or completely saturated rocks. Furthermore, this mechanism must result primarily in bulk rather than shear loss.

The effect of fluid type, i.e. viscosity, has been discussed in detail by Wyllie et al. (1962) and Nur and Simmons (1969a). The dependence of attenuation on fluid viscosity is complicated and not at all obvious from results presented by Wyllie et al. (1962). Taking these data at face value, it would appear that very large viscosity fluids (e.g. glycerol) result in small fluid contributions to attenuation. This makes sense for some

attenuation mechanisms such as fluid flow in that higher viscosity fluids are equivalent to a decrease in the effective permeability. However, Nur and Simmons (1969a) have shown that the viscosity effect is frequency dependent, consistent with a relaxation type mechanism. In their experiment, a Barre granite (porosity = 0.6%) was saturated with glycerol which has a viscosity extremely dependent on temperature. Thus by varying the temperature of the saturated sample, the effect of viscosity on velocities and relative attenuation of P and S waves is measured. The attenuation of S waves as a function of pore fluid viscosity is shown in Figure 2-7. The relaxation peak occurs at a viscosity where the characteristic time is equal to the wave period. An experiment reported by Gordon (1974) shows similar results.

#### 2.2d Attenuation as a Function of Pressure

The pressure dependence of attenuation has been generally neglected by most investigators yet the behavior of  $Q$  with pressure can yield as much information about mechanisms as the frequency dependence. When a rock is subjected to hydrostatic pressure such as overburden pressure, its elastic and anelastic properties will change. The behavior of elastic properties may be found in Toksöz et al. (1976). The most important factor causing changes in the velocity is the change of porosity with pressure;

in particular, the closing of thin cracks. This also holds true for changes in attenuation as will be discussed in the next section. In all cases, attenuation decreases ( $Q$  increases) with increasing pressure. Experimental data verifying this are found in Gardner et al. (1964), Klima et al., (1964), Levykin (1965), Gordon and Davis (1968), Al-Sinawi (1968), Walsh et al., (1970) and Toksöz et al. (1978). For these data the pressure given is the differential or effective pressure,  $P_d = P_c - P_f$ , where  $P_c$  is the confining pressure and  $P_f$  is the fluid or pore pressure. This relationship generally holds for velocity as demonstrated by laboratory tests (Wyllie et al., 1958; Nur and Simmons, 1969b).

The attenuation of P waves in diabase and greywacke were measured by Klima et al. (1964) up to a pressure of 4 kilobars (kb) by a pulse transmission method with a prevailing frequency of 0.9 MHz. Although not stated explicitly, the samples are assumed to be air dry. The results of this experiment are shown in Figure 2-8 which plots the change in the attenuation coefficient,  $\alpha$ , as a function of pressure. In all cases a clear decrease in  $\alpha$  is observed up to about 1 kb. The relative changes in attenuation are greater than those of the velocity measured in the same type rocks under the same conditions (Pros et al., 1962).

Levykin (1965) investigated the attenuation of both P and S waves in several igneous and metamorphic rock types up to pressures of about 4 kb. A pulse echo technique at a frequency of 1 MHz was used. Samples were air dry. The results of these experiments for several gneiss samples are shown in Figure 2-9. Again, the attenuation decreases rapidly with increasing pressure, leveling off after about 1 kb. Levykin attributes the different extent to which attenuation is changed under pressure to be due to differences in the weathering of the rocks.

Gordon and Davis (1968) studied the effect of pressure (up to 4 kb) on a fluid saturated granite using slow stress cycles ( $f = 10$  MHz). Their data are reproduced in Figure 2-10. The same features as seen in the previous works are evident here.

So far only data for low porosity rocks, either dry or completely saturated have been considered. However, the pressure effect for a partially saturated Berea sandstone has been studied by Gardner et al. (1964). Both extensional and torsional  $Q$  values were determined using resonance techniques at frequencies up to 30 KHz. External influences on the sample, such as losses into the pressure medium were considered. These data are shown in Figures 2-4 and 2-5. The same general behavior is seen for the

data in Toksöz et al. (1978) for dry, methane, and water-saturated Berea sandstone at ultrasonic frequencies using the pulse transmission technique. The  $Q$ , however, levels off at a lower pressure than for the igneous and metamorphic rocks.

The variation of attenuation of P and S with pressure was also studied for a variety of rock types by Al-Sinawi (1968). A pulse transmission technique using 122 KHz transducers was used and the pressures for which measurements were taken were 0.5, 1, and 2 kb. All of the rocks studied were sedimentary except a granite gneiss and a volcanic tuff. Al-Sinawi found, as observed before, that both  $\alpha_p$  and  $\alpha_s$  decreased with pressure. In some rocks, particularly limestones, the pressure effect is different, however, this is not completely described.



Table 2.1 Measured Body Wave Q For Several Rock Types

Rock	Q	Frequency, Hz	Method	Reference
Quincy Granite	125	$(.14-4.5) \times 10^3$	long resonance	Birch and Bancroft (1938)
	166		tors. resonance	
Solenhofen Limestone	112	$(3-15) \times 10^6$	P wave pulses	Peselnick and Zietz (1959)
	188		S wave pulses	
I-1 Limestone	165	$(5-10) \times 10^6$	P wave pulses	Peselnick and Zietz (1959)
Hunton Limestone	65	$(2.8-10.6) \times 10^3$	long. resonance	Born (1941)
Amherst Sandstone	52	$(.930-12.8) \times 10^3$	long. resonance	Born (1941)
Berea Sandstone (brine saturated)	10	$(.2-.8) \times 10^6$	P and S wave pulses	Toksóz et al. (1978)
Navajo Sandstone	21	50 - 120	flexural vibrations	Bruckshaw and Mahanta (1954)
Pierre Shale	32	50 - 450	P waves in situ	McDonel et al. (1958)
	10		S wave in situ	

## FIGURE CAPTIONS

Figure 2-1.  $Q$  as a function of porosity. Data for igneous and metamorphic rocks (triangles), limestones (squares), and sandstones (circles) are taken from Bradley and Fort (1966) and cover wide frequency and saturation ranges.

Figure 2-2. Change in  $Q$  as a function of saturation. Data from Obert et al. (1946) and Martin, reported in Collins and Lee (1956).

Figure 2-3. Change in  $Q$  as a function of soltrol and water saturation in alundum at about 10 kHz. Data from Wyllie et al. (1962). Samples 7915-B and 7928-B for soltrol and water, respectively.

Figure 2-4.  $Q$  as a function of saturation and differential pressure in Berea sandstone, extensional mode. Data from Gardner et al. (1964).

Figure 2-5.  $Q$  as a function of saturation and differential pressure in Berea sandstone, torsional mode. Data from Gardner et al. (1964).

Figure 2-6. Shear attenuation ( $Q_{\mu}$ ) and bulk attenuation ( $Q_K$ ) as functions of saturation in Berea sandstone at a differential pressure of 500 psi (35 bars). Data are calculated from the  $Q$  values shown in Figures 2-4 and 2-5.

Figure 2-7. Relative attenuation of S waves as a function of pore fluid viscosity in Barre granite. Data from Nur and Simmons (1969a).

Figure 2-8. Change in the attenuation coefficient as a function of pressure for several rocks. Data from Klima et al. (1964).

Figure 2-9. Change in the attenuation coefficients of P and S waves as functions of pressure for several gneisses. Data from Levykin (1965).

Figure 2-10.  $Q^{-1}$  as a function of differential pressure in a granite. Data from Gordon and Davis (1968).

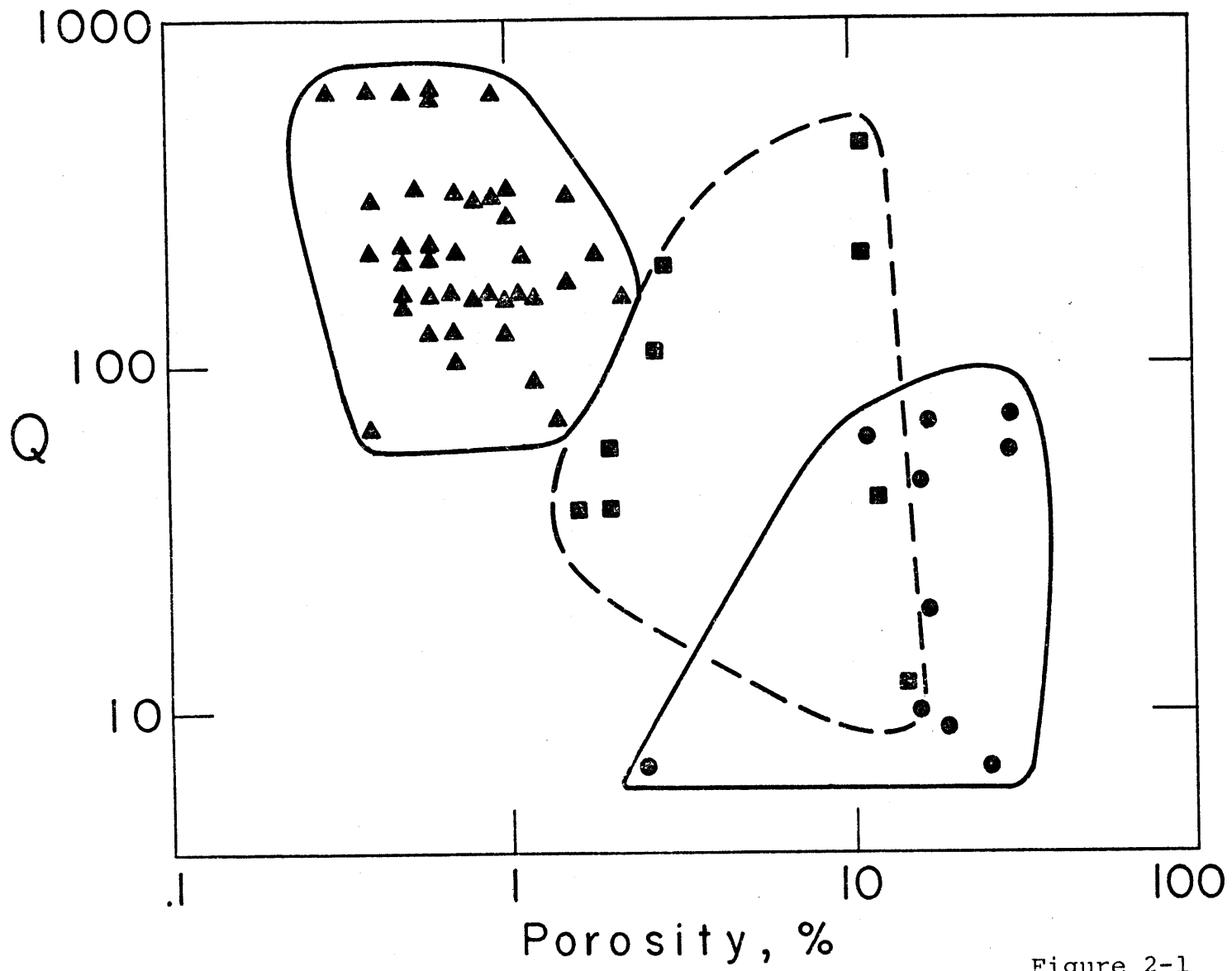


Figure 2-1

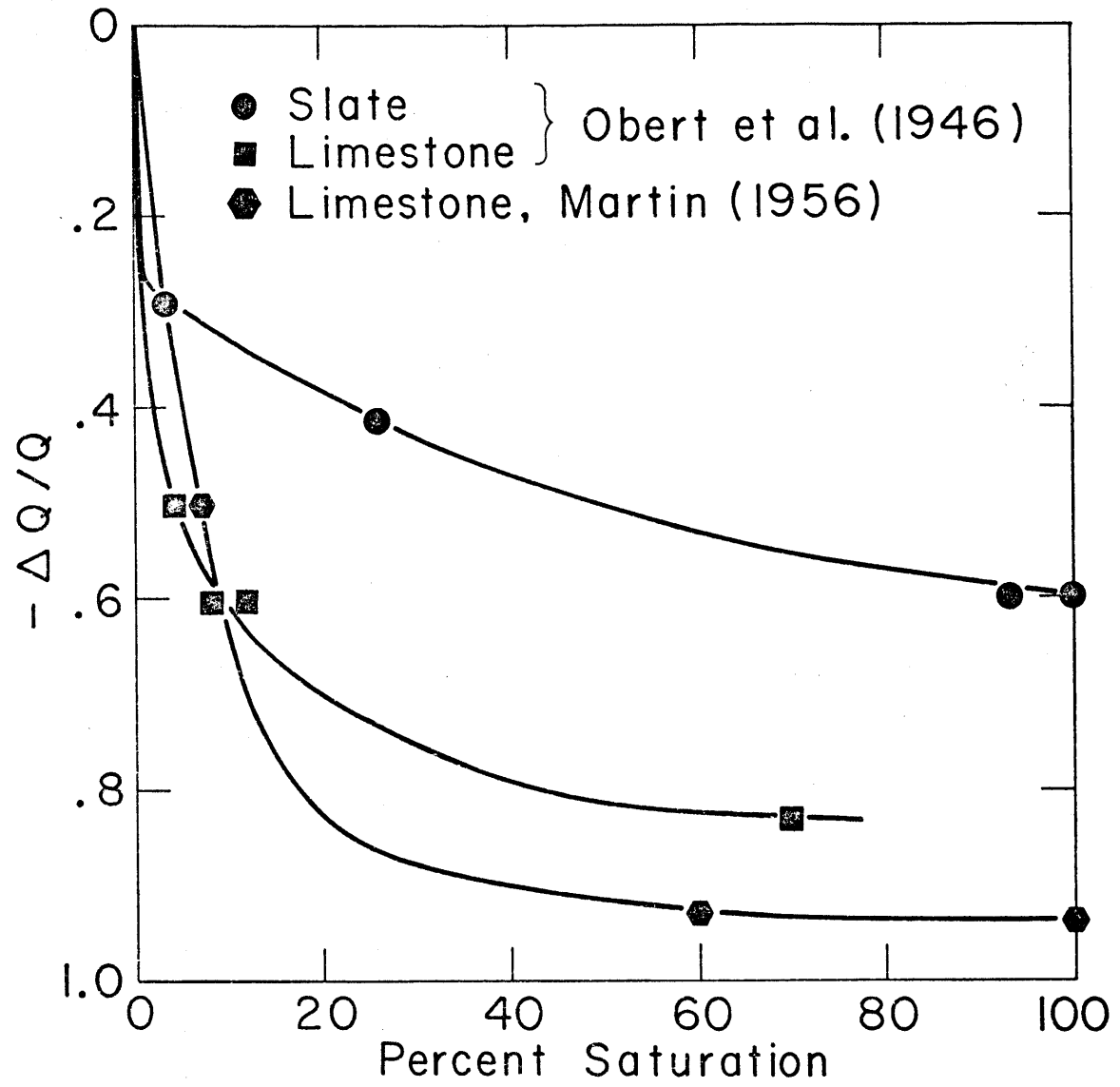


Figure 2-2

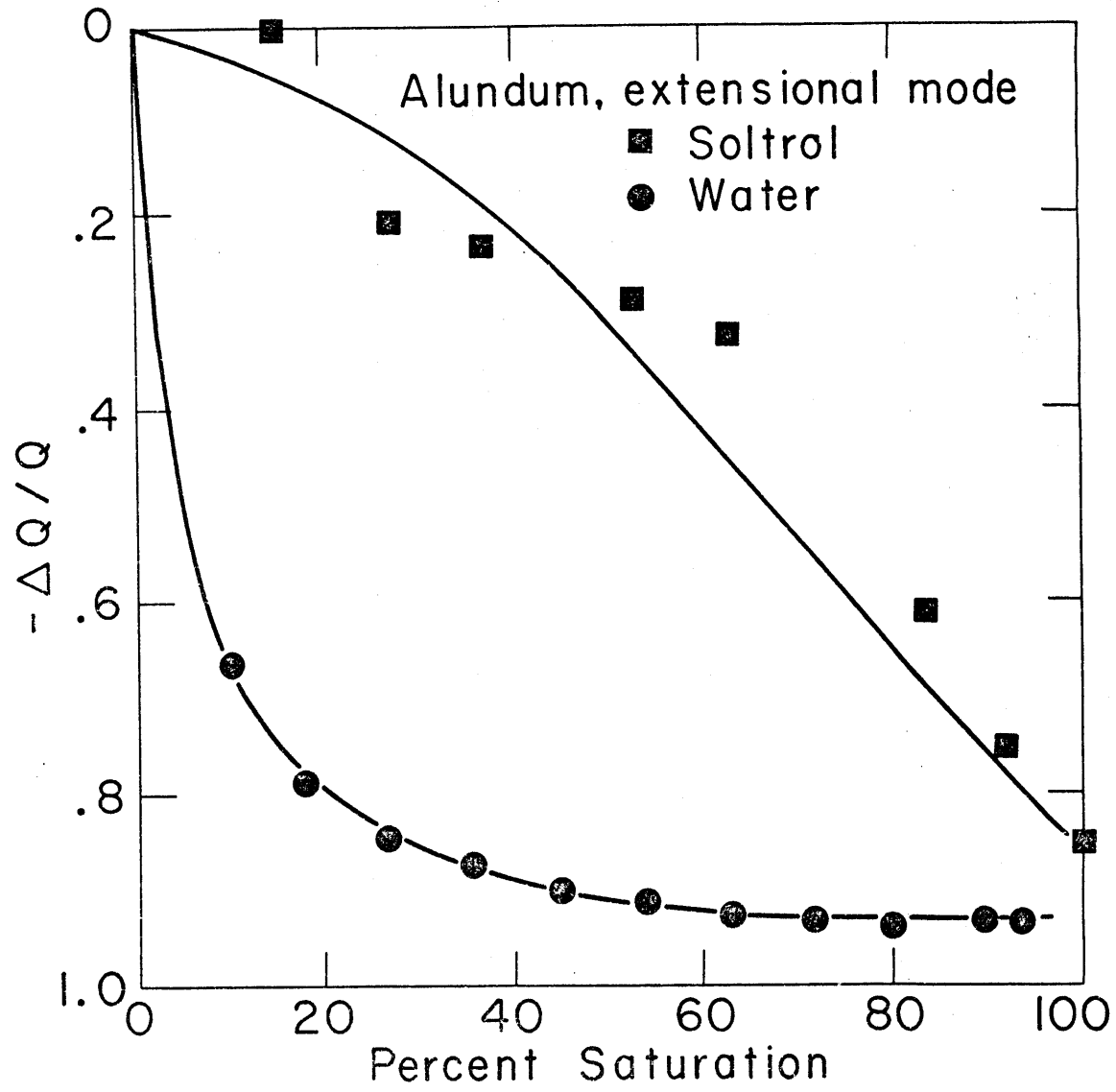


Figure 2-3

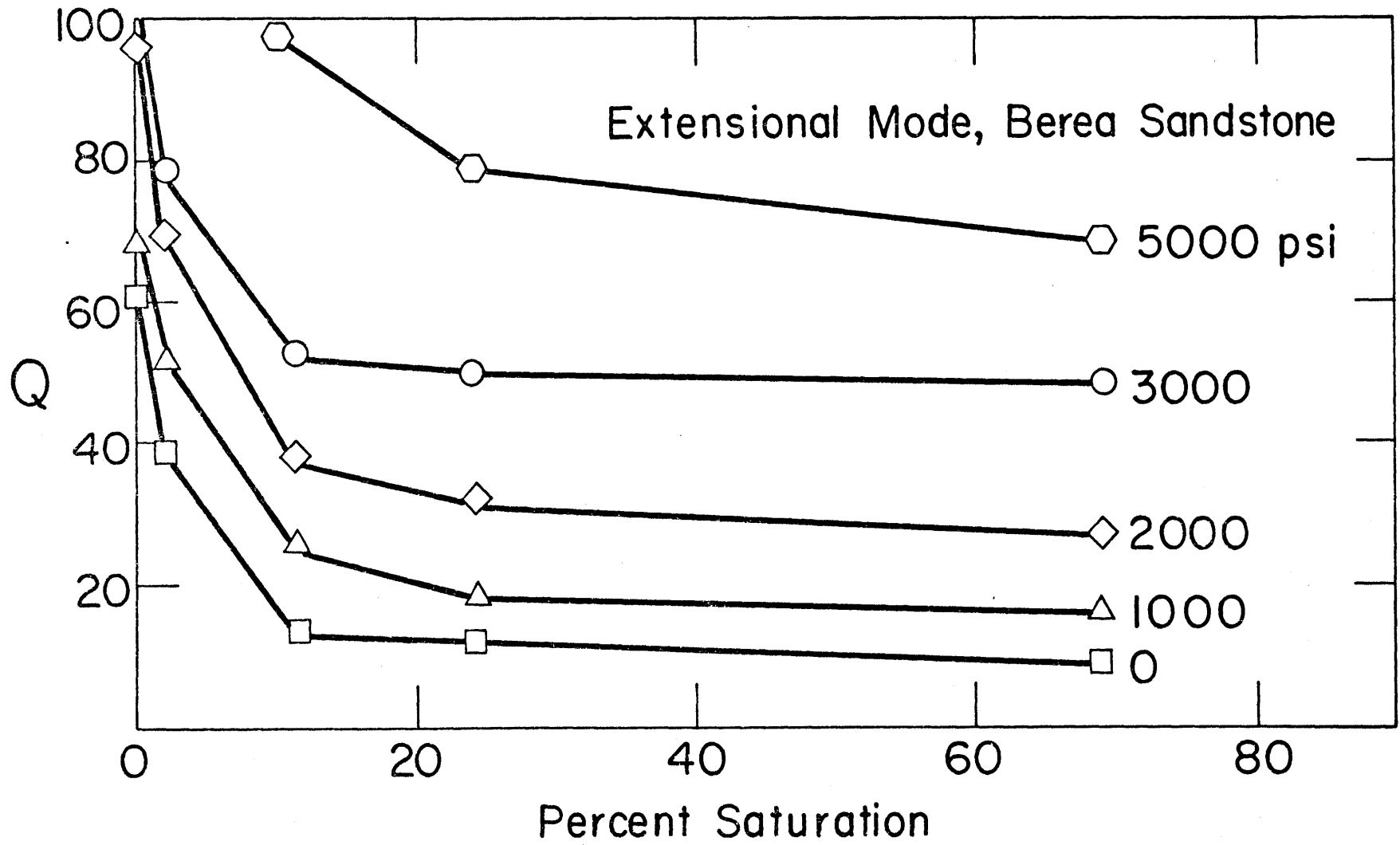


Figure 2-4

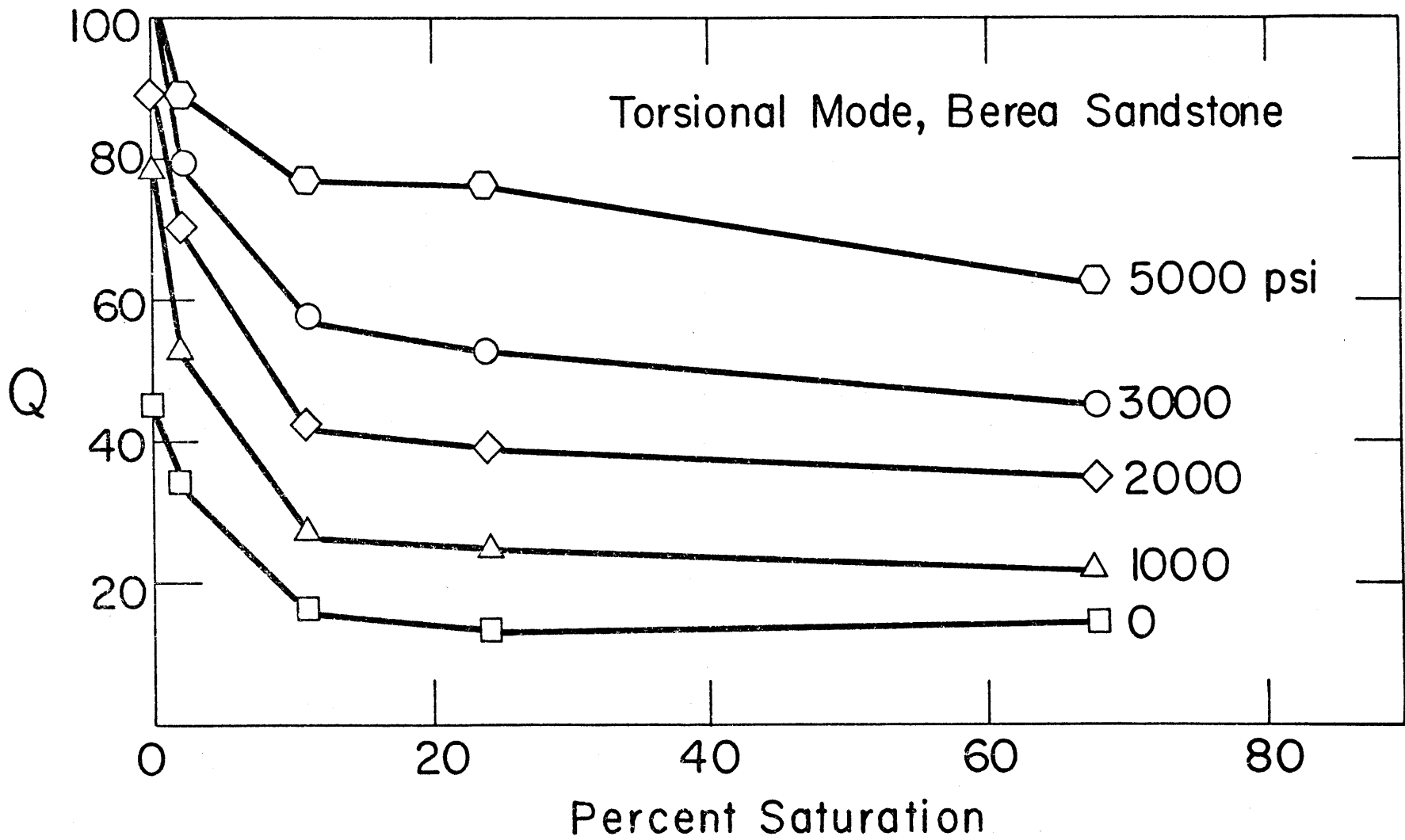


Figure 2-5



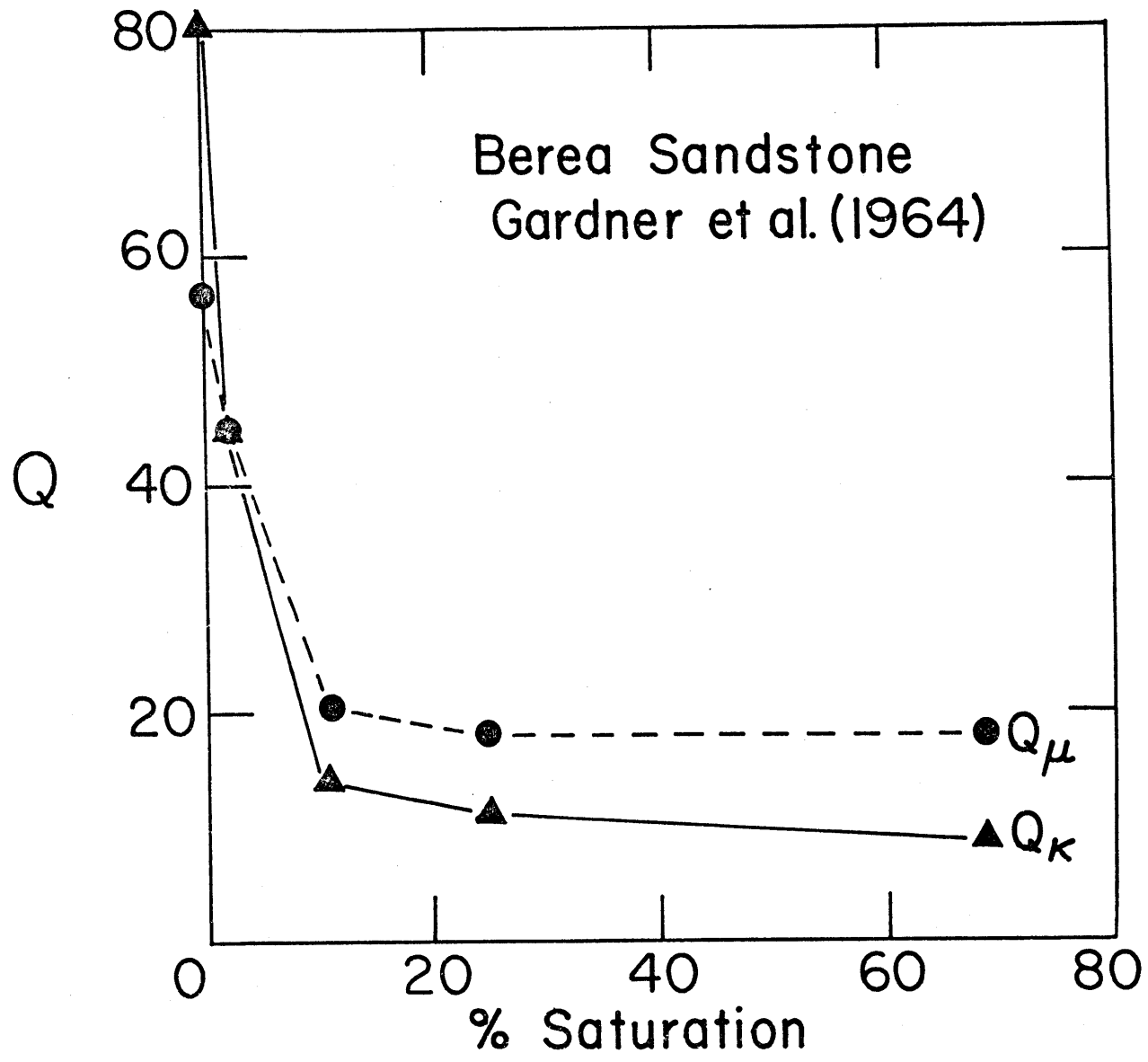


Figure 2-6

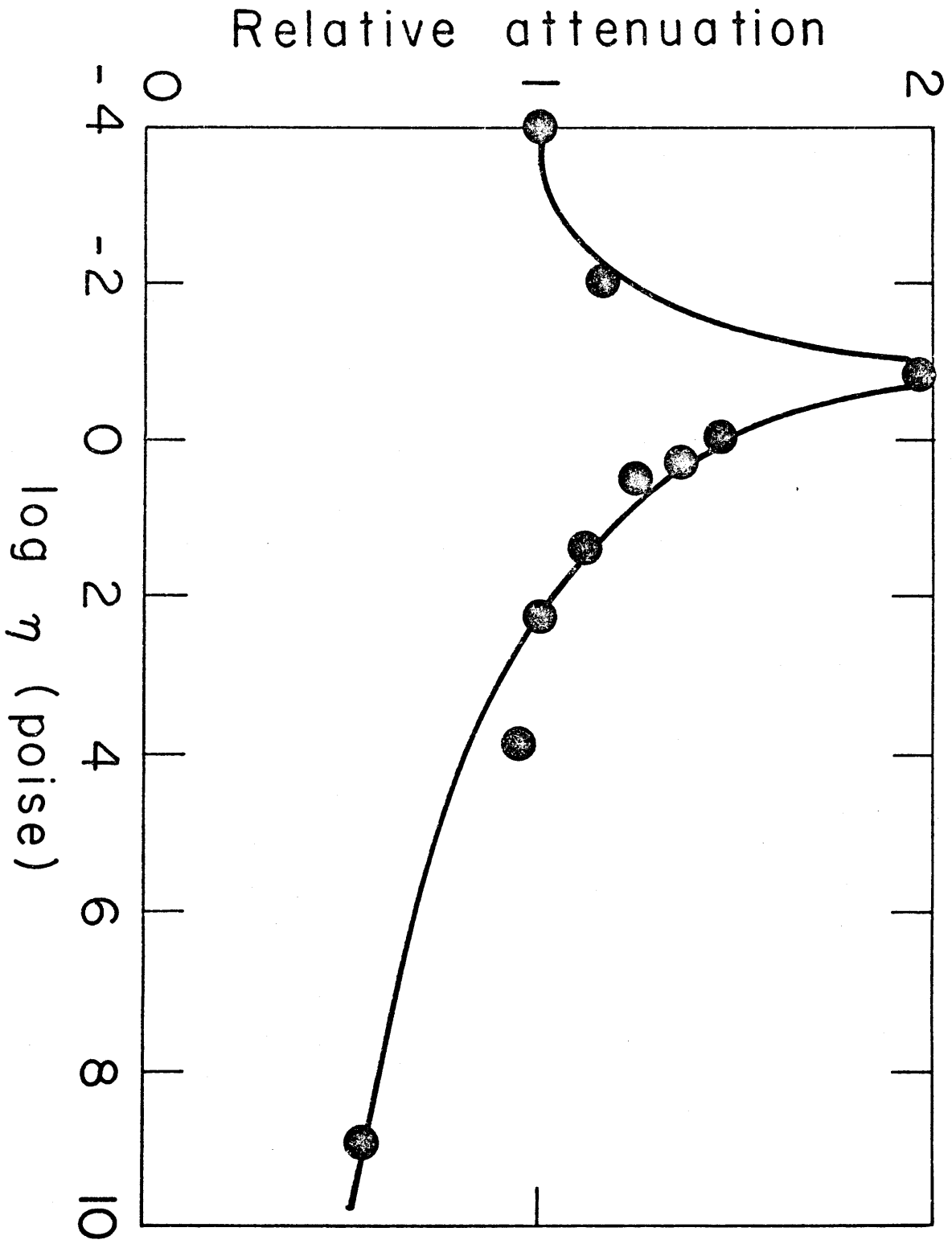


Figure 2-7

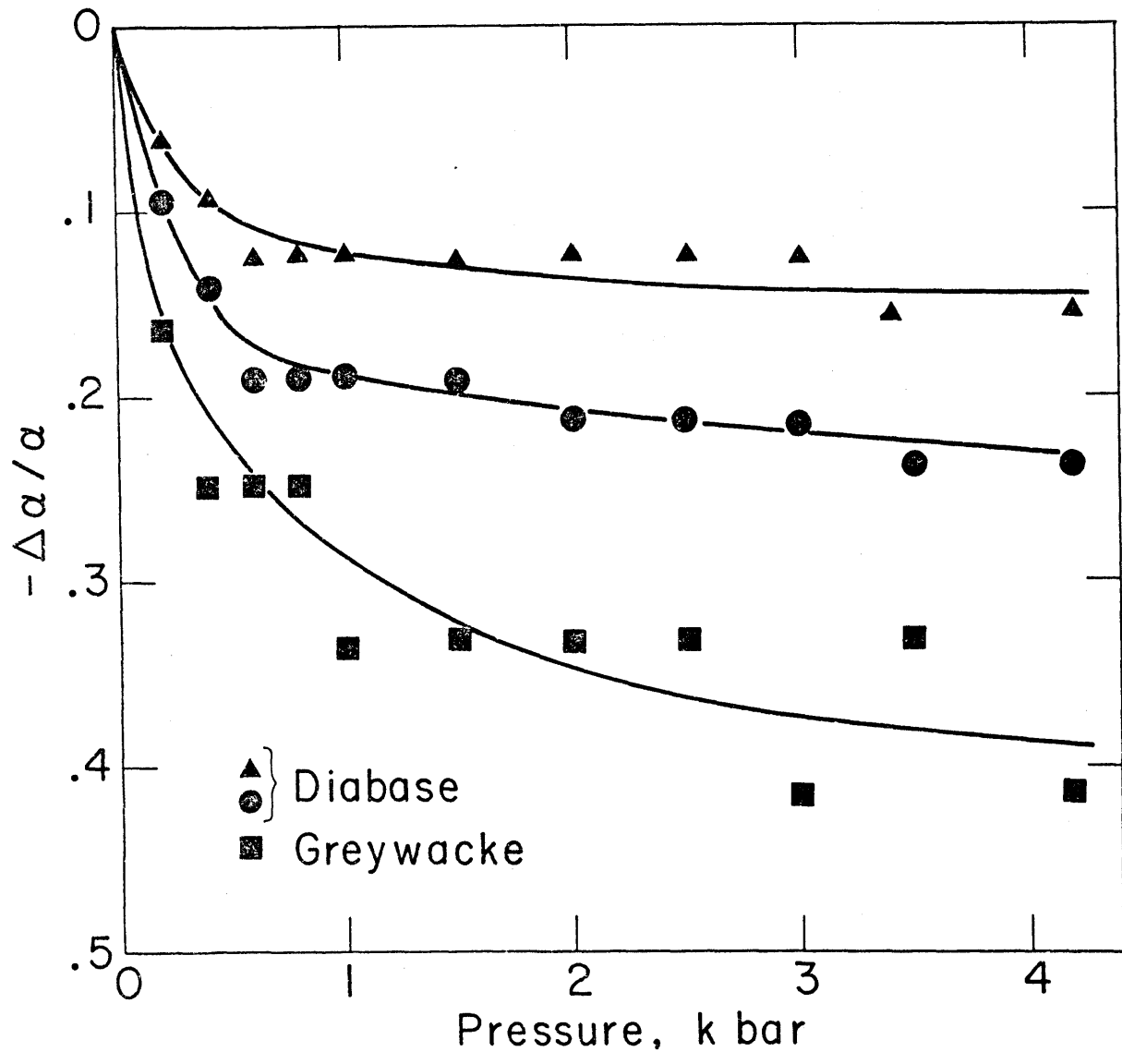


Figure 2-8

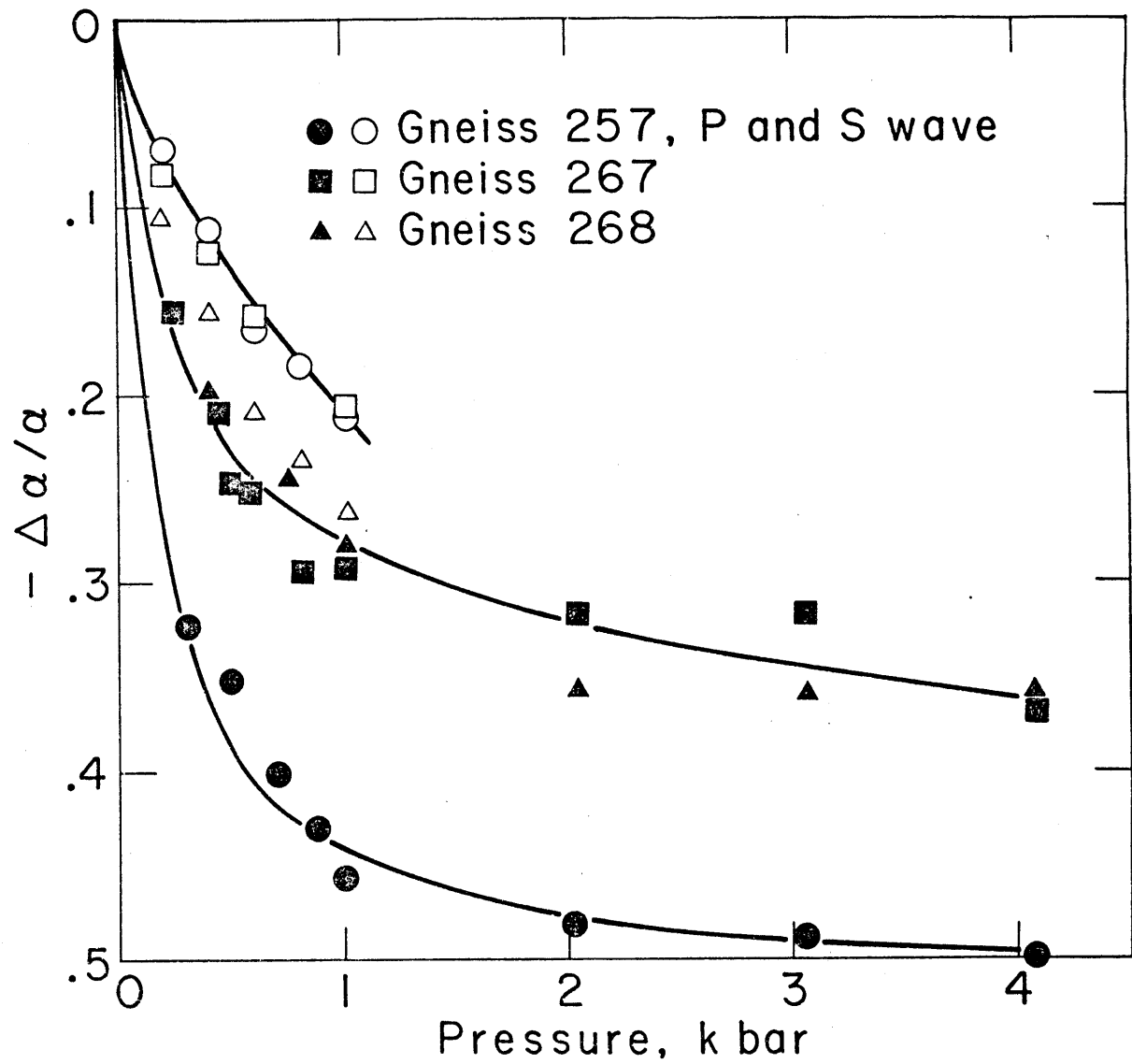


Figure 2-9

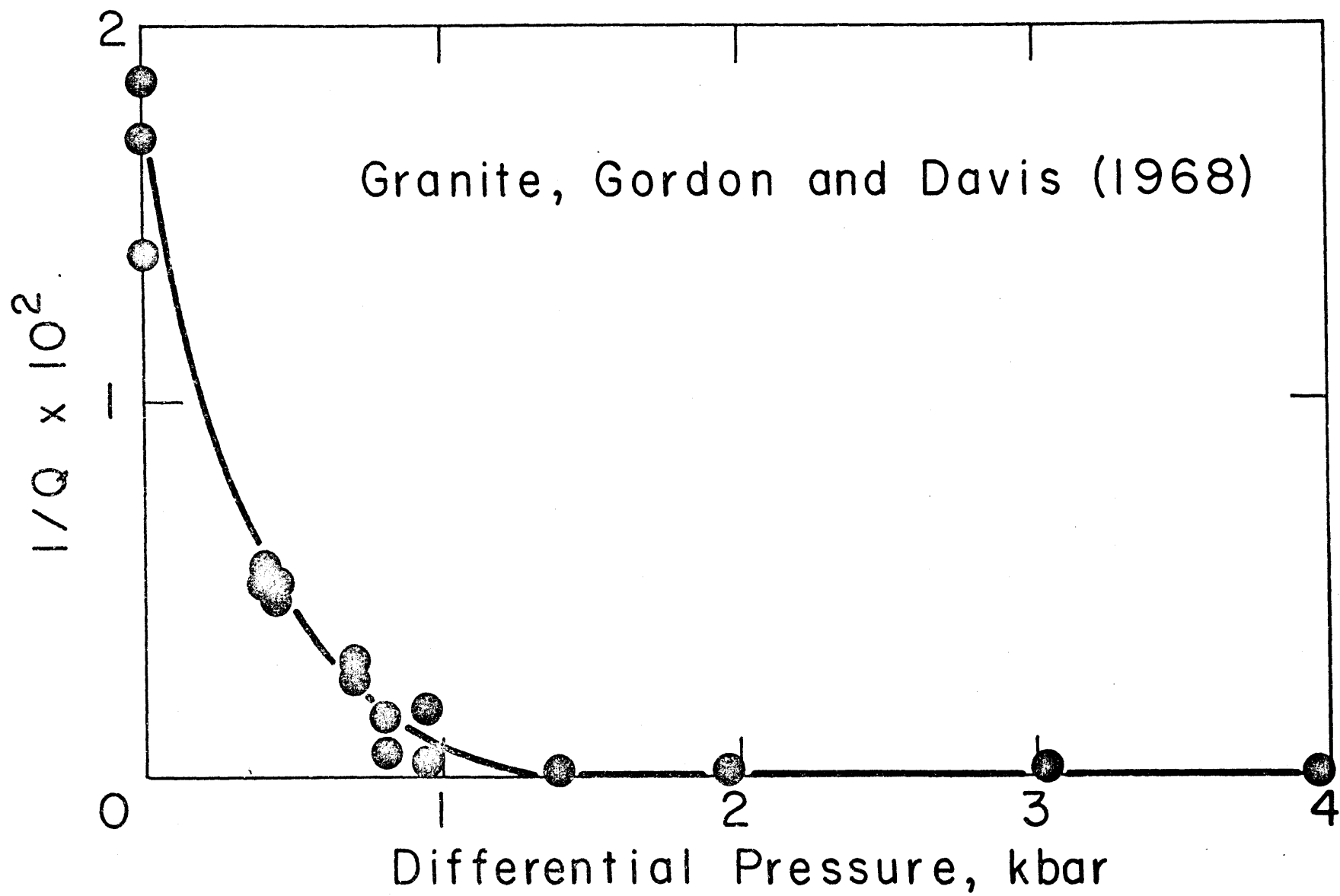


Figure 2-10

## CHAPTER 3

## ATTENUATION MECHANISMS

The phenomenon of attenuation is complex. While elastic wave propagation is generally well understood, anelasticity is not. As observed from attenuation data, its variations with changes in physical state are complicated and probably not amenable to a single model or mechanism. However, in order to reasonably evaluate and interpret laboratory and field measurements, precise definitions of the possible attenuation mechanisms involved are needed.

The investigation of the behavior of  $Q$  in the earth has classically been approached along two lines. The first method is to explain the nature of attenuation in terms of a generalized equation of linear elasticity (Hooke's Law) or by modified equations allowing certain nonlinearities. These phenomenological models have been well studied but yield little information on the microscopic properties of the rock. The second approach, favored in this thesis, is the physical and mathematical description of possible attenuation mechanisms. Numerous mechanisms have been proposed and each may be considered to have a greater degree of importance to the overall attenuation under certain physical conditions.

These mechanisms cover: matrix anelasticity including frictional dissipation due to relative motions at the grain boundaries and across crack surfaces (Walsh, 1966); attenuation due to fluid flow including relaxation due to shear motions at pore-fluid boundaries (Walsh, 1968 and 1969; Solomon, 1973), dissipation in a fully saturated rock due to relative motion of the frame with respect to fluid inclusions (Biot, 1956a,b; Stoll and Bryan, 1970), and "squirting" phenomena (Mavko and Nur, 1975; O'Connell and Budiansky, 1977); partial saturation effects such as gas pocket squeezing (White, 1975); energy absorbed in systems undergoing phase changes (Spetzler and Anderson, 1968); and a large category of geometrical effects including scattering off small pores and large irregularities and selective reflection from thin beds (O'Doherty and Anstey, 1971; Spencer et al., 1977). Several of the important mechanisms are schematically illustrated in Figure 3-1. The mechanistic approach is satisfying in that the physics of attenuation may be better understood. However, as will be seen, mathematical models based on these mechanisms suffer, many times, from excessive free parameters. Thus they have little predictive ability.

This chapter begins by briefly introducing several common phenomenological models, serving

to introduce important concepts such as relaxation. Then, hypothesized attenuation mechanisms along with their pressure and frequency dependences will be presented. Assuming that these mechanisms are uncoupled, each may be considered separately and the total attenuation ( $1/Q$ ) may be obtained from the sum. In all these cases, the theoretical formulations presented are not very rigorous. They are guided primarily by experimental observations and as a whole, should be treated as empirical relationships.

Finally, all of the attenuation mechanisms considered in this chapter require the knowledge of the elastic moduli. The method used in this thesis to calculate effective elastic properties and pore-crack aspect ratio distribution is that of Kuster and Toksöz (1974) and Toksöz et al. (1976). This is briefly discussed in Appendix B. Furthermore, this method allows the use of complex moduli, thus facilitating the introduction of attenuation into the calculations.

### 3.1 Phenomenological Models of Attenuation

Numerous attempts have been made to model attenuation based on small deviations from perfect elasticity. These models fall into two categories - linear and nonlinear. Much effort is spent to find under what conditions these models provide a constant  $Q$  loss. It is generally



assumed that attenuation is independent of strain magnitude and thus all of the processes are linear in amplitude. As shown by the data in this thesis, that assumption may not always be true.

### 3.1a Linear Models

One of the most common methods of investigating attenuation is the modification of Hooke's Law so that stress is directly proportional not only to strain but also to strain rate. Investigated by Meyer (1874), Kelvin (1878), and Voigt (1892), this type of medium is known as a Voigt or viscoelastic solid. For one dimension, the model is equivalent to a spring and dashpot in parallel. In general:

$$\sigma = M\varepsilon + M' \frac{d\varepsilon}{dt} \quad (3-1)$$

where  $\sigma$  is the stress,  $M$  is the elastic modulus,  $M'$  the anelastic modulus,  $\varepsilon$  is strain and  $d\varepsilon/dt$  the strain rate. The advantage of this model is that it yields a linear wave equation. The Voigt solid, however, does not provide a constant  $Q$ . For low frequencies,  $Q^{-1}$  is proportional to  $f$  and for high frequencies,  $f^{-1/2}$ . Since this behavior corresponds to that observed for sound attenuation in liquids, it has been proposed as a likely model in that case where  $M' = \eta$  (viscosity).

Another model in which viscosity is commonly used as the anelastic modulus is the Maxwell solid where:

$$\frac{d\sigma}{dt} = M \frac{d\varepsilon}{dt} - \frac{\sigma}{\eta} \quad (3-2)$$

This is equivalent to series combination of a spring and dashpot.

More generally, the linear solid using the superposition principle employing relaxation functions (Boltzmann, 1876). If stress is applied to a solid, strain will be delayed. Or, if a component of strain is suddenly applied, the associated stress component will suddenly increase and then "relax". If the time behavior of strain relaxation is described by the function  $f(t)$  then the stress strain relationship for the solid is given by:

$$\sigma(t) = M\varepsilon - \int_{-\infty}^t \varepsilon(\tau) f(t-\tau) d\tau \quad (3-3)$$

The relaxation function is also known as the "memory" function and the departure from Hooke's Law is simply the convolution of strain with the relaxation function.

Many investigators have reviewed models such as those described above and have attempted to determine under what conditions a constant  $Q$  loss may be

approximated - either with complicated combinations of masses, springs, and dashpots or with special relaxation functions. For each model one may obtain a transfer function,  $M(\omega)$  (Knopoff, 1964):

$$M(\omega) = \int_{-\infty}^{\infty} M(t)e^{i\omega t} dt \quad (3-4)$$

In the case of relaxation models,  $M(t) = f(t)$ . If  $C(\omega)$  and  $S(\omega)$  are the real and imaginary parts of  $M(\omega)$  respectively and assuming that attenuation is associated only with complex moduli and not density, then the complex velocity may be written as:

$$v = \left\{ \frac{C + iS}{\rho} \right\}^{1/2} \quad (3-5)$$

with  $1/Q$  written as:

$$\frac{1}{Q} = 2 \left( \frac{(C^2 + S^2)^{1/2} - C}{(C^2 + S^2)^{1/2} + C} \right)^{1/2} \quad (3-6)$$

(Knopoff, 1964). For small losses,  $Q \gg 1$  and  $C \gg S$ , equation 3-6 can be approximated by:

$$1/Q = S/C \quad (3-7)$$

Thus, one would want to find a loss function,  $M(t)$ , so that its associated transform pair,  $S(\omega)$  and  $C(\omega)$ , provide

a constant  $Q$ . An infinite set of such functions exist.

Lomnitz (1957) has suggested a relaxation function of the form  $\ln(1 + \omega_0 t)$  and claims that this does give constant  $Q$  and velocity. The characteristic frequency,  $\omega_0$ , is introduced to avoid a singularity at  $t = 0$  and may be found from causality.

Futterman (1962) examined further possible transform pairs for which causality is obeyed. In particular, he found that  $Q$  is independent of frequency above a certain characteristic cut-off frequency. In principle, this absorption cut-off frequency can be arbitrarily small. Velocity is dispersed and group and phase velocities can be determined from the  $Q$  of the solid.

### 3.1b Nonlinear Models

Several investigators have proposed nonlinear models of attenuation. In each case, certain aspects of linear theory are assumed, such as superposition for low stress and strains. One approach in finding a constant  $Q$  nonlinear model has been to consider a solid with a non-Hookian stress-strain relation (Loeb, 1961). In this case, a material undergoing stress-strain cycling will exhibit nonelliptical hysteresis. The relationship between stress and strain given by Loeb is:

$$\sigma = M \epsilon \sin(\omega t + 4K'/\pi K) \quad (3-8)$$

where  $M$  is the elastic modulus with  $K$  and  $K'$  the linear and nonlinear amplitudes respectively.

Coulomb friction has also been proposed as a nonlinear mechanism (Fortsch, 1956). This provides the proper frequency dependence. Walsh (1966) examined this problem in great detail for rocks and his results are presented and discussed in the next section.

Finally, Knopoff and MacDonald (1960) have suggested a lumped parameter model in which a linear system is damped by frictional forces. This mechanism is linear in amplitude but nonlinear in directionality. The equation of motion given by the authors is:

$$\rho \frac{\partial^2 u}{\partial t^2} - \mu \frac{\partial^2 u}{\partial x^2} = -f_0 \left| \frac{\partial^2 u}{\partial t^2} \right| \operatorname{sgn} \frac{\partial u}{\partial t} \quad (3-9)$$

where  $u$  is displacement and  $f_0$  is a constant. This type of a damping term, dependent on both the sign of the displacement and the velocity, provides for a frequency independent  $Q$ .

### 3.2 Attenuation Due to Matrix Anelasticity

Here the study of the mechanistic approach to attenuation is begun. In this section, losses in the rock matrix are emphasized. Later sections discuss the role of fluids and partial saturation on the attenuation.

Attenuation of seismic waves in a rock matrix can

be attributed to two factors: (1) intrinsic anelasticity of matrix minerals and (2) frictional dissipation due to relative motions at the grain boundaries and across crack surfaces. The intrinsic attenuation of minerals is generally small. In individual crystals  $Q$  values are generally higher than a few thousand, while in the whole rock  $Q$  values are normally lower than a few hundred. Thus, in considering matrix attenuation, it is reasonable to neglect the intrinsic attenuation in minerals and to consider only the attenuation across grain surfaces and thin cracks.

The importance of frictional dissipation is supported by the observation that  $Q$  is generally independent of frequency as predicted by this mechanism. However, friction across crack surfaces cannot account for all the anelasticity of the matrix. As pointed out by Walsh (1966), rocks subjected to confining pressures high enough to close all cracks still exhibit non-zero attenuation. Thus, it is necessary to consider in addition to dissipation across crack surfaces, an "intrinsic" anelasticity of the mineral aggregate.

The exact mechanism of grain boundary and crack dissipation is not known but frictional loss due to relative motions of the two sides may be the major factor (Walsh, 1966). If this is the case, then the attenuation should

depend very strongly on the surface conditions that effect friction between grains. Among these are whether rocks are saturated or dry, the properties of saturating fluids, and the amount of clay or other soft components in the matrix.

From laboratory experiments and the lunar experience it is found that granular materials exhibit very high  $Q$  values when totally dry and in a vacuum. In the absence of atmosphere and water, the Coulomb forces across grains are very strong and friction coefficients are high. Hence, no sliding motion can take place across the surfaces. This accounts for the very high  $Q$  values measured for seismic waves in the moon ( $Q = 2000-5000$ : Dainty et al., 1976; Nakamura et al., 1974; Latham et al., 1974; Toksöz et al., 1974) and in the laboratory under hard vacuum conditions (Pandit and Tozer, 1970; Warren et al., 1974; Tittmann et al., 1972, 1975). In the laboratory, when a little water vapor was introduced into the vacuum chamber,  $Q$  values decreased significantly.

It is difficult to formulate attenuation due to grain boundary and "frame anelasticity" effects since this would require the detailed knowledge of the crack and grain boundary properties. Walsh (1966) formulated the problem by approximating cracks as ellipsoids in plane strain. For a random orientation of cracks, the  $Q$

values for compressional and shear waves were computed using the friction coefficient,  $\kappa$ , effective Poisson's ratio,  $\sigma^*$ , matrix and effective rock moduli as parameters. The resulting expression for P waves in an infinite medium is too complicated to be presented conveniently but has the following form:

$$Q_P^{-1} = \frac{E^* (1 - \sigma^*)}{E (1 - 2\sigma^{*2})} \frac{\ell^3 N}{V_0} F(\kappa, \sigma^*) \quad (3-10)$$

where  $E^*$  and  $E$  are the effective and matrix moduli respectively, and  $N$  is the number of cracks with half length,  $\ell$ , in a volume,  $V_0$ . The function  $F(\kappa, \sigma^*)$  is implicitly dependent on the angle between the normal to the crack plane and the direction of wave propagation. Only cracks of certain orientations, determined by  $\kappa$  and  $\sigma^*$ , will contribute to the attenuation.

A closed form solution for the attenuation of S waves is impossible to obtain, but again from the Walsh formulation one may write the general form as:

$$Q_S^{-1} = \frac{1}{(1 + \sigma^*)} \frac{E^*}{E} \frac{\ell^3 N}{V_0} F'(\kappa) \quad (3-11)$$

where  $F'(\kappa)$  is a function of the friction coefficient. Fewer orientations of cracks are available to contribute to the attenuation of S waves compared to P waves in most



cases of interest.

For reasonable values of the friction coefficient and Poisson's ratio,  $Q_p/Q_s$  may be found by numerically evaluating equations 3-10 and 3-11 (Walsh, 1966). For  $\kappa$  between 0.0 and 0.5 with  $\sigma^*$  between 0.15 and 0.25,  $Q_p/Q_s$  is found to be between about 0.4 and 1.5. For most dry rocks  $Q_p/Q_s \leq 1$ , while for saturated rocks,  $Q_p/Q_s \geq 1$  (see Table 2.1).

Many data (Peselnick and Outerbridge, 1961; Peselnick and Zeitz, 1959; Knopoff, 1964) can be explained by the frictional dissipation mechanism. This mechanism which yields a constant  $Q$  with frequency also explains the "frame anelasticity" incorporated in Biot's (1956a,b) formulations.

Although friction explains much of the observed behavior of attenuation in rocks, the calculation of absolute values requires the specification of too many unknown parameters (friction coefficients, number and lengths of cracks whose surfaces are in contact). Furthermore, these parameters most likely change with variations in the physical conditions experienced by the rock. However, the Walsh formulation is useful in determining the effect of pressure on the frictional mechanism.

In order to formulate this dependence it is assumed:

1. The cracks and grain boundaries that contribute to friction can be characterized by very thin spheroids with a small aspect ratio,  $\alpha_m$ , (= thickness/diameter). From equation B-3, the relative change in the fractional volume,  $c$ , for this family of cracks as a function of differential pressure is:

$$\frac{dc}{c} = \frac{-P}{K_A^*} \left\{ \frac{4}{3\pi\alpha_m} \frac{(1 - \sigma^2)}{(1 - 2\sigma)} \right\} \quad (3-12)$$

where  $\sigma$  is the matrix Poisson's ratio and  $K_A^*$  is the effective static or frame bulk modulus.

2. The effective coefficient of friction,  $\kappa$ , is constant with pressure. Thus,  $F(\kappa)$  in equation 3-11 is a constant. If the effective Poisson's ratio,  $\sigma^*$ , varies more slowly with pressure than  $c$ , then  $F(\kappa, \sigma^*)$  in equation 3-10 is essentially a constant also.

Since the fractional volume of cracks with aspect ratio,  $\alpha_m$ , is:

$$c(\alpha_m) = \frac{4\pi\alpha_m}{3} \frac{N(\alpha_m) \ell^3}{V_0} \quad (3-13)$$

equation 3-10 may be written as:

$$Q_p^{-1} = \frac{3}{4} \frac{E^*}{E} \frac{(1 - \sigma^*)}{(1 - 2\sigma^{*2})} \frac{c(\alpha_m)}{\pi\alpha_m} F(\kappa, \sigma^*) \quad (3-14)$$

with a similar change for equation 3-11. Then:

$$\frac{dQ_p^{-1}}{Q_p^{-1}} = \frac{dE^*}{E} + \frac{dc}{c} + \epsilon \quad (3-15)$$

where  $\epsilon$  includes variations in  $\sigma^*$  and  $F(\kappa, \sigma^*)$ . Using assumption 2,  $\epsilon \rightarrow 0$ . Substituting equation 3-12 into 3-15 and then integrating, one finally obtains:

$$Q_p^{-1} = Q_{p_0}^{-1} \frac{E^*}{E_0^*} \exp(-AP/K_A^*) \quad (3-16)$$

where  $A = 4/3\pi\alpha_m \{(1-\sigma^2)/(1-2\sigma)\} = \text{constant}$ . A similar expression is obtained for the attenuation of S waves.  $Q_p^{-1}$  and  $Q_s^{-1}$  at  $P = 0$  must be determined empirically. Then the imaginary parts of the matrix can be set as described in Appendix B. From the calculated attenuations at each pressure, the imaginary parts of the moduli are given by:

$$\begin{aligned} K_I &= (K_R + 4\mu_R/3)Q_p^{-1} - 4\mu_R Q_s^{-1}/3 \\ \mu_I &= \mu_R Q_s^{-1} \end{aligned} \quad (3-17)$$

These results can then be used in equations B-1 and B-2 to determine the effective moduli, velocities, and attenuation. Since  $\alpha_m$  is arbitrary, the constant A is a free parameter and must be found empirically.

At first glance, the exponential decay of  $Q^{-1}$  with pressure predicted by equation 3-16 may not seem reasonable. As stated before, the attenuation of many rocks at high pressure is not zero. However, equation 3-16 describes only the effects of cracks which control the behavior of elastic and anelastic properties at relatively low pressure. If one considers a rock with an extremely low total porosity but moderate crack porosity such as a granite, then equation 3-16 may truly represent the pressure behavior of  $Q^{-1}$ . This is indeed observed in the data from Gordon and Davis (1968) shown in Figure 2-10. For rocks such as sandstones, however, one must consider the intrinsic aggregate anelasticity to contribute to the observed attenuation at pressures where the cracks are closed. In the models this is determined empirically and assumed to be constant with pressure.

One further consideration, discussed in detail in Chapter 6, is the dependence of attenuation on strain amplitude.  $Q$  values determined by ultrasonic pulse methods are generally lower than those obtained under the same conditions by dynamic resonance. For example, in a dry Berea sandstone,  $Q_p$  at low pressure from the pulse technique is about 20 while for the resonance method,  $Q$  is higher than 50. This discrepancy appears smaller for

saturated rocks. Two explanations are possible. Either the dry friction mechanism is frequency dependent, not supported by the data, or  $Q$  is dependent on strain amplitude. As will be seen, much evidence supports the latter. Higher amplitude ultrasonic pulses (strain  $>10^{-6}$ ) result in higher attenuation or lower  $Q$ . Data to be presented in Chapter 6 on several sandstones, limestone, diabase, granite, and Plexiglass imply that the presence and nature of crack or sliding surfaces control the amplitude behavior even though not explicitly predicted by Walsh theory. In general, it is observed that  $Q$  is independent of amplitude at low strains ( $<10^{-7}$ ) but decreases rapidly at higher amplitudes. This effect turns out to be a most important consideration, especially in comparing laboratory data of different experimental techniques with insitu measurements.

Finally, the effect of fluid saturation on the friction mechanism must be inspected. As was shown in section 2.2c and briefly discussed earlier in this section, the introduction of small amounts of liquid into a rock lowers  $Q$  substantially. This may be a result of the wetting and lubrication properties of the liquid or chemical interaction of the liquid with intergranular clay material, softening the matrix. Experimental evidence favors the former mechanism as being dominant but certainly

softening can be important too. This is evident from the need to lower the matrix shear modulus for many saturated sandstones relative to the dry rock cases in order to fit velocity data using the elastic moduli model (Toksöz et al., 1976). In either case, it is extremely difficult to quantify the behavior of attenuation as a function of saturation primarily because the process of friction in real rocks is complicated and not well understood. At best, the problem may be discussed qualitatively.

The phenomenon of lubrication consists of two types, film or perfect lubrication and boundary or imperfect lubrication. In the case of film lubrication, a small amount of fluid is placed between the sliding surfaces. The solid friction coefficient is eliminated and replaced by the viscosity of the fluid (Gemant, 1950). This is the mechanism for oil lubrication of moving metal parts. Minimum film thicknesses of  $10^{-4}$  to  $10^{-3}$  cm are required. Since attenuation in essentially zero width cracks is considered, film lubrication is probably not applicable to rocks.

If the distance between the two crack faces decreases to the point where the lubricating film breaks down, one might generally expect the crack to lock. This is not true, however, for dipolar type liquids and in fact, very

thin, even monomolecular layers of liquid are sufficient in this case to reduce the coefficient of friction (Adam, 1938). This is boundary lubrication and this mechanism has no connection whatsoever with the bulk viscosity of the liquid. Rather, the motion of molecules in the liquid behaves more like plastic flow in a solid. In many cases, lubrication can even be achieved by the adsorption of vapor.

The formation of the boundary layer depends critically on the wetting properties of the liquid with respect to the solid. It is because of this and the fact that the "rigidity" of the first monolayer of the liquid depends strongly on the properties of the solid that makes modeling of this mechanism so difficult. Even if the boundary layer increases in thickness, the effect of the solid remains, even though diminished. However, experimental evidence shows that qualitatively, the friction coefficient drops with increasing layer thickness. This is schematically illustrated in Figure 3-2 (from Gemant, 1950). The sharp decrease presumably occurs once the first complete monomolecular layer is formed. Eventually, friction approaches a constant value. It is evident that many of the features observed in attenuation in rocks resemble the process of boundary lubrication and that this mechanism is a likely candidate for explaining

the behavior of  $Q$  with partial saturation.

One might finally ask what the effect of elastic moduli are on the Walsh model. In other words, does this model predict any change in  $Q$  with increasing saturation after the point where all sliding cracks are lubricated. The answer is no. We compare a typical consolidated sandstone fully saturated with water with the same rock for 50% saturation. For the fully saturated case,  $E^* = 0.241$  Mb and  $\sigma^* = 0.302$  while for the partially saturated case,  $E^* = 0.233$  Mb and  $\sigma^* = 0.225$ . Applying equation 3-10 and assuming  $F(\kappa, \sigma^*)$  to be constant, it is found that  $Q_{50\%}/Q_{100\%} = 1.02$ .

The effect of changing elastic moduli might be more pronounced for partially saturated (gas saturated) unconsolidated or granular sands. The greatly increased compressibility due to the presence of gas may permit greater bulk deformation, grain sliding, and thus attenuation. There should be little or no change for an applied shear stress.

### 3.3 Attenuation Due to Viscosity and Flow of Fluids

All rocks in the upper crust are partially or completely saturated with some fluid. It is of special interest then to consider the effect of viscous fluids in a solid rock matrix. Some mechanisms by which fluids contribute to attenuation are illustrated in Figure 3-1.



These fluids in elongated pores and fine cracks contribute to attenuation in a complex manner. First, attenuation peaks due to viscous shear relaxation will develop at frequencies dependent both on the pore geometry and fluid viscosity. For a rock with a wide spectrum of pore aspect ratios, the attenuation spectrum is of a complicated form. This problem has been discussed by Walsh (1968,1969), Solomon (1973), and Kuster and Toksöz (1974) for spheroidal pores.

Second, fluid flow between pores, induced by the stress (seismic) wave, may cause attenuation. These flow mechanisms fall into two categories, inertial flow (Biot, 1956a,b), important at ultrasonic frequencies, and "squirting" flow (Mavko and Nur, 1975; O'Connell and Budiansky, 1977), more prominent at lower frequencies. Each will be considered separately and the analysis of "squirting" flow will also include the formulation for viscous relaxation.

### 3.3a Biot Fluid Flow

In highly porous and permeable rocks, relative motion may take place between the rock frame and the saturating liquid as seismic waves propagate. Biot (1956a,b and 1962a,b) derived a theory for acoustical wave propagation in an isotropic solid with connected pores. This theory can be used to calculate both phase velocity and

attenuation due to this mechanism. In the absence of boundaries, Biot theory predicts the existence of three types of body waves, two dilatational and one shear. One dilatational wave is highly attenuated and resembles a diffusion wave. The other is the P body wave that travels with little attenuation or dispersion. A formulation of Biot's theory has been developed by Stoll and Bryan (1970) and Stoll (1974,1977) and has been adopted for this study.

To formulate the Biot theory for compressional waves, two equations of motion may be written. The first describes the motion of a volume element attached to the rock frame or the fluid flow into or out of that volume and is given by:

$$\nabla^2 (H\theta - C\xi) = \frac{\partial^2}{\partial t^2} (\rho^*\theta - \rho'\xi) \quad (3-18)$$

The second equation describes the motion of the fluid relative to the frame:

$$\nabla^2 (C\theta - M\xi) = \frac{\partial^2}{\partial t^2} (\rho^*\theta - m\xi) - \frac{\eta}{\chi} \frac{\partial \xi}{\partial t} \quad (3-19)$$

In equations 3-18 and 3-19, H, C, and M are operators describing the constitutive relations for the medium and are given by:

$$\begin{aligned}
 H &= \frac{(K - K_A)^2}{D - K_A} + K_A + \frac{4\mu^*}{3} \\
 C &= \frac{K(K - K_A)}{D - K_A} \\
 M &= \frac{K^2}{D - K_A}
 \end{aligned}
 \tag{3-20}$$

where  $D = K(1 + \phi(K/K' - 1))$

For the above equations,  $\theta$  is the dilatation,  $\rho^*$  and  $\rho'$  are the effective and fluid densities,  $K$  is the matrix bulk modulus,  $K'$  the fluid bulk modulus and  $K_A$  is the frame modulus.  $\chi$  is the permeability,  $\phi$  the porosity,  $\eta$  the fluid viscosity and  $\mu^*$  is the effective shear modulus. In equations 3-18 and 3-19,  $\xi$  is the volume of fluid that has flowed into or out of the unit volume. The parameter  $m$  in equation 3-19 is given by:

$$m = a'\rho'/\phi \quad a' \geq 1 \tag{3-21}$$

and is included to take into account the tortuosity of the flow paths. For a uniform system of pores with all orientations,  $a'$  has a theoretical value of 3 (Stoll and Bryan, 1970).

In equation 3-19, the term  $\eta/\chi \cdot \partial\xi/\partial t$  is the resistance to flow. This constant ratio of fluid flow to pressure gradient describes Poiseuille flow and is valid only for low frequencies. At high frequencies turbulent

flow develops in which the effects of viscosity are only felt in a thin boundary layer. To correct the flow resistance for high frequencies, the viscosity is written as  $F(\zeta)\eta$  where  $F(\zeta)$  is a complex correction factor derived by Biot and given as:

$$F(\zeta) = F_R(\zeta) + iF_I(\zeta) = \frac{1}{4} \frac{\zeta T(\zeta)}{1 - 2T(\zeta)/i\zeta} \quad (3-22)$$

where

$$T(\zeta) = \frac{\text{ber}'(\zeta) + i \text{bei}'(\zeta)}{\text{ber}(\zeta) + i \text{bei}(\zeta)}$$

and

$$\zeta = a(\omega\rho'/\eta)^{1/2}$$

The functions ber and bei are the real and imaginary parts of the Kelvin function and their primes denote derivatives. The parameter,  $a$ , is a function of the size and shape of the pores. Stoll (1974) found that values between  $1/6$  and  $1/7$  the mean grain diameter resulted in good agreement to experimental data for unconsolidated sands. It may be considered a free parameter. The correction factor is only valid where the wavelength is large compared to the pore size.

To obtain velocity and attenuation, assume solutions to equations 3-19 and 3-20 of the form:

$$\theta = A_1 \exp\{i(\omega t - kx)\}$$

and

$$\xi = A_2 \exp\{i(\omega t - kx)\}$$

(3-23)

The wavenumber,  $k$ , is complex so that  $k = k_R + ik_I$ , and is found from the solution of the following period equation:

$$\begin{vmatrix} Hk^2 - \rho^*\omega^2 & \rho'\omega^2 - Ck^2 \\ Ck^2 - \rho'\omega^2 & m\omega^2 - Mk^2 - i\omega F\eta/\chi \end{vmatrix} = 0 \quad (3-24)$$

The attenuation coefficient is obtained from  $k_I$ . There are two roots to 3-24, one representing the diffusion wave and the other the propagating P wave. For frequencies at which Poiseuille flow is valid, the attenuation coefficient,  $\alpha$ , for the P wave varies as the square of the frequency ( $Q^{-1}\alpha f$ ). At higher frequencies,  $\alpha$  is proportional to  $f^{1/2}$  ( $Q^{-1}\alpha f^{-1/2}$ ).

Shear attenuation involves only the idea that the moving solid frame drags the viscous fluid with it. Since the fluid motion is due only to inertial stresses, this mechanism must be treated in addition to the viscous relaxation model described later in this chapter. A simpler period equation for S waves may be obtained and is given by (Stoll, 1977):

$$\begin{vmatrix} \rho\omega^2 - \mu^*k^2 & \rho'\omega^2 \\ \rho'\omega^2 & m\omega^2 - i\omega F\eta/\chi \end{vmatrix} = 0 \quad (3-25)$$

Here there is only one root. Viscous drag at the pore-fluid interface results in greater loss than flow induced by pressure gradients. Thus the model predicts

that the attenuation of S waves is greater than for P waves in the case of the fluid flow mechanism.

In general, the elastic moduli of the frame in this formulation may be complex, allowing for the anelasticity of the frame. Since this effect is considered separately in this study, the imaginary parts of the frame moduli are set to zero. Numerical calculations carried out by Stoll and Bryan (1970), though, indicate that frame anelasticity dominates over the fluid flow effects at low frequencies ( $f < 10^4$  Hz). At high frequencies, the fluid flow contribution could be detected in permeable, high porosity rocks. For most sedimentary rocks saturated with water, the effects of fluid flow are small at seismic frequencies ( $f = 10 - 200$  Hz), but could become important at ultrasonic frequencies.

The pressure dependence of attenuation due to fluid flow depends primarily on the change in the permeability in the rock due to compaction, crack closure, and pore collapse and on the stiffening of the matrix. The elastic moduli and total porosity are easily obtained as functions of pressure using the method of Toksöz et al. (1976). Furthermore, it is assumed that the viscosity of the fluid inclusion remains relatively constant in the pressure range of interest.

Experimental determinations of permeability as a

function of confining hydrostatic pressure have been made for several sandstones (Fatt and Davis, 1952), Westerly granite (Frangos, 1967), and Ottawa sand (Zoback and Byerlee, 1976). In general, permeability decreases with increasing pressure but the rate of decrease depends on the total porosity and fraction of crack porosity. In highly porous and permeable consolidated rocks, the bulk of the porosity and permeability is contained in the large aspect ratio pores which do not close under pressure. Fatt and Davis (1952) found a maximum reduction in permeability of 25% at moderate pressures for sandstones while in granites, order of magnitude changes are common. Measurements of permeability in unconsolidated Ottawa sand (Zoback and Byerlee, 1976) show a slow reduction up to about 800 bars where it drops off rapidly to level off again between 2000 and 3000 bars. The acceleration in permeability loss at 800 bars is presumably due to grain crushing and pore collapse. However, the applicability of this study to consolidated rocks is uncertain nor could it be easily modeled. It will be assumed that permeability in highly porous rocks is constant with pressure. The effect of this is to give an upper bound on the contribution due to fluid flow on attenuation.

The effect of partial

saturation in the form of gas-liquid mixtures in the rock's pore spaces is finally considered. The presence of gas (or air) in the pores will tend to block flow and thus the resistance term in equation 3-19 is increased. The logical way to approach this problem is through the concept of relative permeability,  $\chi_r$ . The flow of liquid in the pores is affected by the presence of gas so that, in effect, the flow channels for the liquid are narrowed. This reduced permeability is called the effective permeability,  $\chi_w$ , or if written as a fraction of the physical or specific permeability,  $\chi$ , the relative permeability. For a gas-water mixture:

$$\chi_w + \chi_g < \chi$$

and

$$\chi_{rw} + \chi_{rg} < 1$$

A plot of relative permeabilities for gas and liquid (wetting phase) is shown schematically in Figure 3-3 as a function of liquid saturation,  $S_w$ .  $S_{wi}$  refers to the irreducible or connate saturation. The shape of the curves is due primarily to the effect of capillary forces.

Unfortunately, no exact theory exists to calculate relative permeability curves for a given rock. One must rely on experimental observations. Based on many experimental data, Wyllie (1962) developed empirical relative permeability equations. The appropriate



equation for consolidated sandstones used in this thesis is:

$$\chi_{rw} = \left( \frac{S_w - S_{wi}}{1 - S_{wi}} \right)^4 \quad (3-26)$$

Thus, the permeability in the Biot flow equations is modified by substituting  $\chi_{rw} \cdot \chi$  in place of  $\chi$ . The liquid remains the flowing medium and  $K'$  and  $\rho'$  remain that of the liquid. This model gives the correct results for both end members. For  $\chi_{rw} = 1$ , the attenuation due to fluid flow is that for full saturation. If  $\chi_{rw}$  decreases (decreasing  $S_w$ ) then the attenuation decreases. At some point the liquid may no longer be considered the flowing medium, however for gas, the solution is essentially that of a dry rock and no attenuation due to Biot flow occurs. The effect of relative permeability and examples of Biot flow attenuation will be shown in Chapter 5.

### 3.3b Squirting Flow

Several investigators have proposed attenuation mechanisms by which flow is induced between two adjacent interacting cracks due to the relative volume change caused by the stress wave (Mavko and Nur, 1975; O'Connell and Budiansky, 1977). These are commonly known as "squirting" mechanisms and while they are not important at ultrasonic frequencies, they may be so at

sonic or seismic frequencies. The elastic model of Toksöz et al. (1976) is particularly useful in treating these mechanisms in that a distribution of crack aspect ratios is uniquely determined from velocity data and that pressure gradients between cracks may be readily calculated.

Flow in any squirting mechanism is from small aspect ratio (thin) cracks to larger ones (pores). Thus the flow field within the crack may be approximated by the flow between two infinite plates as is done by Mavko and Nur (1975) and O'Connell and Budiansky (1977). Here an approach to the problem consistent with the concepts and formulations introduced by Toksöz et al. (1976) is considered. The details of the calculations may be found in Appendix C. Assuming that flow will take place between very thin cracks with  $\alpha_m \approx 0$  and pores with  $\alpha_m \approx 1$  due to a differential volume change induced by the stress wave, then the pressure difference, the equalized pressure after flow, the instantaneous flow,  $q$ , and the total flow,  $q_T$  can be easily calculated. Given a relaxation of the form:

$$q_T = q \int_0^{\infty} e^{-t/\tau} dt = q\tau \quad (3-27)$$

where  $\tau$  is the relaxation time, one finds that

$$\tau = 8\eta/\alpha_m^2 K' (1 + \epsilon) \quad (3-28)$$

where  $\eta$  is the viscosity of the fluid,  $K'$  is the fluid bulk modulus and  $\epsilon$  is the ratio of connected crack to pore volume. For most porous rocks we can approximate  $\epsilon \approx 0$ . Taking  $K' = 2 \times 10^{10}$  dynes/cm<sup>2</sup>,  $\eta = 10^{-2}$  poise, with  $\alpha_m$  ranging from  $10^{-3}$  to  $10^{-4}$ , one obtains relaxation times ranging from  $4 \times 10^{-6}$  to  $4 \times 10^{-4}$  sec.

The formulation of this mechanism in terms of complex moduli yields an expression that also includes the viscous relaxation mechanism in pores discussed earlier. This is a result of applying the correspondence principle for the shear modulus,  $\mu' = i\omega\eta$  and expressing the bulk modulus of the fluid as  $K' = K'_R + i\omega g$ , where  $g$  is considered an unknown to be determined from the relaxation time for the squirting flow. It is shown in Appendix C that equations B-1 and B-2 for the effective moduli can be written in terms of two characteristic frequencies:  $\omega_c = K/g$  and  $\omega_d = 3K/4\eta$  (equation C-13).  $\omega_d$  is recognized as the characteristic frequency for viscous relaxation (Walsh, 1969) and  $\omega_c$  is the characteristic frequency for fluid flow from cracks. From the estimate of the relaxation time for this mechanism:

$$g = \frac{8\eta}{\alpha_m^2(1 + \epsilon)} \frac{K}{K'_R} \quad (3-29)$$

For example, with  $\epsilon = 0$ ,  $\alpha_m = 10^{-3}$ ,  $\eta = 10^{-2}$  poise,

$K = 4 \times 10^{11}$  dynes/cm<sup>2</sup> and  $K'_R = 2 \times 10^{10}$  dynes/cm<sup>2</sup>, we find that  $g = 1.6 \times 10^6$  poise or more generally,  $g = 1.6/\alpha_m^2$  poise. This mechanism is readily included in the elastic moduli formulations by finding  $g$  from equation 3-29 and then substituting to give the value of  $K'$  required. Knowledge of crack aspect ratio distributions from the elastic model eliminates the need to specify these as free parameters.

Squirting flow is enhanced for partial saturation. As will be discussed in the next section, one may assume that for all but the lowest fluid saturations, the gas (or air) phase is restricted to the larger pores. Because of the high compressibility of the gas, volume changes of the pore due to the seismic wave offer no resistance to flow from the thinner cracks. One may therefore proceed with the analysis of Appendix C except that for partial saturation, the equalized pressure,  $\bar{P} = 0$ , and the total flow,  $q_T = -dC_o$ . The result is the same as equation 3-28 except that  $\epsilon$  is identically zero. Thus, partial saturation has the effect of increasing  $\tau$  or shifting the attenuation peak to lower frequencies.

#### 3.4 Gas Bubbles

The presence of gas bubbles in a porous rock can have a great effect on the acoustical properties. This is especially true for unconsolidated sands such as

ocean bottom sediments. The acoustics of gas bearing sediments has been extensively studied and an excellent review of the topic may be found in Anderson (1974). This section begins by discussing the nature of gas occurrence in natural sediments, a proposed model for gas release under laboratory and reservoir production conditions, the types of loss mechanisms involved and the mathematical formulations for attenuation. Much of the original work on attenuation due to gas bubbles was motivated by the need to understand the acoustic properties of ship's wakes and the ocean environment. This work is then extended to the problem of bubbles in materials of finite rigidity.

#### 5.4a The Occurrence of Gas in Nature

Partial saturation and gas bubbles may occur in the earth in several ways. The first is in ocean bottom sediments where gas is formed by the decomposition of organic matter. Close to shore, bubbles may be formed by wave action. Of more interest, however, is the presence of gas in reservoir sands. Only partial saturations of two phases (water-gas for example) are considered. More common is a three phase system such as water-oil-gas. In gas reservoirs, the distribution of saturants is a function of depth. In all cases the liquid phase is wetting and the gas non-wetting. Because

of capillary forces, there is no sharp discontinuity between the gas and liquid phases. Rather, a transition zone exists in which gas saturation,  $S_g$ , increases from 0 to near 1. This is illustrated in Figure 3-4a. In natural rocks there is a lower limit to the water saturation,  $S_w$ , called the irreducible or connate water saturation,  $S_{wi}$ , that cannot be removed under gravitational separation. Since gas is the non-wetting phase, as  $S_g$  increases, the gas will occur in pockets (bubbles) located in the larger aspect ratio pores. Eventually, these pockets will expand to fill nearly the entire pore spaces.

A second case of gas occurrence is during gas solution drive of a reservoir. In this case, gas in solution is released as the fluid pressure is dropped. The same situation may be simulated in the laboratory and such an experiment is described in Chapter 5. Gas release is illustrated by the phase diagram in Figure 3-4b. Consider a very simple case of isothermal pressure drawdown. The system initially exists at point A above the bubble point curve. As the fluid pressure drops following the line from A-D, gas will begin to come out of solution at point B. From point B to C,  $S_g$  increases from 0 to 1.

Here, a simple model for the occurrence of gas bubbles in a solution drive situation is proposed. This is

illustrated in Figure 3-5. For small values of  $S_g$ , the gas first appears as small bubbles (Figure 3-5a). During this phase, the acoustical properties of the gas are dependent only on the liquid medium surrounding the bubbles. That is, the bubbles do not "see" the rock matrix. As  $S_g$  increases, the small bubbles will coalesce into larger ones (Figure 3-5b). At this stage, the bubble properties are determined by the effective properties of the surrounding media. Eventually (Figure 3-5c),  $S_g$  will increase to the point where the gas fills the entire pore space. This condition will essentially eliminate any acoustical losses due to the bubbles. It will be seen in the next section how this model may be used with the theoretical formulations of attenuation.

#### 3.4b Bubble Resonances

The theory of gas bubble dynamics in water has been well studied particularly in terms of the acoustical properties of ship's wakes. The theory of bubble dynamics in solids is not as well developed. Fundamental to this study is the resonance frequency of bubble pulsations, driven by the acoustic wave. While for small bubbles or low frequencies, an adiabatic equation of state may be assumed for the bubble, a more general polytropic equation, valid for all conditions, is used:

$$K_b = \gamma P/AV$$

where  $K_b$  is the bubble stiffness,  $P$  is the bubble pressure,  $V$  the volume,  $\gamma$  is the ratio of specific heats, and  $A$  is the polytropic coefficient defined by:

$$A = \{1 + B^2\} \left\{ 1 + \frac{3(\gamma-1)}{X} \frac{\sinh X - \sin X}{\cosh X - \cos X} \right\} \quad (3-31)$$

where

$$B = 3(\gamma-1) \left\{ \frac{X(\sinh X + \sin X) - 2(\cosh X - \cos X)}{X^2(\cosh X - \cos X) + 3(\gamma-1)X(\sinh X - \sin X)} \right\} \quad (3-32)$$

and  $X = r_o (2\omega/\kappa)^{1/2}$ .

$r_o$  is the bubble radius,  $\omega$  is the angular frequency and  $\kappa$  is the thermal diffusivity of the gas. It should be pointed out at this stage that the gas properties may be found as a function of  $P$  and  $T$  using the kinetic theory of gases. This allows the estimate of bubble losses under actual subsurface conditions.

The basic equation for the bubble resonant frequency was derived by Minnaert (1938) based on energy considerations. The resonance frequency,  $f_o$ , is given by:

$$f_o = \frac{1}{2\pi r_o} \left\{ \frac{3\gamma P}{A\rho} \right\}^{1/2} \quad (3-33)$$

or,  $f_o$  is inversely proportional to the bubble radius and directly proportional to the acoustic velocity. Equation 3-33 is valid for most conditions except for small bubbles which are, unfortunately, of primary interest to this study. Many investigators since Minnaert have studied the



resonance problem (Smith, 1935; Richardson, reported by Briggs et al., 1947; Houghton, 1963; Shima, 1970), the important developments being the inclusion of viscous, elastic, and surface tension effects. The latter is most important for small bubbles. A review of these frequency relations may be found in Anderson (1974). In this work, the Shima equation, which includes all the important effects, is used. This is given by:

$$f_o = \frac{1}{2\pi r_o (1+LM)} \{N(1+LM) - (M+LN)^2/4\}^{1/2} \quad (3-34)$$

where

$$L = \{\rho'/7P(1 + K)\}^{1/2}$$

$$M = 4\eta/\rho'r_o$$

$$N = \{P(1 - 1/3\gamma)2\sigma_s/r_o\}3\gamma/\rho$$

and  $L \approx 3$  kilobars / P.

$\sigma_s$  is the surface tension and  $\eta$  is the fluid viscosity.

The theory of gas bubble pulsations in materials of some rigidity has been developed primarily to study the acoustical effects of fish bladders on sonar signals (Andreeva, 1964; Weston, 1967). Their approach may be modified for bubbles in rock. The main effect, as one would expect, is to shift the resonance to higher frequencies. The best available equation (Anderson, 1974) for the resonance frequency of gas bubbles in a solid is the Minneart equation modified by the elastic properties

of the surrounding matrix (Andreeva, 1964):

$$f_o = \frac{1}{2\pi r_o} \left[ \frac{3\gamma P}{A\rho} + \frac{4\mu}{\rho} \right]^{1/2} \quad (3-35)$$

This equation is used in this thesis.

### 3.4c Bubble Losses

Bubble losses are due to three mechanisms: thermal, radiation, and viscous. Devin (1959) discussed these losses at resonance and later, Eller (1970) extended Devin's work to losses at frequencies other than at resonance. Eller's results will be presented here.

If one assumes an equation of motion for the pulsating bubble of the form:

$$M\ddot{u} + b\dot{u} + K_b u + Ae^{-i\omega t} = 0 \quad (3-36)$$

where  $b$  is the damping coefficient and  $A$  is the driving amplitude, then a damping constant,  $d$ , may be defined as:

$$d = \omega b / K_b \quad (3-37)$$

$d$  is the sum of the thermal, radiation and viscous losses.

Thermal losses are due to the fact that compression in a bubble is polytropic. The work done by the acoustic wave in compressing the gas is greater than the work done by the gas in expanding into the liquid surrounding it. The difference is a flow of heat into the liquid.

Radiation damping is due to the generation of spherical sound waves by the volume pulsation of the bubble.

Viscous damping for bubbles in a liquid may be due to momentum transfer from a bubble moving in translation or rotation. For no external forces acting on each unit mass of liquid, the equation of motion may be obtained from the Navier-Stokes equation. But, this is not valid for a pulsating bubble. However, distortion in a liquid volume surrounding the bubble is caused by viscous stresses.

Equations for the damping constants,  $d_{th}$ ,  $d_{rad}$ , and  $d_{vis}$  for the three types of losses are valid only for wavelengths longer than the bubble radius. This presents no difficulty in the work here. The damping constants for bubbles in liquid are (Eller, 1970):

$$d_{th} = B$$

$$d_{rad} = \frac{\rho' r_o^3 \omega^3 A}{3\gamma P C_o} \quad (3-38)$$

$$d_{vis} = \frac{4\omega\eta A}{3\gamma P}$$

where  $C_o$  is the acoustic velocity of bubble free liquid,  $\rho'$  is the liquid density, and  $B$  is defined in equation 3-32.

Thermal damping for bubbles in a solid material is the same as for bubbles in water. Radiation damping is

modified by the wavelength of the acoustic wave in the solid and is given by Weston (1967) as:

$$d_{\text{rad}} = \frac{\omega^3 r_o^3}{C_o} \left[ \frac{A}{3\gamma P} + \frac{\rho}{4\mu} \right] \quad (3-39)$$

where  $C_o$  is now the acoustic velocity in the effective (rock) medium. Viscous damping is more appropriately considered frictional damping for bubbles in the rock. Since this is studied separately in this thesis,  $d_{\text{vis}} = 0$  for bubbles in a solid medium.

#### 3.4d Attenuation Formulations

We shall now present the equations which describe the attenuation due to a homogeneous distribution of bubbles in both water and rock. The assumption of homogeneity may, however, be questioned. Certainly on a scale from pore to pore the gas bubbles are not evenly distributed. In the long wavelength approximation, though, the pores, and therefore the bubbles will appear to be homogeneously located.

In order to calculate the effective properties of attenuation, one needs not only the damping constant but also the variation of the medium compressibility (or sound speed) with gas content. For bubbles in water, Wood's (1955) formula of volume averaged compressibilities is valid for frequencies well below resonance where there

is little attenuation. Spitzer (1943), though, derived the following general formulas for both velocity and attenuation for a homogeneous mixture of bubbles of uniform radius in a liquid (water):

$$\frac{C_o^2}{C} = \frac{1+aX}{2} \left[ 1 \pm \{1+(aY/(1+aX))^2\}^{1/2} \right] \quad (3-40)$$

$$\alpha = \frac{\pi f C}{C_o^2} aY \quad (3-41)$$

where

$$X = \frac{S_g (1 - f_*^2)}{(1-f_*^2)^2 + d_*^2} \quad a = \rho' C_o^2 / \gamma P$$

$$Y = \frac{S_g d_*}{(1-f_*^2)^2 + d_*^2} \quad f_* = f/f_o$$

$$d_* = df_*^2$$

$\alpha$  is the attenuation coefficient and  $C$  is the effective sound speed. Spitzer's theory has been tested experimentally. Silberman (1957) has also shown that equations 3-40 and 3-41 are valid for non-uniform bubble sizes.

For a distribution of bubbles with radii  $r_i$ ,  $i = 1, 2, \dots, n$  and concentrations  $S_{g_i}$ , with associated normalized frequencies,  $f_{*i}$ , then the terms,  $X$  and  $Y$ , in equations 3-40 and 3-41 may be written as a summation over  $i$ .

For bubbles in rock, equations 3-40 and 3-41 remain the same except that:

$$a = \frac{K^*}{P + 4\mu/3} \quad \text{and} \quad S_g = S_g \phi \quad (3-42)$$

where  $K^*$  is the effective bulk modulus of the saturated rock and  $\phi$  is the porosity.  $f_o$ ,  $d$  and therefore  $d_*$  and  $f_*$  are modified as discussed before. The equation for the attenuation coefficient becomes:

$$\alpha = \frac{\pi f C}{C_o^2} \frac{K^* Y}{P + 4\mu/3} \quad (3-43)$$

where  $C_o$  is the acoustic velocity in the bubble free medium as before.

It has been shown in this section that the attenuation due to gas bubbles may be calculated for both the case of bubbles in water or in a rigid medium (rock). In terms of the model proposed in section 3.5a, for small values of  $S_g$ , one would find the attenuation from equation 3-41. For larger values of  $S_g$ , equation 3-43 is appropriate. The actual transition between these two stages would be difficult to model. While a detailed discussion of a gas release experiment and the results of calculations for these mechanisms will be deferred to Chapter 5, one can at least conclude that bubble losses are much greater only if the bubbles "see" water. The losses are substantially reduced for gas in a rigid medium.

### 3.5 Other Sources of Attenuation

An attenuation model describing the effects of large scale irregularities (on the order of 10 cm) in saturation

conditions has been proposed by White (1975). The porous rock is modeled as containing spherical pockets saturated with gas with the rest of the volume saturated with liquid. Loss due to fluid flow is enhanced at the gas-liquid interfaces. White showed that for this particular model chosen, attenuation due to this mechanism can be important at seismic frequencies. There is some debate, however, as to the occurrence of the type of saturation irregularities proposed.

Several other mechanisms for attenuation have been proposed although their applicability to upper crustal rocks is debatable. Several of these mechanisms may be operable in the upper mantle, however, such as grain boundary relaxation, relaxation caused by a phase change, and a "high temperature background attenuation" probably related to Nabarro diffusion (Jackson and Anderson, 1970). Experimental evidence suggests little change in attenuation as a function of temperature at relatively low temperatures (Volarovich and Gurvich, 1957) when the rock is not thermally cracked and the saturating fluids are not altered. However, near phase changes, attenuation could change rapidly with temperature. High attenuation has been observed at critical points in multi-component systems (Spetzler and Anderson, 1968; Wang and Meltzer, 1972). Energy is absorbed by a medium whose equilibrium is

disturbed by a stress wave. The frequency at which this occurs depends on the rate at which phase equilibrium can follow the changes imposed upon it by the wave (Spetzler and Anderson, 1968). This mechanism may result in high attenuation in certain geothermal areas.

The effective attenuation due to scattering by inclusions in the rock is now evaluated. Although this is a geometrical effect, it can, in some cases, affect the observed attenuation. Yamakawa (1962) has analyzed the scattering of compressional waves by spherical pores. The equivalent attenuation coefficient,  $\alpha$ , is given by:

$$\alpha = \frac{12\pi^4 f^4 r^3 \phi}{V_p^4} \left\{ 2B_0^2 + \frac{2}{3}(1+2\nu^3)B_1^2 + \frac{(2+3\nu^5)}{5}B_2^2 \right\} \quad (3-44)$$

where

$$B_0 = \frac{K - K'}{3K' + 4\mu}$$

$$B_2 = \frac{-20\mu^2}{3\mu(9K + 8\mu)}$$

$$B_1 = (\rho - \rho')/3\rho$$

$$\nu = V_p/V_s .$$

$r$  is the radius of the inclusions and  $f$  is the frequency.

Primed coefficients represent inclusion properties.

Although the effective attenuation of incident S waves has not been calculated, one may estimate this effect by noting that the energy scattered due to SP reflections is equivalent to PS reflections because of the reciprocal theorem. While losses due to SS reflections are not the same as PP, they are probably close and one can reevaluate



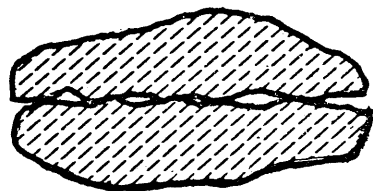
equation 3-44 for incident S waves assuming SS $\equiv$ PP. Doing so, the only changes in the equation are that  $V_p$  is replaced by  $V_s$  and  $\nu = V_s/V_p$ . Attenuation due to scattering is strongly dependent on frequency ( $\propto f^4$ ). As will be shown in Chapter 5, scattering effects can be important, if not dominant, at high ultrasonic frequencies ( $f > 1$  MHz) or lower if the inclusion radius is large. At seismic frequencies, scattering due to pores is negligible.

Another geometric effect is the apparent attenuation due to selective reflection of the short wavelength component of seismic waves in thin beds. Although of little importance with respect to laboratory measurements, this mechanism may, under certain conditions, contribute to observed amplitude loss in seismic sections. O'Doherty and Anstey (1971), Schoenberger and Levin (1974), and Spencer et al. (1977) have examined these cases in detail. In general, selective reflection due to cyclic stratification contributes a small but important part to the overall attenuation. If high reflection coefficients occur, the apparent attenuation can be high.

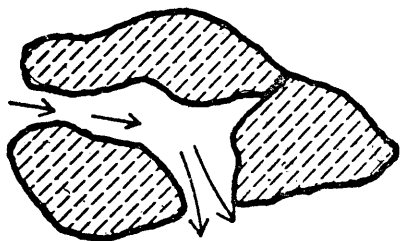
## FIGURE CAPTIONS

- Figure 3-1. Schematic illustration of several proposed attenuation mechanisms for saturated and partially saturated porous rocks.
- Figure 3-2. Friction coefficient as a function of boundary layer thickness for the imperfect lubrication model (from Gemant, 1950). Boundary layer thickness may be related to fluid saturation,  $S_w$ .
- Figure 3-3. Relative permeability,  $\chi_r$ , for wetting and non-wetting phases as functions of wetting fluid saturation.  $S_{wi}$  is the irreducible saturation.
- Figure 3-4. a) The effect of capillary action on the distribution of water and gas within a natural rock formation.  $P_c$  is capillary pressure. The figure is from Mayer-Gürr (1976). b) Phase diagram of a two component liquid and gas mixture. The effect of pore pressure reduction is shown in line A-D.
- Figure 3-5. Schematic illustration of a simple model for the occurrence of gas bubbles in a solution drive situation.  $S_g$  is the gas saturation.

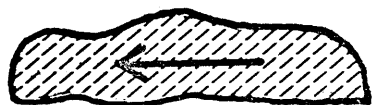
## Effects of Fluid Saturation



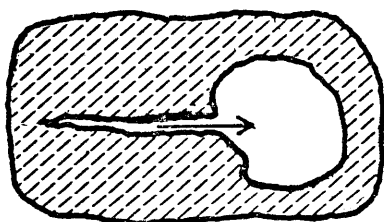
Crack Lubrication  
Facilitating Friction



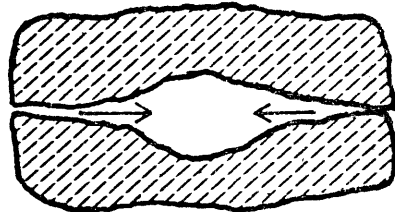
Biot Fluid Flow with  
Boundary Shear



Squirting Flow  
crack to pore



edge to center



Gas Bubble Motion  
and Squeezing

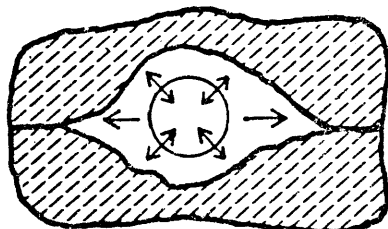


Figure 3-1

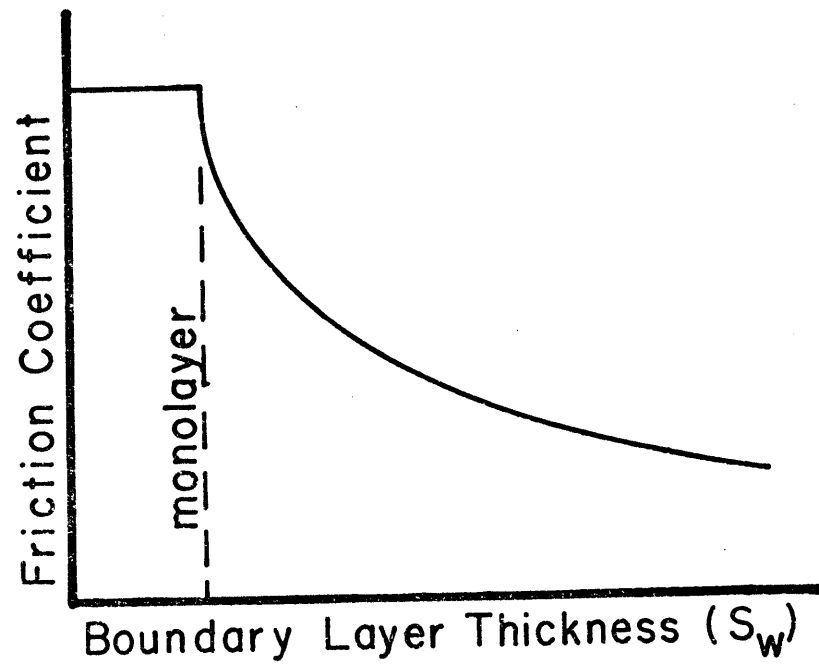


Figure 3-2

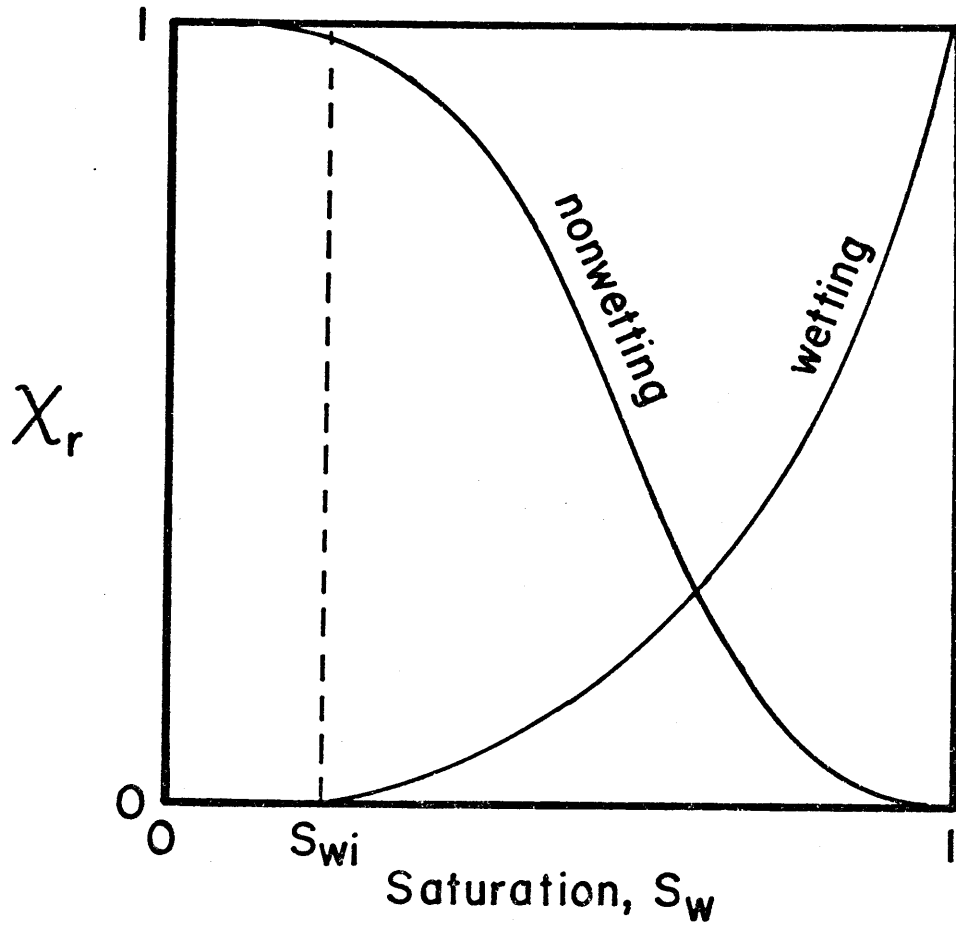
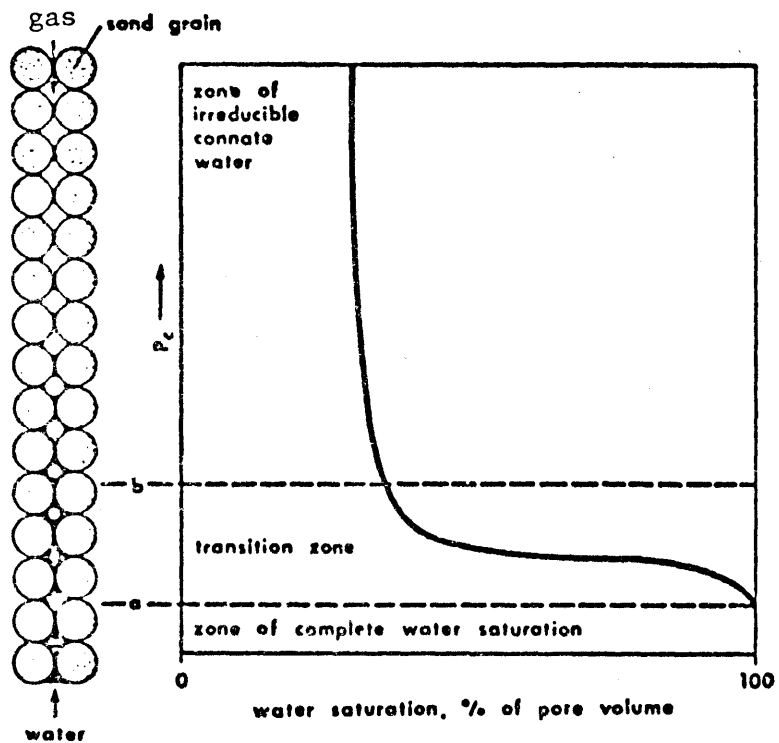
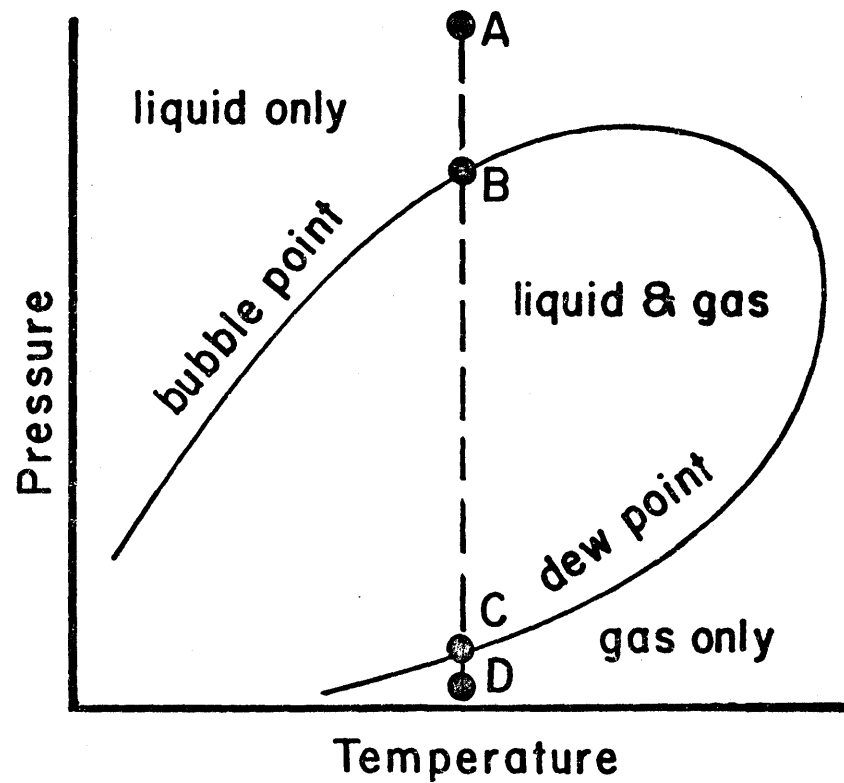


Figure 3-3



(a)



(b)

Figure 3-4

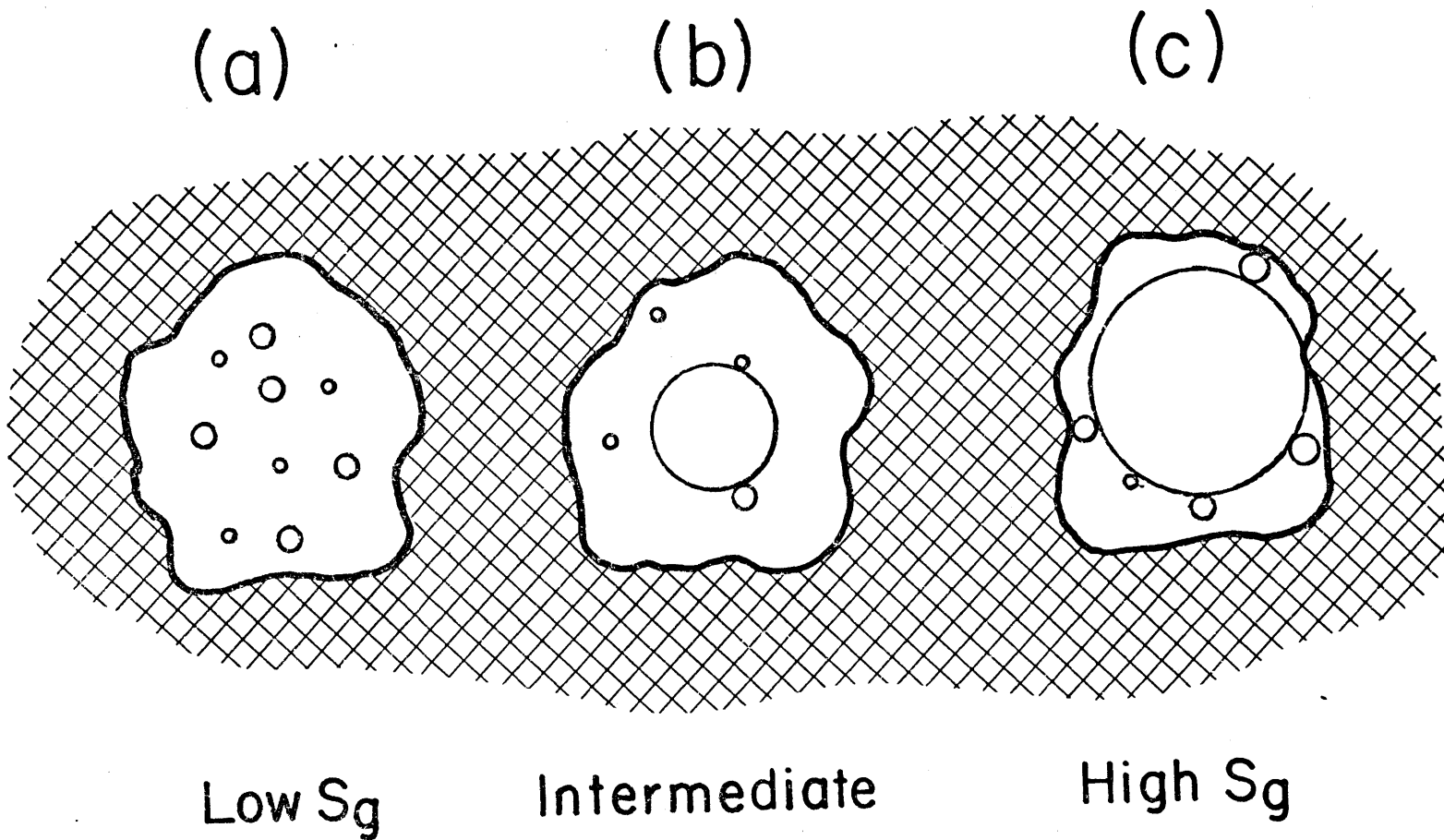


Figure 3-5

## CHAPTER 4

## EXPERIMENTAL TECHNIQUES

The methods used in this thesis for measuring attenuation are pulse transmission using spectral ratios and resonant bars. As discussed in Chapter 2, the pulse transmission technique is most suited for jacketed samples in pressure vessels. However, the method does require some rather cumbersome data processing and thus, for experiments where pressure is not a variable, the simpler bar resonance technique is used. Furthermore, several of the samples studied have  $Q > 100$  and thus the pulse method is inappropriate. In this chapter the experimental methods and equipment are described. Data processing and potential errors are also discussed. In the case of pulse transmission, the effect of stress amplitude is briefly examined. Finally, important aspects of sample preparation and treatment are presented. A detailed discussion of the specific experiments and samples studied are deferred to the next chapter.

#### 4.1 Pulse Transmission - Amplitude Ratio

The accurate measurement of attenuation using pulse transmission can be difficult since amplitudes are strongly affected by geometrical spreading, reflections and scattering in addition to intrinsic damping. Correction for these effects can be a formidable task. This difficulty is



removed by determining the attenuation of a rock sample relative to a reference sample which has very low attenuation, using the spectral ratio technique. Only one-way transmission effects are measured. The sample to be studied and reference sample have exactly the same shape and geometry. Essentially, two measurements are made using identical procedures, one with the rock of interest and again with the reference sample.

The amplitudes of plane seismic waves for the reference and the sample can be expressed as

$$A_1(f) = G_1(x) e^{-\alpha_1(f)x} e^{i(2\pi ft - k_1x)} \quad (4-1)$$

$$A_2(f) = G_2(x) e^{-\alpha_2(f)x} e^{i(2\pi ft - k_2x)}$$

where  $A$  = amplitude,  $f$  = frequency,  $x$  = distance,  $k = 2\pi f/v$  = wavenumber,  $v$  = velocity, and  $G(x)$  is a geometrical factor which includes spreading, reflections, etc.  $\alpha(f)$  is the frequency dependent attenuation coefficient. Subscripts 1 and 2 refer to the reference and sample respectively. From available data it is reasonable to assume that over the frequency range of the measurements, 0.1 - 1.0 MHz,  $\alpha$  is a linear function of frequency, although the method itself tests this assumption (Knopoff, 1964; Jackson and Anderson, 1970; McDonal, et al., 1958). Then one can write:

$$\alpha(f) = \gamma f \quad (4-2)$$

where  $\gamma$  is constant and related to the quality factor  $Q$  by

$$Q = \frac{\pi}{\gamma V} \quad (4-3)$$

When the same geometry is used for both the sample and standard (i.e., same sample dimensions, transducers, arrangements) then  $G_1$  and  $G_2$  are frequency independent scale factors. The ratio of the Fourier amplitudes are:

$$\frac{A_1}{A_2} = \frac{G_1}{G_2} e^{-(\gamma_1 - \gamma_2)fx} \quad (4-4)$$

or

$$\ln \frac{A_1}{A_2} = (\gamma_2 - \gamma_1)xf + \ln \frac{G_1}{G_2} \quad (4-5)$$

where  $x$  is the sample length. When  $G_1/G_2$  is independent of frequency  $(\gamma_2 - \gamma_1)$  can be found from the slope of the line fitted to  $\ln(A_1/A_2)$  versus frequency. If the  $Q$  of the standard reference is known,  $\gamma_2$  of the sample can be determined. When the  $Q$  of the standard is very high (i.e.  $Q_1 = \infty$ ) then  $\gamma_1 = 0$  and  $\gamma_2$  of the rock sample can be determined directly from the slope.

Aluminum is used as the standard reference.  $Q$  for aluminum is about 150,000 (Zamanek and Rudnick, 1961), as opposed to  $Q \leq 1000$  for rocks. Thus taking  $\gamma_1 = 0$  never introduces more than 1% error. For typical rocks where  $Q = 10-100$ , the error is less than 0.1% and is negligible. A more serious concern is the validity of assumption that the geometric factors  $G_1$  and  $G_2$  have the same frequency dependence, and  $G_1/G_2$  is independent of frequency. With polished rock surfaces and good coupling between the transducer holder and sample, one would not expect frequency dependent reflection coefficients at the interface. Repeated measurements showed that pulse amplitudes, shapes and spectra were duplicated.

The error introduced by assuming an infinite  $Q$  for the aluminum is obviously not associated with the error or accuracy of the results. The problem of accuracy and repeatability is discussed in a section 4.5. It should also be noted, as mentioned in Chapter 2, that this method is useful only for rocks with low  $Q$  ( $<100$ ) due to the difficulty in using linear regression analysis resulting in a low slope and correlation coefficient for high  $Q$  samples. The technique, while conceptually and mathematically simple, does require a great deal of data processing. This problem will be addressed later.

## 4.2 Ultrasonic Measurement System

An ultrasonic measurements system has been developed to determine acoustical waveforms and velocities under various pressure conditions. Piezoelectric transducers mounted on the ends of the sample generate and receive P and S waves. Coupling is provided primarily by the confining pressure in a modified Birch (1960) technique. The resulting waveforms are then displayed and digitized for subsequent analysis. Travel times through the sample are obtained to determine wave velocities.

A block diagram of the system's electronics is shown in Figure 4-1, with a photograph shown in Figure 4-2. A Dumont model 404B pulse generator is used to produce a low voltage (10 V), 1 $\mu$ s pulse and oscilloscope trigger. Variable pulse repetition rates and trigger delay are available. The pulse is used to drive a Velonex model 350 high power pulse generator, the output of which drives the transducers. An output voltage of 250 V into 50 $\Omega$  is used. The trigger output of the Dumont unit is used to trigger a Tektronix 545B oscilloscope which provides a delayed pulse to trigger the display oscilloscope. This feature allows the display of any portion of the waveform desired. A Tektronix IL5 spectrum analyzer installed in the 545B was not used for data analysis but did prove useful in transducer design.

The low voltage pulse from the Dumont unit also serves the purpose of providing a reference mark for timing measurements. The pulse is fed into a Hewlett-Packard 5308A Timer counter and a continuously variable (1-30 $\mu$ s) delay generator. The output of the delay is a 1 $\mu$ s pulse which is then filtered to provide a variable rise time. This filtered timing pulse is connected to the second input of the timer so that a direct measurement of the time interval between the driving and timing pulses can be obtained. The use of time interval averaging in the timer results in a resolution of 1 ns. The rise time of the timing pulse is matched to the rise time of the signal as shown in Figure 4-3 and the "first arrival" is defined as 50 mV above zero on the timing pulse. Thus the transit time of the signal through the sample is unambiguously determined regardless of the attenuation. The transit time is measured several times and then averaged to eliminate bias in fitting the timing pulse to the signal.

The signal from the receiver transducer and the timing pulse are simultaneously displayed on a Hewlett-Packard 175A oscilloscope. The relative position between these signals is unaffected by the delay trigger operation. If needed, a broad band linear preamplifier

(HP model 465A) may be used to amplify the received signal. An HP 1782A Display Scanner is used to trace the displayed waveform onto an HP 7035A X-Y plotter for subsequent digitization.

Rock samples used in this study are 1 inch (2.54 cm) long and 1.25 inches (3.18 cm) in diameter. The sample is placed between two transducer holders and jacketed using a urethane strip bonded with tetrahydrofuran. This assembly, connected to a plug is then placed in the pressure vessel as shown in Figures 4-4 and 4-5. The vessel, with a 1.5 inch (3.81 cm) inner diameter, is rated to 10 kb. External confining pressure is applied via a kerosene medium using a two stage pump system. The confining pressure is monitored with a bourdon tube gage and a manganin coil. The coil is connected with a bridge circuit, instrumentation amplifier and panel meter to provide a direct, digital pressure reading. Confining pressure is determined to within 2 bars.

Pore fluid pressure may be controlled independently from the confining pressure and ranges from 0-2 kb. Access to the sample is through the plug and transmitter transducer holder as shown in Figure 4-4. Pore pressure is measured on a bourdon tube type gage and can be determined to 10 bars. Ideally, one would like to have an outlet and second gage for the pore pressure system to determine pressure equilibrium within the sample.

Lacking space for this, sufficient time (depending on the rock permeability) must be allowed for the fluid pressure to stabilize.

Furthermore, time must be allowed between measurements for the temperature within the vessel to stabilize after compression or decompression. A copper-constantan thermocouple mounted next to the sample connected to a Fluke 2170 digital thermometer monitors these temperature changes to within 0.2°C. Constant vessel temperature is maintained by a circulating water system coiled around the vessel.

Transducer holders are used instead of mounting the transducers directly on the sample for two reasons. First, it is imperative that the coupling between the transducers and sample be constant. By using the same holders for each experiment and by inserting a thin copper disc between the holder and sample, this is accomplished. Second, pore pressure must be brought in through the transmitter holder requiring a certain thickness for mounting the high pressure tubing.

A cutaway view of the transmitter transducer holder is shown in Figure 4-6. The holder is 2 inches (5.08 cm) long, 1.25 inches (3.175 cm) in diameter with 0.5 inches (1.27 cm) between the transducers and sample. Pore pressure is introduced via the tube through the center. The

receiver holder is different only in that no pressure tube is needed so that the bottom thickness is 0.030 inches (0.076 cm). Titanium is used due to its similar acoustic impedance compared to most rocks and because of its hardness so that the holder will not deform into the rock under high pressure.

Lead-zirconate-titanate piezoelectric transducers are used in a stacked P and S mode arrangement as shown in Figure 4-6. The transmitter transducers are 1 MHz Gulton HDT-31 (PZT, 4 equivalent) material of high efficiency and high  $Q$  ( $>500$ ), while the receiver transducers are Gulton G1500 (PZT 5 equivalent) with a low  $Q$  (80) to reduce ringing. P waves are generated using standard thickness mode discs. The S wave transducers, on the other hand are fabricated using pie-shaped shear plate wedges (provided by Valtec, Valpey Fisher Corporation) epoxied to an aluminum backing plate as shown in Figure 4-7. The result is a torsional transducer which produces very little precursory P modes.

The stacked P-S transducer system has the advantage that either mode may be selected externally to the pressure vessel by switching the leads to the high voltage or ground as shown in Figure 4-7. Thus, both modes may be studied without running a separate experiment. All electrical connections both inside



and outside the vessel are made with coaxial connectors and cable to reduce spurious electrical noise and RF coupling.

Some difficulty was encountered in the construction of the transducer stacks and holders. Ideally, one would like to keep the transducers exposed only to atmospheric pressure. This reduces transducer-holder coupling effects under pressure since the transducers could then be glued directly to the holder. The physical constraints of the system, however, prohibited this arrangement and it was found that glue under high pressures would crack. This presented little problem for the P wave but coupling for the S wave was variable due to slippage on the time scale of a minute or two. A compromise solution was found in the use of a nonhardening, pliable sealant (Permatex, Formagasket no. 2) as the bonding agent. Spread in a thin film, the sealant is impervious to kerosene and allows capacitive coupling between the electrodes and transducers, sufficient at the voltages and frequencies used. The bond is supplemented by a stiff backing spring as shown in Figure 4-6.

Another problem arose in the placement of the pore pressure tubing. Due to size considerations it was necessary to locate this through the center of the

transmitter holder and transducers. This presents no particular distortion in the S waveforms since the displacement along the center line is zero. Some distortion exists for the P waves but was found to be of minor consequence.

#### 4.2a Determination of Velocity

At each pressure, the travel time,  $t$ , of the P or S wave is measured. From this, the total system delay,  $t_s$ , must be subtracted, giving the transit time through the sample,  $t$ .  $t_s$  is due primarily to the travel time of the waves through the titanium transducer holders and was determined by running the experiment with the holders face to face. This was repeated several times to check on reliability and, as discussed in the next section, samples of fused quartz with known velocities were used to insure correct calibration of the system delay.

Velocity, then, is found from  $V = \ell / (t - t_s)$  where  $\ell$  is the sample length. Linear strain as a function of pressure may be corrected for using the static measurements discussed later. In general, as will be shown in the next section, such a correction is small in terms of the overall accuracy of the system.

#### 4.2b Data Processing

Full waveforms of both P and S waves were plotted on the X-Y recorder and then manually digitized. It was discovered that the HP 1782A Display Scanner did not produce a constant peak voltage for the x axis during an experimental run. However, careful testing showed that the same x interval on the oscilloscope was recorded each time. Thus the plotted waveforms may be stretched or contracted relative to each other. To correct for this, the waveforms were digitized at 40 ns per point, one half the interval to be used (80 ns) for signal processing. The time base was then adjusted according to the time between the end points of the signal and scaled to a total record length of 18.4  $\mu$ s. The data was then scanned and interpolated to obtain a constant digitization interval of 80 ns with a resolution in the y direction of one part in  $10^4$ . The Nyquist frequency for this sampling rate is 6.25 MHz. No antialiasing filter was needed.

Sidewall reflections and reflections within the transducer package interfere with the direct pulse. Because these components have ray paths longer than the sample length, the Q values obtained by using the direct pulse plus interfering waves are altered. The reflections may be eliminated by one of two techniques: homomorphic

deconvolution or time windowing and taper.

Homomorphic signal processing is a nonlinear technique based on a frequency invariant filter operation on the complex cepstrum and allows the separation of the direct pulse from the reflection components (Oppenheim and Shafer, 1975, pp. 480-531). The method has been successfully applied to seismic problems (Ulryck, 1971; Tribolet, 1977a). The essential advantage of this method over other forms of deconvolution is that no a priori knowledge of the nature of the direct pulse or medium transfer function is required. It does, however, assume that the recorded signal is the result of a convolution of the direct pulse and medium response. The mathematical basis of the method is discussed in Appendix D.

While homomorphic deconvolution represents a precise way to remove unwanted reflections, in practice the method is cumbersome and expensive for large quantities of data. In fact, it was only used in this thesis for special cases and as a guide to time windowing. Most of the data has been windowed to accept about the first 4-5  $\mu$ s of the signal with a cosine taper applied to the end. As it turns out, this technique is nearly as effective as deconvolution in removing the reflection components because these are fairly well separated in time.

If needed, a simple linear termination filter may be applied to the signal. In this case, of course, the same filter must be applied to the aluminum standard waveform before spectral ratios are determined. The standard filter used has a bandpass between 0.2 and 0.8 MHz with a 0.2 MHz cut-off at each end. These parameters could be changed if necessary.

After the preliminary processing, the resultant waveform is Fourier transformed using a 1024 point FFT routine to obtain the amplitudes used in the spectral ratio method. In order to efficiently handle the large amounts of data obtained for each experiment, an interactive graphics program package was developed. Time windowing the waveform and frequency windowing the spectral ratios is done by means of a graphics cursor on the terminal. Hard copy plots of the spectra and line fits may be obtained. The frequencies over which spectral ratios were taken were dictated by the bandwidth of the received signal. Only those frequencies occurring in the peak energy of the spectrum were used in determining  $Q$ .

#### 4.2c Sources of Error

In this section the sources and nature of errors in the velocity and attenuation are discussed. As will be shown, it is difficult to assign a formal accuracy

figure to the attenuation and at the present time, the reliability of such measurements must be considered in terms of repeatability. Errors in velocity, though, may come from among the following:

1. Time interval measurement. The use of the HP 5308A time interval counter permits timing through averaging to a resolution of 1 ns. In practice, however, the true resolution is limited by the operator's ability to judge the position of the first arrival and accurately match this with the timing pulse. While the use of a variable rise time timing pulse facilitates this match for all but the most distorted waveforms, it is found that the resolution obtained is better than or equal to  $\pm 10$  ns.

By comparing measured time between several separate experimental runs of the transducer holders face-to-face under identical conditions, it is found that time interval is repeatable with a standard deviation,  $\sigma_t$  of 20 ns. for both P and S waves. The deviation is larger, about 50 ns at pressures lower than 200 bars.

2. Sample length. Initial sample length is measured to within  $\pm 0.0001$  inches (0.0003 cm). For the determination of velocity this may be corrected for linear strain under hydrostatic load. As will be discussed later, these types of measurements were done. In the worst case, the

maximum strain for any sample studied was about 3%.

If the initial length is uncorrected for pressure then for one inch (2.54 cm) samples, there can be a maximum error of 0.03 inches (.076 cm). One may use this to evaluate the worst case accuracy for velocity. Letting the standard deviation for the sample length,  $\sigma_l$  be the maximum error (an overestimate), then the variance of the velocity estimate,  $\sigma_v^2$  may be written as:

$$\begin{aligned}\sigma_v^2 &\approx \sigma_l^2 \left(\frac{\partial V}{\partial l}\right)^2 + \sigma_t^2 \left(\frac{\partial V}{\partial t}\right)^2 \\ &= \frac{\sigma_l^2}{t^2} + \frac{\sigma_t^2}{l^4}\end{aligned}\tag{4-6}$$

Thus, the variance is reduced for long sample lengths and/or time intervals. Unless the velocity is very high (for our constant,  $l$  of one inch) the  $\sigma_t^2$  term dominates  $\sigma_v^2$ . From the above equation we find that velocity is determined to within 3% for both P and S waves except at low pressures where this figure increases to 9-10%. These numbers were confirmed by determining the velocity of fused quartz with  $V_p = 5.9$  km/s and  $V_s = 3.75$  km/s for several sample lengths. The results were well within the calculated errors and also suggest that the 10% figure for low pressures might well be an overestimate, the true value being closer to 5%.

3. Dispersion of  $V_p$ . Several trade-offs involving sample dimensions,  $\ell$  and  $d$  and the wavelength,  $\lambda$ , may involve the accuracy of  $V_p$  determinations (Anderson and Liebermann, 1966). In general, the length to diameter ratio,  $\ell/d$  should be less than 5 for clear observation of the P wave arrival. Otherwise, the arrival amplitude decreases as compressional energy is delayed by sidewall reflections. For  $\ell/d \gg 5$  the wave also travels near the bar velocity  $(E/\rho)^{1/2}$ . Furthermore, to minimize dispersion of the P-wave,  $d/\lambda$  must be greater than 5 (Tu et al., 1955). However, if  $\lambda$  is too small (about three times the grain size) then substantial scattering and waveform distortion will occur (Mason and McSkimin, 1947).

For the system used for this thesis,  $\ell = 2.54$  cm,  $d = 3.18$  cm. Thus  $\ell/d = 0.80$  and the first criterion holds. However, for reasonable values of  $\lambda$  for 0.5-1.0 MHz waves,  $d/\lambda$  is about equal to 5. Since  $\lambda$  cannot be decreased without entering the scattering region, this number must be accepted.

In summary, P and S wave velocities may be determined with an accuracy of 3% at pressures greater than 200 bars. For lower pressures the accuracy is decreased to a calculated value of 10% but measurements of P and S velocities in fused quartz suggest that this value is actually lower.



The accuracy of ultrasonic attenuation measurements is not easily determined. In fact, no formal equation for the variance may be written that makes any sense. For example, one may examine the formal errors on line fitting to data. Define  $S = \text{slope}/\sigma$ , where  $\sigma$  is the standard deviation of the estimate. Then, in terms of statistical reliability, a large value of  $S$  corresponds to a good fit to the data and for  $S < 1$ , the fit must be rejected. This is precisely the reason why the amplitude ratio method is limited to low  $Q$  samples (large slope) but it has no bearing on the accuracy or resolution. Using synthetic data, Millahn and Jurczyk (1977) showed that in some cases a high  $S$  was associated with large errors and concluded that  $S$  only measures the modulation character of the spectral ratio and not the accuracy of the method.

It is apparent that the accuracy of the attenuation measurement can only be based on repeatability and comparison to other techniques. The validity of the assumption that  $G_1/G_2$  in equation 4-5 is constant will, however, be discussed. Any one of the following sources of error can result in non-exponential decay in amplitude as a function of frequency. Generally, these effects are second order.

1. Deviation from plane waves: For large distances from the transmitting transducer, the plane wave assumption of equation 4.1 may not be valid. Theoretical formulations of the diffraction field from a circular compressional source are based on fluids and are thus not applicable to shear waves and perhaps compressional waves in solids especially if there is appreciable anisotropy (Truell et al., 1969). It appears, however, that plane wave deviation is not a major source of error. Q values have been obtained for Lucite and Berea sandstone relative to aluminum for 1, 2, and 3 inch (2.54, 5.08, and 7.62 cm) sample lengths under unconfined uniaxial stress of about 300 bars. In both sets of samples the Q values for P and S waves were consistent. Furthermore, as will be shown in the next chapter, attenuation measurements made on the same rock under the same conditions but with different sample dimensions also produce consistent results.

2. Wave distortion: The transmitted wave may be distorted by the superposition of other waves and modes. As discussed in section 2.1c this may be overcome by ensuring a large sample to transducer diameter ratio. In this thesis, however, such effects are removed by deconvolution or time windowing.

3. Parallelism: If the sample faces are not planar and parallel, significant errors can occur since the wave is not reflected or transmitted in phase at the boundary. However, as noted in section 2.1c this effect is pronounced only at very high frequencies ( $>>1$  MHz). In any event, the faces of the samples are parallel to within  $\pm 0.001$  inches (0.0025 cm).

4. Digitizing errors: This may represent the most likely source of error in the attenuation measurement and is, of course, human error. If one assumes that digitizing errors are random, then if we were to sample a waveform  $n$  times, the resulting measured values would fall on a normal distribution about the expected value. Furthermore, errors in frequency space would also be normal. For truly unbiased errors this would present little difficulty in that spectral ratios are used although significant errors could occur for narrow bands.

Unfortunately, there are few ways to test this and other sources of errors. To determine probable error, one technique used was the repeatability of measurements. This was done for the Navajo sandstone and the results are shown in Figure 4-8. Here, waveforms are shown for a single run plotted and digitized three times (trials 1, 2, and 3) plus a waveform taken from a different experiment but at the same pressure (trial 4). The

percent deviation in the  $Q$  values obtained from the spectral ratio method are shown relative to trial 1 (an arbitrary choice). It is clear that the results fall within a standard deviation of 7% and that digitizing errors are no larger than the repeatability in this case. Furthermore, during the course of the experiments, identical conditions were encountered for the same rock but in different runs. These cases provided a further check on reproducibility. Also, as will be discussed in the next chapter, the results obtained with the system described in this chapter may be compared to data found for the same rock under the same conditions but with a different experimental setup and sample dimensions. The reproducibility or precision of the  $Q$  measurements then, is conservatively estimated at 15-20% depending on waveform quality. However, this makes no statement on accuracy. It may be that the estimates of  $Q$  obtained with the spectral ratio method are biased. One way of checking this possibility is to compare results from this technique with those found from other methods. There are several severe problems in doing this, though. First, all will be seen in the later chapters, a direct comparison would be valid only if parameters such as frequency and strain amplitude were the same. This is very difficult to achieve. Second, most of the rocks suitable for comparison have high  $Q$ 's and are thus not

amenable to the spectral ratio method. One material that may be used, however, is plexiglass. Since plexiglass is crack free, amplitude effects are insignificant, but it has a relatively low  $Q$ .  $Q$  values obtained using a dynamic resonance technique (22) and the ultrasonic method (20) agreed to within the precision of the spectral ratio method and thus we may assume the results of this method are not overly biased. While error bars are not drawn for every point, they are included for several representative data on each graph.

#### 4.3 Forced Vibration - Resonance

Attenuation is found using longitudinal vibrations for several experiments where pressure is not a parameter. The simplicity of the method combined with easy data analysis makes this technique attractive. As discussed in Chapter 2, the resonance method is based on the phenomenon of standing waves. In particular, for longitudinal (and torsional) vibrations in a bar of length  $\ell$ , the velocity is given by:

$$v = \lambda f = \frac{2\ell f_n}{n} \quad (4-7)$$

where  $\lambda$  is the wavelength and  $f_n$  is the frequency of mode  $n$ . The relationships between velocities and moduli are functions of the sample geometry and were given for

longitudinal and torsional vibrations in equations 2-6 through 2-8. For longitudinal waves in long, thin bars ( $d/\lambda \ll 1$ , where  $d$  is the sample diameter) the velocity determined by the resonance method is known as the bar or Young's modulus velocity:

$$v = (E/\rho)^{1/2} \quad (4-8)$$

where  $E$  is the Young's modulus and  $\rho$  is the density.

The attenuation of the sample,  $Q_E^{-1}$ , is found by measuring the half-power frequency bandwidth,  $\Delta f$  about a resonance peak at  $f_n$ . From equations A-25 and A-26:

$$Q_E^{-1} = \frac{\Delta f}{f_n} \quad (4-9)$$

$\Delta f$  may also be defined as the bandwidth between points -3db in amplitude from the peak.

A block diagram of the resonance measurement system used in this study is shown in Figure 4-9. A Hewlett-Packard model 3300A function generator with a built-in frequency sweep option (HP 3304A) can generate a sine wave varying between 1 Hz and 100 kHz. This is used to quickly scan a decade of frequency in order to locate resonance peaks. The sweep output provides a voltage ramp proportional to frequency and enables a plot of amplitude

versus frequency to be made on an x-y plotter. A General Radio 1161-A frequency synthesizer provides a sine wave output with frequency settable to 0.01 Hz in a range of 0-100 kHz. This highly accurate frequency source is used to determine the half power bandwidth of a resonance peak. The exact frequencies are read from an HP5308A universal counter.

The signal from the function generator or frequency synthesizer is amplified by an HP 467A power amplifier which drives the sample. The amplitude of the driving signal is monitored on the Fluke voltmeter. The signal from the detector on the sample is then amplified by an HP 465A preamplifier. This output may be fed to an oscilloscope or an HP 400E AC Voltmeter. The output of the function generator can thus be connected to the horizontal trace of the oscilloscope. As the frequency approaches resonance, a Lissajous pattern may be observed. This pattern could be used to determine phase shift and thus attenuation but its use here was to identify nodal points and vibration modes.

The AC voltmeter is used to determine the shape of the resonance peak. Once the resonance condition is achieved, the gain of the power amplifier is adjusted so that the meter reads 0 db. The frequency is then

adjusted to obtain the two -3 db points in amplitude. The difference between these frequencies is the  $\Delta f$  bandwidth of equation 4-9.

A DC output proportional to the RMS voltage of the received signal is provided by the AC voltmeter. This is used to obtain plots of amplitude versus frequency for a graphical display of the resonance spectra. Theoretical resonance frequencies were calculated using previously published elastic constant data in order to facilitate the location of peaks.

The samples used in this study are about 15 cm (6 inches) in length and 0.635 cm (1/4 inch) in diameter. The large length to diameter ratio reduces dispersion of the wave. Longitudinal vibrations are driven and detected by a pair of 0.635 cm diameter coaxial plated PZT-4 piezoelectric transducers. These are bonded to the ends of the sample with shellac. Operated well below their resonance frequency of 1 MHz, the transducers tend to be more efficient at the higher frequencies. This makes the Q analysis of higher modes difficult for low loss samples since the effect is to spread the bandwidth.

During the experiment, the sample is supported exactly at the fundamental mode nodal point ( $l/2$ ).



This is important for high  $Q$  ( $>100$ ) samples since deviations of the support from the node will result in extraneous energy loss. For low  $Q$  samples, however, it is sufficient to place the sample on a soft pad. Unfortunately, the rigid support method eliminates the possibility of studying even modes since nodal points for these do not occur at  $\ell/2$ . In general, it was found that given the simple sample supports used in this experiment, only the fundamental mode is reliable for  $Q$  measurements. A photograph of the resonance set-up and sample holder is included in Figure 4-10. Not shown are the frequency counter, x-y plotter, or oscilloscope.

The use of a piezoelectric transducer cemented to the sample presents several difficulties. First, there is a shift in the measured resonance frequency versus the actual frequency due to the added mass of the transducer. For equal transducer-sample cross-sections, the mechanical resonant frequencies are given by (Bozorth et al., 1951):

$$M_s f_s \tan\left(\frac{\pi f_c}{f_s}\right) + M_t f_t \tan\left(\frac{\pi f_c}{f_t}\right) = 0 \quad (4-10)$$

where  $M_s$  and  $M_t$  are the masses of the sample and transducer respectively.  $f_s$  is the transducer resonant frequency and  $f_c$  is the measured frequency.  $M_s$  and  $M_t$  are found by

weighing the transducer and specimen beforehand. Equation 4-10 is then solved for  $f_s$  using a simple Newton method. Second, the layer of shellac used to bond the transducers to the sample also effects the measured frequency (Terry, 1957). This effect is small, however, and will be neglected.

Finally, one must consider the effect of the mechanical  $Q$  of the transducers on the actual  $Q$  of the rock. This relationship is most easily expressed in terms of the decrement,  $\delta = \pi/Q$  and masses (Marx, 1951):

$$\delta_s = (M_c \delta_c - 2M_t \delta_t) / M_s \quad (4-11)$$

where the subscripts are as defined in equation 4-10. For PZT-4 transducers with a mechanical  $Q > 500$  ( $\delta_t < 6 \times 10^{-3}$ ) and  $M_t = 0.5164$  g one may evaluate this effect. For the Solenhofen limestone studied in this thesis,  $M_s \approx 12$  g giving  $M_c = 13.15$  g, and  $Q_c = 260$  ( $\delta_c = 1.2 \times 10^{-2}$ ). Thus from equation 3.28,  $Q_s/Q_c = 0.93$ . Frederick diabase with  $M_s \approx 14.6$  g and  $Q = 770$ , results in  $Q_s/Q_c = 1.04$ . In the other extreme, the Berea sandstone samples have  $M_s \approx 10$  g with a  $Q$  of 30. In this case,  $Q_s/Q_c = 0.9$ . Therefore, with no corrections for transducer loss,  $Q$  values less than 1000 are determined

within 10% even though differences between actual and measured  $Q$  may be large for low loss rock such as the diabase.

Given that the corrections mentioned above are applied to the data, checks on the repeatability of the  $Q$  determinations indicate a resolution of 5% or better. This could be improved by a more sophisticated sample support and a more accurate method of finding the -3 db points. Comparison with previously published data imply equal accuracy. A typical resonance peak is shown in Figure 4-11 for the fundamental mode of the Solenhofen limestone.

#### 4.4 Static Measurements

Linear strain as a function of hydrostatic confining pressure is determined for all the samples studied. This is done for two reasons. First, from these experiments, the correction term for the sample length may be found for use in determining the ultrasonic velocities. Second, the sample may be characterized in terms of crack density as discussed by Walsh (1965). This interpretation will be particularly useful in the study of attenuation in thermally cracked rocks.

In the experimental method used, two BLH SR-4, FAE-50-12S6 electric resistance strain gages are epoxied directly to the sample, parallel to its length. Samples

are about 0.5 inches (1.27 cm) in diameter by 1.25 inches (3.18 cm) long. The use of duplicate gages provides a backup in case of failure of a gage and is also a check on the reliability. In the case of porous rocks, the surface is coated with  $\text{Al}_2\text{O}_3$  filled epoxy prior to gage installation. This insures a smooth surface to prevent gage collapse into pores at high pressure. The epoxy filler has a negligible effect on the elastic properties of the rock.

The samples are then potted in an RTV compound to isolate them from the pressure medium. Since the most likely place for the pressure medium to leak is along the gage leads, these are coiled to provide a longer path for any possible leak. The potted sample is then coated several times in kerosene impervious "K-Kote". The gage leads along with thermocouple leads are then connected to the pressure vessel plug.

A block diagram of the static measurement system is illustrated in Figure 4-12 and a photograph of the system is shown in Figure 4-13. The experiments are run in the same pressure vessel as the ultrasonics. Pressure is determined by a Manganin coil with the output of the associated bridge circuit fed to the horizontal axis of dual trace HP X-Y recorder. Similarly, the strain gages

are connected to duplicate bridges with the outputs connected to the  $Y_1$  and  $Y_2$  axis of the recorder.

The experiments are generally run with a strain gage calibration so that one inch on the record is equal to a strain of 500 su ( $5 \times 10^{-4}$ ). In using this technique to find  $d\ell/\ell$  for a length correction, the pressure axis is calibrated so that one inch is equal to 250 bars. Otherwise, one inch is set equal to 500 bars. These settings provide more than enough resolution needed.

During the experiments, pressure is increased slowly to maintain thermal equilibrium as monitored by the thermocouple. In all experiments, strain as a function of increasing and decreasing pressure is found to determine hysteresis effects. If there is evidence of plastic flow, a second cycle is run.

#### 4.5 Sample Preparation

##### 4.5a Pulse Experiment

Rock samples are cored using a diamond core drill with sufficient water flushing to prevent damages to the sample. The rocks are then cylindrically ground to a diameter of  $1.250 \pm 0.001$  inches. Following this the sample faces are ground flat and parallel to within  $\pm 0.001$  inches. Care is taken during the grinding procedures to keep the samples cooled so that thermal cracking near the surface is minimized.

All samples are dried out at 80°C in a vacuum system with 10 microns of pressure ( $10^{-2}$  torr). For experiments requiring a dry rock, the sample is removed from the vacuum oven and immediately jacketed. It is unavoidable, however, that some moisture from the air will be adsorbed by the rock. To saturate a rock, the sample is again placed in the vacuum along with a tub of the saturating fluid. Both are held at the maximum obtainable vacuum determined by the boiling point of the fluid. The sample is then dunked into the tub and the vacuum then released. This procedure insures full saturation for most porous and relatively permeable rocks. For rocks that are difficult to saturate, the sample, still immersed, is placed in a small pressure vessel and about 10 bars pressure of Argon is applied.

#### 4.5b Resonance Experiment

Samples used for the resonance experiments are treated slightly differently than for the pulse method. For soft rocks, such as sandstone, cores are taken with a 1/4 inch (0.635 cm) i.d. drill. Since the samples are about 5 to 6 inches long (13-15 cm) and very thin, it is not possible to cylindrically grind them without breaking. Thus, only the ends are faced off with the grinder. For hard rocks, however, cores are made using a 5/16 inch (0.794 cm) i.d. drill and the samples are

able to be ground down to a 1/4 inch (0.635 cm) diameter and the ends faced off parallel. If done carefully, little surface damage results. As with the pulse experiment, each sample is dried out in the vacuum oven.

Many of the resonance experiments require the heating of the samples to thermally crack them. In order to compare the results with data obtained using differential strain analysis (Simmons et al., 1974; Richter and Simmons, 1974; and Cooper and Simmons, 1977) a heating rate of no more than 1-2°C/min is required. The technique used is very similar to that described by Richter and Simmons. A diagram of the furnace system is shown in Figure 4-14. The rate at which the motor drives the controller determines the heating rate. Furnace temperature is monitored by a thermocouple and strip chart recorder. For all the runs, temperature is increased to the desired level and held constant for at least one hour. The temperature is then lowered at the same rate as before.

Of some concern is the variation of temperature within the furnace as a function of distance from the center. Both ends of the furnace are packed with fire brick in order to minimize temperature differences. An experimental determination of temperature changes showed that there was no more than 5% variation across

*the length of the furnace.*

the length of a sample in the furnace.

#### 4.6 Description of Samples

The rock samples used for this study were chosen for two distinct reasons. First, several porous upper-crustal rocks, two sandstones and a limestone, were chosen because one would expect low Q's and thus these are amenable to the pulse technique. Furthermore, these rock types are commonly encountered in exploration and might be considered good reservoir rocks. Two tuffs were chosen due to their high porosity but, as will be shown later, low crack porosity compared to the sandstones. A Colorado oil shale and a New York calcareous shale complete the samples used in the ultrasonic experiments. Secondly, three additional rocks were chosen for use in the resonance experiment. Two of these, the Solenhofen limestone and Maryland diabase, are particularly well suited for thermal cracking experiments since they have zero crack porosity initially. Westerly granite was also chosen for this type of experiment.

In general, all of the samples chosen are quite commonly used in the laboratory and thus much subsidiary information on their properties may be obtained. In fact, several of the rocks: Berea sandstone, Bedford limestone, and Westerly granite, are accepted "standard" rocks by the



U.S. Bureau of Mines (Krech et al., 1974). In this section, each rock will be discussed in terms of its petrographic description, physical properties such as density, porosity, permeability and grain size. Porosity and densities are determined by first weighing the sample dry and then saturated and immersed in  $\text{CCl}_4$ .

Further information on the mechanical properties of most of the samples were obtained from static linear strain versus pressure curves. According to the theory proposed by Walsh (1965), these may be interpreted in terms of crack porosity. It is assumed that the total change in porosity when all the cracks have closed is equal to the initial crack porosity,  $\phi_c$ . Very simply,  $\phi_c$  is the intercept on the volumetric strain axis of the straight line section of the stress-strain curve extrapolated to zero pressure. In this analysis, volumetric strain is three times linear strain. Furthermore, the maximum crack aspect ratio,  $\alpha$ , may be estimated from the pressure required to completely close the cracks,  $P_c$ . From Walsh theory

$$P_c = \pi E \alpha / 4 (1 - \sigma^2)$$

or to order of magnitude:

$$P_c = E \alpha$$

where  $E$  is the matrix Young's modulus and  $\sigma$  is the Poisson's ratio. This aspect ratio, in and of itself, is little use however. Of more direct interest is the closure pressure,  $P_c$ . One may consider a rock with a high closure pressure to contain, on the average, higher aspect ratio cracks than one with a low closure pressure.

#### 1. Berea Sandstone

The Berea sandstone is a relatively clean, flat bedded, light gray, medium to fine-grained protoquartzite with a silica and clay cement. The Berea is Mississippian in age, deposited in deeply cut channels in northern Ohio (Krech et al., 1974). Classified as a feldspathic sandstone, the Berea contains about 75-78% quartz, with feldspar ranging from 2 to 16% (Timur, 1968; Krech et al., 1974). Carbonates make up 4-5% and clays about 5-10%. Physical parameters for the Berea and other samples are listed in Table 4.1. While the porosity may vary only 5%, there are wide variations in permeability up to 40%. Grain size and maximum pore diameter is about 0.1 mm. Grain contacts are point to concave-convex. Acoustically, the Berea is about 9% anisotropic with nearly orthohombic elastic symmetry (Krech et al., 1974). For all of the experiments, cores were taken perpendicular to the bedding plane. While cross-bedding in this sandstone is common, no evidence of such was seen in the samples.

Linear strain as a function of hydrostatic pressure is shown in Figure 4-15. This represents a classic example of the effect of cracks. As pressure increases, cracks close and the rock stiffens. After 1000 bars the small cracks are completely closed and the sample behaves as an elastic material with constant modulus. On the return cycle permanent hysteresis is noted - not all the cracks having closed elastically. There is no evidence of plastic flow or pore collapse.

Applying the Walsh analysis to the Berea data we obtain  $\phi_c = 0.465\%$  with a closure pressure of 1000 bars. This is somewhat lower than the 0.2% crack porosity estimated from seismic velocities as a function of pressure (Toksöz et al., 1976). The discrepancy is probably due to the fact that pressures for the velocity data did not exceed 1 Kb. Thus, aspect ratios on the order of  $10^{-3}$  are not as well determined as for smaller ratios.

## 2. Navajo Sandstone

The Navajo sandstone is included in the Glen Canyon group of the Colorado Plateau eolian sandstones. Lower Jurassic in age, the Navajo is found in beds up to 300 feet thick, exposed primarily along the Colorado River. Brownish red in color, it is composed of medium to fine grains and is well sorted. Dune bedding is found throughout the formation. Classified as an orthoquartzite, the Navajo

contains about 85% quartz and 2% feldspar. The grains are cemented primarily by silica with minor amounts of clay. Porosity and permeability vary greatly within the formation, ranging from 11 to 28% and 100 to over 1000 md respectively. The sample studied had a porosity of 16% and the permeability given in Table 4.1 is an estimate. The grains, subrounded, are about 0.15 mm in diameter with planar contacts.

Linear strain for the Navajo is shown in Figure 4-16. In general appearance, it is very similar to the Berea. Crack porosity determined by the zero pressure intercept is 0.411% with  $P_c = 1250$  bars. The hysteresis on the Navajo run is slightly smaller than the Berea. Intuitively then, given this fact plus the lower porosity, one would expect higher velocities and  $Q$  compared to the Berea. This is observed (Timur, 1968; Toksöz et al., 1978).

### 3. Bedford Limestone

The Bedford limestone is also known as Salem, Spergen and Indiana. The Bedford is a flat lying Mississippian age limestone. Primarily found in Indiana, it occurs as massive and lenticular attaining thicknesses of 50 to 60 feet. Layers of shale are associated with the limestone. Light tan in color, the Bedford is fossiliferous and may even be referred to as a Spergenite or Coquina. It is coarse grained, made of poorly sorted fossil debris. The fossil material (69%) may be recrystallized and is always well

cemented by crystalline calcite (31%). The pore spaces are vuggy and irregularly scattered (Timur, 1968; Krech, et al., 1974). The grains are about 0.75 mm in diameter. Porosity is about 12% and the permeability may vary as much as 18% (Krech, et al., 1974). The Bedford is nearly isotropic acoustically, with only a 3% velocity anisotropy with the low value elastic axis perpendicular to the bedding. Bedding planes, however, were nearly impossible to pick out visually on the lab samples.

Linear strain for the Bedford limestone is shown in Figure 4-17. Here a classic example of plastic flow and pore collapse is seen. In the first cycle, it is noticed that the crack porosity is extremely low, 0.09% with  $P_c = 350$  bars. The rock behaves elastically from 250 to 1000 bars where the onset of plastic behavior occurs. During the experiment, in the zone of plastic flow the pressure was increased in increments of 250 bars and kept at pressure until the material had completely deformed. For decreasing pressure, the rock behaves more or less elastically but a large increase in crack porosity due to pore collapse is noted. In the second cycle, the rock is stiffer for increasing pressure compared to the unloading curve of the first cycle due to the effect of friction. Crack porosity and closure pressure obtained from the second cycle are 0.4% and 1100 bars. Elastic behavior continues up to about 2250 bars where a slight

amount of plastic flow reoccurs.

#### 4. Ammonia Tanks Tuff

The Ammonia Tanks tuff is the upper member of the Timber Mountain Tuff series. It is part of a quartz bearing ash flow erupted 11 m.y. ago from the Timber Mountains caldera center in southern Nevada near the nuclear test site (NTS). The Ammonia Tanks formation attains a thickness of about 900 feet beneath the Timber Mountain dome (Byers et al., 1976).

Classified as a moderately welded quartz latite, the Ammonia Tanks is compositionally complex. Brown to red in color, its most outstanding feature is the presence of quartz phenocrysts that are commonly 3 mm long. These and other phenocrysts make up anywhere from 30-40% of the rock. Of the total, mafic phenocrysts represent 5-10% while felsic phenocrysts make up the bulk of the remainder. The felsic component is generally found with about 20% quartz, 40-50% alkali feldspar and 20% plagioclase.

The porosity of the samples used in this thesis was measured as 5.8% but can be quite variable within the formation. The grain (phenocryst) sizes average about 1-2 mm but can be as large as 5 mm. Grain contacts are point to floating. The large grain size implies that scattering dominates the acoustic properties of the rock. As will be seen later, this is indeed true.

Linear strain for the Ammonia tanks is shown in Figures 4-18 (Morrow et al., 1977) and 4-19. An interesting comparison between this tuff and the sandstones can be made in terms of crack populations. For low stresses (<60 bars) the tuff behaves elastically with no hysteresis while the sandstones show evidence of crack closure. However, for high stresses, the maximum strain and crack porosity is obviously larger for the tuff. This implies that the tuff, while having a larger total crack porosity than the sandstones, contains cracks with a larger average aspect ratio. Apparently the Ammonia Tanks Tuff has no very fine cracks, a hypothesis that could be tested from attenuation measurements if scattering were unimportant. The volume strain analysis of Figure 4-19 gives  $\phi_c \approx 1.25\%$  with  $P_c = 1600$  bars.

##### 5. Tunnel Beds Tuff

The Tunnel Beds Tuff (for lack of a better name) is an ash fall tuff from NTS in Nevada. The particular sample studied was obtained near the side of Aqueduct Mesa Road near T tunnel in Area 12 and represents a typical example of the latest eruptions from the peralkaline Silent Canyon caldera (F.M. Byers, personal communication). Tunnel Beds is yellowish-gray, poorly sorted with fine to very coarse grains 2-4 mm in diameter. Pumice granules are common and zeolitization is nearly complete. While

the porosity is extremely variable, the value obtained for this sample was 29.6%.

An estimate of the mineral and rock constituents of the Tunnel Beds Tuff (F.M. Byers) gives a phenocryst content of 20% of which 5% (of total rock) is quartz, 14% feldspar and 1% biotite. 5% of the rock is peralkaline lithic fragments while the remaining 75% is groundmass including 40% clinoptilote, 10% clay, 15% opal and silica minerals and 10% glass.

Linear strain for the Tunnel Beds is shown in Figures 4-18 and 4-20. As with the Ammonia Tanks Tuff, low stresses produce little hysteresis in strain as compared to the sandstones. At higher pressures (Figure 4-20), however, this tuff behaves differently even compared to Ammonia Tanks. Pore collapse during the first loading cycle begins at about 500 bars and the total linear strain at 2850 bars is 2.7%. Permanent hysteresis for the first cycle is 0.8% linear strain. The second loading cycle shows that a large population of fairly high aspect ratio cracks has been produced by the initial pore collapse. Crack porosity and closure pressure for the first loading cycle are about 0.3% and 300 bars respectively but these values are unreliable due to the onset of pore collapse. For the second cycle,  $\phi_c \approx 0.9\%$  and  $P_c \approx 1000$  bars.



## 6. Colorado Oil Shale

The oil shale used in this thesis was obtained from the Anvil Points Mine located in the Naval Petroleum and Oil Shale Reserve about 5 miles northwest of Rifle, Colorado. While its exact origin is not well-determined, the sample is part of the Parachute Creek member of the Green River Formation of the Piceance Creek Basin and represents a typical, medium grade oil shale with about 20% kerogen by weight. The Green River Formation was deposited during the Eocene in what was then, Lake Uinta. The oil shale members were deposited in quiet waters far from shore (Donnell, 1964).

The Parachute Creek member, about 500 feet thick at the Anvil Points mine, consists of three oil bearing zones, the upper two being the richest and exposed at the mine.

The oil shale is an impure fine-grained carbonate rock containing varying amounts of organic matter, clay minerals, and small amounts of volcanic ash or tuff (Duncan and Denson, 1949). The particular sample studied is dark brown and resembles wood both in color and grain texture. As with most oil shales, there is little or no measureable porosity or permeability. The measured density is  $2.004 \text{ g/cm}^3$ . The sample is visually anisotropic and thus cores were taken both normal and parallel to the bedding planes.

Linear strain as a function of pressure for both orientations is shown in Figure 4-21. Oil shale has the peculiar property of behaving elastically similar to some polymers (B. Bonner, personal communication). As will be seen from the velocities, a typical Poisson's ratio is 0.4. The static measurements clearly show a 30% anisotropy in linear strain. Little or no crack porosity is evident and there is little permanent hysteresis.

## 7. Esopus Shale

The Esopus Shale is a dark gray, calcareous silty shale found in eastern New York State. Devonian in age, outcrops run from Port Jervis to Kingston and up to Albany County. The formation is fairly uniform with thicknesses ranging from 110-150 feet. The rock has a sandy texture and weathers easily. When dry, it is extremely friable and difficult to work with.

The sample used was collected at the Atlantic Cement Co. quarry in Ravena, New York. The following mineralogical analysis is based on a sample from a site about 5 miles from the quarry (New York Dept. of Commerce, 1951). The distinguishing feature of the Esopus shale is its large quantity of quartz, greater than 30%. It also contains more than 30% illite clay with 5-10% calcite and dolomite. Muscovite occurs with about 1-5%.

Esopus has a very low permeability and thus porosity is impossible to measure by the methods available. However, water content is about 14% of the dry weight and the bulk density is  $2.666 \text{ g/cm}^3$ . Linear strain curves were not obtained for this sample. Furthermore, a normal experimental run could not be accomplished since it requires over a week for pore pressure to completely equilibrate.

## 8. Westerly Granite

The Westerly Granite is an extremely well studied rock and despite its reputation as a 'standard' its properties are quite variable. Late Pennsylvanian or Permian in age, Westerly and associated pegmatites intrude folded Pennsylvanian sedimentary rocks along the southwestern shore of Narragansett Bay (Krech et al., 1974). Samples used for analysis are quarried in and near Westerly, Rhode Island.

Westerly granite varies from fine-grained rocks to small pegmatites with compositions ranging from granite to granodiorite. Light gray in color, the sample used in this study has a massive, fine-grained, equigranular texture. Classified as a granite, it contains 27.5% quartz, 35.4% microcline, 31.4% plagioclase ( $an_{17}$ ) and 4.9% mica (Brace, 1965). The porosity can vary between 0.3 and 1%. Grain diameters average about 0.175 mm. Despite its apparent homogeneity, the Westerly granite is acoustically about 10% anisotropic with orthorhombic symmetry (Krech et al., 1974; Birch, 1960). Cores used in this study were taken both parallel and normal to the presumed fast axis.

Linear strain for the two orientations of Westerly granite is shown in Figure 4-22. The deformation behavior

is very well-behaved and analysis of crack closing gives a crack porosity of 0.3% and a closure pressure of 1000 bars for the 'soft' direction and 0.12% and 500 bars for the 'stiff' direction. Hysteresis and permanent strain are both larger for the core cut in the slow direction. The intrinsic (high pressure) modulus is nearly equivalent for both cores.

#### 9. Solenhofen Limestone

The Solenhofen is an extremely fine-grained, buff colored, crystalline limestone. It is considered to be one of the finest lithographic limestones available, Jurassic in age, its original source is Solenhofen, Bavaria. The Solenhofen is homogeneous both in appearance and elastically (Birch, 1960) and is of fairly high purity. While the bulk of the rock is  $\text{CaCO}_3$  (calcite), it also contains 0.2%  $\text{Al}_2\text{O}_3$ , 0.3%  $\text{FeO}$ , 0.1%  $\text{K}_2\text{O}$  and  $\text{Na}_2\text{O}$  and varying small amounts of water (Robertson, 1955). It has an interlocking grain structure with a mean grain diameter of 0.005 to 0.008 mm.

Solenhofen is relatively porous for a lithographic limestone ( $\phi \approx 1-4\%$ ) but is essentially crack free in its virgin state. This is readily apparent in Figure 4-23 where linear strain as a function of pressure is virtually a straight line for pressures less than 2 Kb. At higher pressures, however, pores begin to collapse

plastically.

#### 10. Frederick Diabase

The Frederick Diabase is a fine-grained olivine basalt from a Triassic dike in Frederick, Maryland. Like the Solenhofen limestone, it is crack free and homogeneous in its virgin state. It is composed of about 48%  $an_{67}$  (plagioclase), 49% augite hypersthene and 1% mica. The average grain size is 0.175 mm and the porosity varies from 0.1 to 0.3% (Brace, 1965).

Linear strain is shown in Figure 4-23 together with Solenhofen. Again, complete linear elastic behavior with little or no evidence of crack porosity is seen. In fact, some consider the Frederick diabase in its virgin state to be close in mechanical behavior to metals.

Table 4.1 Sample Parameters

Rock Name	Total Porosity %	Crack Porosity %	Closure Pressure bars	Permeability md	Grain Diameter mm	$\rho$ Bulk g/cm <sup>3</sup>	$\rho$ Grain g/cm <sup>3</sup>
Berea Sandstone	18.4	0.465	1000	75	0.10	2.137	2.620
Navajo Sandstone	16.4	0.411	1200	100	0.15	2.189	2.619
Bedford Limestone	11.9	0.090	350	1 <sup>a</sup>	0.75	2.335	2.652
Ammonia Tanks Tuff	5.8	1.25	1500	-	1-2	2.314	2.457
Tunnel Beds Tuff	29.6	0.30	300	-	2-5	1.607	2.283
Colorado Oil Shale	--	--	--	-	-	2.004	--
Esopus Shale	--	--	--	-	-	2.666	--
Westerly Granite	0.3-1 <sup>b</sup>	0.30 0.12	1000 500	10 <sup>-3</sup> c	0.750	2.62	2.646
Solenhofen Limestone (Peselnick, 1962)	4	0	--	-	0.008	2.55	2.66
Frederick Diabase (Brace, 1965)	0.2	0	--	-	0.175	3.020	3.026

<sup>a</sup> Krech et al. (1974)

<sup>b</sup> Brace (1965)

<sup>c</sup> Frangos (1967)

## FIGURE CAPTIONS

- Figure 4-1. Block diagram of the ultrasonic measurement system, including both signal and timing circuits.
- Figure 4-2. Photograph of the ultrasonic measurement system electronics. The coaxial cable from the pulse generator leads to the pressure vessel.
- Figure 4-3. P and S waveforms superimposed with the timing pulses. The rise time of the timing pulse is variable to match the rise of the received signal.
- Figure 4-4. Diagram of the transducer holder - sample assembly mounted inside the pressure vessel. TR and RC are the transmitter and receiver transducer holders. SM is the sample and TC is the thermocouple. PC and PF refer to the confining and fluid pressures. Signal electrical leads are labelled P and S.
- Figure 4-5. Photograph of the transducer holder-sample assembly.
- Figure 4-6. Cutaway view of the transmitter holder showing the P and S wave transducers and electrical leads, the backing spring, and the pore pressure tubing.



Figure 4-7. S wave transducer assembly and wiring diagrams for the stacked P-S transducer arrangement. Switches are shown for the generation and reception of S waves.

Figure 4-8. Reproducibility of waveforms and Q values for the Navajo sandstone. See the text for explanations.

Figure 4-9. Block diagram of the resonance measurement system.

Figure 4-10. Photograph of the resonance system including the sample and support. Not shown are the oscilloscope, preamplifier, frequency counter, or X-Y plotter.

Figure 4-11. Resonance peak for the fundamental longitudinal mode in Solenhofen limestone.

Figure 4-12. Block diagram of the static stress-strain measurement system.

Figure 4-13. Photograph of the static measurement system.

Figure 4-14. Block diagram of the heat treating furnace system. The voltage of the power supply is set so that the motor drives the controller at a rate to produce the desired heating rate.

Figure 4-15. Linear strain as a function of hydrostatic confining pressure for the Berea sandstone. In this and later figures, the loading and unloading paths are shown and denoted by the arrows.

- Figure 4-16. Linear strain as a function of confining pressure for the Navajo sandstone.
- Figure 4-17. Linear strain as a function of confining pressure for the Bedford limestone for two successive pressure cycles.
- Figure 4-18. Linear strain as a function of unconfined uniaxial stress for the Tunnel Beds (TB) and Ammonia Tanks (AT) tuffs and the Berea sandstone (from Morrow et al., 1977).
- Figure 4-19. Linear strain as a function of confining pressure for the Ammonia Tanks tuff.
- Figure 4-20. Linear strain as a function of confining pressure for the Tunnel Beds tuff for two successive pressure cycles.
- Figure 4-21. Linear strain as a function of confining pressure in the Colorado oil shale in the directions perpendicular and parallel to the bedding.
- Figure 4-22. Linear strain as a function of confining pressure for the Westerly granite for two mutually perpendicular directions. The curve labelled L is presumably the slow or soft direction based on the measured acoustic velocity.
- Figure 4-23. Linear strain as a function of confining pressure for both the Solenhofen limestone and Frederick diabase.

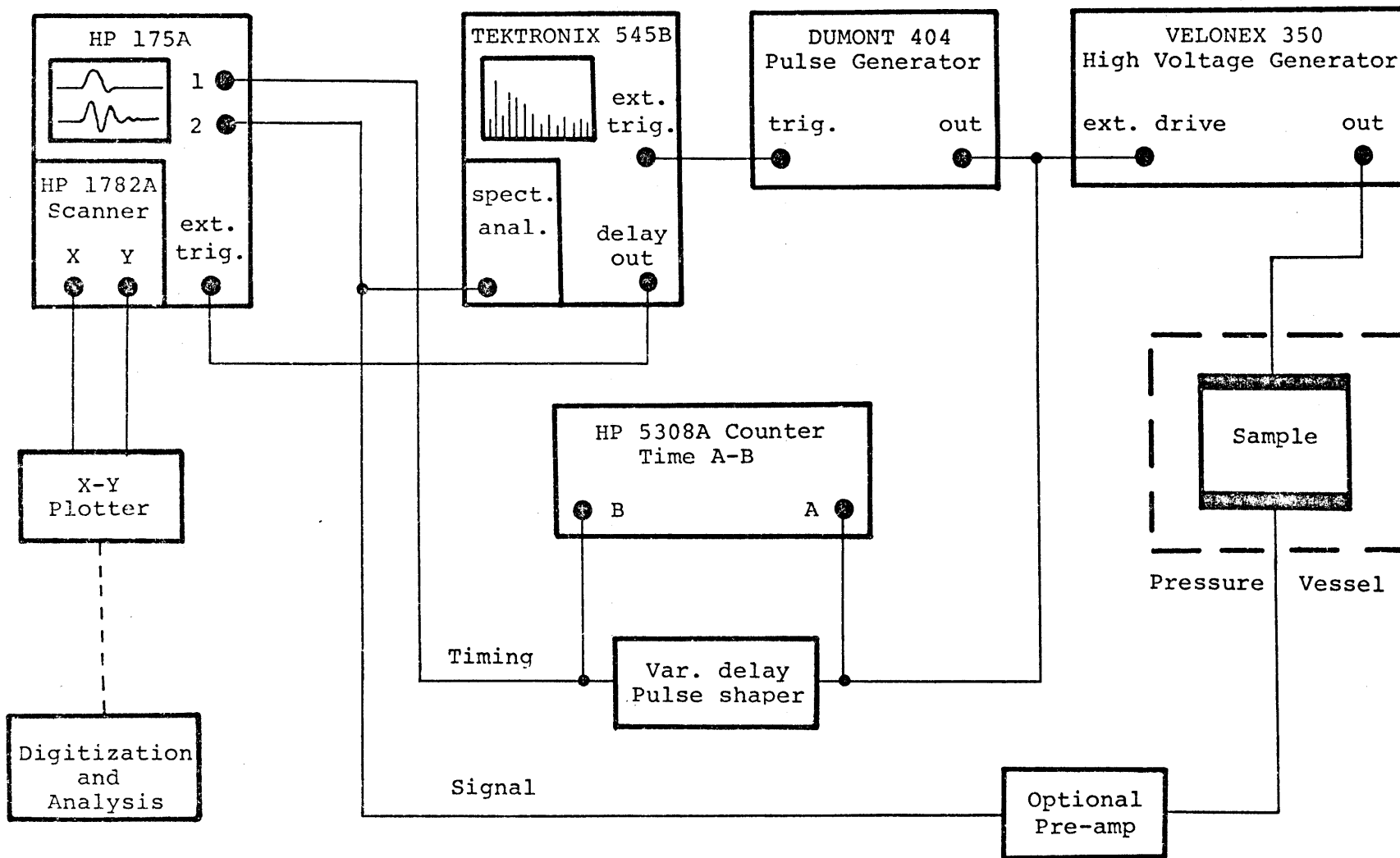


Figure 4-1

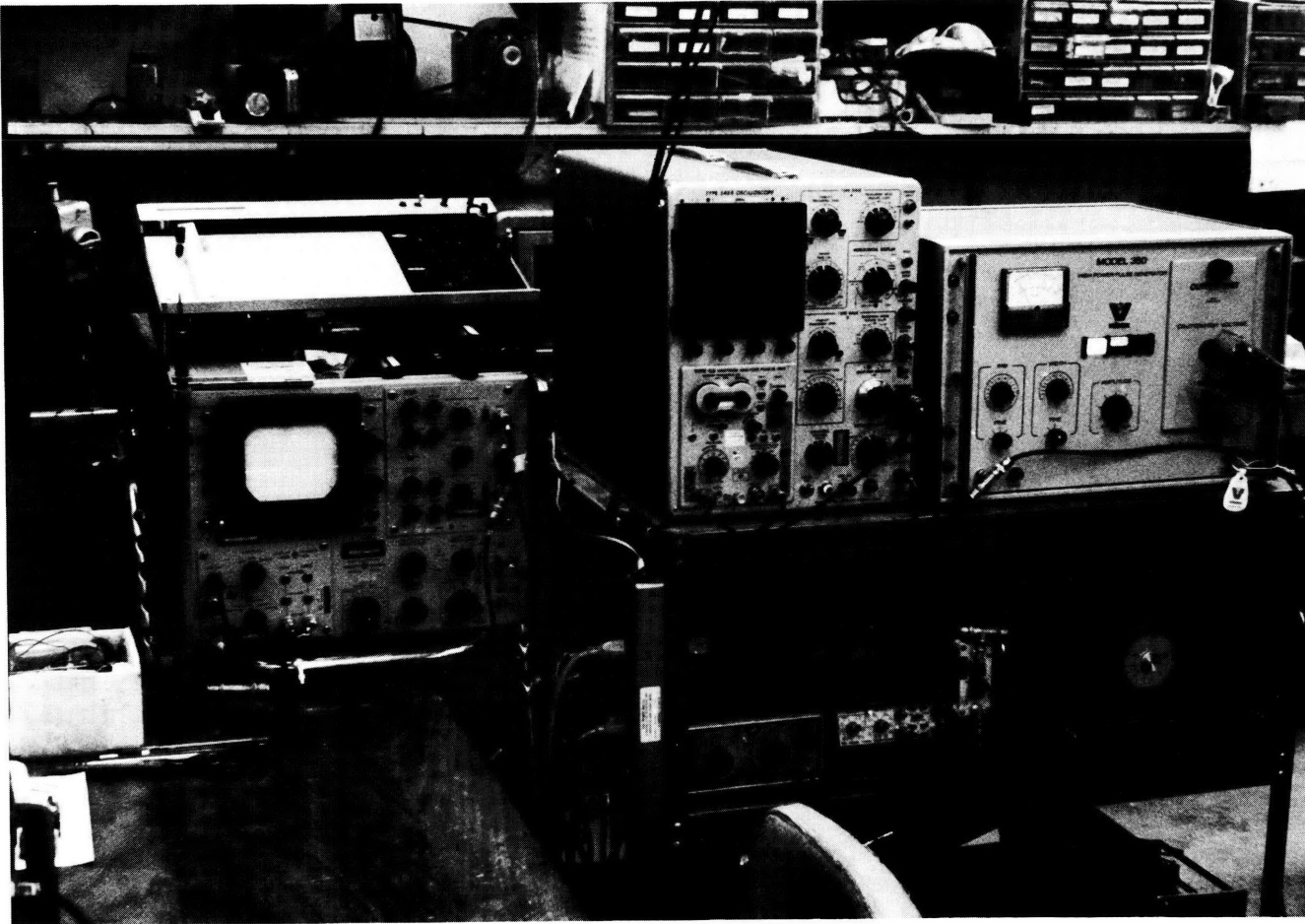
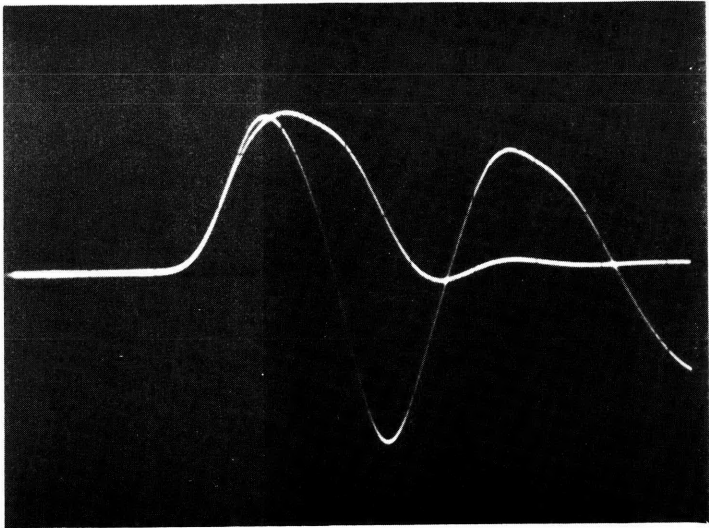
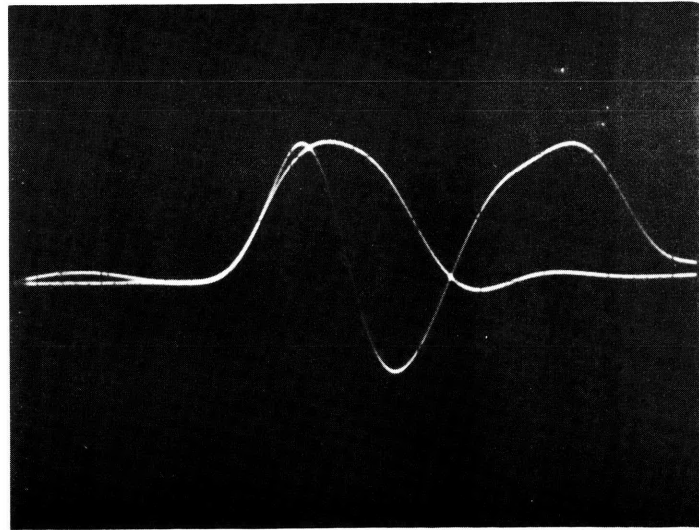


Figure 4-2



P WAVE



S WAVE

Figure 4-3

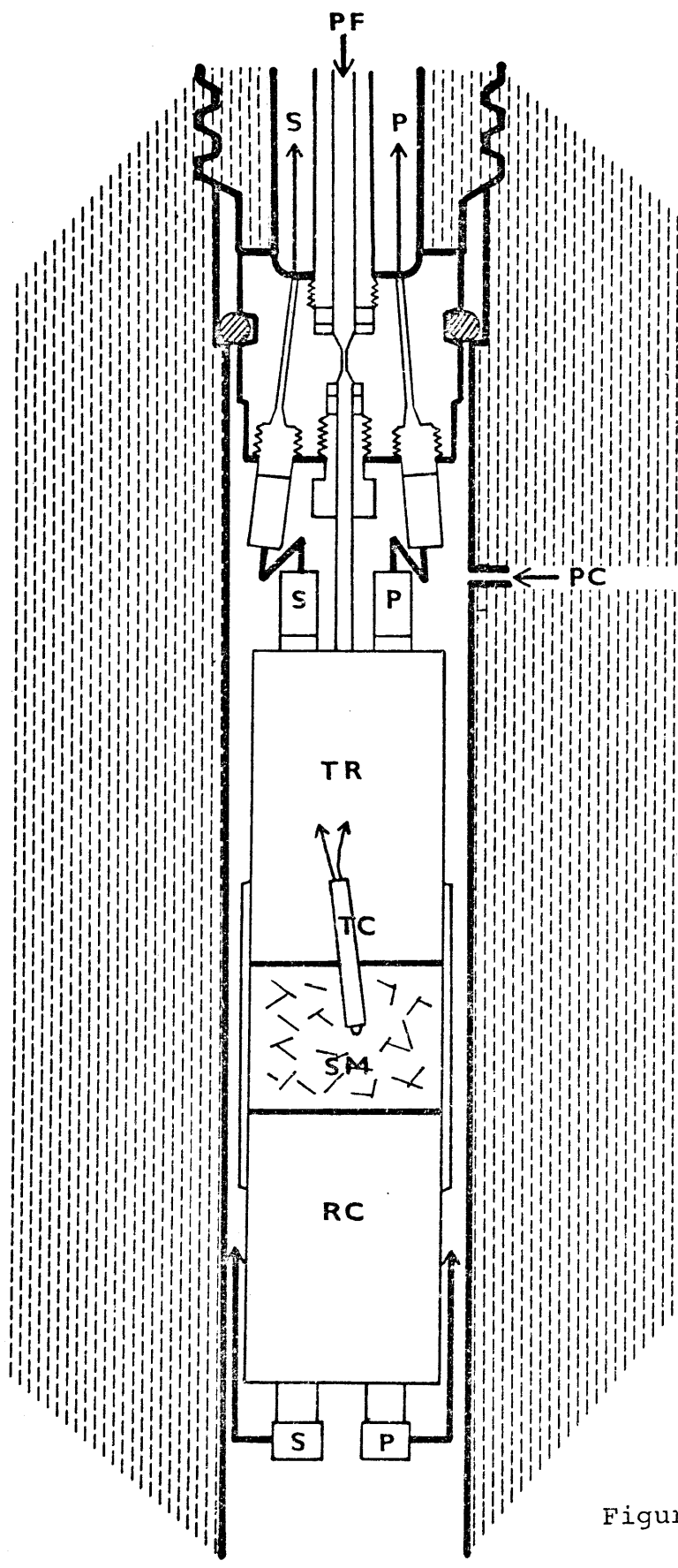


Figure 4-4



Figure 4-5

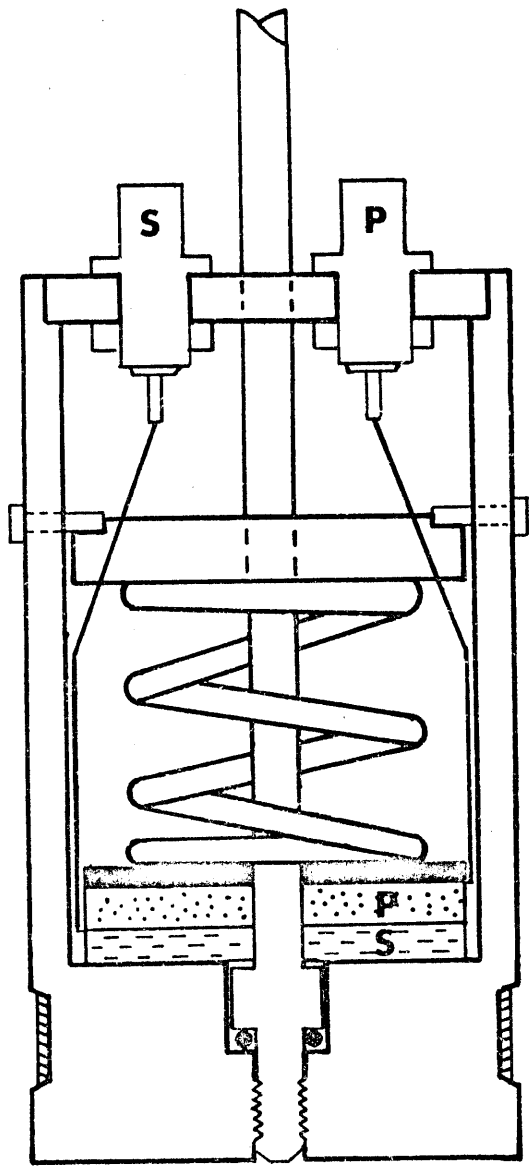


Figure 4-6



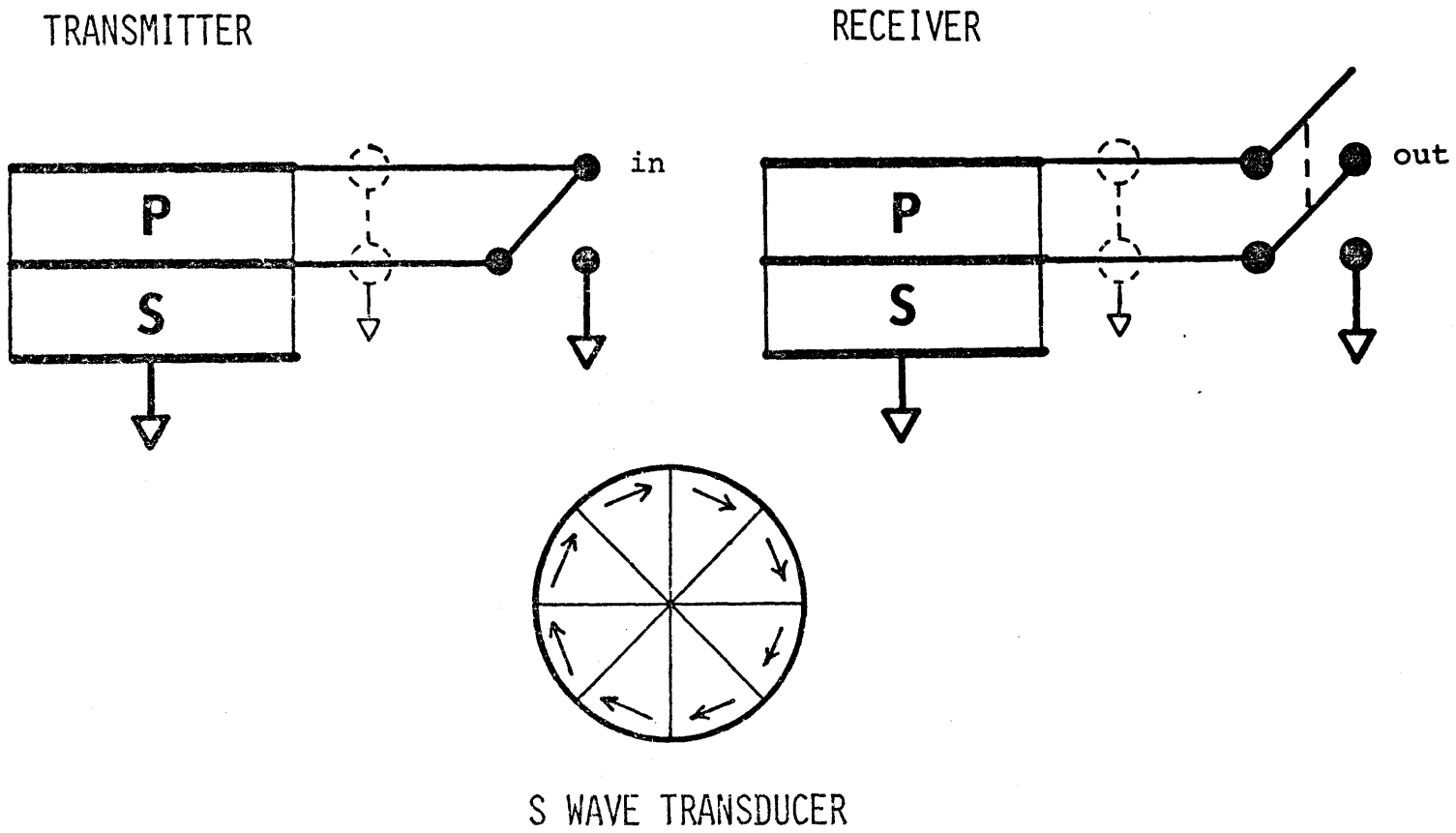


Figure 4-7

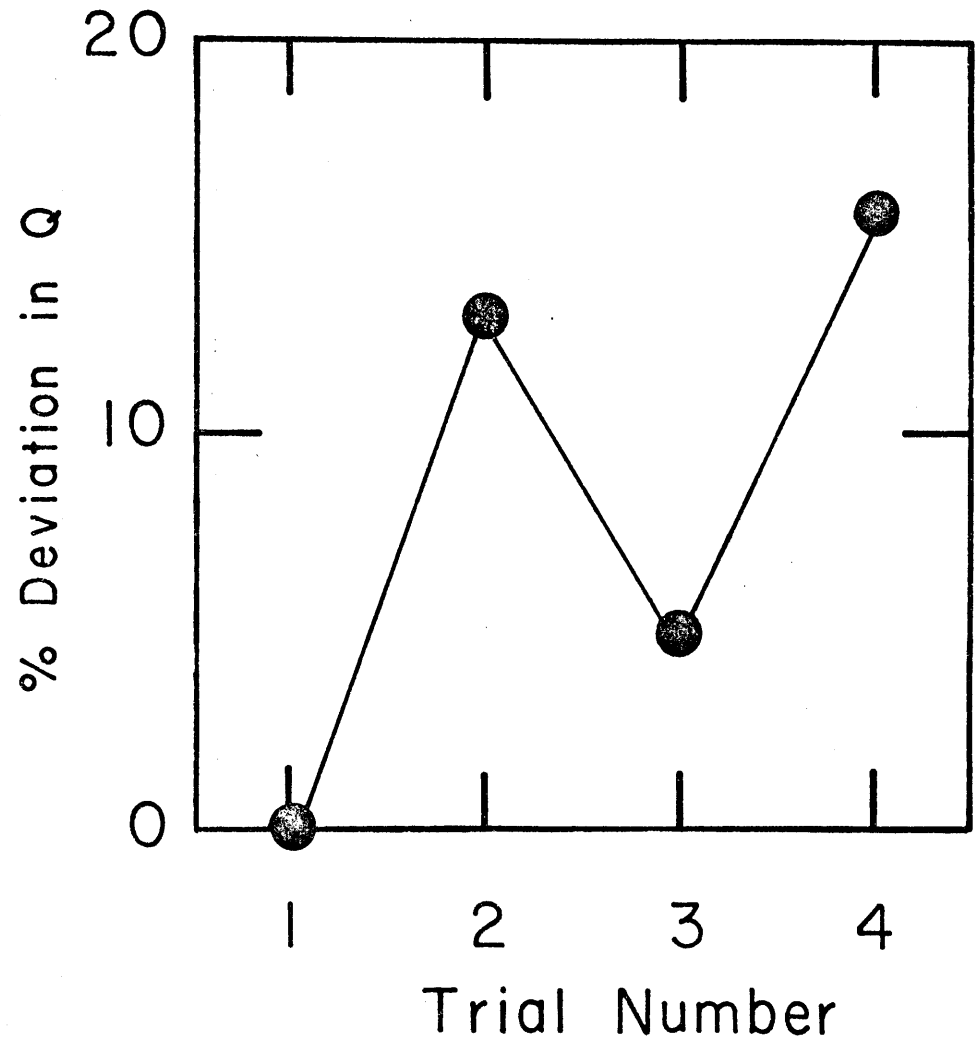
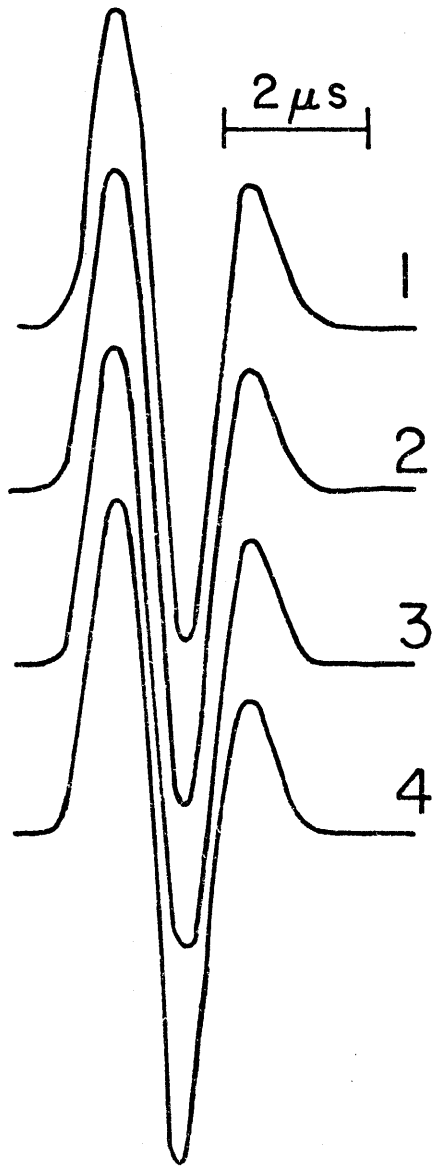


Figure 4-8

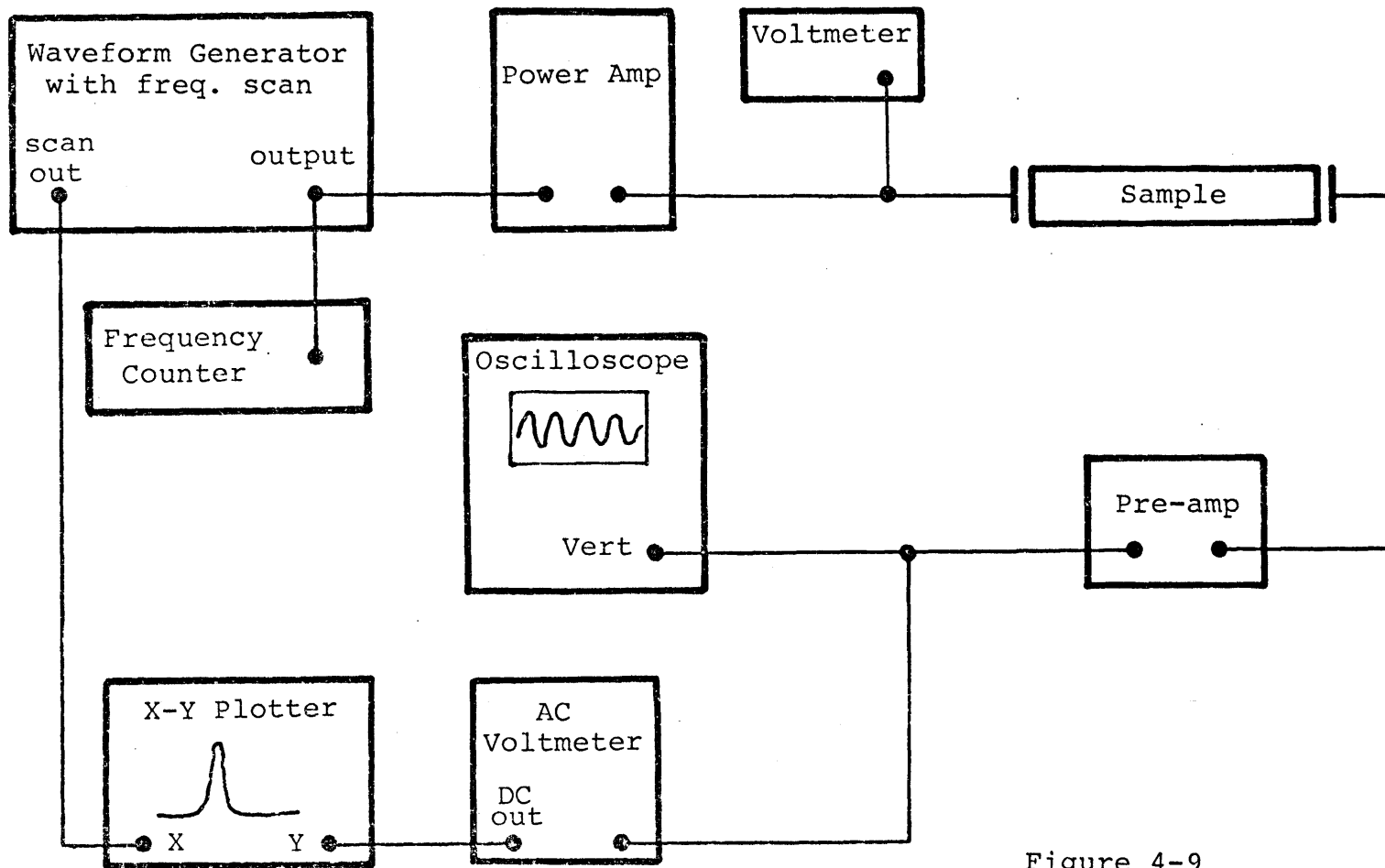


Figure 4-9

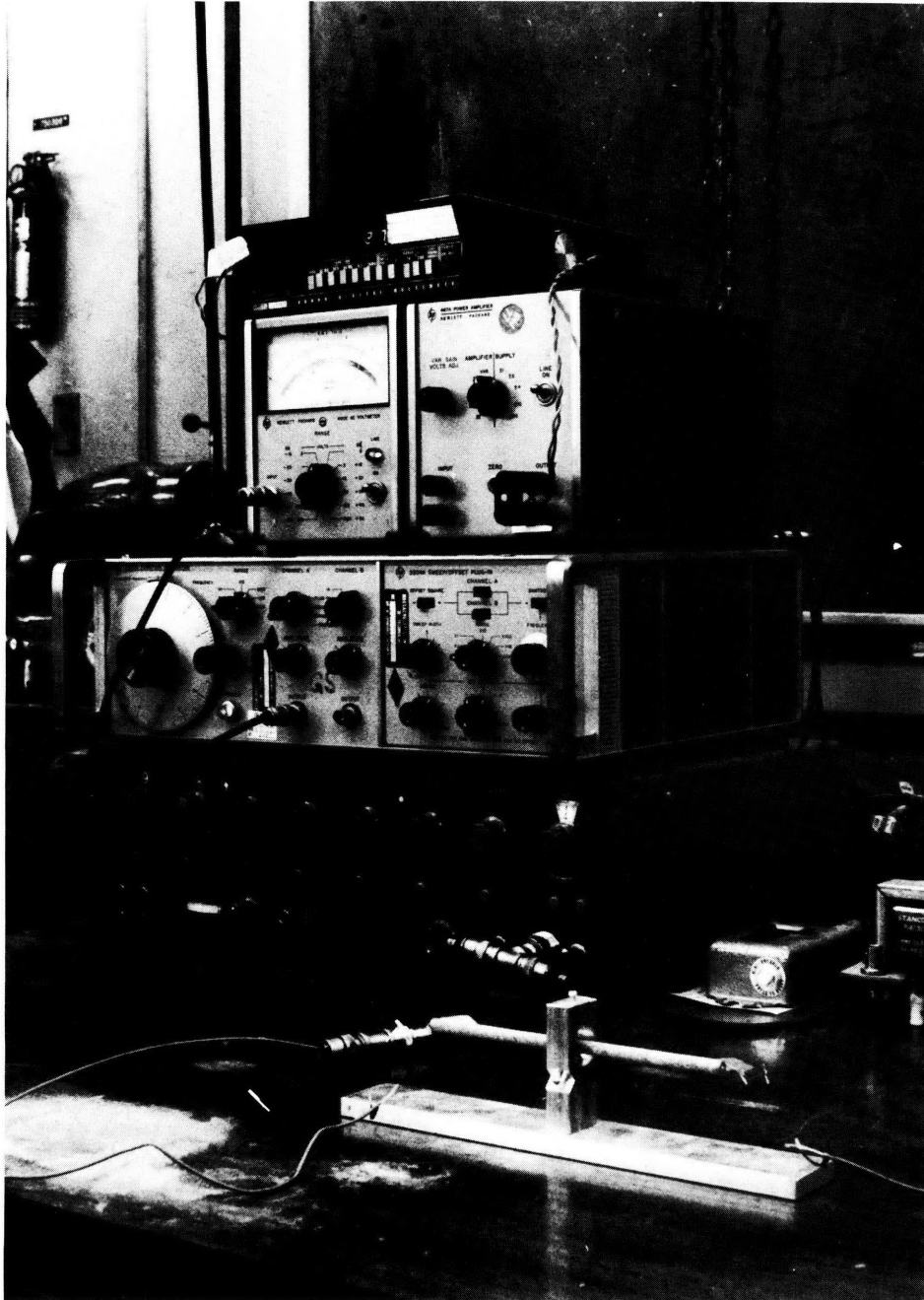


Figure 4-10

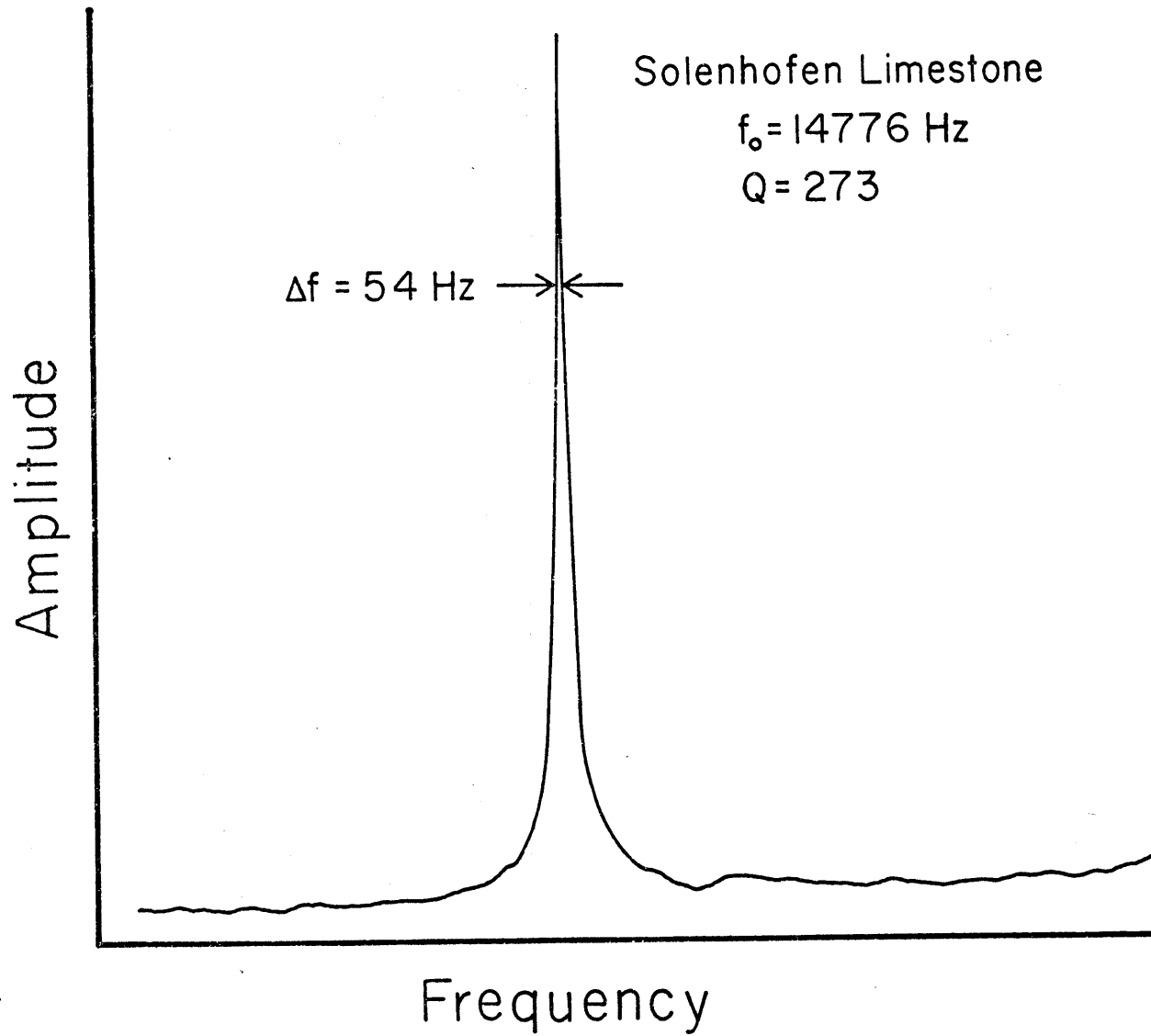


Figure 4-11

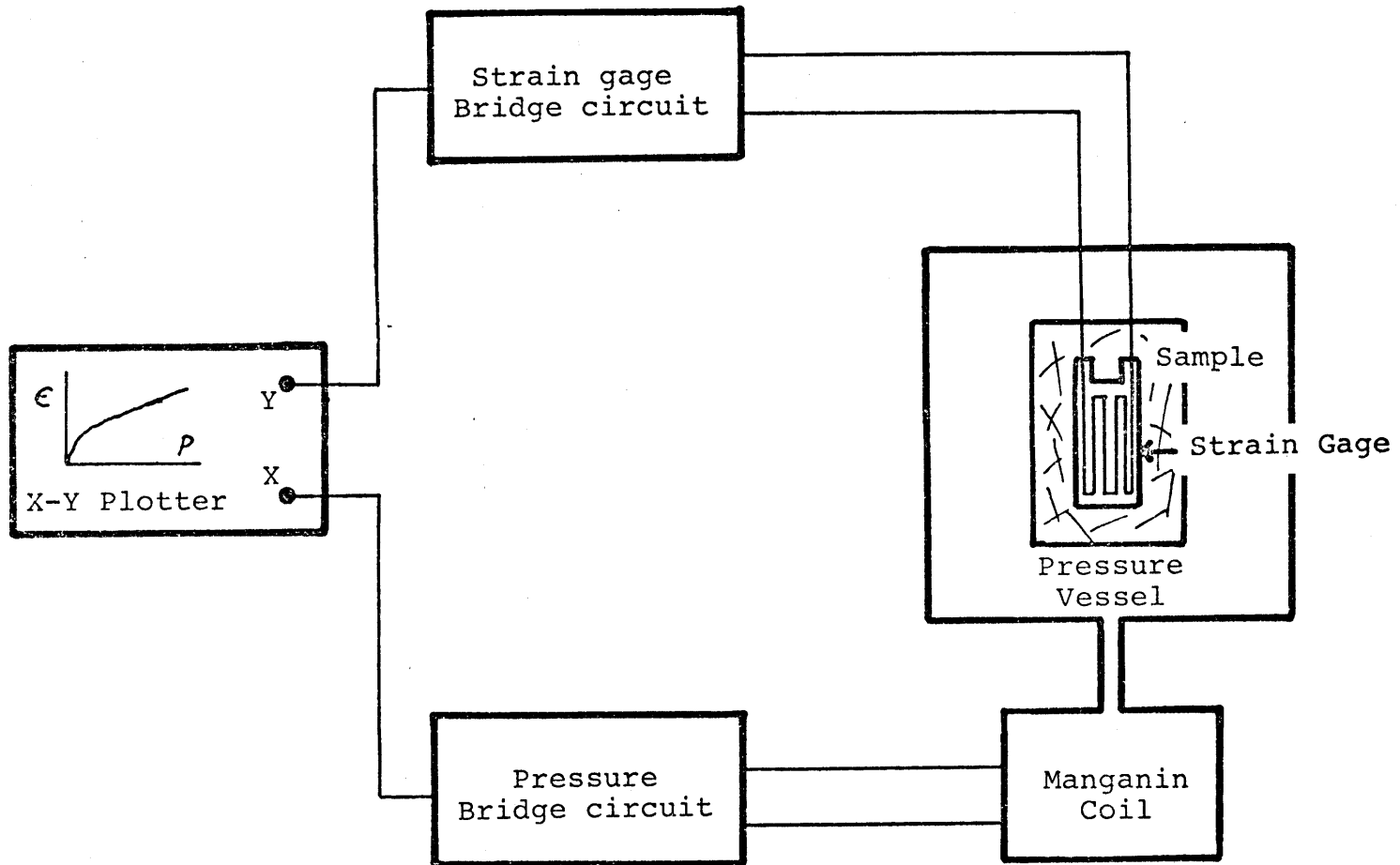


Figure 4-12

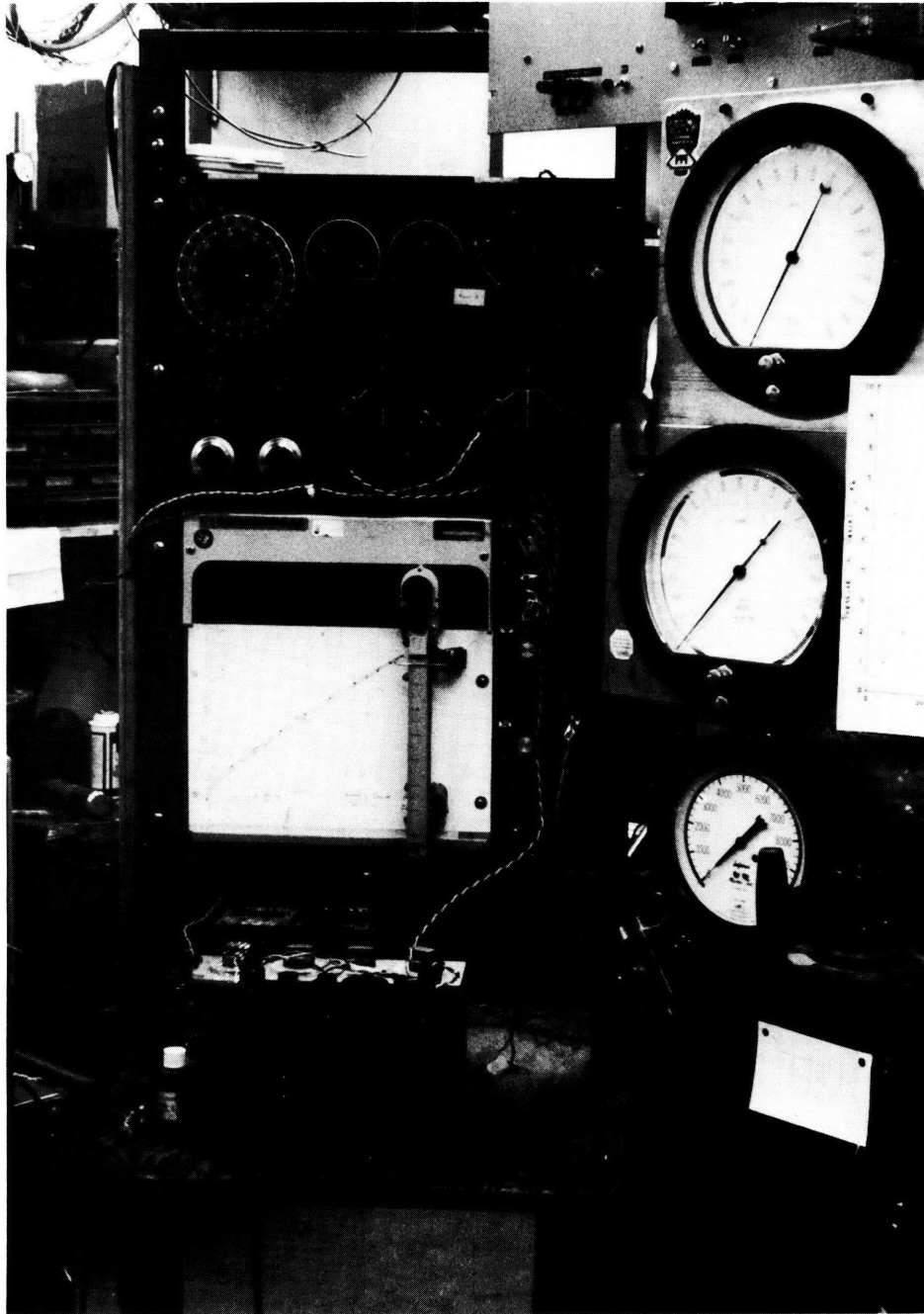


Figure 4-13

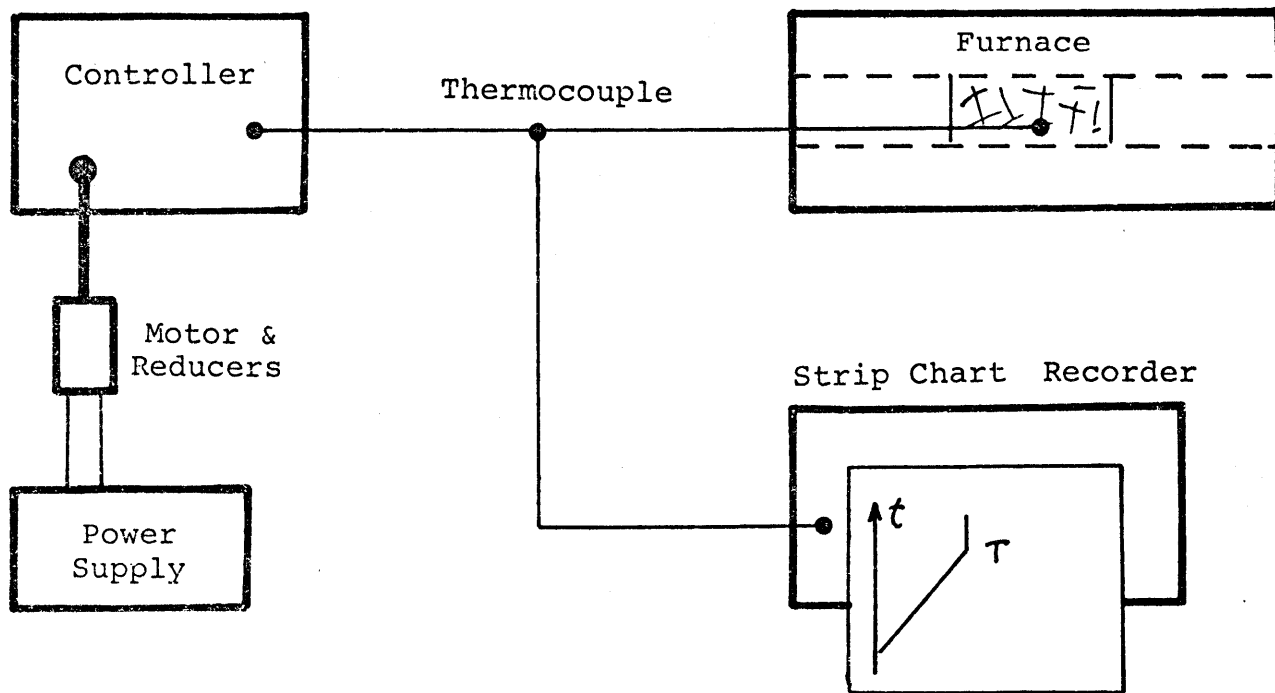


Figure 4-14



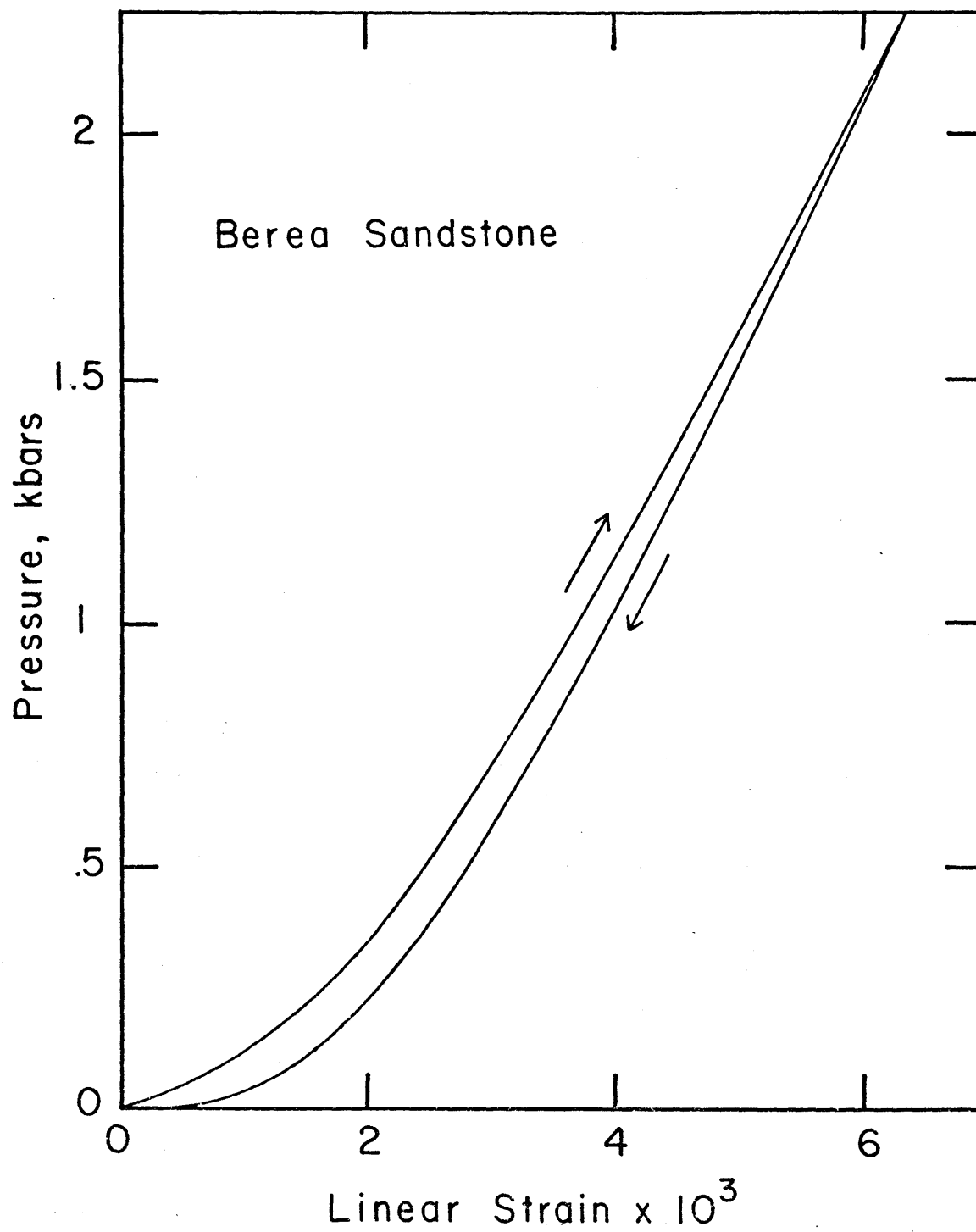


Figure 4-15

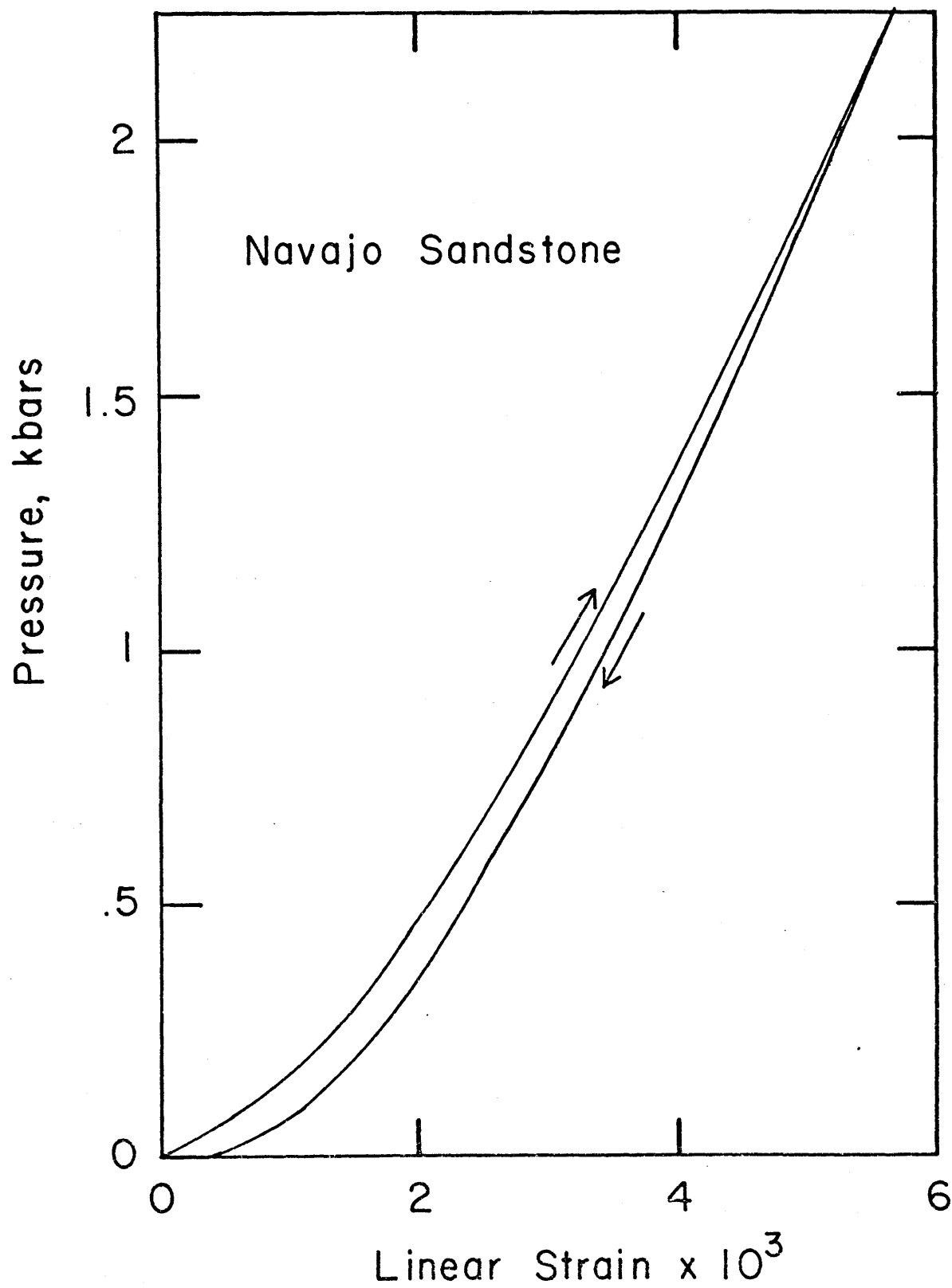


Figure 4-16

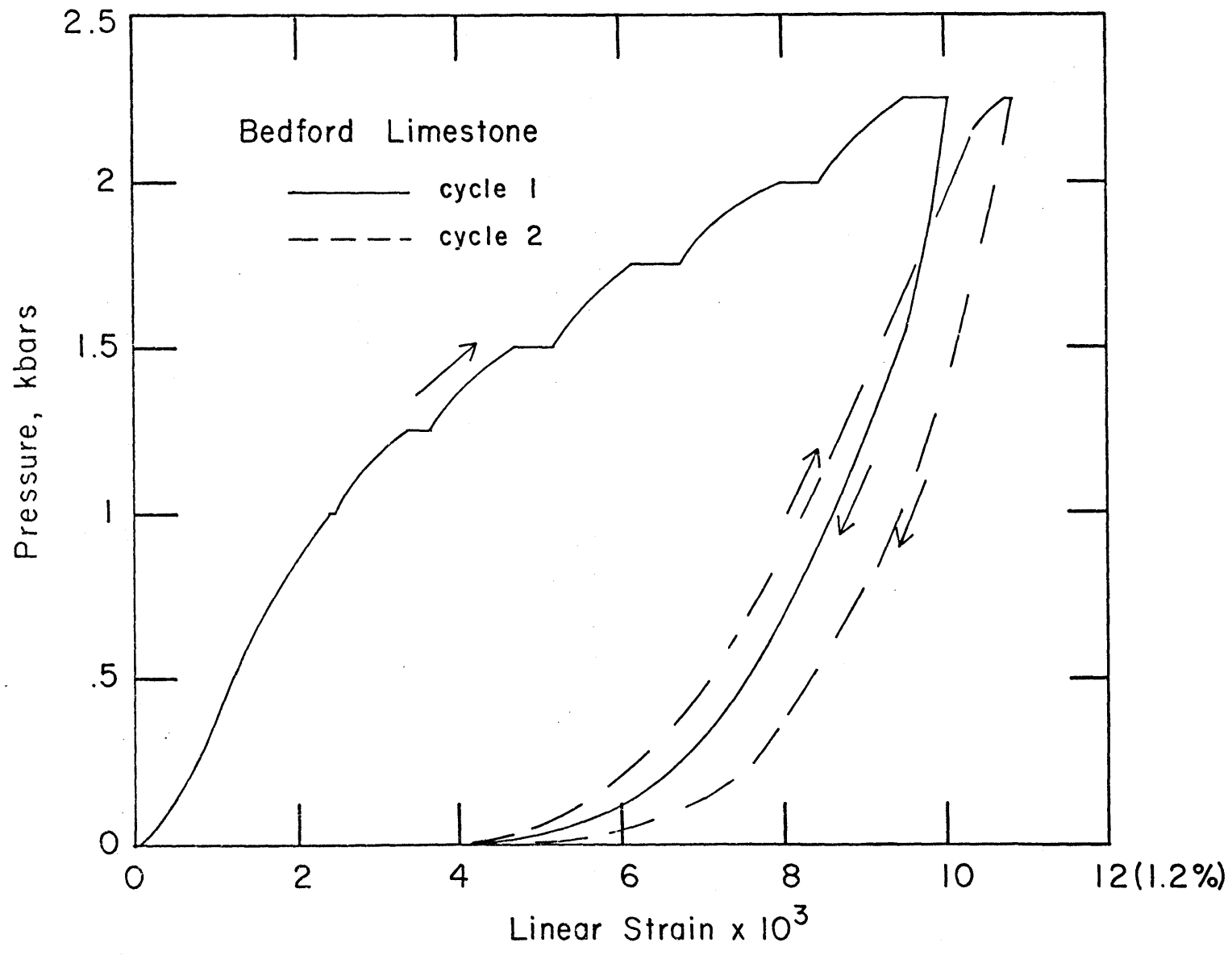


Figure 4-17

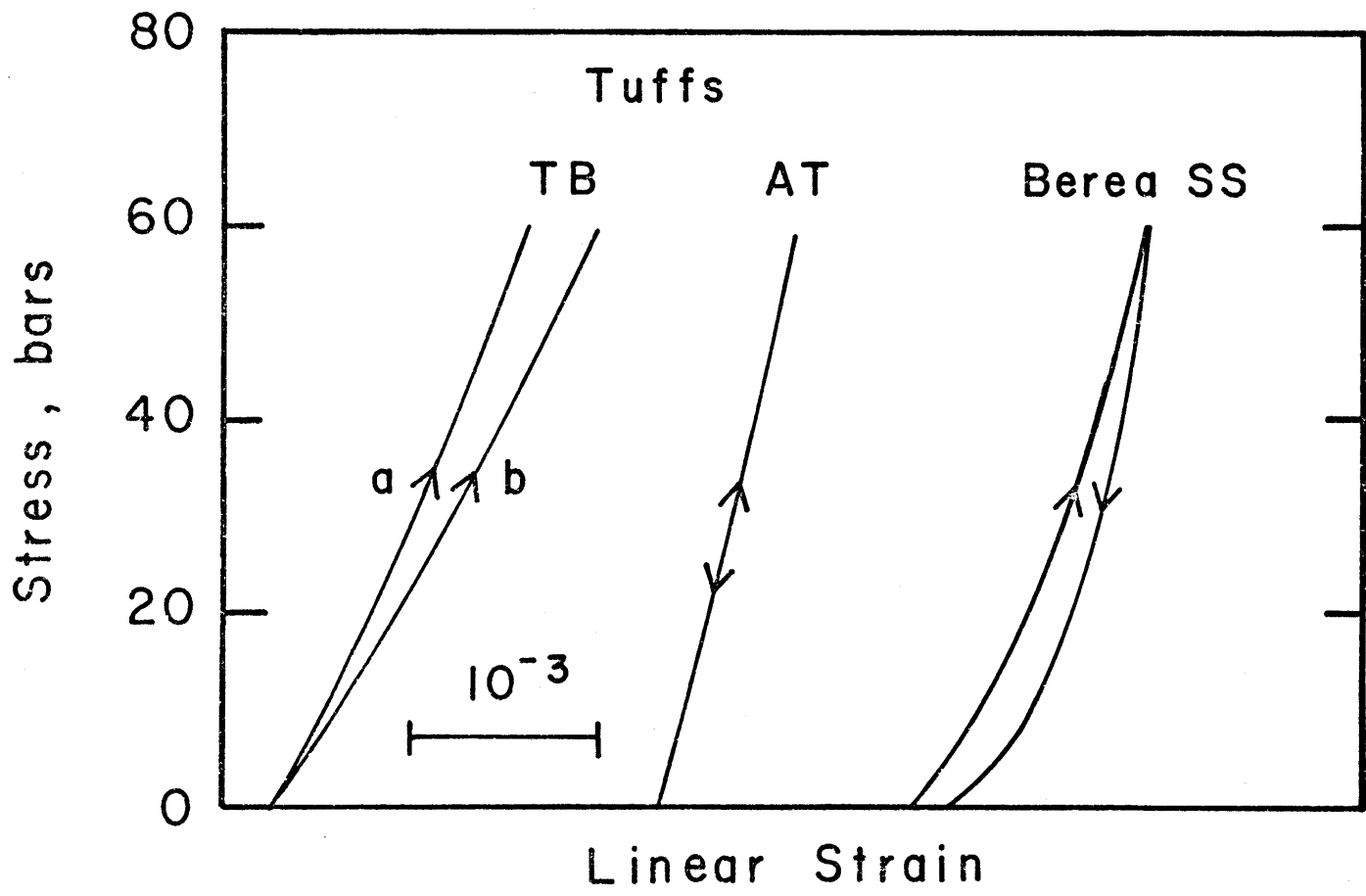


Figure 4-18

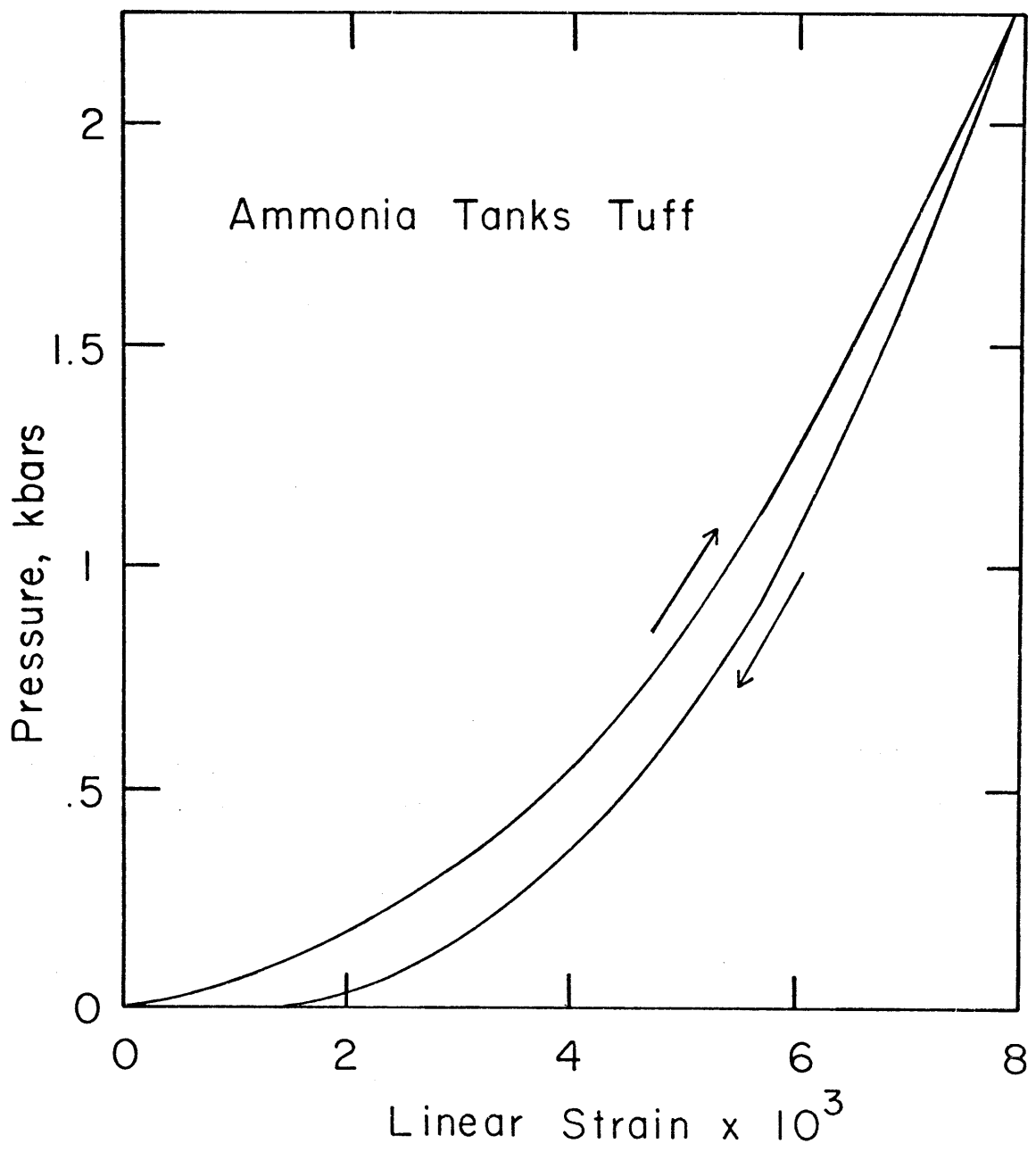


Figure 4-19

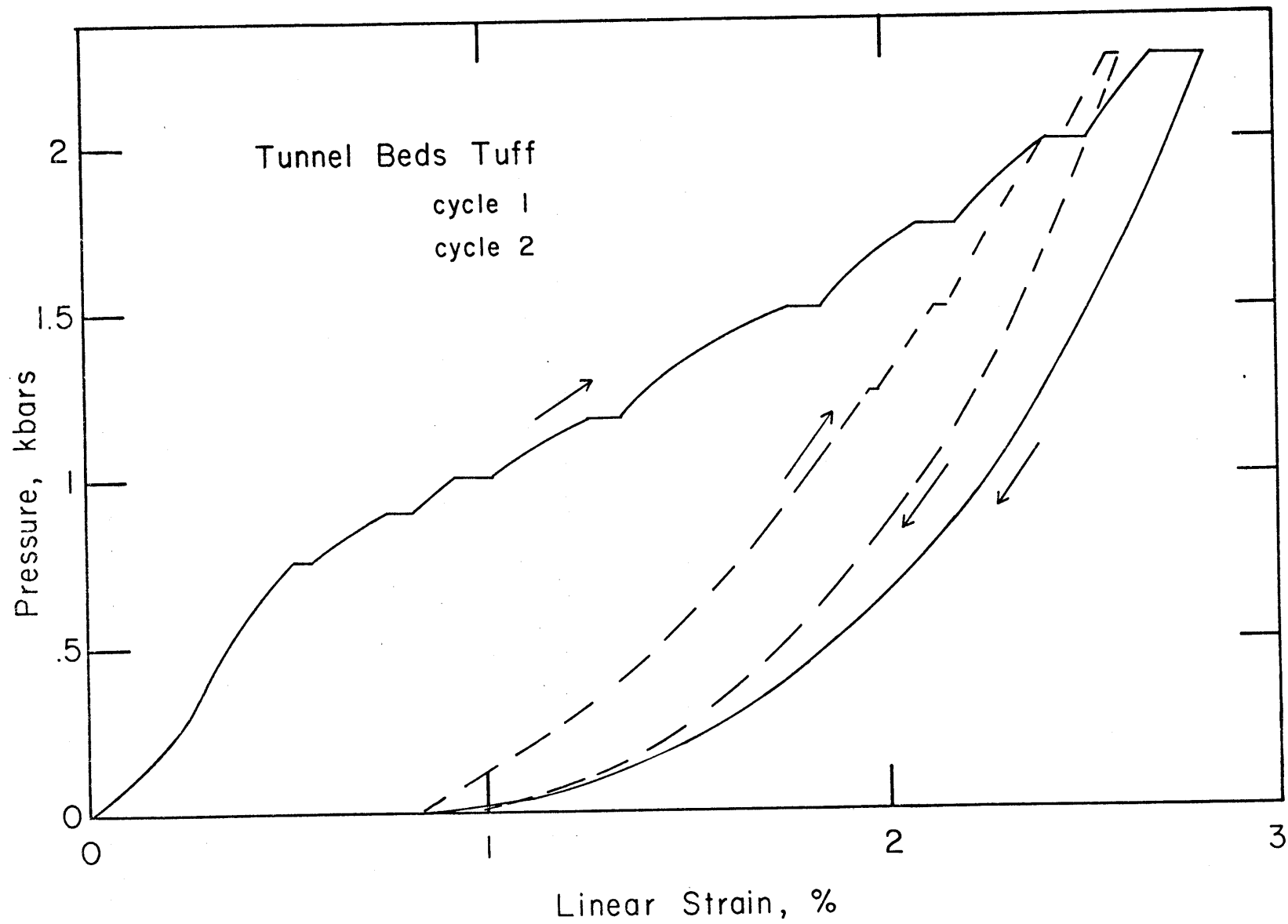


Figure 4-20

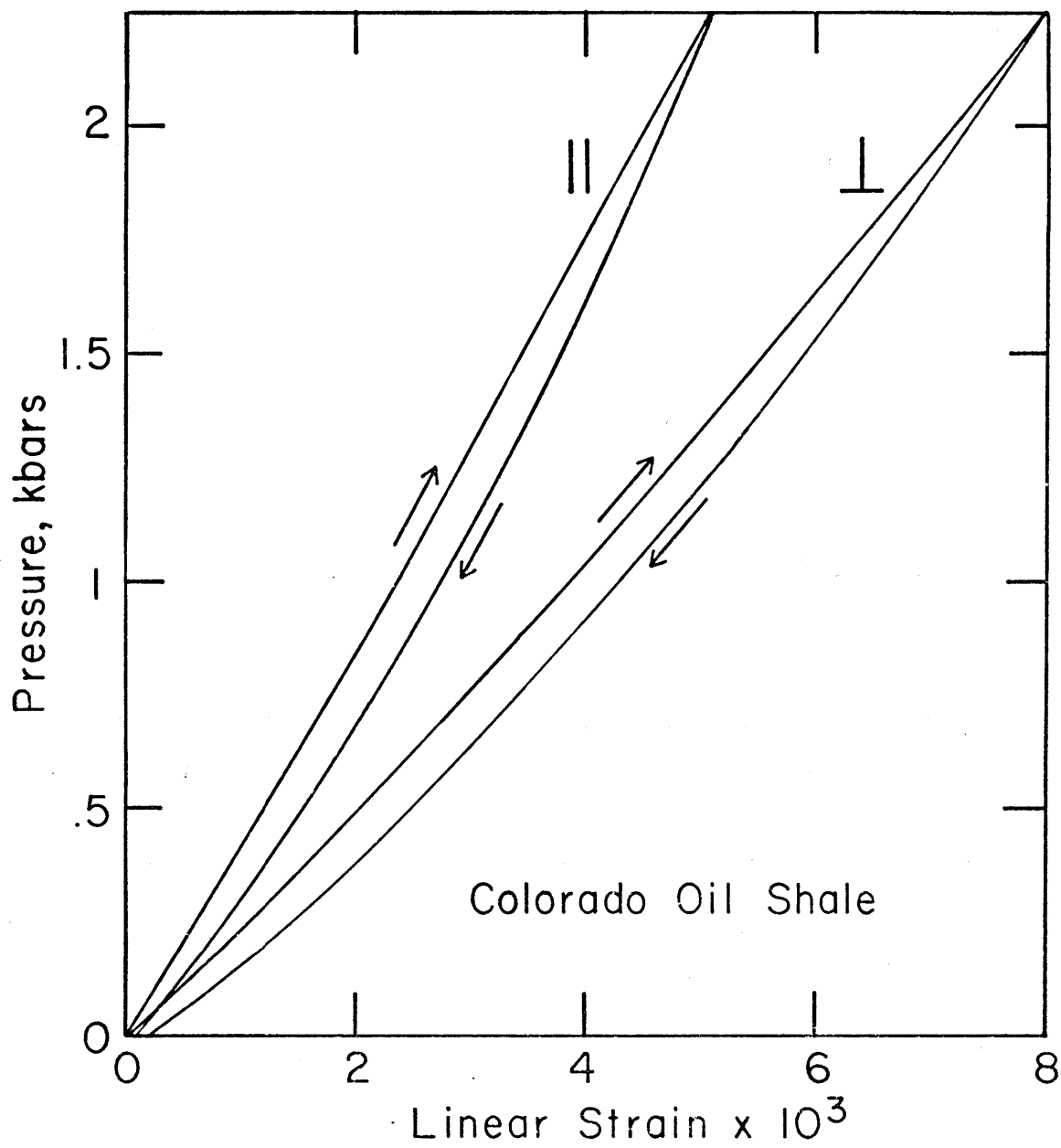


Figure 4-21

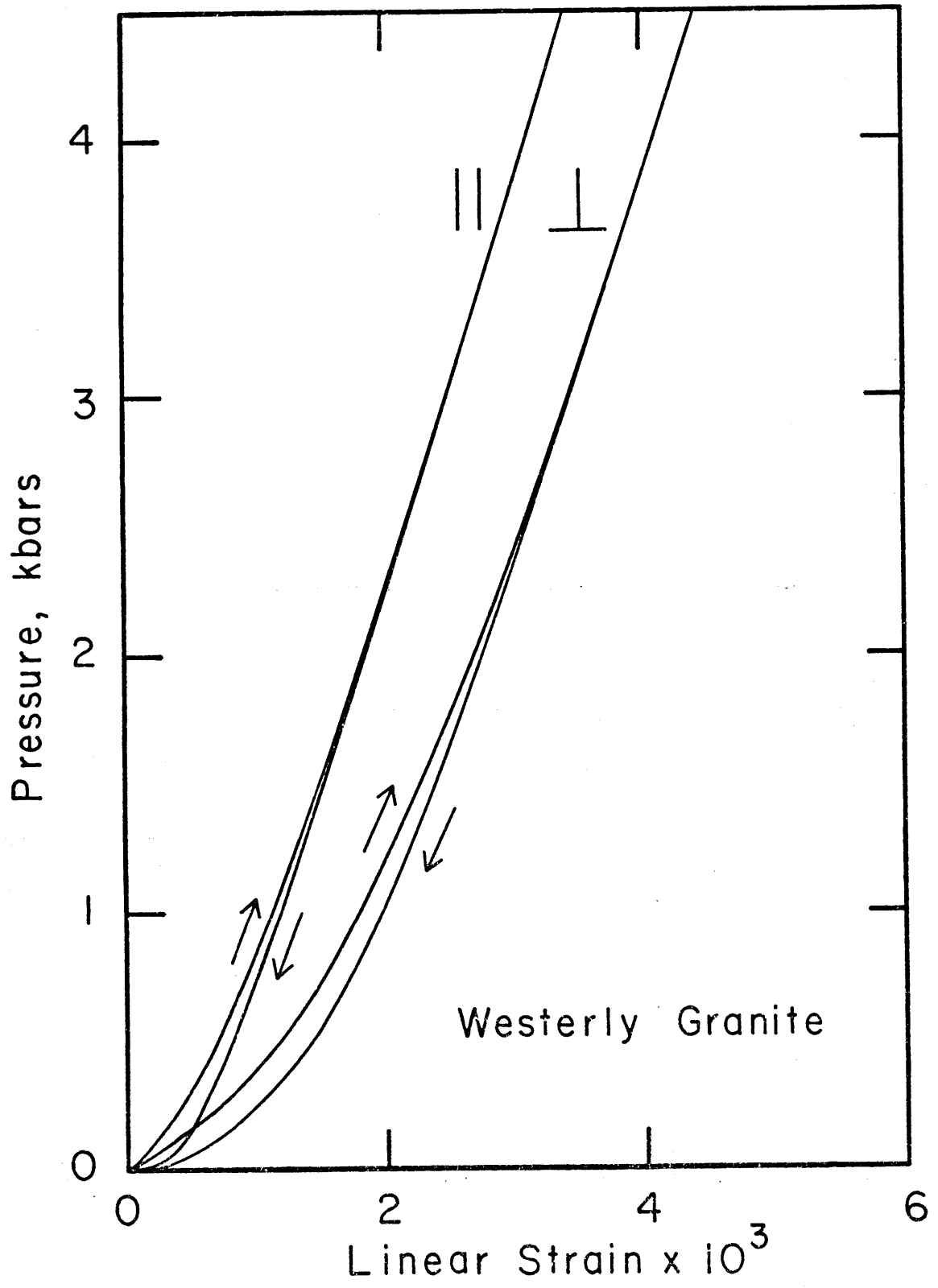


Figure 4-22



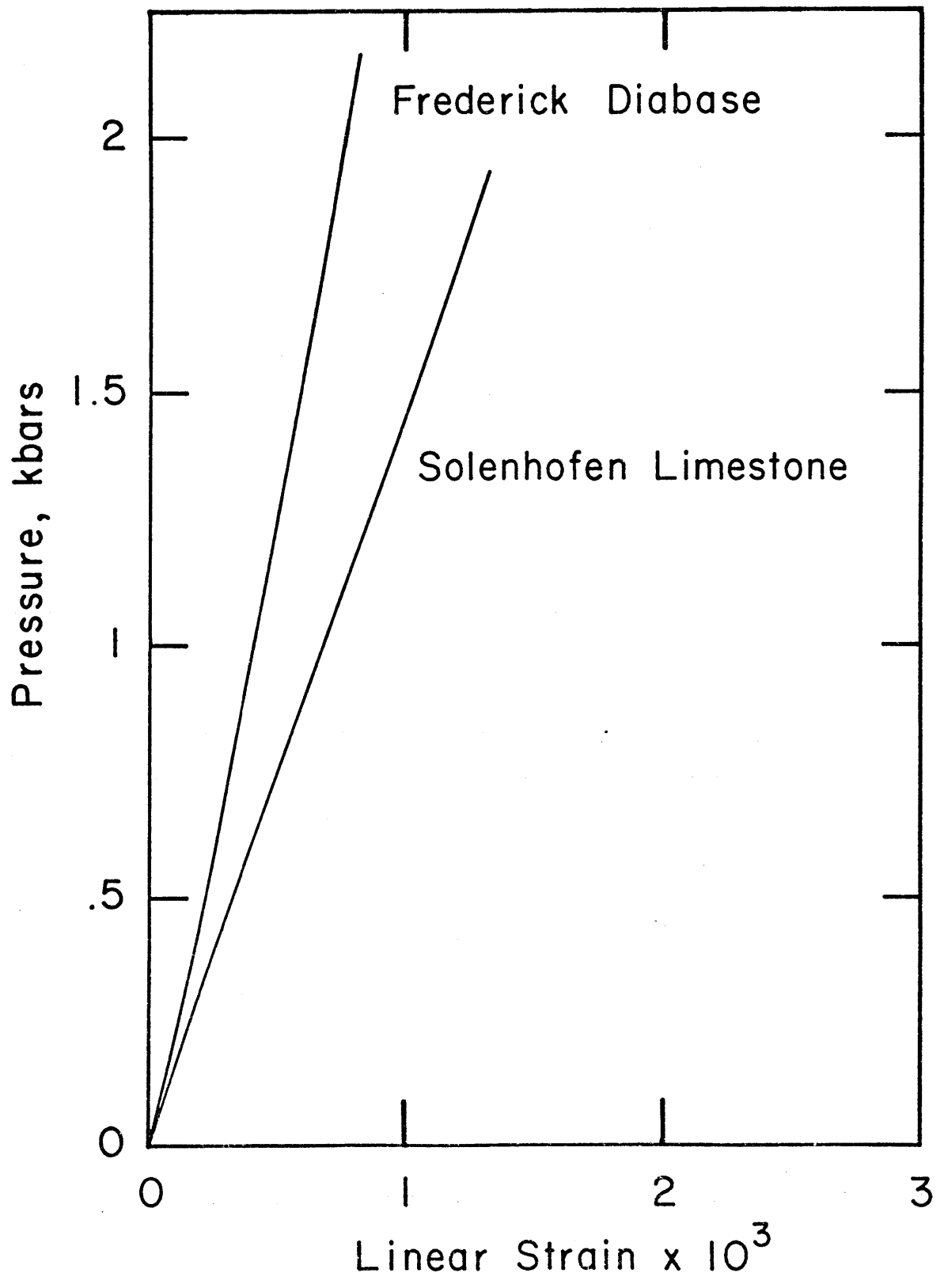


Figure 4-23

## CHAPTER 5

## THE EFFECT OF PRESSURE AND SATURATION ON Q

It is clear from previous experimental work and theoretical considerations outlined in the previous chapters, that fine cracks control the pressure behavior of Q in much the same way as velocity. The effect of saturation conditions, though, are much less predictable. It is the purpose of this chapter to study both of these aspects of attenuation in more detail. The emphasis is placed on porous rocks. First Q data as a function of pressure obtained using the ultrasonic pulse technique, for both dry and completely saturated samples, is examined. For the Berea sandstone, partial saturation effects will also be investigated. The data will be compared to each other on a qualitative basis - in terms of the known physical properties and crack distribution characteristics described in Chapter 4.

The pressure dependent data also provide a valuable tool in quantitatively describing the contributions of the several attenuation mechanisms discussed in Chapter 3. Using the mathematical formulations developed in that chapter, an unusually complete set of data for the Berea sandstone obtained at the Chevron Oil Field Research Co. (COFRC) and described by Toksöz et al. (1978), will be modeled.

The attenuation model developed is then extended, theoretically, to other frequencies, thus enabling a comparison with low frequency seismic data. In fact, an important part of this work is to determine the extent to which laboratory data may be used to infer rock properties from seismic data obtained in the field. The final discussion of this aspect, though, must be put off to the last chapter. It will seem from the modeling, however, that crack and grain boundary frictional sliding is the dominant mechanism of attenuation in the upper crust. Other mechanisms such as fluid flow play secondary roles. The presence of fluids does increase the attenuation due to friction but at this stage the effect can only be treated empirically.

Finally, the attenuation model will serve as a basis for the understanding the effects of partial saturation and the comparison of the Berea  $Q$  data with those obtained for other rocks.

### 5.1 Experimental Data

In this section, ultrasonic  $Q$  data as functions of pressure and saturation will be presented. The rocks studied are the Berea and Navajo sandstones, Bedford limestone, Esopus shale, Colorado Oil Shale, and Ammonia Tanks and Tunnel Beds tuffs. For all the

experiments, an aluminum sample with the same shape of the rock sample was used as a standard reference.  $Q$  values were calculated from spectral ratios of rock-aluminum pairs at each pressure (see equation 4-5).

#### 5.1a Berea Sandstone

The Berea sandstone is a particularly important rock to investigate because it is considered a "standard", well studied by many investigators. In particular we have, in this case, the opportunity to compare  $Q$  values obtained under similar conditions using the same ultrasonic pulse technique but at different laboratories (MIT and COFRC) with different sample dimensions. Furthermore, one may also compare the ultrasonic data with resonant bar data (Gardner et al., 1964) for the same saturation and pressure conditions. It is because of this unique position the Berea occupies, that it is studied in the most detail and is used for theoretical modelling.

Four experiments were performed at MIT: one with a completely dry sample, the second fully water saturated, the third partially saturated and the fourth an experiment where gas is released from solution in water by the reduction of pore pressure. Four experiments were also run at COFRC. Again, dry and saturated rocks were studied but with two saturated experiments of different pore pressure to confining pressure ratios. Also,  $Q$  values were obtained for a methane saturated sample.

Unless otherwise noted, for the saturated runs of the Berea and other rocks presented in this thesis,  $Q$  values are plotted as a function of differential or effective pressure,  $P_d$ , defined as  $P_c - P_f$  where  $P_c$  is the confining or overburden pressure and  $P_f$  is the fluid or pore pressure.

In the first experiment, done at MIT,  $Q$  values and velocities were determined for a vacuum dried sample at confining pressures up to 1 kbar. The velocity determinations are shown in Figure 5-1. The increase for P and S waves at low pressures is due to the closing of cracks (Toksöz et al., 1976) and corresponds to non-linear region of the static stress strain curve in Figure 4-14. Waveforms normalized spectra, and spectral ratios are shown for P and S waves in Figures 5-2 and 5-3 respectively for several confining pressures. In these and later figures, the dashed line in the spectrum plot corresponds to the aluminum standard (A1). Only the waveforms for the rock sample are shown. A rather large DC shift is noted for the S waves. This feature, common to many of the experiments presented in this chapter, is due to low frequency noise. This could be filtered out prior to time windowing but was not necessary since the low frequency portion of the spectrum is not used in determining  $Q$ . Clearly, the slopes of the spectral ratio plots decrease with increasing pressure indicating

an increase in  $Q$  for both P and S waves. The resulting  $Q$  values, calculated from the slopes and velocities are shown in Figure 5-4.

$Q$  for the dry Berea sandstone increases rapidly with pressure, approaching a value over 100. As stated in Chapter 4, these high pressure, high  $Q$ , values are particularly unreliable and thus, from this experiment, we are unable to determine ultimate  $Q$  values. However, the trend in pressure is obvious and furthermore,  $Q_s$  is about equal to  $Q_p$  as predicted by the dry friction attenuation model (Walsh, 1966).

A Berea sample was then saturated with distilled water and the experiment repeated. The fluid pressure was maintained at 0.465 the confining pressure for differential pressures ranging from 45 to 2000 bars. This ratio of pore-fluid and confining pressures is a nominal value for saturated sedimentary rocks where the fluid pressure is equal to the hydrostatic pressure of a water column.

The presence of water increases the velocity of P waves while slightly decreasing the velocity of S waves as illustrated in Figure 5-1. The increase in velocity with pressure is not as great as for the dry sample.

Again, waveforms, normalized spectra, and spectral ratios are shown for the saturated Berea sandstone in Figures 5-5 and 5-6. The slopes of the ratios at a given

pressure are larger than for the dry sample but as with the dry case, decrease with pressure. The resulting  $Q$  values are shown in Figure 5-7 as functions of differential pressure. Both  $Q_p$  and  $Q_s$  are substantially lower than their dry counterparts and in the saturated case  $Q_s$  is much lower than  $Q_p$ , approaching a value of only about 30 even at high pressure.  $Q_p$  increases to a value of about 60 by a pressure of about 750 to 1000 bars. While it appears that the effect of fluid saturation is to dramatically increase the attenuation, especially for S waves, the dependency of the  $Q$  values on crack closing is still observed. Thus, the bulk of the effect of saturation seems to be the altering of the friction mechanism.

A similar set of  $Q$  determinations for the Berea sandstone were obtained at the COFRC (Toksöz et al., 1978). While the physical conditions (pressure and saturation) of the experiments were similar to those performed at MIT, the geometry was somewhat different. A description of the laboratory set-up and high pressure system is given by Timur (1977). The samples used were cylindrical, 8.9 cm in diameter and 5.1 cm long. The increased length relative to the MIT system improves the resolution of the  $Q$  values since the slope of the spectral ratios versus frequency, for a given  $Q$ , is

larger. Also, pre-processing and deconvolution or windowing were not required since the reflections were further delayed in time and did not interfere with the direct wave.

In the first experiment, the sample was dried in a vacuum oven while being periodically flushed with argon.  $Q$  values were determined in the range of 1 bar (14.7 psi) to 550 bars (8000 psi). These results are shown in Figure 5-8 for both P and S waves. Again it is seen that both  $Q_p$  and  $Q_s$  increase rapidly with confining pressure with a slight leveling off at higher pressures. Also,  $Q_s$  is slightly higher than, or equal to  $Q_p$ .

In the second experiment, a Berea sample was fully saturated with methane and the experiment repeated with  $P_f = 0.465 P_c$ . The resulting  $Q$  values are plotted as a function of differential pressure in Figure 5-9.  $Q_p$  increases rapidly at first with pressure but appears to begin to level off at higher pressures.  $Q_s$  is again, either equal to or slightly larger than  $Q_p$ . It exhibits a similar but a little more gradual behavior. As would be expected, the differences between the dry rock and the methane saturated rock are small.

Following this, a sample was completely saturated using the same techniques described in section 4.8 with an NaCl brine of 67,191 ppm concentration. Again  $P_f$  was



maintained at  $0.465 P_c$  throughout the experiment.  $Q$  values obtained are shown as a function of differential pressure in Figure 5-10. It is seen again that  $Q$  increases with pressure but that  $Q_s$  is less than  $Q_p$ .

A final brine saturated ( $\text{NaCl} = 161,334$  ppm) experiment was run in which  $P_c$  was fixed at 1035 bars (15,000 psi) and  $P_f$  decreased from 1000 bars (14,500 psi). The results are shown in Figure 5-11 and agree quite well with the data shown in Figure 5-10. This implies that the law of effective pressure may apply for attenuation as well as velocity. The slight increase in  $Q$  at high pressure is not significant.

The remarkable aspect of these data is that they agree very well with data obtained under nearly identical conditions at MIT but with different sample dimensions. This fact greatly enhances our confidence in the experimental technique and implies that the assumptions made in Chapter 4 are valid.  $Q$  values obtained, if not with great resolution, are at least reasonable.

From another point of view, these data imply that  $Q$  is not very sensitive to the brine content of the pore water. Both  $Q_p$  and  $Q_s$  remain about the same for saturations of distilled water, 67,191 ppm brine and 161,334 ppm brines at all pressures.

Finally, two experiments were done at MIT to

investigate the effects of partial water saturation on  $Q$ . The primary influence of water saturation is known from data like those of Gardner et al., 1964. The motivation for these experiments, however, lies in reported high P wave attenuation from gas sands relative to what would be expected for completely water saturated sediments. The data from Gardner et al. imply that the  $Q$  for a partially saturated sandstone should be about the same as for a completely saturated sample (see Figures 2-4 and 2-5) in apparent contradiction with the in-situ observations. The question we wish to answer here is if there is any evidence to support a higher P wave attenuation (lower  $Q$ ) for the partially saturated case.

The first experiment was essentially a repeat of the conditions examined by Gardner et al. for which  $Q_p$  and  $Q_s$  are determined as a function of pressure for a sample of given saturation. Partial saturation was obtained by slowly drying out a completely saturated sample until a mass,  $M$ , given by the following equation was reached:

$$M = V\{\rho(1 - \phi) + \rho'S_w\phi\}$$

$V$  is the sample volume,  $\rho$  is the matrix density,  $\rho'$  the water density and  $S_w$  is the water saturation. After the

correct mass was obtained, the sample was stored in an air-tight plastic bag to allow the pore water to equilibrate throughout the rock. The Berea sandstone is relatively permeable and storage of over a week was considered adequate. Prior to jacketing the sample was reweighed and the saturation was determined to be 37% ( $S_w = 0.37$ ).

P and S wave velocities and Q's were then found as a function of confining pressure ( $P_f = 0$ ). Velocities for this experiment are shown in Figure 5-12. These values are as would be expected from theoretical considerations (Toksöz et al., 1976). Waveforms, spectra, and spectral ratios are shown for several pressures in Figures 5-13 and 5-14. Q values are shown in Figure 5-15. Comparing these data with those of the completely water saturated Berea sandstone (Figures 5-8, 5-11 and 5-12), we find that both  $Q_p$  and  $Q_s$  are essentially unchanged for most pressures. While  $Q_p$  is slightly lower relative to the fully saturated sample at higher pressures, there is by no means any evidence to support high P wave attenuation in this saturation range.

In order to examine this in greater detail, an experiment was designed so that partial saturation could be achieved by the release of gas from saturated pore water by reducing the fluid pressure in a closed system. The pore pressure apparatus used for this experiment is illustrated in Figure 5-16. The critical part of the

set-up was the pressure generator-volumeter from which volume changes could be found with a resolution  $0.0052 \text{ cm}^3$ . The range of partial saturation for the experiment was determined by back pressure required to operate the volumeter properly (due to the friction of the packing material) - about 150 to 200 bars and the maximum fluid pressure obtainable before the gas converts to liquid phase. Helium was chosen as the gas since fluid pressures up to 1000 bars could be used and since it is soluble enough in water so that comparatively large quantities of the gas, relative to the resolution of the volumeter could be used.

The procedure used during the experiment was as follows: a completely saturated sample of Berea sandstone was jacketed, placed in the pressure vessel and connected to the pore pressure system. Care was taken to flush the system with water to eliminate trapped air pockets. With valve A open and B closed, (Figure 5-16), the pore pressure was set to 200 bars using the hand pump. The confining pressure was simultaneously raised maintaining a differential pressure of 200 bars. It was extremely important to keep the differential pressure constant throughout the experiment so that the effect of crack closure was eliminated.

After this first step, valve A was closed so that the pore pressure system was now closed. The total volume,  $V_T$ , of the water was calculated. This included the volume of the volumeter, pressure tubing, gage, and the pore space in the rock. From  $V_T$ , the volume of gas at 200 bars,  $V_g$ , required to completely saturate the water at a fluid pressure of 1000 bars was calculated using solubility curves found in Stephen and Stephen (1963). For this experiment,  $V_T$  at 200 bars was  $21.5856 \text{ cm}^3$  and  $V_g$  was  $0.7784 \text{ cm}^3$ . To insert the helium into the system, valve B was opened and the volumeter piston backed off so that  $P_f$  was kept at 200 bars until the system volume was increased by the amount  $V_g$ . Valve B was then closed.

Following this step, the fluid pressure was increased using the volumeter piston, in order to force the free helium into solution. A final fluid pressure of 1200 bars was chosen to insure complete saturation. Of course, confining pressure was raised at the same time to 1400 bars. The pressure was held constant for one hour so that the helium had adequate time to diffuse throughout the pore pressure system. Once this step was accomplished, the fluid pressure could be dropped, allowing the gas to come out of solution. Since the volume of the entire system was known at any pressure, the volume percentage of liberated helium could be calculated. It was implicitly assumed that

this gas fraction was the same throughout the system, including the pore spaces in the rock. Starting from zero gas saturation at 1000 bars fluid pressure, a total gas saturation of 5% could be obtained if the fluid pressure were reduced to 150 bars. Thus, the pore pressure was lowered from 1200 bars using the volumeter and the confining pressure simultaneously lowered maintaining the 200 bar differential pressure. Velocities were determined and waveforms recorded at discrete pressures.

The presence of free gas in the rock was confirmed two ways. First, the compressibility of the pore fluid could be roughly determined by the volume change required to affect a given pressure drop. This clearly indicated an increase in compressibility at fluid pressures below 1000 bars but assumed that the gas phase was homogeneously distributed throughout the system. More concrete evidence was found in the velocities shown in Figure 5-17. Here,  $V_p$  and  $V_s$  are plotted as functions of pore fluid pressure and calculated gas saturation. Clearly,  $V_p$  decreases with increasing gas saturation while  $V_s$  remains constant. This behavior is exactly as would be expected from theory but as a check,  $V_p$  was determined theoretically (see Appendix B) for a completely water saturated Berea sandstone in which the only change was the compressibility

of the water as a function of fluid pressure. This calculation is shown as the dashed line in Figure 5-17 and obviously does not explain the data except for the two high pressure points which are supposed to be completely water saturated anyway. It appears then, that the experiment was indeed successful in releasing helium gas from solution in the rock.

$Q_p$  and  $Q_s$  are shown as functions of gas saturation and fluid pressure in Figure 5-18. The average values of both are comparable to those obtained at 200 bars differential pressure in the previous experiments. Clearly, there is no change in  $Q_s$  as a function of gas saturation. There are variations in  $Q_p$  and even though they are within the resolution of the experimental technique, they might be significant. In particular, there is a slight reduction in  $Q_p$  up to a gas saturation of 3 or 4% at which  $Q_p$  increases to its full water saturation value. This type of behavior is predicted from the gas release model presented in section 3.4a but this data is by no means hard evidence of gas or gas bubbles decreasing  $Q_p$ . One cannot even say that the data disproves any relation between gas saturation and  $Q_p$  since the gas properties change with pressure and one would theoretically expect the largest effect at only

low fluid pressures. Furthermore,  $Q$  may depend on pore pressure and thus keeping the differential pressure constant may not eliminate the effects of other mechanisms. However, the apparent decrease in  $Q_p$  followed by a recovery is intriguing in light of the models for gas bubble losses and will be further discussed later in this chapter.

#### 5.1b Navajo Sandstone

As with the Berea sandstone,  $Q$  values were obtained for the Navajo for a vacuum dry sample and a water saturated sample. Recalling section 4.6, one might expect that since the Navajo has a lower crack density compared to the Berea, the  $Q$  values might be higher. As will be seen, this is confirmed by the data.

Velocity as a function of pressure ( $P_d$  for the saturated case) is shown in Figure 5-19 for P and S waves. Consistent with the static stress-strain measurements, velocity increases more rapidly at lower pressures than for the Berea. Furthermore, the values for velocity are higher - 3.56 km/s versus 3.22 km/s for P waves in dry rock at 45 bars and 4.37 km/s versus 4.23 km/s at 1000 bars as examples. Similar comparisons may be made for the saturated samples and for S waves.

Waveforms, spectra, and spectral ratios for the dry rock experiment are shown in Figures 5-20 and 5-21 for P and S waves respectively.  $Q$  values obtained from the spectral ratios are shown in Figure 5-22. Again, it must be mentioned that the high  $Q$  values at the higher



pressures are unreliable - a restriction of the experimental technique. However, for pressures less than 500 bars, one may say that the  $Q$ 's calculated for both P and S waves behave in much the same manner as for the dry Berea sandstone. The absolute values of  $Q$  are higher than for the Berea - 30 compared to 24 for P waves at 45 bars confining pressure.  $Q$  also seems to increase at a slightly faster rate with pressure.

In the second experiment the sample was saturated with distilled water and as with several of the Berea runs,  $P_f$  was maintained at  $0.465 P_c$ . Waveforms, spectra, and spectral ratios are shown in Figures 5-23 and 5-24 and  $Q$  values are shown in Figure 5-25. In this case, the differences between the Navajo and Berea sandstones are more clearly observed. While the  $Q$ 's obtained for the Navajo are substantially the same as those for the Berea at pressures greater than 600-700 bars, the increase in  $Q$  at low pressures is much faster for the Navajo. Also, as with the dry case, the absolute  $Q$  values, particularly for P waves, are higher for the Navajo. This is in good agreement with the inferences made from both the static stress strain curves and the velocity measurements. Clearly, this is a good example of how the same parameters that determine elastic properties also affect attenuation.

### 5.1c Bedford Limestone

The Bedford limestone presents an interesting comparison to the sandstone. Although the total porosity is rather high (12%), the crack porosity is somewhat lower than the sandstones. Also, pore collapse, initiated at 1000 bars, alters the typical behavior of both velocity and  $Q$  observed in the sandstones. Again, two experiments were run, one dry and the other saturated. For the water saturated case  $P_f$  was maintained at  $.465 P_c$  throughout the experiment.

P and S wave velocities for the Bedford limestone are shown in Figure 5-26. Note the general features of an increase in velocity due to crack closure up to about 500 bars and higher P wave and lower S wave velocities for the saturated sample. At 1000 bars the effect of pore collapse becomes evident. During the loading cycle (increasing differential pressure), velocity increases as the large pores collapse due to localized plastic flow. As the rock is unloaded (decreasing pressure), it behaves elastically until about 1000 bars at which point, cracks induced by pore collapse open, reducing the velocities to a point well below those obtained during the loading cycle. This type of behavior was correctly identified by Nur (1969) and, of course, confirmation lies in the static

stress-strain measurements shown in Figure 4-16. The effect is observed for both P and S waves in both dry and saturated samples.

P and S waveforms, spectra and spectral ratios are shown for the dry rock in Figures 5-27 and 5-28 respectively. It is clear for the P waves at least, that the attenuation is very low. There was some question as to the quality of the shear waves and thus the results should be used with caution. As will be seen, the dry  $Q_s$  values are not consistent with the other data. There is no explanation at the present time as to why this is so.

The resulting  $Q$  values are plotted as functions of confining pressure ( $P_f = 0$ ) in Figure 5-29. Concentrating on the P wave values, one sees that  $Q_p$  is much higher than for sandstones at low pressures - around 70 at 105 bars. The rate of increase with pressure is lower than the sandstones however, and at pressures of 700-800 bars,  $Q_p$  is only slightly higher than the values attained by the sandstones. While the data is shown only to a pressure of 1000 bars (subjected to the constraints of the experimental method), the sample was run to a maximum pressure of 2250 bars. During the unloading cycle, the effect of pore collapse is evident at the lower pressures.  $Q_p$  is sharply reduced at pressures less than 1000 bars due to the large increase in crack porosity. At 100 bars the  $Q$  is lowered by 52% (118% increase in attenuation). This may be

compared to the 344% increase in crack porosity obtained from the static measurements. Clearly, not all of these cracks are of sufficiently low aspect ratio at 100 bars to contribute to the attenuation. Indeed,  $Q$  appears to level off from 250 to 100 bars on the unloading cycle implying a lower limit to the induced crack aspect ratio spectrum at surface pressure.

Waveforms spectra and spectral ratios are shown for the saturated Bedford experiment in Figures 5-30 and 5-31 with the calculated  $Q$  values in Figure 5-32. Again the  $Q$  is lower than for the dry case - by a factor of two for P waves at 500 bars for example, and  $Q_s$  is lower than  $Q_p$ . However, there is little difference between the supposed dry  $Q_s$  values (Figure 5-29) and the wet ones. Nor do the dry S results increase with pressure as the wet data. One would expect from what has been seen in the velocities, that the changes in  $Q$  for the dry rock at pressures less than 500 bars would be more rapid than the wet rock.

In any event, the rapid increase in  $Q$  at low pressures is followed by a levelling off up to about 900 bars. An increase in  $Q$ , particularly for S waves, occurs at that point due to pore collapse. The final value of  $Q_s$  obtained at 2000 bars is nearly twice that obtained by the sandstones. The increase in  $Q_p$  is not as dramatic. However, upon unloading the sample, the effect of induced

cracks is much greater for P waves than S waves although both obtain lower values than during the loading cycle.

#### 5.1d Shales

The first experiment run was on the Esopus shale. Because the porosity and permeability of this sample is so low, a full series of pressures was not used. Furthermore, since the rock becomes very friable when dry, only a water saturated test was run. For this experiment, an Esopus shale sample cored perpendicular to the bedding was fully saturated under argon pressure. Rather than applying pore pressure, the sample remained with atmospheric pore pressure during the course of the experiment.

Data was obtained at 105, 500, 1000, and 2000 bars confining pressure. The sample was held at each pressure for two hours to allow the pore pressure to equilibrate. Velocities were continuously monitored during this time and the experiment continued once the velocity leveled off to a constant value. However, the sample was kept at 1000 bars overnight (16 hours) resulting in a further increase in velocity. This implied that 2 hours were not enough to equilibrate pore pressure. Velocities obtained unloading the sample show that the data from 1000 bars (after the 16 hour wait) and 2000 bars probably most closely represent the completely equilibrated values.

$V_p$  and  $V_s$  for the 2 hour equilibrated points and the 16 hour equilibrated run at 1000 bars are shown as functions of confining pressure in Figure 5-33. The changes in velocity are not nearly as great as for the sandstones or limestone due to the absence of fine cracks implied by the lack of effective porosity or permeability. The unloading portions of the velocity curves, while offset from the low pressure loading curves due to pore pressure equilibration, have essentially the same curvature, further corroborating the absence of fine cracks.

Waveforms, spectra, and spectral ratios for P and S waves are shown in Figures 5-34 and 5-35 respectively. There is very little obvious change in the nature of the waveforms and spectra implying that  $Q$  does not change very drastically. This is, in fact, clear in Figure 5-36 where the  $Q$  values obtained from the spectral ratios are plotted as functions of confining pressure. The effect of pore pressure equilibrium and unloading is the same for attenuation as velocity. The  $Q$  values for the Esopus shale are consistently higher than for the saturated sandstones at all pressures although the difference is minimized at higher pressures where the fine cracks in the sandstones have closed. The large difference between  $Q_p$  and  $Q_s$  may be due to slippage in clay lubricated grain

contacts oriented parallel to the bedding and perpendicular to the direction of S wave propagation. Both  $Q_p$  and  $Q_s$  are also higher than in situ values (32 and 10 respectively) obtained for the Pierre shale by McDonal et al. (1958) but lie well within the range of Q values for various shales listed by Bradley and Fort (1966).

Two experiments were run for the Colorado oil shale - one perpendicular to the bedding and the other parallel. As with the Esopus shale the samples were completely saturated but  $P_f = 0$  throughout the experiment. The velocities, plotted in Figure 5-37 are consistent with the static measurements of linear strain discussed in the last chapter. For both P and S waves, velocity is higher in the direction parallel to the bedding. There is little evidence of microcracks since the velocities show no rapid changes at low pressures and increase less than 20% by 2000 bars compared to an increase of over 30% for sandstones.

Because the slopes of velocity versus pressure are virtually identical for both orientations, one may assume that the variations in velocity observed are not controlled by cracks. Furthermore, the presence of kerogen in the shale seems to play an important role in determining both the elastic and anelastic properties. First, the Poisson's ratio calculated from the velocities is

0.40 - implying that the shale is behaving more like some polymers than rock. For comparison, the Poisson's ratio of the Esopus shale is 0.27. Secondly, as seen from the waveforms, spectra and spectral ratios plotted in Figures 5-38 and 5-39, it was very difficult to propagate S waves, particularly those in the direction normal to the bedding (plane of polarization parallel to bedding). Furthermore, a frequency dependent component of the spectral ratios is observed. This was not true for the Esopus shale.

Q versus confining pressure ( $P_f = 0$ ) for both P and S waves in both directions are shown in Figure 5-40. The results are peculiar - not all expected. First note that Q in all cases remains unchanged with pressure - confirming the lack of cracks.  $Q_S$  is very low, as would be expected, and  $Q_S$  for the perpendicular direction is lower than the parallel one, mimicking the anisotropic velocity behavior. However, the anisotropy of Q in P waves is reversed from that of velocity. Furthermore, there is a large discrepancy in the differences between  $Q_P$  and  $Q_S$  for the two orientations. In the parallel case  $Q_S$  is nearly equal to  $Q_P$ , with  $Q_P/Q_S = 2$  in the perpendicular direction. The large differences between the  $Q_P$  values for the two orientations are not particularly obvious from the spectral ratios but it should be pointed out that the velocities of the perpendicular direction are lower than for the parallel direction, emphasizing the difference in attenuation.



Finally, this is the only case studied in which the changes in  $Q$  with pressure are less than the changes in velocity. As to what attenuation mechanisms can account for this data is not certain. At first glance it seems that none of the mechanisms discussed in Chapter 3 do the job. While it may be premature to propose an attenuation mechanism for oil shales, especially since their properties are so variable, the problem will be discussed further in section 5.2.

#### 5.1e Tuffs

The study of attenuation in tuffs was prompted by the interesting differences in crack distributions compared to the sandstones implied by the static measurements discussed in section 4.9. It was found that the tuffs contain fewer small aspect ratio cracks than either the Berea or Navajo sandstones even though the total porosities are roughly equivalent. Thus, any observed differences in  $Q$  might be attributed to the dissimilar crack distributions. However, the observed attenuation in both Ammonia Tanks and Tunnel Beds tuffs appear to be dominated by scattering even though the effect of cracks is evident. In Tunnel Beds, the  $Q$  measurements are further complicated by the presence of pore collapse under pressure.

The following presentation of the  $Q$  data for the two tuffs is not intended to be a study of the scattering

problem. It will be shown, however, that the formulation of Yamakawa (1962) for scattering roughly accounts for the observed attenuations.

For both tuffs it was difficult to work with saturated samples primarily because the large grains in the rocks blocked the pore pressure tube. Furthermore, especially for Tunnel Beds with about 30% porosity, it was nearly impossible to propagate good quality waves. Thus, only dry samples are studied here.

P and S wave velocities for the Ammonia Tanks tuff are shown as functions of confining pressure ( $P_f = 0$ ) in Figure 5-41. As suspected from the static measurements (Figure 4-18), velocity increases more gradually with pressure than for the sandstones and does not begin to level off until about 1500 bars. P wave velocities are similar in magnitude to the Navajo and about 5% higher than the Berea even though the measured porosity is much less, 5% compared to 16-18%. S wave velocities are uniformly lower than the sandstones by about 5%. This implies that isolated pores and cracks may exist in the rock and that the actual porosity is higher than that measured by  $\text{CCl}_4$  saturation.

The Q analysis was complicated by the presence of scattering which introduces a frequency dependent component to the apparent attenuation. Thus the spectral

ratios are not linear over a broad frequency range. The  $Q$  values calculated are strictly applicable only to a frequency bandwidth limited to the peak power portion of the spectrum. For the Ammonia Tanks, this occurs at about 0.4 MHz for P waves and 0.5 MHz for S waves. Waveforms, spectra and spectral ratios are shown in Figures 5-42 and 5-43. The resulting  $Q$  values are shown in Figure 5-44. The most outstanding features of the data are the low  $Q$  values at all pressures and that  $Q_s$  is nearly 1.5 times  $Q_p$ . Since one would intuitively expect that the attenuation due to scattering would be relatively constant with pressure, the increase in  $Q_p$  and  $Q_s$  with pressure may be due to crack closure just as with the sandstones. However, as with velocity, the rate of increase is slow compared to the sandstones.

The large difference between  $Q_s$  and  $Q_p$  (also observed in the Tunnel Beds as will be seen) is obtainable from Walsh theory but requires a lower coefficient of friction than for the dry sandstone since the Poisson's ratio is 0.24 compared to 0.17. Another explanation is that the attenuation due to scattering of incident S waves is less than for incident P waves.

The Tunnel Beds tuff was even more difficult to work with than the Ammonia Tanks. With its very high porosity

(30%), vugular pore spaces, and large grain sizes, scattering completely dominates the anelastic behavior at ultrasonic frequencies. Pore collapse, initiated at about 800 bars and observed in the velocities shown in Figure 5-45, further complicates the picture. P and S wave velocities, about 25-30% lower than for the Ammonia Tanks do, however, behave predictably and in a manner similar to the Bedford limestone. Under loading, velocity increases slightly at low pressures due to crack closure and then levels off. At 800 bars, velocity increases again as pores collapse. During unloading of the sample, velocities are higher than the loading cycle for pressures greater than 800 bars but are lower at lower pressures due to cracks generated during pore collapse.

The effect of scattering is clearly evident from Figure 5-46 where a typical, non-linear spectral ratio curve is shown for a broad frequency band. Q values were again determined for a limited band width centered on roughly 0.4 MHz for both P and S waves. Typical waveforms, spectra and spectral ratios are shown in Figure 5-47 and resulting Q values are plotted in Figure 5-48. Q is essentially constant with pressure, consistent with the domination of scattering. There is, however, evidence of the effect of pore collapse barely observable in the loading cycle but more evident in the unloading cycle. A clear

decrease in  $Q$  relative to the loading path that can be attributed to crack production during pore collapse.

As with the Bedford limestone, the difference seems to be greater for P waves. Also, as seen for the Ammonia Tanks,  $Q_p$  is less than  $Q_s$  by about the same amount. Here, however, the Poisson's ratios are comparable with the sandstones.

In order to investigate the effect of scattering on the attenuation in the tuffs a little more thoroughly, the formulation of the apparent attenuation coefficient derived by Yamakawa (1962) and listed in equation 3-44 is used to theoretically calculate  $Q$  for P and S waves. One may assume that scattering in the tuffs is due to empty (air-filled) pores and not from phenocrysts which have less elastic property contrasts. The matrix moduli are determined from the acoustic velocities at high pressure and are then corrected for spherical porosity. These, and the other parameters used as well as the results of the calculations are listed in Table 5.1. Velocities from 300 bars and 2000 bars are used. A scattering radius of 1mm is assumed, but the calculations may be scaled using the  $r^3$  dependence in the attenuation coefficient. The frequency is taken to be 0.4 MHz. The results for the Ammonia Tanks tuff show that scattering does indeed account for most of the observed attenuation.

The calculations for the Tunnel Beds tuff are not

nearly as satisfying. First of all, it is necessary to assume that only a fraction of the total porosity actually contributes to scattering. In the example shown, 10% porosity is used. While the calculated  $Q$  values are still low compared to the data, we have seen that scattering does account for most of the observations, including the fact that  $Q$  does not seem to vary much with pressure for the Tunnel Beds. One could expend a great deal of effort trying to characterize scatterers in terms of pore sizes and indeed, this might be a valuable tool for the future using high frequency ultrasonic waves in porous rocks.

## 5.2 Interpretation of Laboratory Data

The relative effects of various attenuation mechanisms in dry and saturated porous rocks are now considered in more detail. The methods and techniques discussed in Chapter 3 will be applied to model the behavior of attenuation as a function of differential pressure for the ultrasonic data obtained for the Berea sandstone at COFRC. These models will then be extrapolated to other frequencies. Next, the effect of partial saturation in the Berea will be examined in terms of gas bubble theory. The models obtained for the Berea sandstone are then used in comparison to the experimental data on other rocks. The attenuation mechanisms given most consideration to are friction and fluid flow. As

will be seen, the other mechanisms are of minor importance for saturated rocks at ultrasonic frequencies.

#### 5.2a Sandstone Model of Attenuation

The procedure taken involves first modeling the attenuation in the dry rock in order to establish the needed parameters for the friction mechanism and intrinsic attenuation in the absence of fluid associated mechanisms. These parameters will then be used in the modeling of the saturated sample data. An important but probably valid assumption made here is that all attenuation mechanisms that occur in dry rocks also occur in wet ones. Given the parameters obtained from the dry case, one may examine in more detail the relative importance of the mechanisms contributing to the attenuation in the brine-saturated case as a function of pressure. In particular, since the attenuation due to Biot-type fluid flow, squirting and scattering are readily calculable, it remains to be seen what the contribution due to the presence of pore fluid is in terms of the friction mechanism and intrinsic aggregate anelasticity. The approach taken here is empirical and thus the models presented have no absolute predictive ability.

The elastic moduli, fluid and frame properties used in modeling the Berea sandstone are listed in Table 5.2. The bulk modulus of brine as a function of pore pressure

is given by Adams (1931) and Long and Chierici (1961). For the dry case, the bulk modulus of air is taken to be one bar and the pore pressure is assumed to be constant at one bar.

The surface pressure aspect ratio distribution listed in Table 5.3 is determined by fitting theoretical calculated elastic properties (equations B-1 and B-2) to the P and S wave velocity versus differential pressure data for both saturated and dry cases as described by Toksöz et al., (1976). The frequency is taken to be .5 MHz.

The contributions to attenuation in the dry case are assumed to be due to friction and the intrinsic aggregate attenuation only. Zero pressure Q's were taken as 23 for P waves and 26 for S waves based on the data in Figure 5-8. The pressure dependence of Q for the dry Berea sandstone may be reasonably modeled with  $A = 0.2 \times 10^4$  (equation 3-16) and an intrinsic aggregate Q for both P and S waves of 120. The possible variations in the parameter A are not as wide as one might expect, ranging from  $0.15 \times 10^4$  to  $0.25 \times 10^4$ . The results of this empirical model fitted to the data are shown in Figure 5-49.

The introduction of brine as the pore saturant results in no change in the parameter A, since the crack closing rate is the same as for the dry case, determined by the static rather than the dynamic effective bulk modulus.



In Chapter 3 the role of fluids in determining the attenuation was discussed. In particular, water may soften and lubricate the matrix resulting in a higher attenuation due to a friction type mechanism, especially for shear waves. Since the contributions due to Biot fluid flow, squirting flow, viscous shear relaxation and scattering are fairly well determined from the properties listed in Table 5.2 it remains to be seen in modelling the saturated data, what the contribution due to friction is. This must be determined empirically. One important constraint, however, is the low  $Q$ , especially  $Q_s$ , at high pressures. This implies that a mechanism which is relatively independent of pressure, such as Biot fluid flow, is required under those conditions.

The fluid flow contributions to the attenuation are calculated as described in section 3.3. Given the attenuation due to all the mechanisms other than friction, it is found that to fit the data, one must choose a zero pressure  $Q_p$  for friction of 15 and a  $Q_s$  of 10. These low values of  $Q$  relative to the dry case indicate that brine saturation increases the attenuation due to friction by almost a factor of two. Although the data may be fit with a fluid viscosity of 1 cp, a better fit is obtained by allowing the effective viscosity to be 4 cp. This might be expected from experimental measurements of the viscosity of water in clay-water systems (Low, 1959).

Such an effect would predict a lower attenuation in rocks with lower clay content. This was indeed observed for the Navajo sandstone. Furthermore, while again not necessary, the best fit to the data, also shown in Figure 5-49, is obtained by reducing the intrinsic aggregate  $Q$  for shear waves by 5%. It is perhaps no coincidence that the seismic velocities are best fit in the saturated case by reducing the matrix shear modulus 5% relative to the dry case. This may reflect the possibility of increased shear and thus higher attenuation at grain boundaries due to the presence of water as discussed earlier.

The relative contributions of the two important mechanisms, friction and Biot-type fluid flow, in the brine-saturated case are easily seen in Figure 5-50 showing  $Q_p^{-1}$  for each mechanism as a function of pressure. The small increase in the fluid flow contribution at low pressures is an artifact of the calculations, a result of the stiffening of the frame moduli. As would be expected, friction across cracks and grain boundaries is dominant at low pressures but becomes less important as cracks close. Since the bulk of the porosity and permeability is unaffected under the pressure conditions of interest, the fluid flow contribution to attenuation remains relatively constant with pressure and becomes an

increasingly important mechanism. Obviously at some pressure, the porosity and permeability of the rock will break down and one should expect a rapid increase in  $Q$ . This is exactly as observed for the Bedford limestone undergoing pore collapse.

Using the Berea sandstone properties from model calculations, one may now examine in more detail the individual contributions of each mechanism for the fully saturated case and extrapolate these results to other frequencies. The interpretation of these models must remain strictly within the confines imposed upon them. That is, it is assumed that strain amplitudes are equivalent to those in the laboratory experiment and that no other mechanisms contribute to attenuation at frequencies other than those calculated at 0.5 MHz.

A theoretical overview of the relative contribution of each mechanism considered is shown in Figure 5-51a. Here, the P wave attenuation coefficients are plotted as functions of frequency for a surface pressure condition. Figure 5-51 was obtained by fixing the attenuation at 0.5 MHz based on the theoretical model of the pressure data (Figure 5-49). The resulting curves are theoretical extrapolations. A constant  $Q$  mechanism for friction is assumed. The same model is shown in Figure 5-51b except that the attenuation coefficients are calculated for a

differential pressure equivalent to a depth of about 3 km. The corresponding aspect ratio distribution is listed in Table 5.3.

Figures 5-51a and b clearly show the relative effects of friction, fluid flow, shear relaxation and scattering on the attenuation of P waves. Similar results are obtained for S waves. If friction is indeed a frequency independent attenuation mechanism, then it dominates the other mechanisms for this case. However, as seen before, friction is of somewhat less importance at higher pressures. As assumed in the models, the contribution of Biot fluid flow remains essentially unchanged between the two cases. While never dominating in this case, it is of importance at about  $10^5$  Hz where Poiseuille flow breaks down. A striking change in the squirt flow and shear relaxation mechanism is apparent however. For surface conditions, the contribution due to these mechanisms is readily seen from Figure 5-52. Here,  $Q^{-1}$  for both P and S waves is shown for the squirting and shear relaxation mechanisms only. Two peaks are evident, the lower frequency one corresponding to the flow mechanism and the other to viscous relaxation. The shape of the relaxation peaks are complicated, reflecting the spectrum of pore and crack shapes. The transition from flow to viscous relaxation takes place at about 50 KHz, below which

$Q_p^{-1} > Q_s^{-1}$  and above which  $Q_s^{-1} > Q_p^{-1}$ . Even though viscous relaxation peaks at  $f = 10^9$  Hz, it is clear from Figures 5-51 and 5-52 that the contribution of these mechanisms to the attenuation in the Berea Sandstone is small in the frequency band of interest, even at surface pressure. Furthermore, the effect of pressure, as seen in Figure 5-51b is to close cracks contributing to both the squirt flow and viscous relaxation, thus lowering even further, their associated attenuations.

Scattering off inclusions produces a negligible effect except at very high frequencies where this mechanism clearly dominates. A larger scatterer radius will shift this curve to lower frequencies. Thus for the tuffs, scattering dominates. The radius assumed for the Berea is  $5 \times 10^{-3}$  cm, based on direct observation of pore sizes. This represents the upper bound since not all the porosity is contained in such large pores.

Finally, the combination of both the frequency and pressure behavior of attenuation in the saturated Berea Sandstone model is shown in Figure 5-53 where the total  $Q_p$  of the rock is plotted. For low pressures,  $Q_p$  remains essentially unchanged as a function of frequency, reflecting the importance of the friction mechanism.  $Q_p$  increases with pressure and at high pressures and low frequencies ( $< 10^4$  Hz)  $Q_p$  is greater than 100.  $Q_p$  decreases with increasing frequency at higher

pressures due to the increasing contribution of Biot flow. Finally, at very high frequencies ( $10^7$  Hz),  $Q_p$  decreases sharply because of scattering.

Considering the effects of partial saturation on the model, one is concerned with the changes (or lack of changes) observed for high water (low gas or air) saturations. If the results shown in Figure 5-18 indicate a decrease in  $Q_p$  only, relative to the fully saturated state, then we are looking for a mechanism that results in bulk rather than shear loss. It has been suggested that Biot type fluid flow may cause high attenuation for partially saturated rocks (White, 1975). However, if the gas or air pockets are distributed on a microscopic scale in small pores, then the model, using relative permeability (section 3.3, equation 3-26) predicts just the opposite. The attenuation coefficients as functions of frequency for Biot flow are shown in Figure 5-54 for the fully saturated case and 90% saturation for P and S waves. The presence of gas in the pores restricts flow generated by pressure gradients (bulk flow) and the attenuation is decreased substantially. Viscous drag is relatively unaffected by small quantities of gas and the shear attenuation remains about the same.

In Chapter 3 a mechanism involving gas bubble resonance was proposed that could explain the behavior

(if it is indeed real) observed in Figure 5-18. Recall that high attenuation may be realized if gas bubble resonance properties are determined only by the surrounding water medium. If the bubble is surrounded by the effective rock properties, resonance frequencies are shifted higher and the attenuation reduced.

The equations outlined in section 3.4 are applied to the Berea model and the attenuation coefficient is plotted as a function of frequency for 5% gas saturation with 50 micron radius bubbles immersed in both water and the effective rock medium. The gas is assumed to be methane and its properties are calculated at a pressure of 100 bars and 20°C using a form of the Beattie-Bridgeman equation of state for non-ideal gases.

One can see that high bulk attenuation may occur for ultrasonic frequencies if one is willing to assume that the bubbles see only the surrounding water. Attenuation is decreased substantially and the resonance frequency increased for bubbles in the rock. However, the case shown here is for the maximum bubble radius permissible in the Berea sandstone - limited by the average pore size. Thus the curve labeled "water" is unrealistic. Smaller bubbles would result in lower attenuation and higher resonance frequencies making bulk attenuation at any frequency of interest difficult to obtain.

While the results shown in Figure 5-55 are not strictly a modeling of the data in Figure 5-18, it is possible to stretch one's imagination a little and suppose that the apparent decrease in  $Q_p$  for low gas saturations is due to bubble resonances. At least the frequency of the maximum effect is of the right order of magnitude. If this were true, then one could infer from the data that the gas bubble resonant properties are determined by the effective rock medium at gas saturations greater than 5%. Thus, any changes in bulk attenuation would be seen only for very low gas saturations in the best of cases.

#### 5.2b Comments On The Other Samples

1. Navajo sandstone: The Navajo behaves in all respects, similarly to the Berea. The faster increase in  $Q$  with pressure is due to a shift in the crack aspect ratio spectrum to lower ratios relative to the Berea. The small differences in the saturated runs may be due to a lower clay content in the Navajo. Thus, the effect of water on the friction mechanism is less.

2. Bedford limestone: The relatively higher  $Q$ , especially at low pressures is certainly due to the far lower crack density compared to the sandstones although these cracks are of lower aspect ratio (see the static measurements, Figures 4-14 to 4-16). Since the



permeability of the Bedford is also lower than the sandstones, there is less of a difference between the saturated and dry runs at high pressures because the effect of fluid flow is minimal. What fluid flow effect there is, is larger for the S waves and thus as permeability is further decreased during pore collapse, the change in  $Q_s$  is larger than for  $Q_p$ . Upon unloading, the change in  $Q_p$  is larger than  $Q_s$ . This may be explained by the friction mechanism with fewer cracks contributing to the attenuation for S waves.

3. Shales: The shales, in general, are characterized by their lack of fine cracks. Thus the changes in  $Q$  with pressure are small. None of the mechanisms as formalized in Chapter 3 can explain the attenuation in shales, particularly the peculiar anisotropic behavior of the oil shale. However, relative motion within the rock due to moduli differences between the kerogen and shale may contribute to attenuation. Munson and Young (1977) observed that the propagation of high amplitude stress pulses show characteristics of rate effects and dispersion suggesting that oil shale responds as a mechanical mixture of rock and kerogen. One may model the oil shale schematically as illustrated in Figure 5-56 with shale being the continuous component. Such a model easily explains the

observed velocity anisotropy. Waves propagating normal to the bedding planes average the moduli of the soft kerogen and stiff shale. Those propagating parallel are affected primarily by the stiff shale - close to simple Voigt-Reuss bounds.

If one assumes that attenuation in oil shale is due to relative shear motion between the shale and kerogen then it is clear that a P wave propagating in a direction perpendicular to the bedding planes will suffer the least loss. S waves propagating in the same direction with the plane of polarization parallel to the bedding will tend to shear the bedding planes and suffer the greatest attenuation. Both P and S waves traveling parallel to the bedding induce relative deformation. Thus their  $Q$ 's are lower than the perpendicular P wave. Since the S wave is circularly polarized, the relative slip induced is of lower magnitude than if the wave were propagating normal to the bedding. This is also shown in Figure 5-56 where the small arrows are proportional to the induced displacement.  $Q_s$  for parallel propagation is then higher than for the perpendicular direction. This model may possibly be extended to other types of shales by assuming a mechanical mixture of a rigid component ("rock") and clay. Thus, clay plays the role of kerogen.

This hypothesis is based on a single sample and requires further testing, especially since the properties of oil shales are extremely variable spatially. The degree and nature of velocity and  $Q$  anisotropy though, should depend critically on the kerogen content. Munson and Young (1977) point out that "the variation of kerogen contents in natural oil shales span a range which should cover the transition between a continuous kerogen and a continuous shale constituent. Potentially, such a system when studied in detail could exhibit all extremes of relaxation (attenuation) behavior of mixtures".

4. Tuffs: Both tuffs studied in this thesis have attenuations at ultrasonic frequencies dominated by scattering. The effects of friction are masked. However, in the case of the Tunnel Beds tuff, the effect of pore collapse is observed to be very similar to the Bedford limestone.

Table 5.1. Scattering in Tuffs

	300 bars				2000 bars			
	$V_P$	$V_S$	$Q_P$	$Q_S$	$V_P$	$V_S$	$Q_P$	$Q_S$
Ammonia Tanks								
$\phi = 5.8\%$								
$K = .281 \text{ Mb}$	4.00	2.30	19.0	22.6	4.56	2.65	29.0	34.0
$\mu = .166 \text{ Mb}$								
$\rho = 2.456 \text{ g/cm}^3$								
Tunnel Beds								
$\phi = 30\% \text{ (10\% used)}$								
$K = .123 \text{ Mb}$	3.00	1.87	7.9	10.5	3.30	2.08	10.0	13.0
$\mu = .077 \text{ Mb}$								
$\rho = 2.296 \text{ g/cm}^3$								

---

$K' = \rho' = 0$  (air inclusions)

$f = 0.4 \text{ MHz}$

$r = 1 \text{ mm}$

Table 5.2

## Physical Properties Used for Modeling the Berea Sandstone

Matrix:	$K = 35 \times 10^{10}$ dynes/cm <sup>2</sup>
	$\mu = 25 \times 10^{10}$ dynes/cm <sup>2</sup>
	$\rho = 2.61$ g/cm <sup>3</sup>
Inclusion:	$K' = 2.6 \times 10^{10}$ dynes/cm <sup>2</sup>
	$\eta = 4 \times 10^{-2}$ poise
	$\rho' = 1.0$ g/cm <sup>3</sup>
Frame:	$\phi \sim 0.16$
	$\chi = 75$ md

Fluid Flow Structure Constants:  $a = 1.0 \times 10^{-4}$ ,  $a' = 3.0$

Table 5.3

## Aspect Ratio Distributions

	Concentration, $c$	Aspect ratio, $\alpha$
Surface	0.12	1.00
	0.04	0.10
	$0.10 \times 10^{-3}$	$0.17 \times 10^{-2}$
	$0.10 \times 10^{-3}$	$0.14 \times 10^{-2}$
	$0.20 \times 10^{-3}$	$0.10 \times 10^{-2}$
	$0.15 \times 10^{-3}$	$0.60 \times 10^{-3}$
	$0.75 \times 10^{-4}$	$0.30 \times 10^{-3}$
	$0.30 \times 10^{-4}$	$0.10 \times 10^{-3}$
	$0.90 \times 10^{-5}$	$0.30 \times 10^{-4}$
	$0.30 \times 10^{-5}$	$0.10 \times 10^{-4}$
3 km	0.119	1.00
	0.395	$0.98 \times 10^{-1}$
	$0.152 \times 10^{-1}$	$0.258 \times 10^{-3}$

## FIGURE CAPTIONS

Figure 5-1. Compressional (P) and shear (S) wave velocities for the dry (open symbols) and water saturated (solid symbols) Berea sandstone as a function of differential pressure. As with the following plots of velocity, the errors, except for the lowest pressures, are within the size of the symbols and thus no error bars are drawn. These velocities are used for the Q calculations.

Figure 5-2. Attenuation characteristics of P waves in the dry Berea sandstone at two confining pressures,  $P_c = 45$  and  $500$  bars ( $P_f = 0$ ). Left: Pulse shapes in the sandstone. Middle: Normalized Fourier amplitude as a function of frequency for the rock (solid line) and aluminium standard (dashed line). Right: Natural logarithm of the aluminum (A1) to rock (A2) amplitude ratios as a function of frequency. Points are actual ratios and the dashed line is the linear fit to the data. The slope of this line is proportional to  $1/Q$ .

Figure 5-3. Attenuation characteristics of S waves in the dry Berea sandstone. See figure 5-2 for explanations.

Figure 5-4. Q values of P and S waves as a function of confining pressure in the dry Berea sandstone ( $P_f=0$ ). In this and later plots of Q, representative error bars are shown.

Figure 5-5. Attenuation characteristics of P waves in the saturated Berea sandstone for two differential pressures,  $P_d = 105$  and  $400$  bars ( $P_f = 0.465 P_c$ ). See figure 5-2 for explanations.

Figure 5-6. Attenuation characteristics of S waves in the saturated Berea sandstone.

Figure 5-7. Q values of P and S waves as a function of differential pressure in the saturated Berea sandstone ( $P_f = 0.465 P_c$ ).

Figure 5-8. Q values of P and S waves as a function of confining pressure in the dry Berea sandstone ( $P_f=0$ ). The data was obtained at the Chevron Oil Field Research Co. (COFRC).

Figure 5-9. Q values of P and S waves as a function of differential pressure in methane saturated Berea sandstone ( $P_f = 0.465 P_c$ ). Data obtained at COFRC.

Figure 5-10. Q values of P and S waves as a function of differential pressure in 67,190 ppm NaCl brine saturated Berea sandstone ( $P_f = 0.465 P_c$ ). Data obtained at COFRC.



Figure 5-11. Q values of P and S waves as a function of differential pressure in 161,335 ppm NaCl brine saturated Berea sandstone ( $P_c = 15000$  psi  $\approx 1000$  bars).

Figure 5-12. P and S wave velocities as a function of confining pressure in 37% water saturated Berea sandstone ( $P_f = 0$ ).

Figure 5-13. Attenuation characteristics of P waves in the partially saturated Berea sandstone for two confining pressures,  $P_c = 105$  and 400 bars ( $P_f = 0$ ). See Figure 5-2 for explanations.

Figure 5-14. Attenuation characteristics of S waves in the partially saturated Berea sandstone.

Figure 5-15. Q values of P and S waves of a function of confining pressure in the partially saturated Berea sandstone ( $P_f = 0$ ).

Figure 5-16. Block diagram of the pore pressure system used for the gas release experiment.

Figure 5-17. P and S wave velocities as a function of fluid pressure and calculated gas saturation for the gas release experiment in the Berea sandstone. The dashed line represents the theoretically calculated P wave velocity for a fully saturated rock. The differential pressure is 200 bars.

Figure 5-18. Q values of P and S waves as a function of fluid pressure and calculated gas saturation in the Berea sandstone ( $P_d = 200$  bars).

Figure 5-19. P and S wave velocities as a function of differential pressure in the dry and saturated Navajo sandstone.

Figure 5-20. Attenuation characteristics of P waves in the dry Navajo sandstone for two confining pressures,  $P_c = 45$  and 300 bars ( $P_f = 0$ ). See Figure 5-2 for explanations.

Figure 5-21. Attenuation characteristics of S waves in the dry Navajo sandstone.

Figure 5-22. Q values of P and S waves as a function of confining pressure in the dry Navajo sandstone ( $P_f = 0$ ).

Figure 5-23. Attenuation characteristics of P waves in the saturated Navajo sandstone for two differential pressures,  $P_d = 45$  and 300 bars ( $P_f = 0.465 P_c$ ). See Figure 5-2 for explanations.

Figure 5-24. Attenuation characteristics of S waves in the saturated Navajo sandstone.

Figure 5-25. Q values of P and S waves as a function of differential pressure in the saturated Navajo sandstone ( $P_f = 0.465 P_c$ ).

Figure 5-26. P and S wave velocities as a function of differential pressure in the dry and saturated Bedford limestone. The unloading path is denoted by the dashed lines.

Figure 5-27. Attenuation characteristics of P waves in the dry Bedford limestone for two confining pressures,  $P_c = 105$  and  $400$  bars ( $P_f = 0$ ). See Figure 5-2 for explanations.

Figure 5-28. Attenuation characteristics of S waves in the dry Bedford limestone.

Figure 5-29. Q values of P and S waves as a function of confining pressure in the dry Bedford limestone ( $P_f = 0$ ). The unloading path for the P wave is denoted by the dashed line.

Figure 5-30. Attenuation characteristics of P waves in the saturated Bedford limestone for two differential pressures,  $P_d = 105$  and  $500$  bars ( $P_f = 0.465 P_c$ ). See Figure 5-2 for explanations.

Figure 5-31. Attenuation characteristics of S waves in the saturated Bedford limestone.

Figure 5-32. Q values of P and S waves as a function of differential pressure in the saturated Bedford limestone ( $P_f = 0.465 P_c$ ). Unloading paths are denoted by dashed lines.

Figure 5-33. P and S wave velocities as a function of confining pressure in the saturated Esopus shale ( $P_f = 0$ ). The sample was held at 1000 bars for 16 hours resulting in the velocity increase due to pore pressure equilibration. Dashed lines denote unloading paths.

Figure 5-34. Attenuation characteristics of P waves in the saturated Esopus shale for two confining pressures,  $P_c = 105$  and 2000 bars ( $P_f = 0$ ). See Figure 5-2 for explanations,

Figure 5-35. Attenuation characteristics of S waves in the saturated Esopus shale.

Figure 5-36. Q values of P and S waves as a function of confining pressure in the saturated Esopus shale ( $P_f = 0$ ). Dashed lines denote unloading paths.

Figure 5-37. P and S wave velocities as a function of confining pressure in the Colorado oil shale ( $P_f = 0$ ) for the directions perpendicular and parallel to the bedding planes.

Figure 5-38. Attenuation characteristics of P waves in the Colorado oil shale at a confining pressure of 500 bars ( $P_f = 0$ ) for the perpendicular and parallel directions. See Figure 5-2 for explanations.

Figure 5-39. Attenuation characteristics of S waves in the Colorado oil shale.

Figure 5-40. Q values of P and S waves as a function of confining pressure in the Colorado oil shale ( $P_f = 0$ ) for directions perpendicular and parallel to the bedding planes.

Figure 5-41. P and S wave velocities as a function of confining pressure for the dry Ammonia Tanks tuff ( $P_f = 0$ ).

Figure 5-42. Attenuation characteristics of P waves in the dry Ammonia Tanks tuff for two confining pressures,  $P_c = 105$  and  $1000$  bars ( $P_f = 0$ ). See Figure 5-2 for explanations.

Figure 5-43. Attenuation characteristics of S waves in the dry Ammonia Tanks tuff.

Figure 5-44. Q values of P and S waves as a function of confining pressure in the dry Ammonia Tanks tuff ( $P_f = 0$ ).

Figure 5-45. P and S wave velocities as a function of confining pressure in the dry Tunnel Beds tuff ( $P_f = 0$ ). Dashed lines denote unloading paths.

Figure 5-46. Logarithm of the spectral ratio for the P wave in the Tunnel Beds tuff at 210 bars showing the effect of scattering.

Figure 5-47. Attenuation characteristics of P and S waves in the dry Tunnel Beds tuff at a confining pressure of 210 bars ( $P_f = 0$ ). See Figure 5-2 for explanations.

Figure 5-48. Q values of P and S waves as a function of confining pressure in the dry Tunnel Beds tuff ( $P_f = 0$ ). Dashed lines denote unloading paths.

Figure 5-49. Fit of the attenuation model to the dry and brine saturated Berea sandstone data shown in Figures 5-8 and 5-10.

Figure 5-50. Relative contributions of the friction and Biot fluid flow mechanisms for P waves from the model of Figure 5-49 as a function of differential pressure.

Figure 5-51. a) P wave attenuation coefficients at surface pressure as a function of frequency, for several mechanisms considered in the saturated Berea sandstone model. Model parameters are listed in Tables 5.2 and 5.3 and the text. The viscous shear relaxation mechanism is included on the line labeled "squirt" flow.

b) P wave attenuation coefficient as a function of frequency for the saturated Berea model as in Figure 5-51a. Here, the contributions for each mechanism are calculated at a differential pressure equivalent to about a 3 km depth. The crack aspect ratio distribution used is listed in Table 5.3.

Figure 5-52.  $Q_p^{-1}$  and  $Q_s^{-1}$  for the "squirt" flow and viscous shear relaxation mechanisms in the saturated Berea sandstone model at surface pressure as functions of frequency.

Figure 5-53. Total  $Q_p$  for the saturated Berea model as a function of frequency and differential pressure based on the results presented in Figures 5-49 and 5-51.

Figure 5-54. P and S wave attenuation coefficients at surface pressure as a function of frequency for the Biot fluid flow model. The solid lines are for a fully saturated rock while the dashed lines represent a rock with 10% gas saturation (90% water).

Figure 5-55. P wave attenuation coefficient as a function of frequency for losses due to gas bubble resonance shown for bubbles of 50 micron radius immersed in both water and the effective rock medium of the Berea model. 5% gas saturation is assumed.

Figure 5-56. Schematic illustration of the oil shale model. Large arrows show the directions of wave propagation used in the experiments. Small arrows denote the amount of relative deformation due to incident parallel S waves.



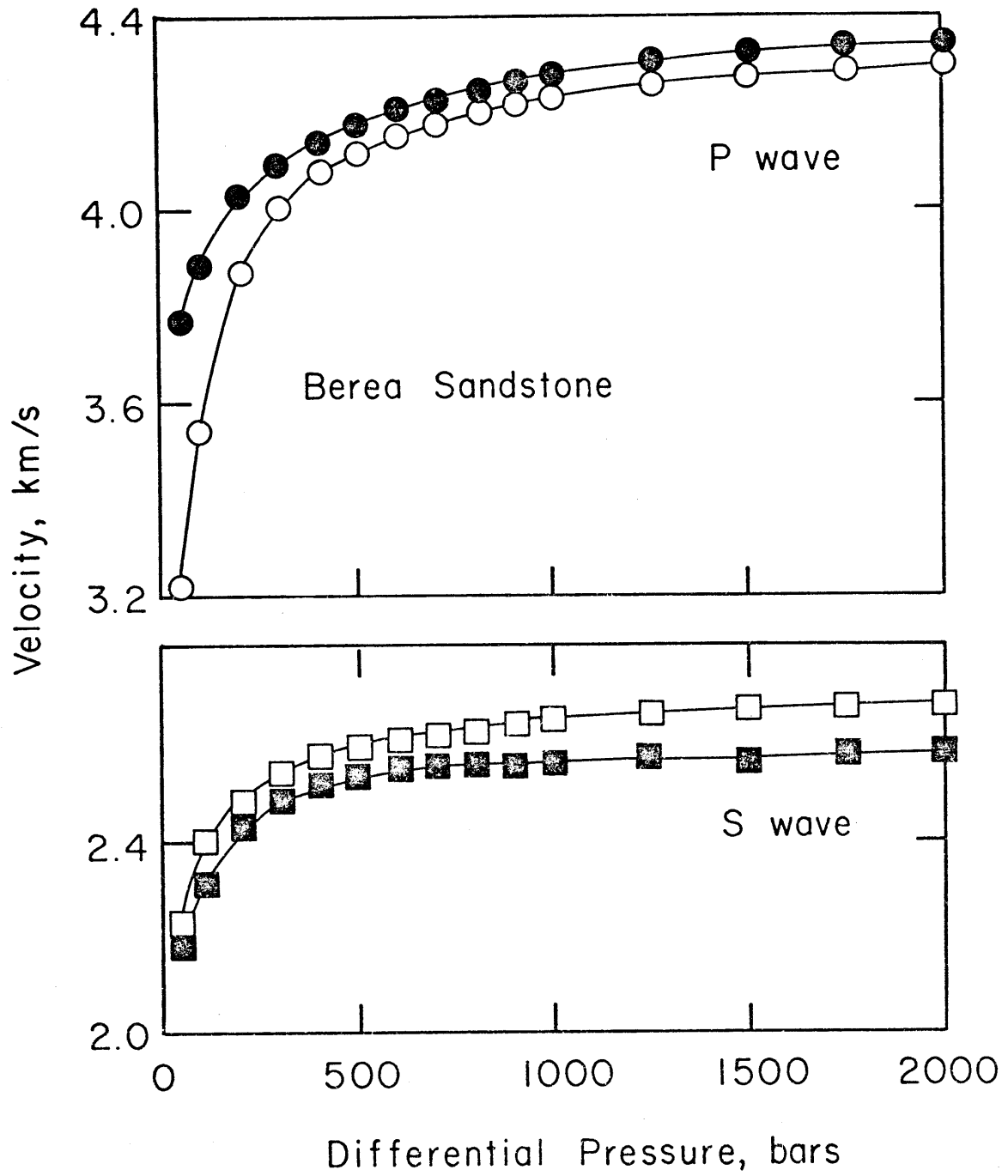


Figure 5-1

# Dry Berea Sandstone - P wave

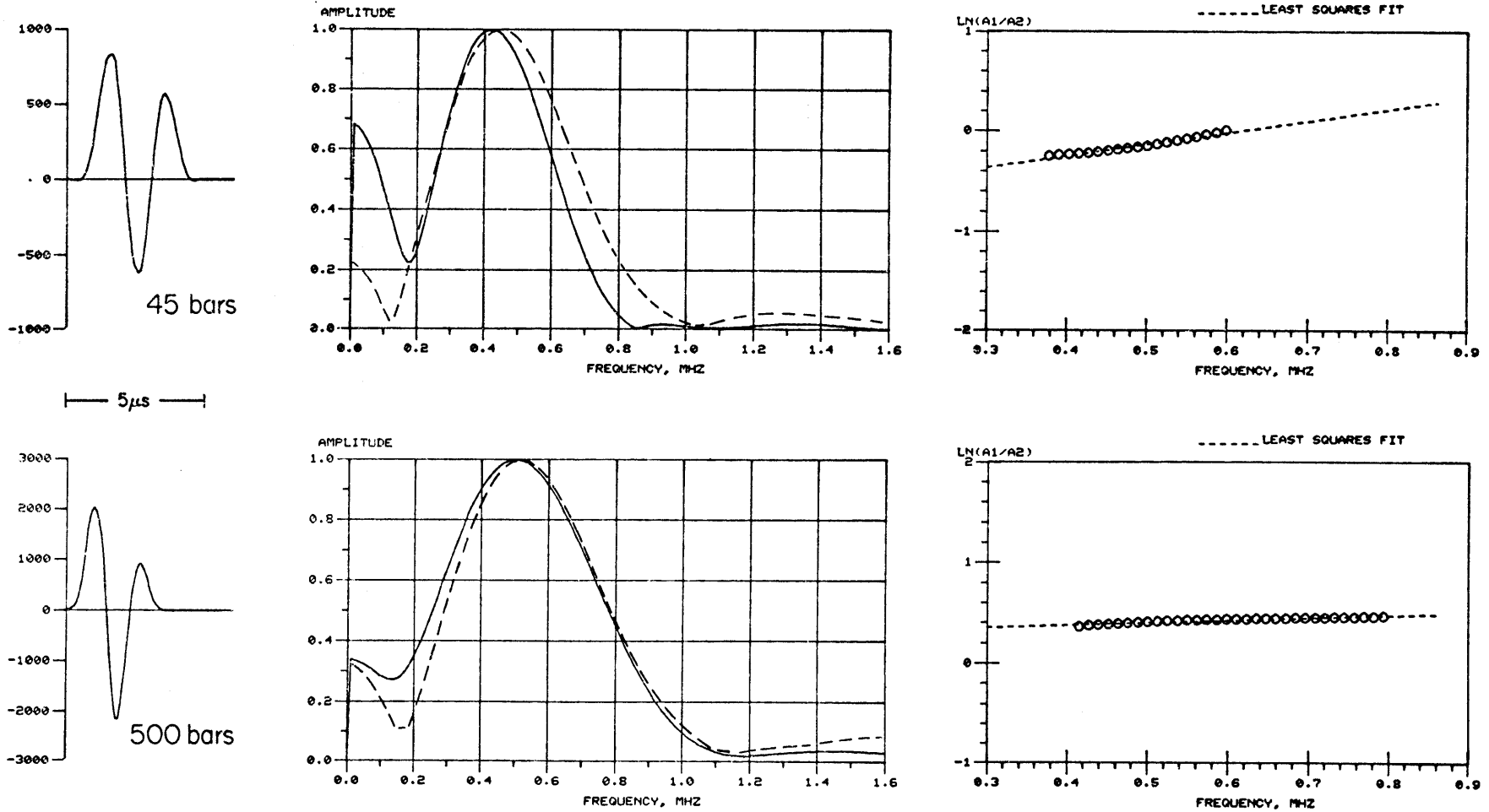


Figure 5-2

# Dry Berea Sandstone - S wave

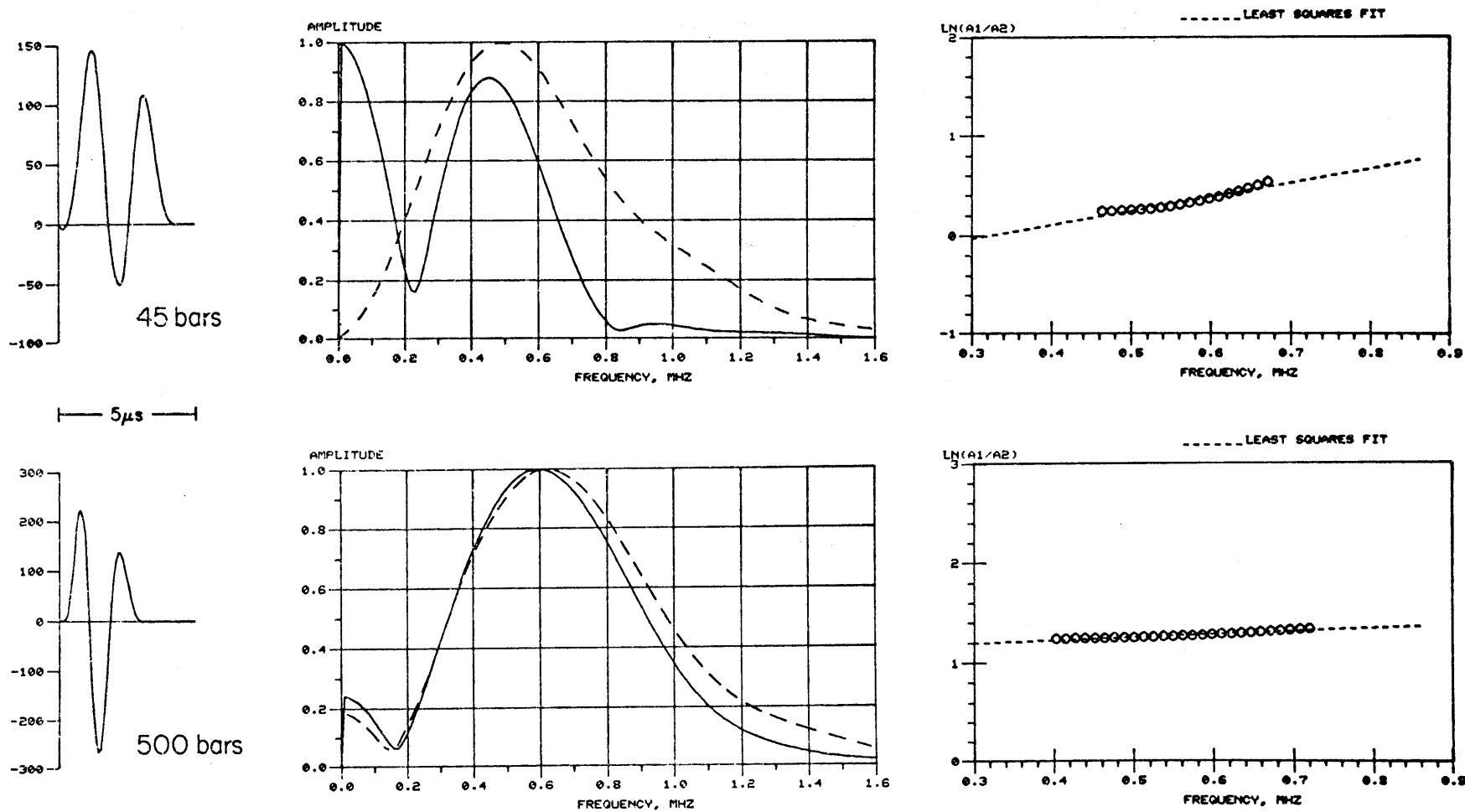


Figure 5-3

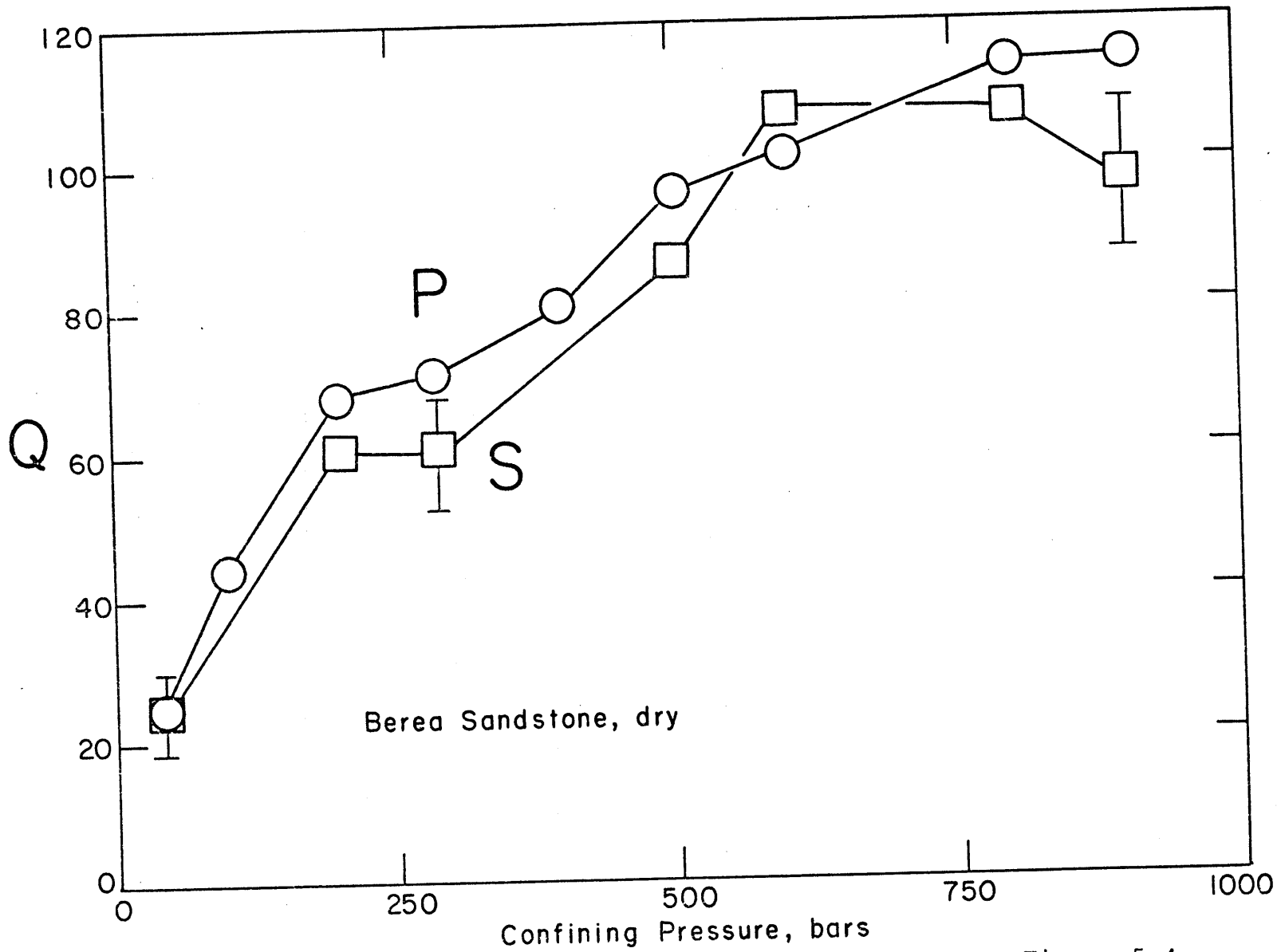


Figure 5-4

# Saturated Berea Sandstone - P wave

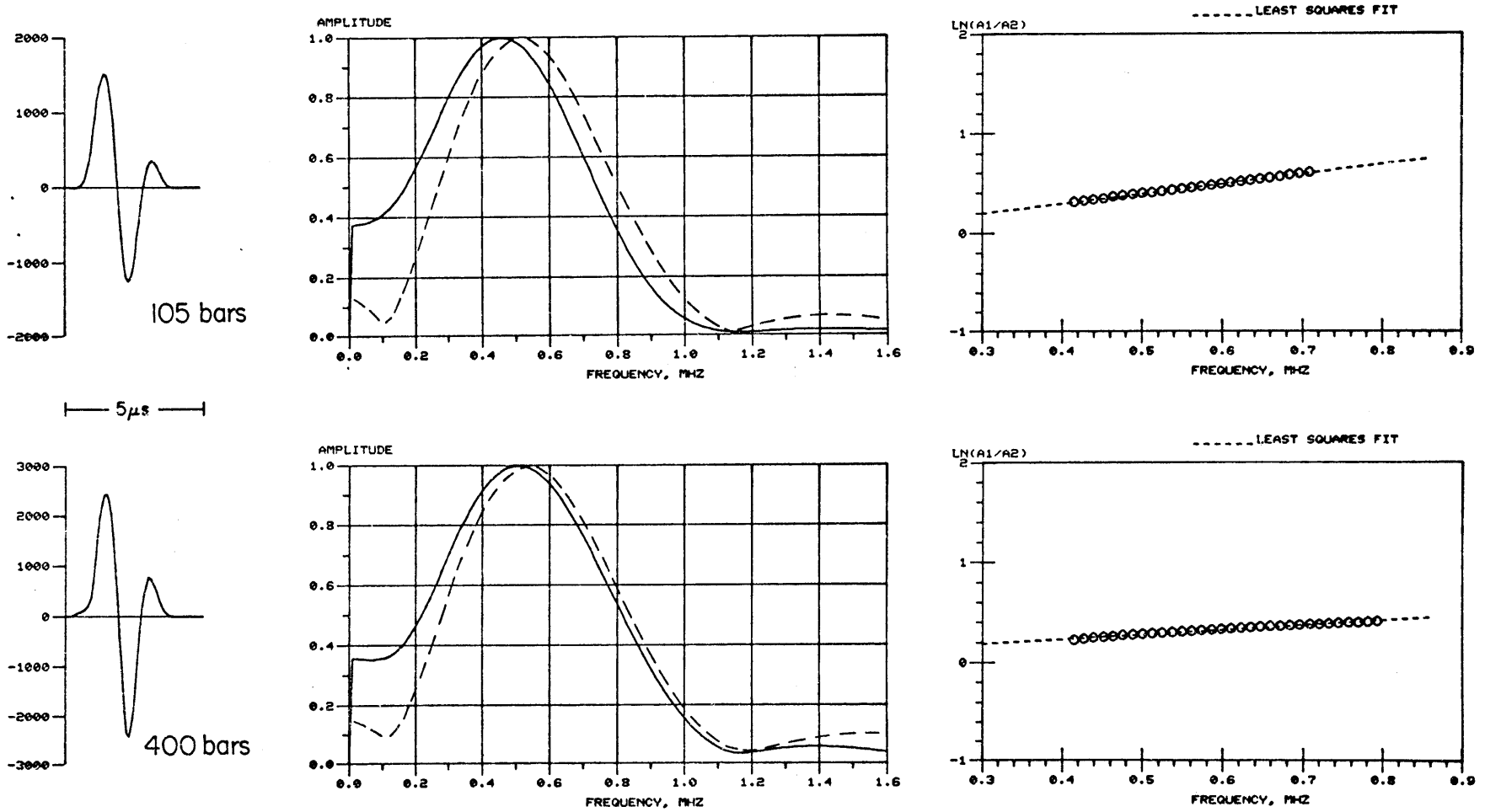


Figure 5-5

### Saturated Berea Sandstone - S wave

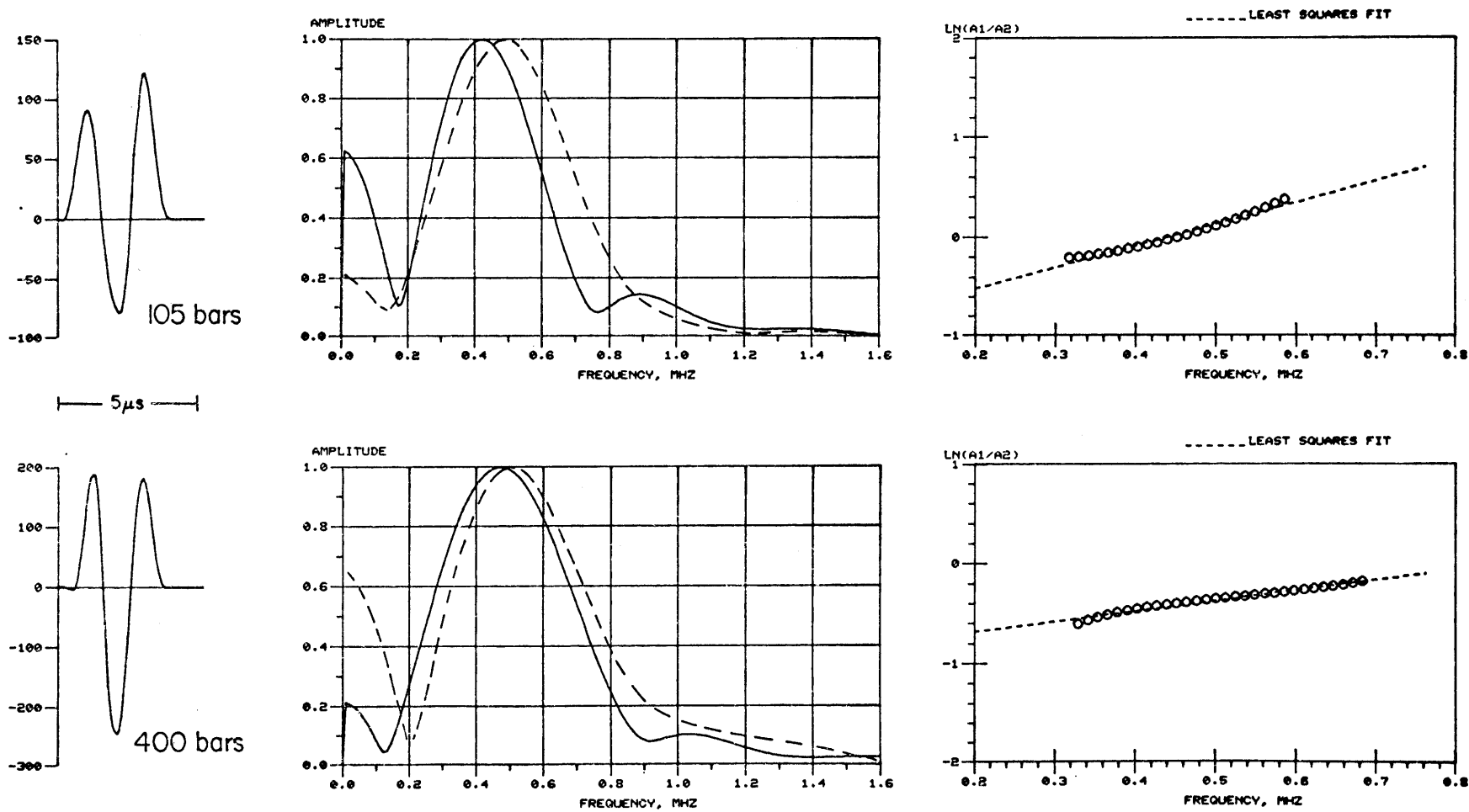


Figure 5-6

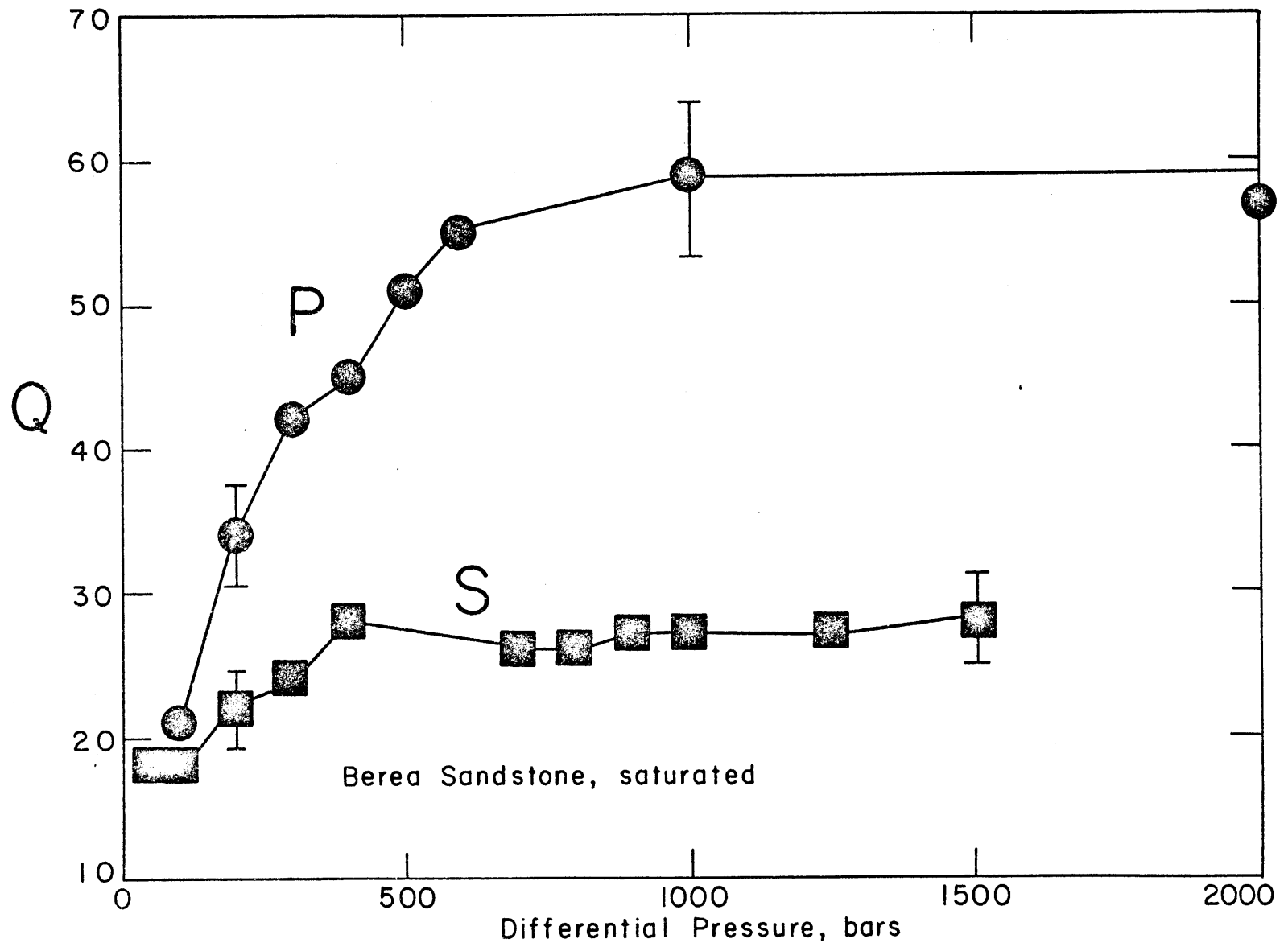


Figure 5-7

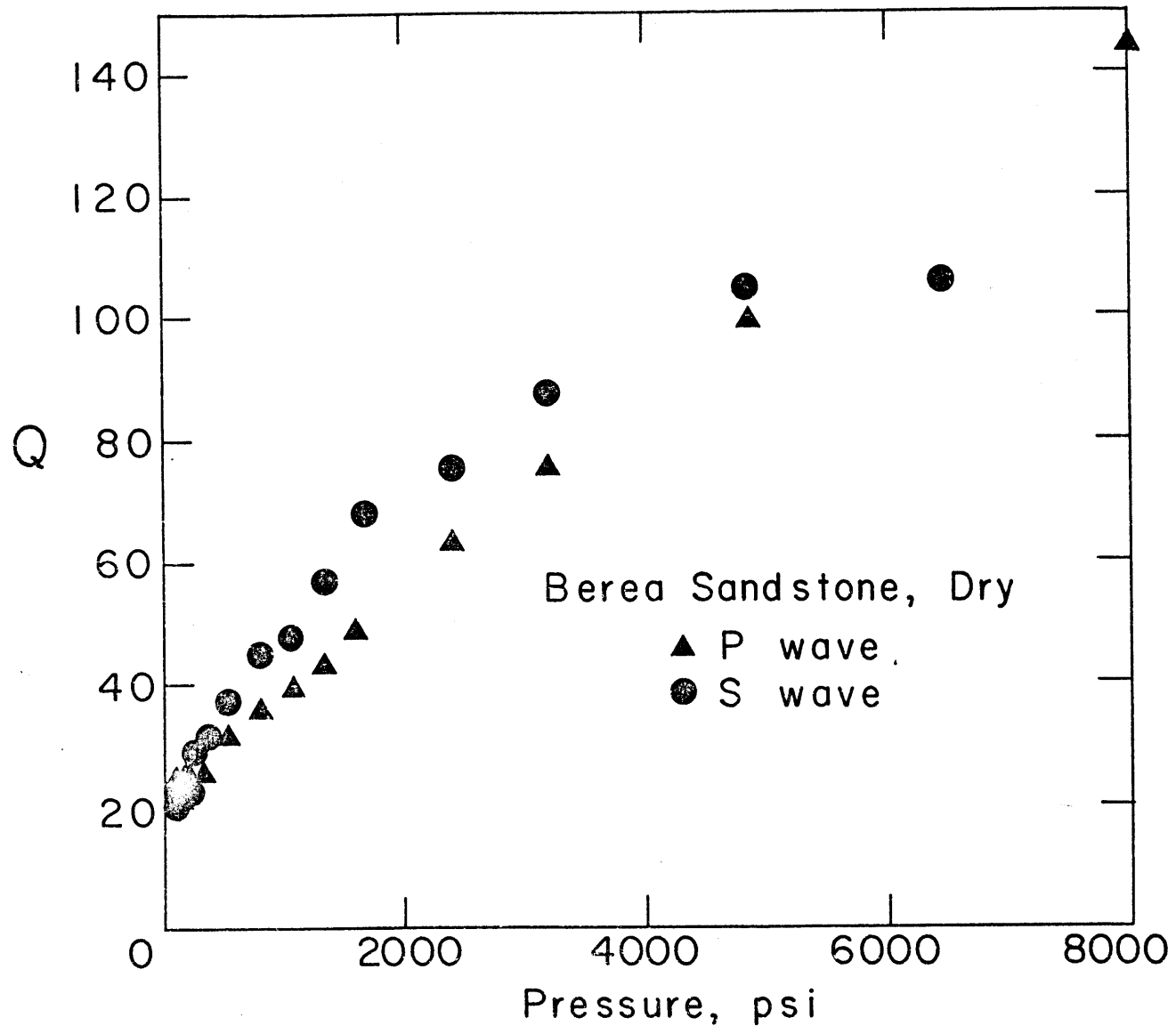


Figure 5-8



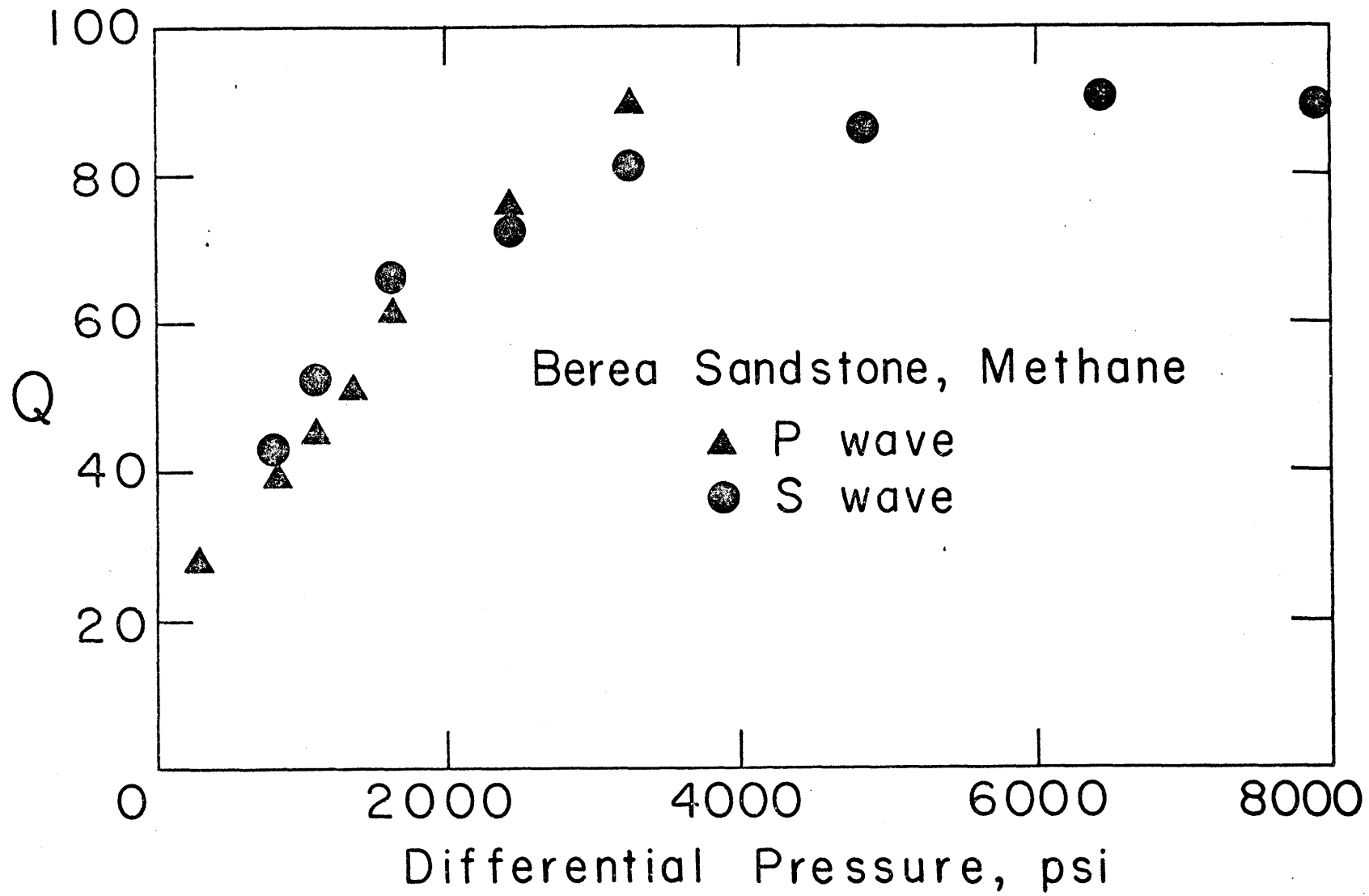


Figure 5-9

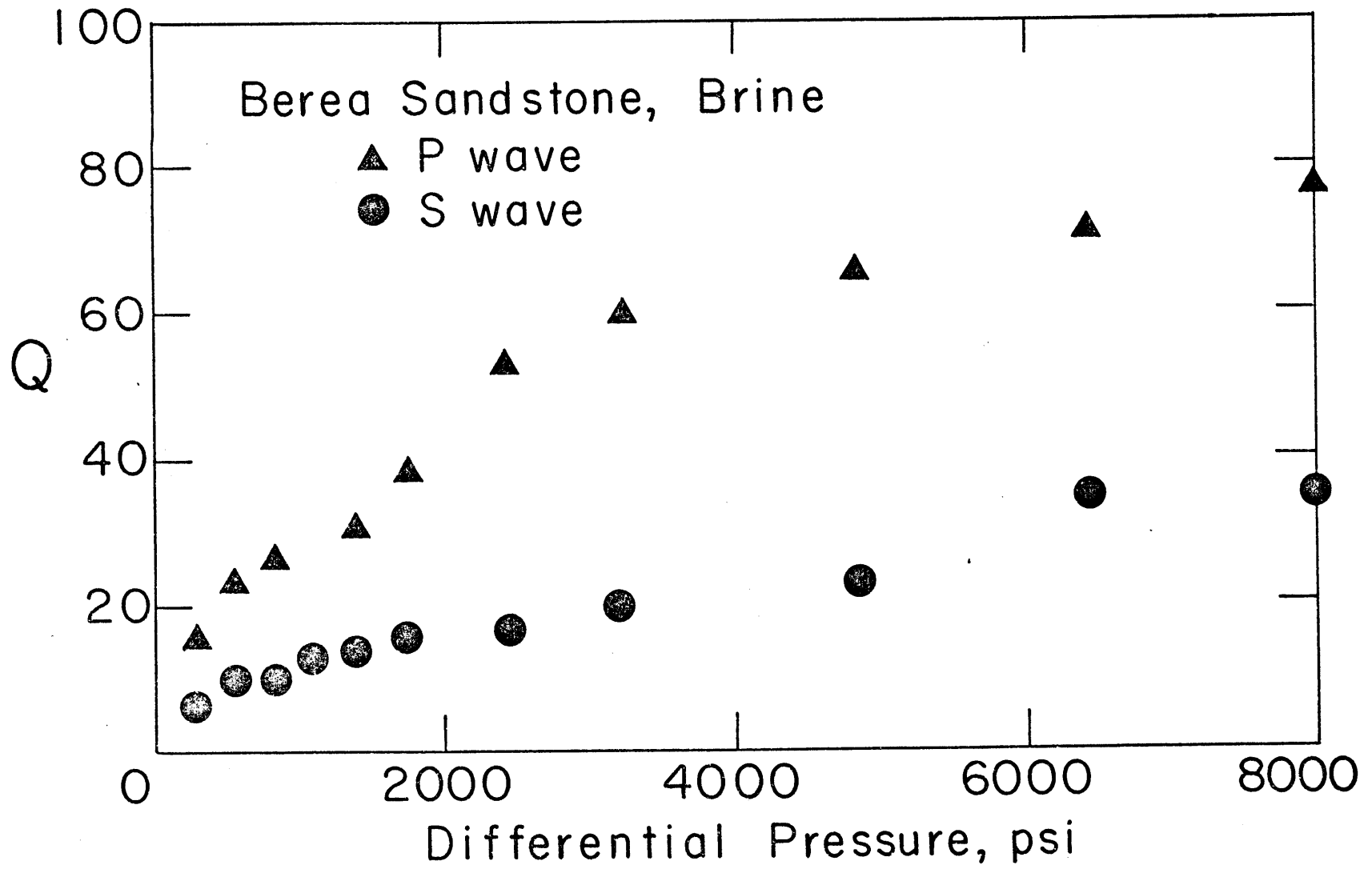


Figure 5-10

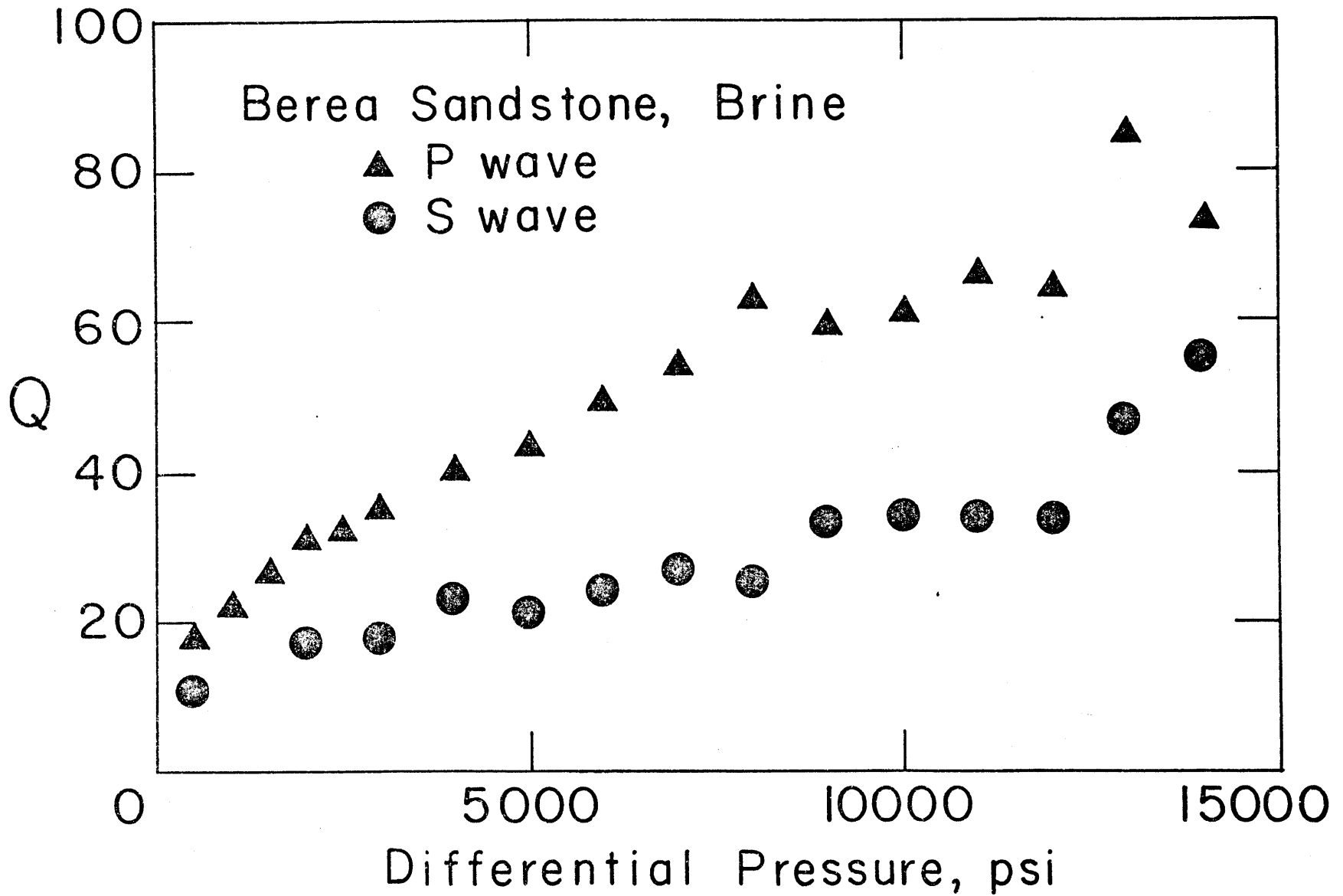


Figure 5-11

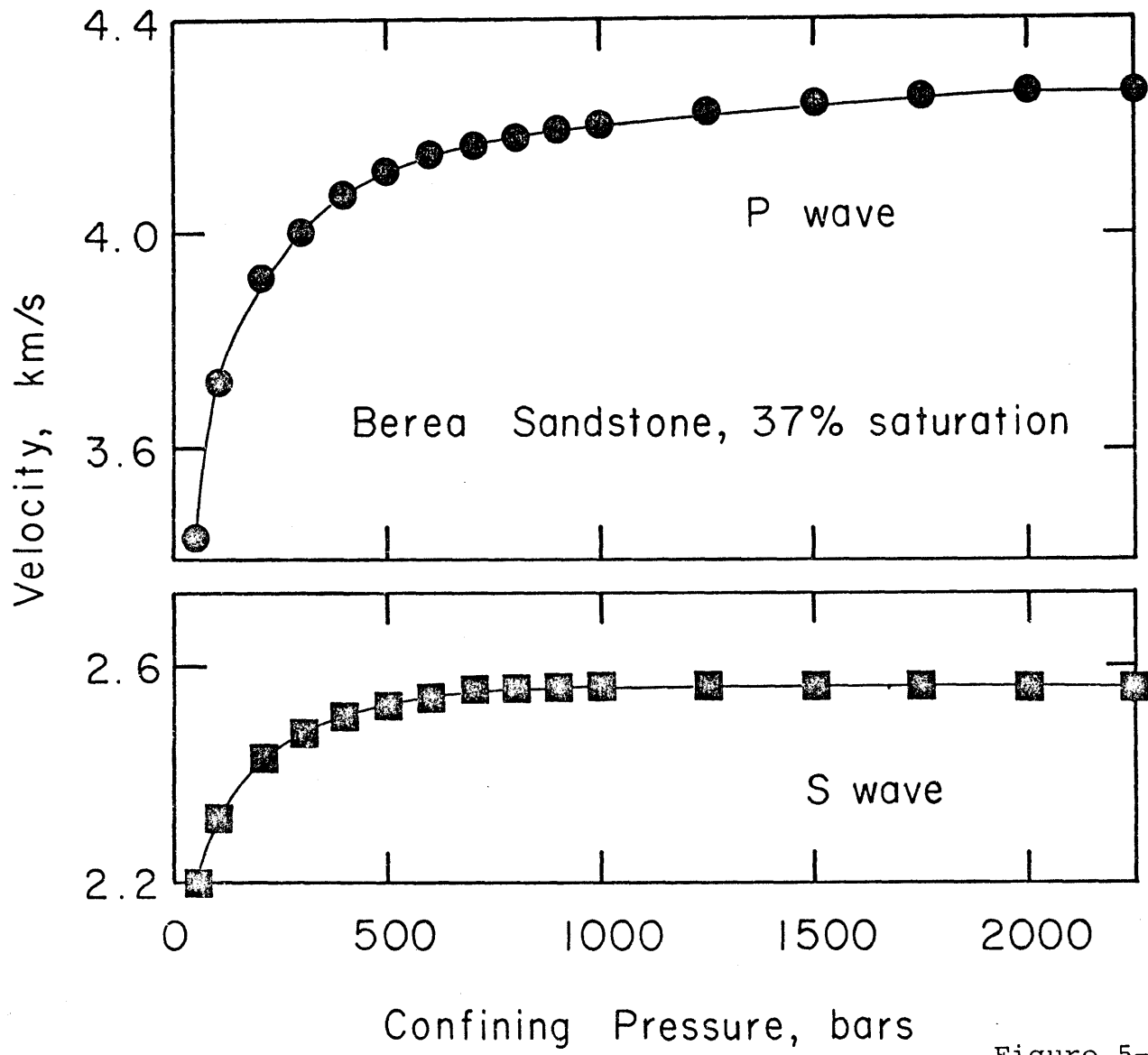


Figure 5-12

# Partially Saturated Berea Sandstone - P wave

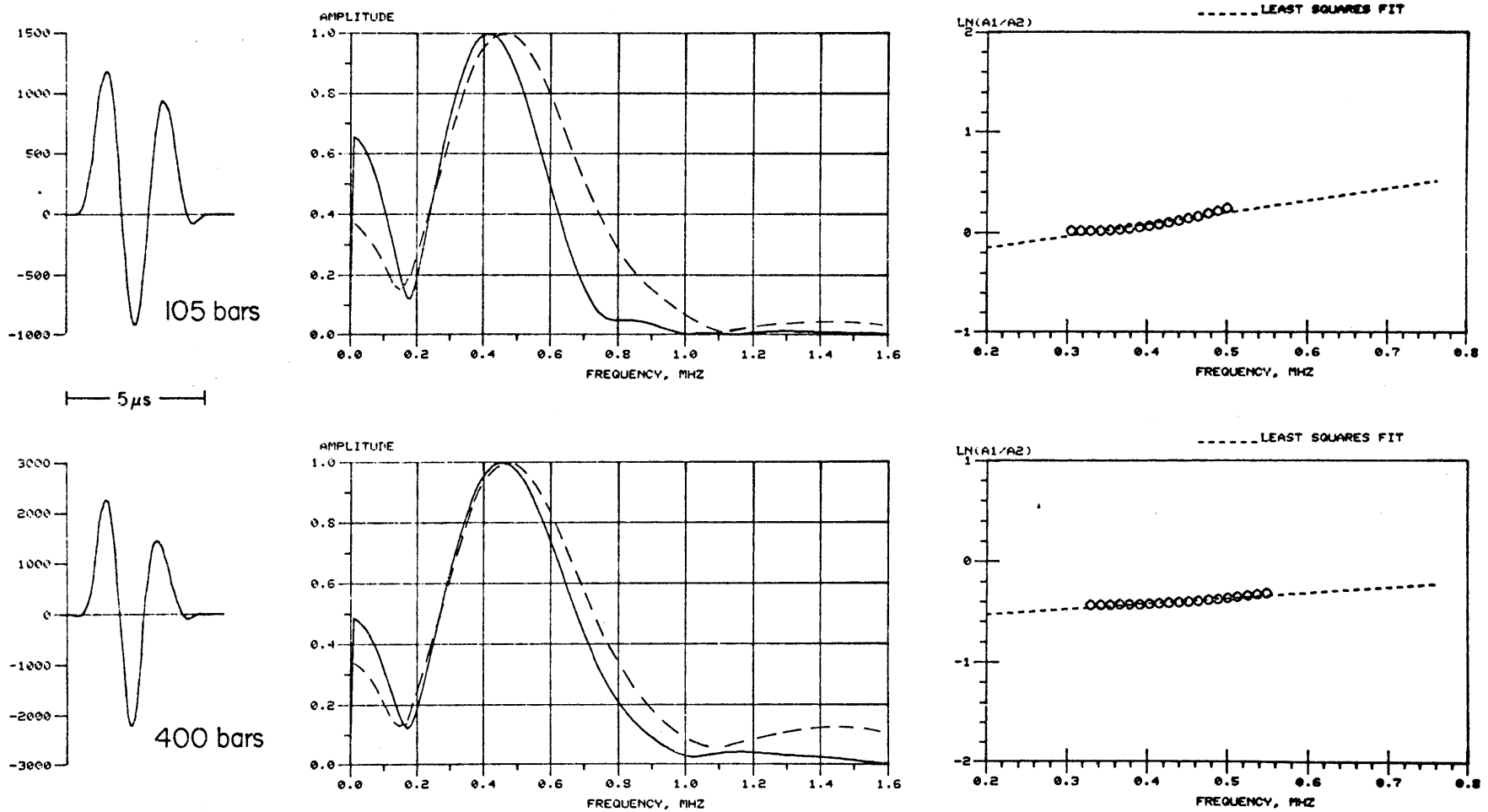


Figure 5-13

# Partially Saturated Berea Sandstone - S wave

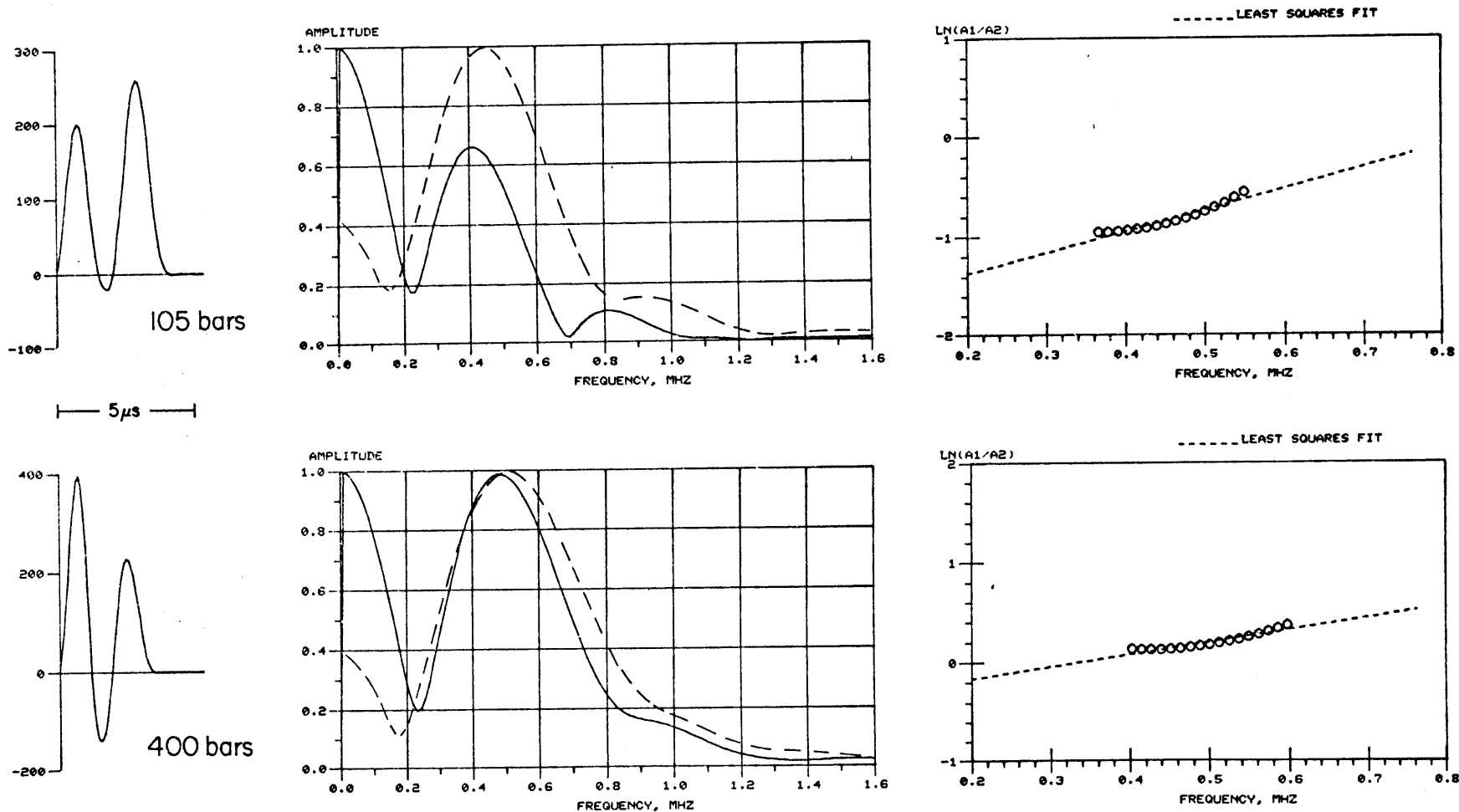


Figure 5-14

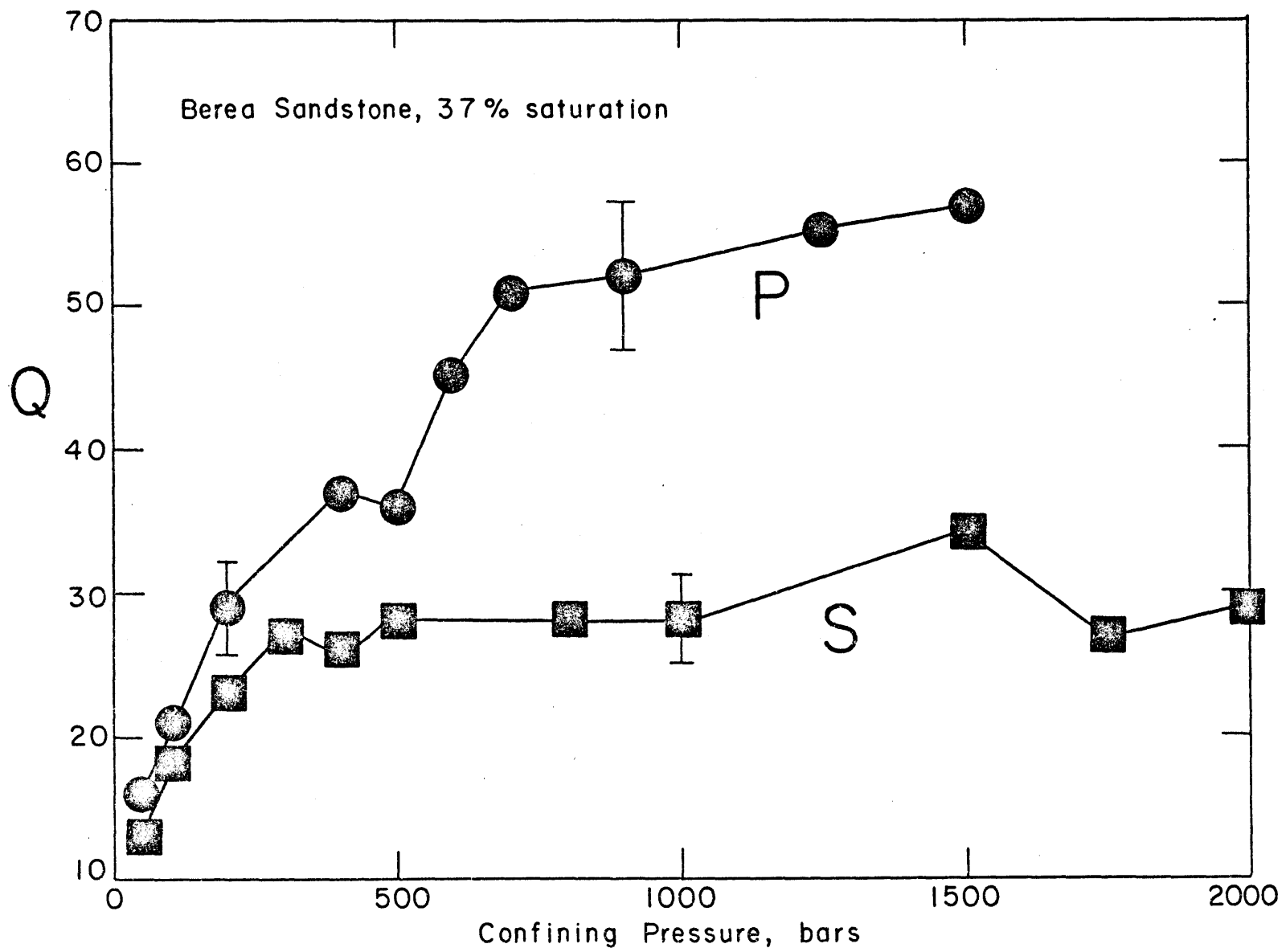


Figure 5-15

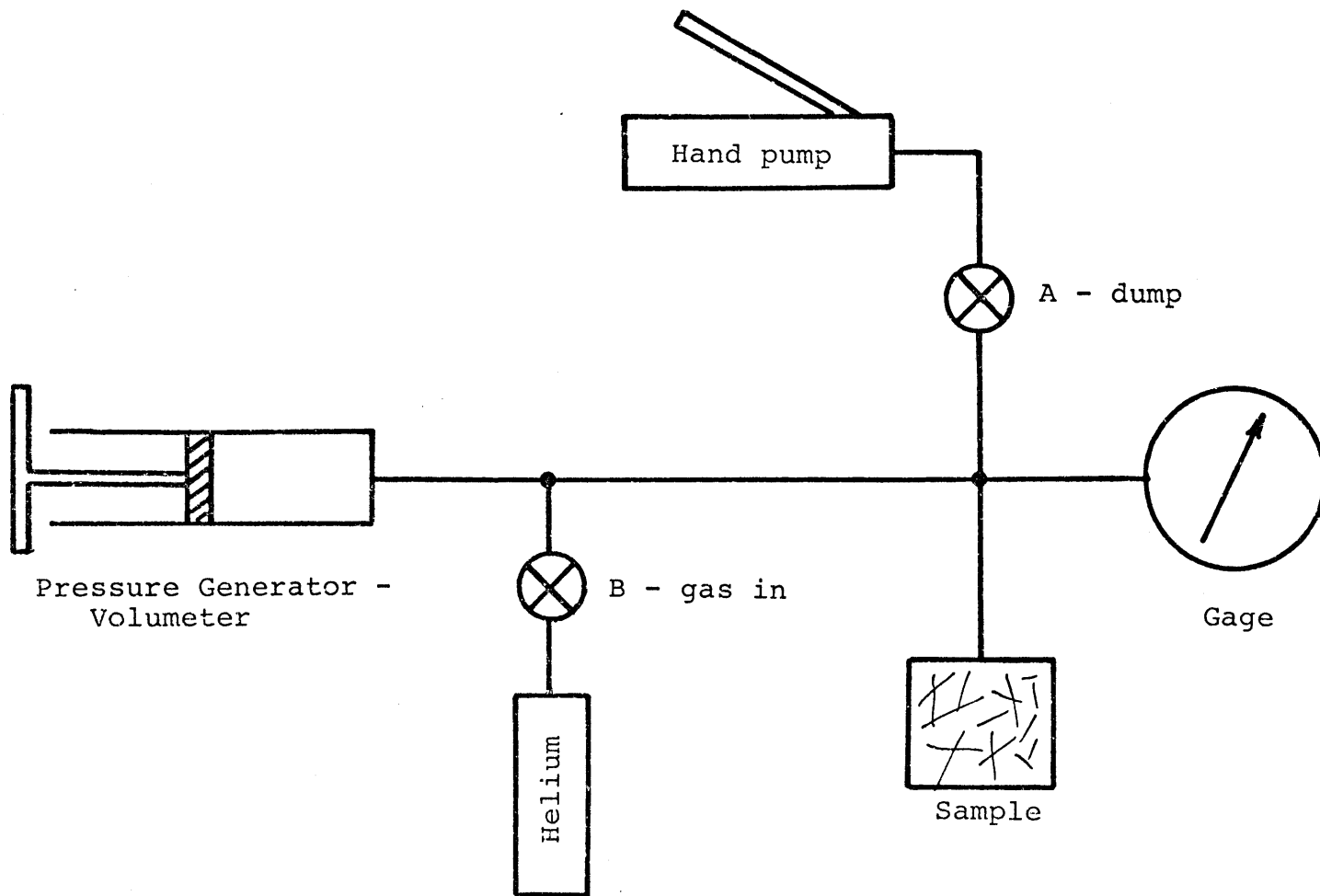


Figure 5-16



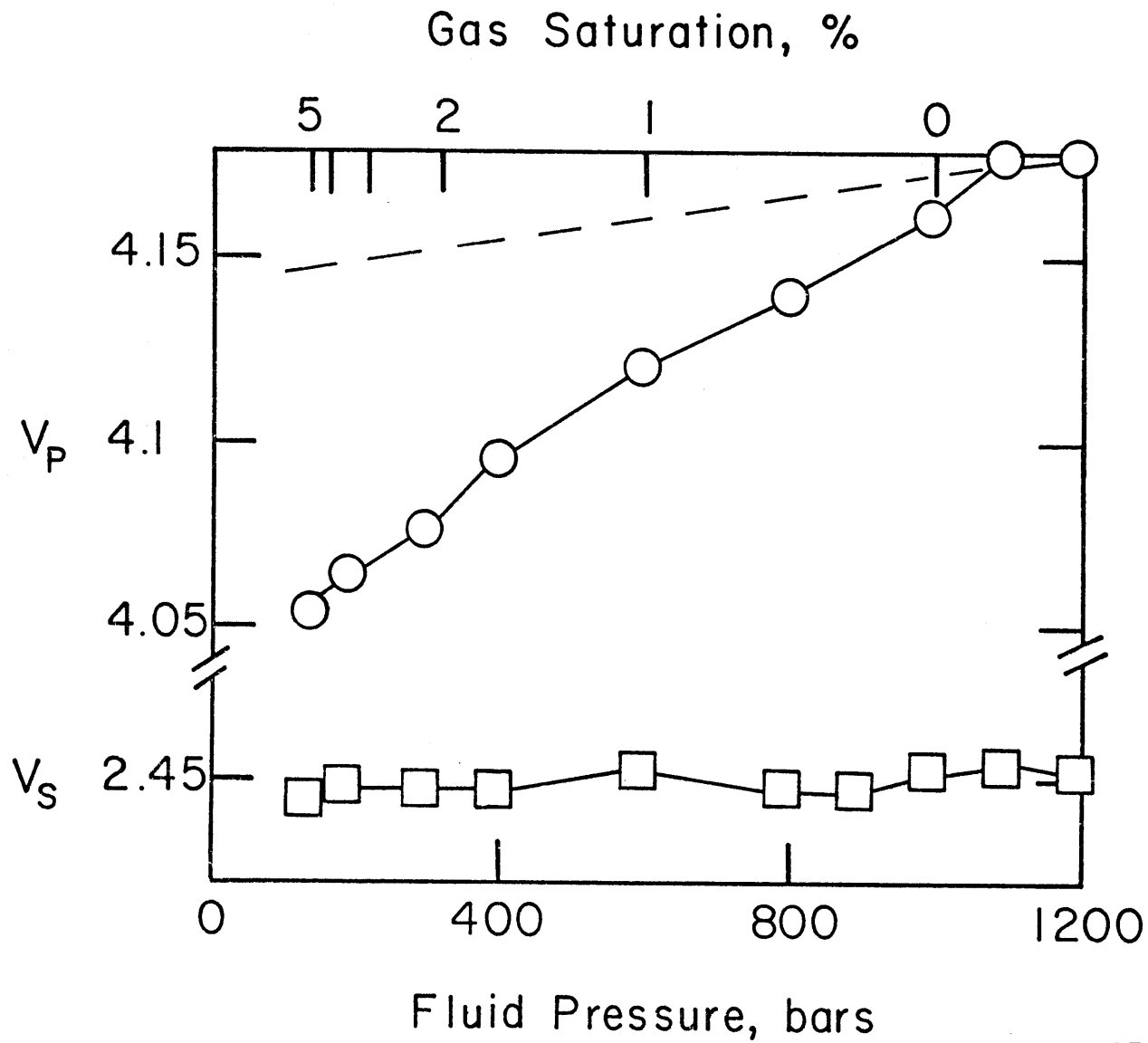


Figure 5-17

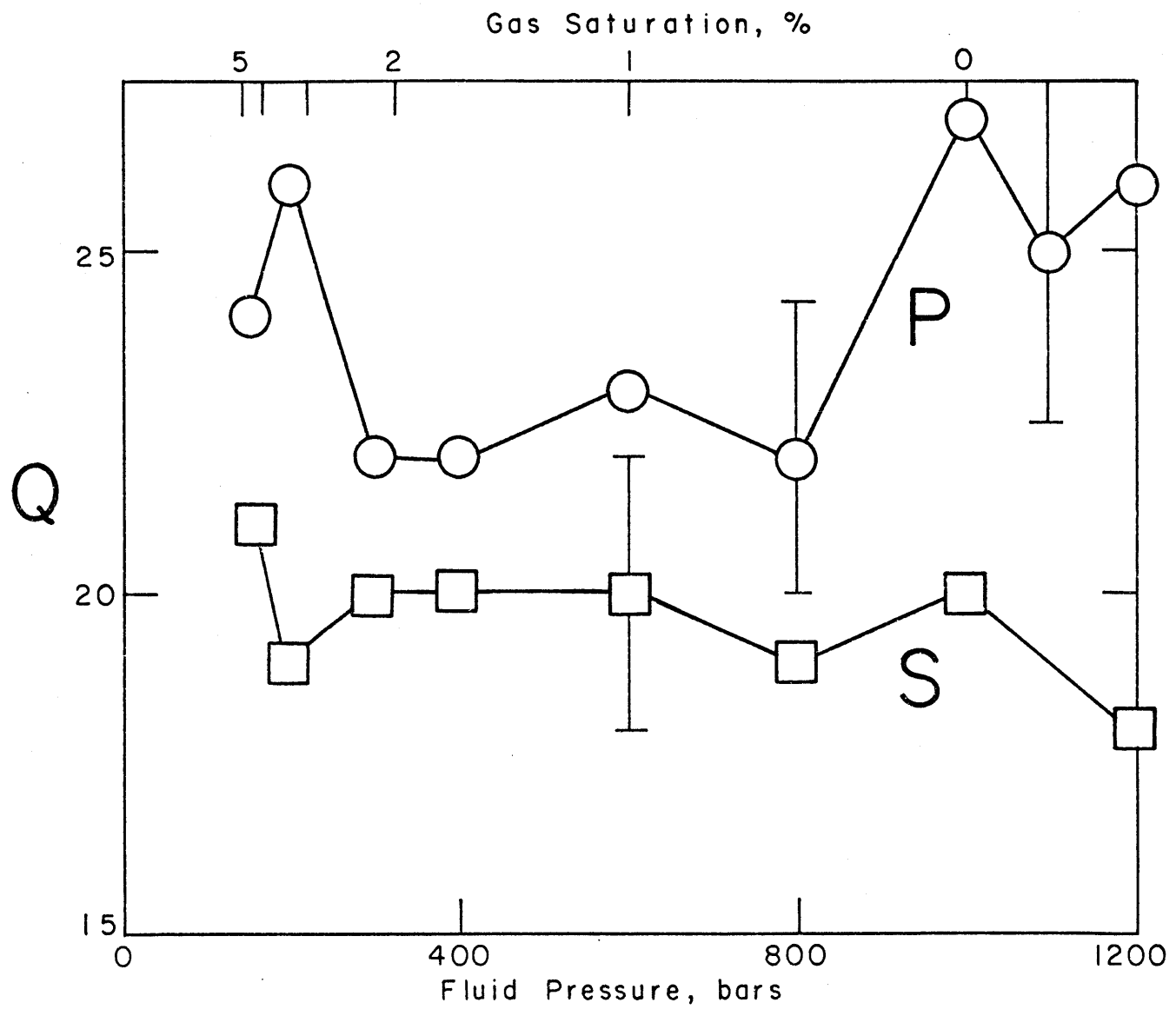


Figure 5-18

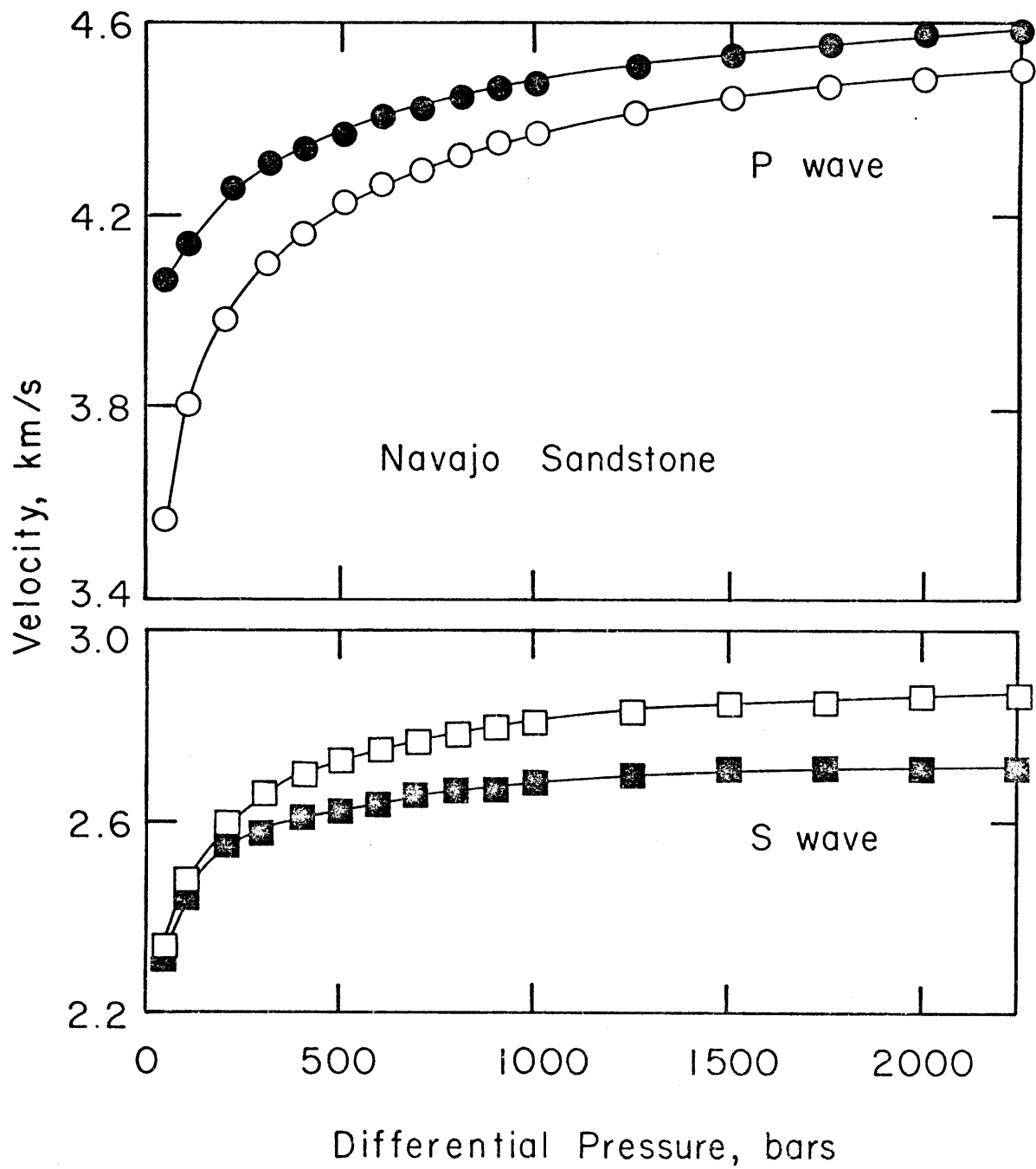


Figure 5-19

# Dry Navajo Sandstone - P wave

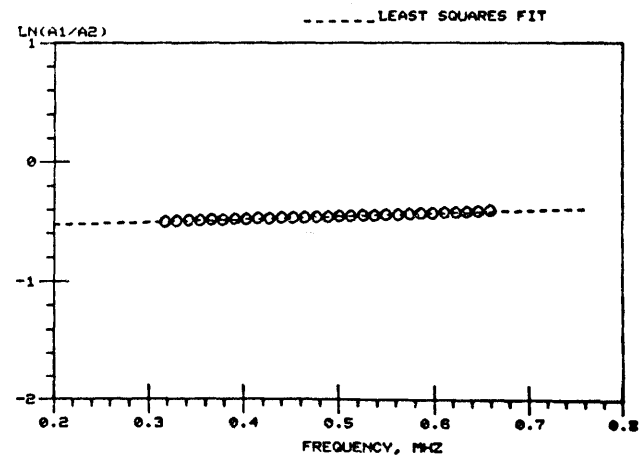
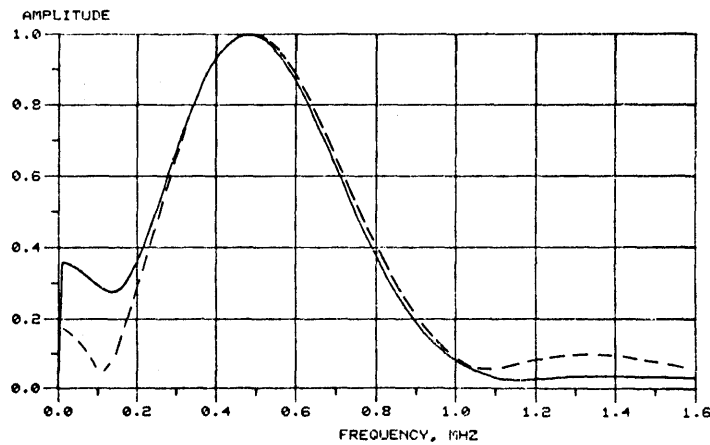
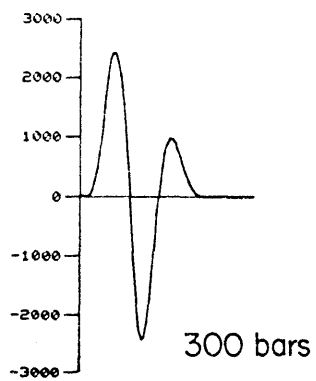
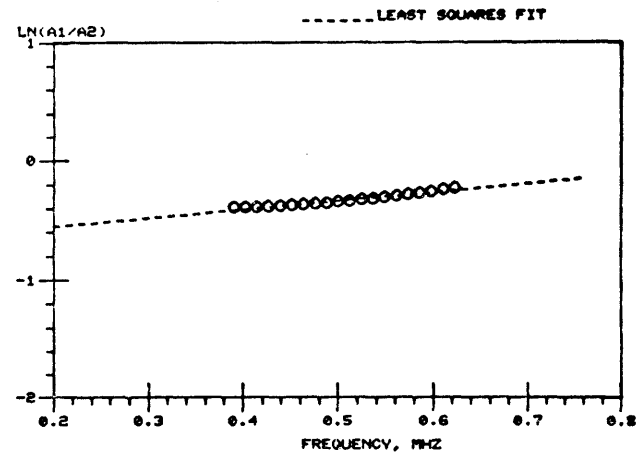
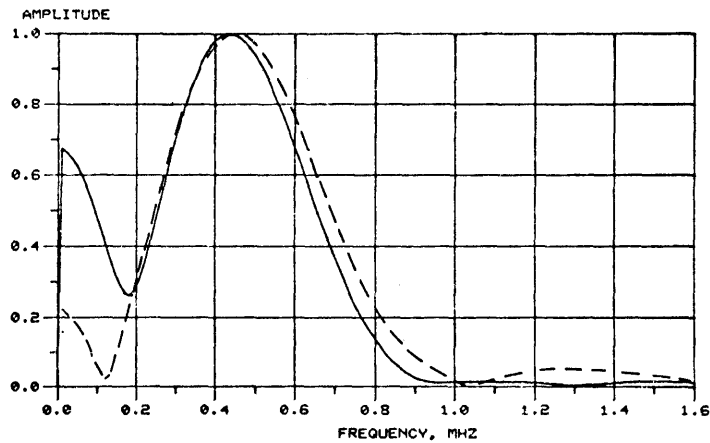
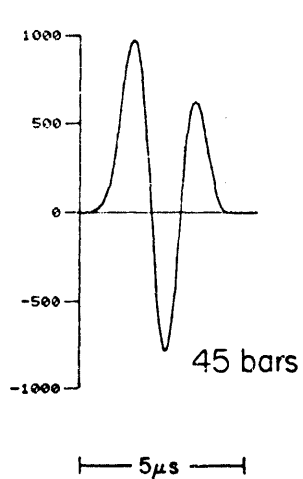


Figure 5-20

# Dry Navajo Sandstone - S wave

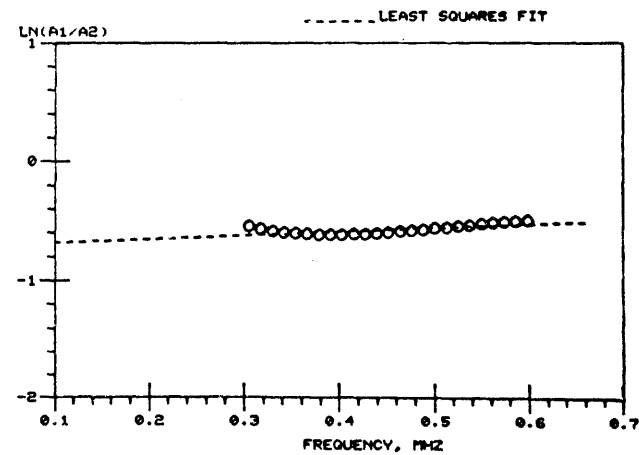
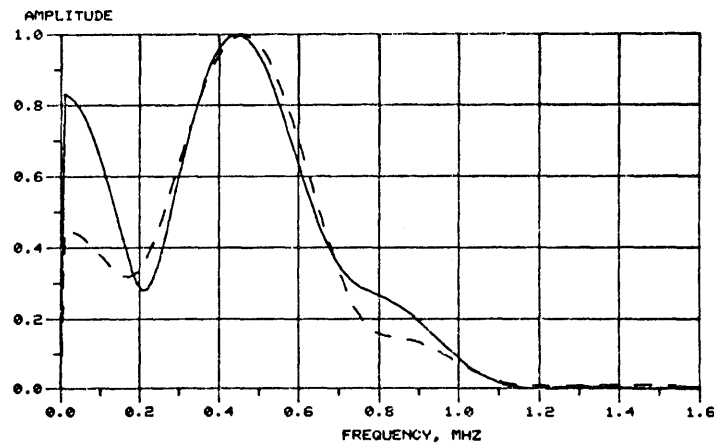
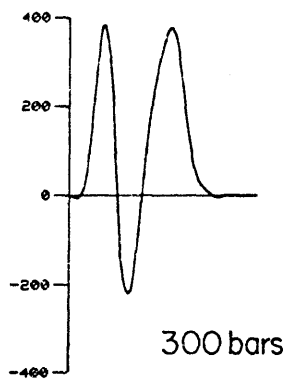
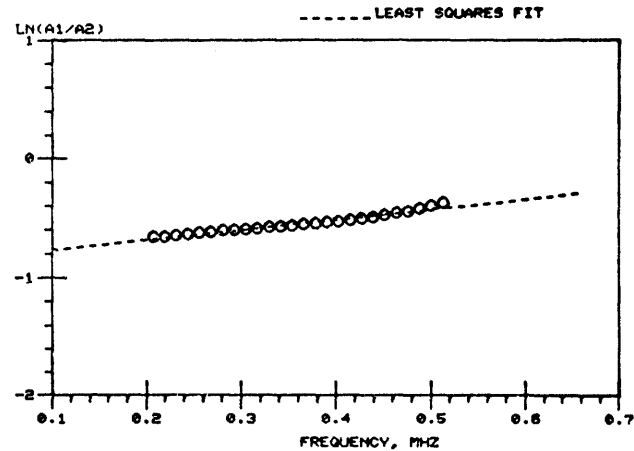
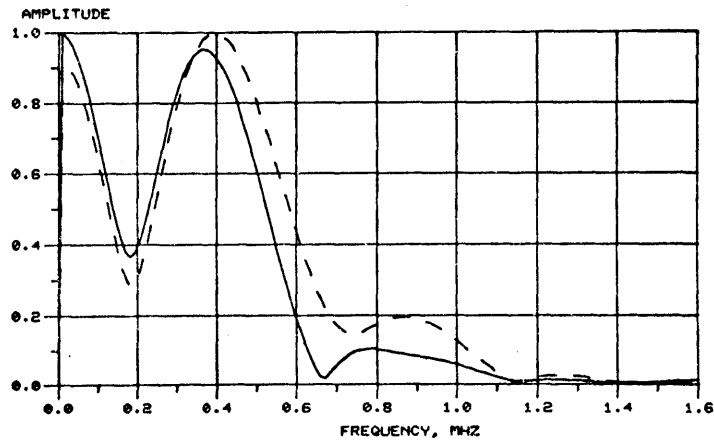
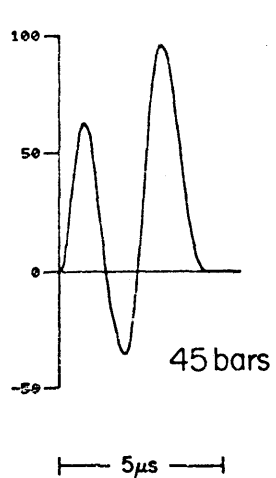


Figure 5-21

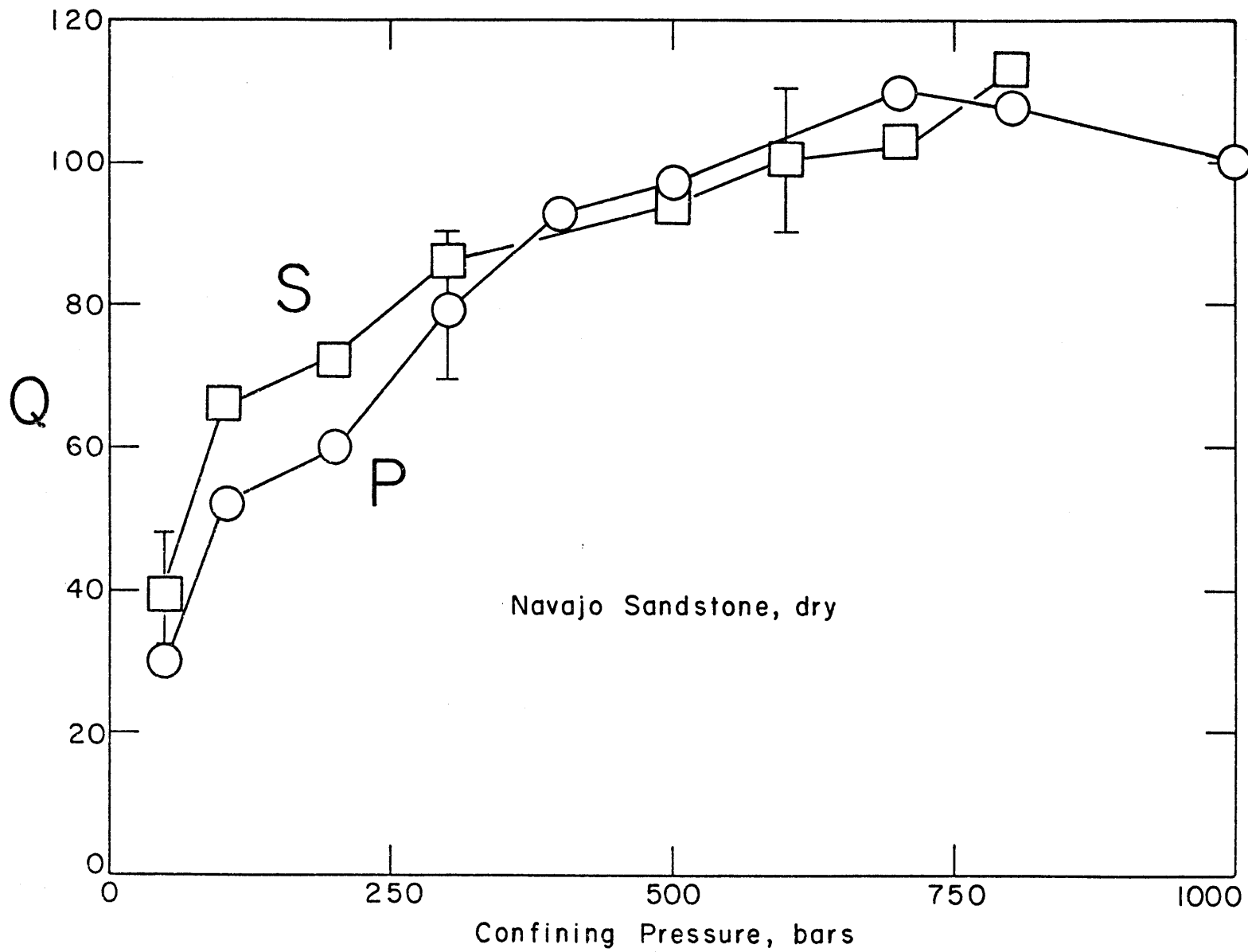


Figure 5-22

# Saturated Navajo Sandstone - P wave

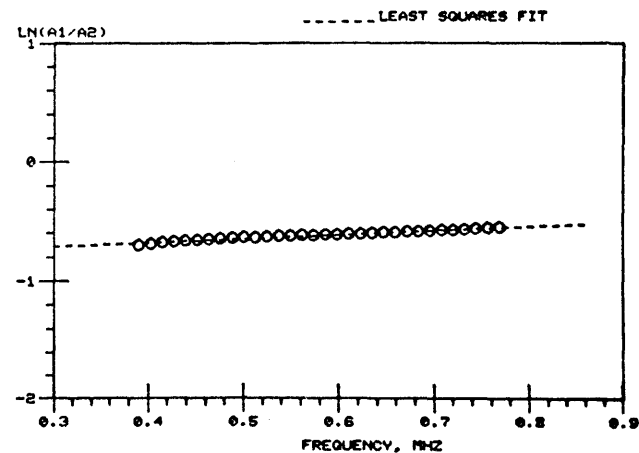
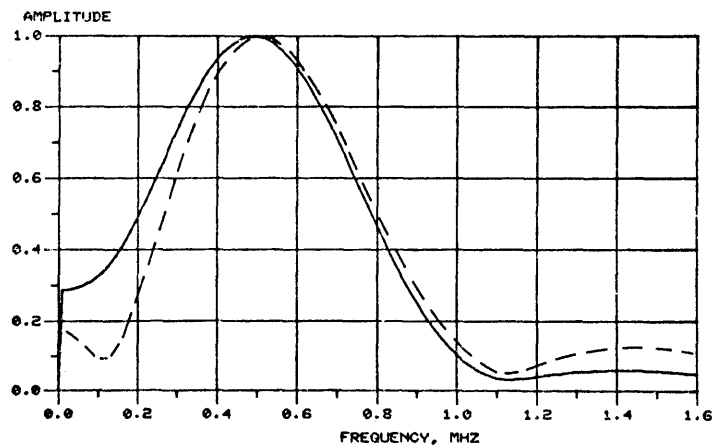
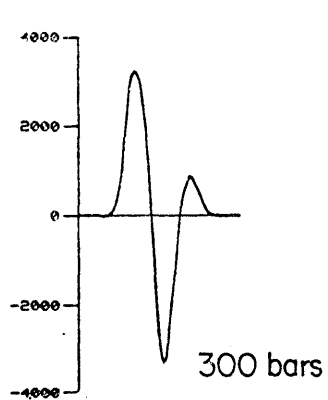
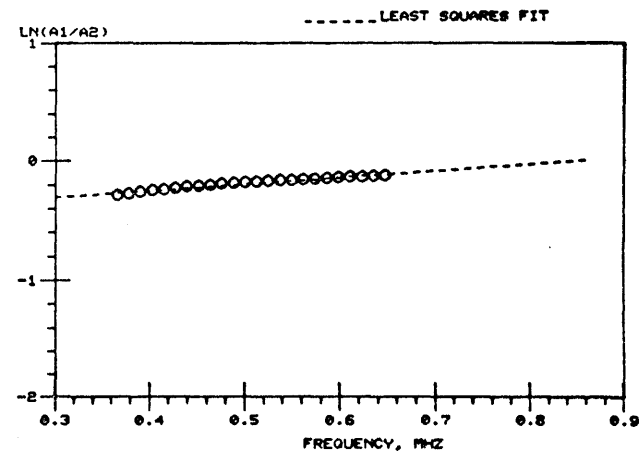
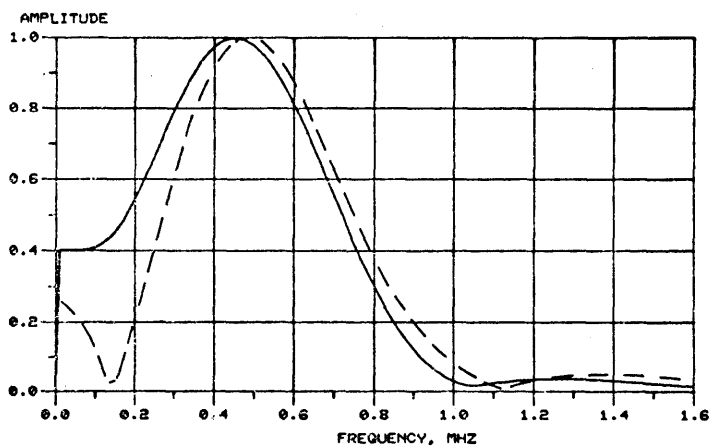
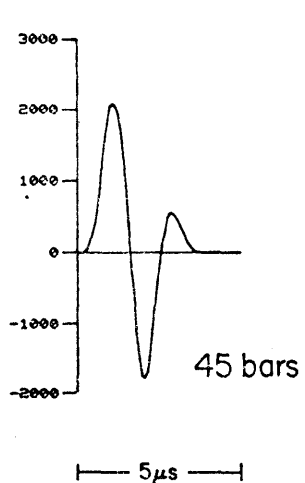


Figure 5-23

### Saturated Navajo Sandstone - S wave

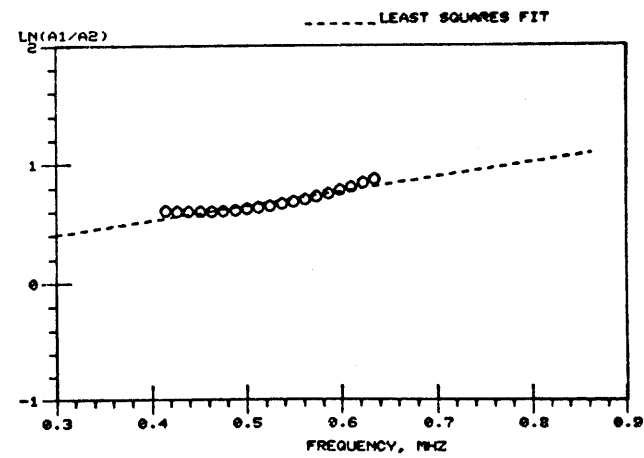
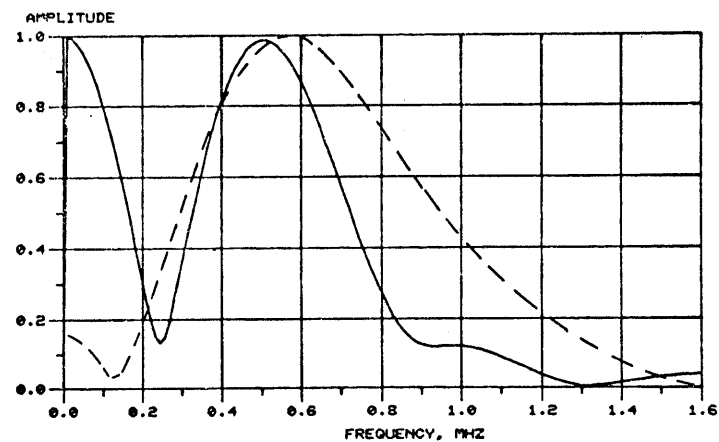
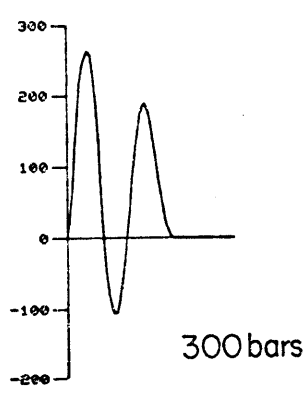
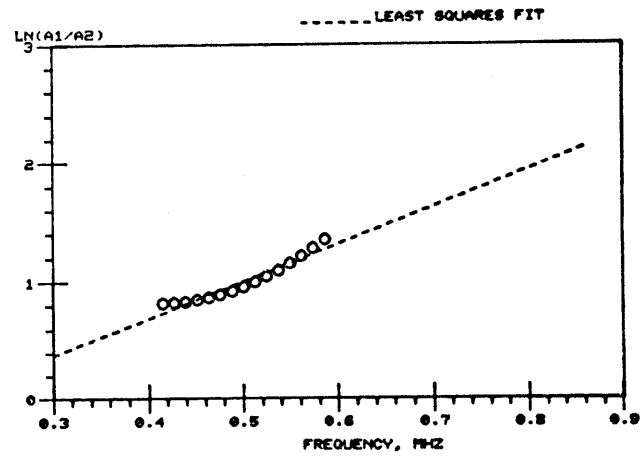
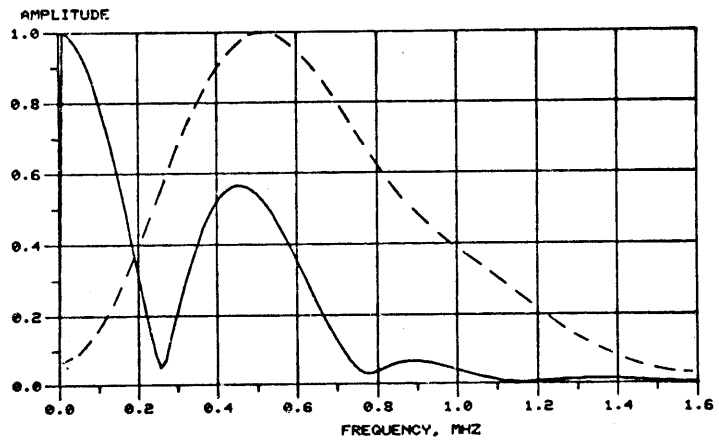
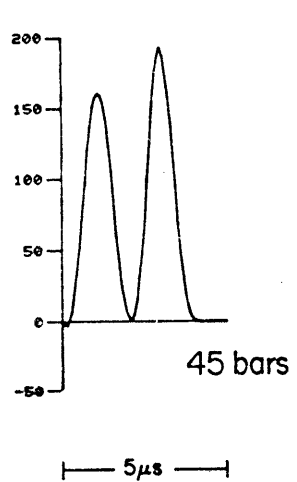


Figure 5-24



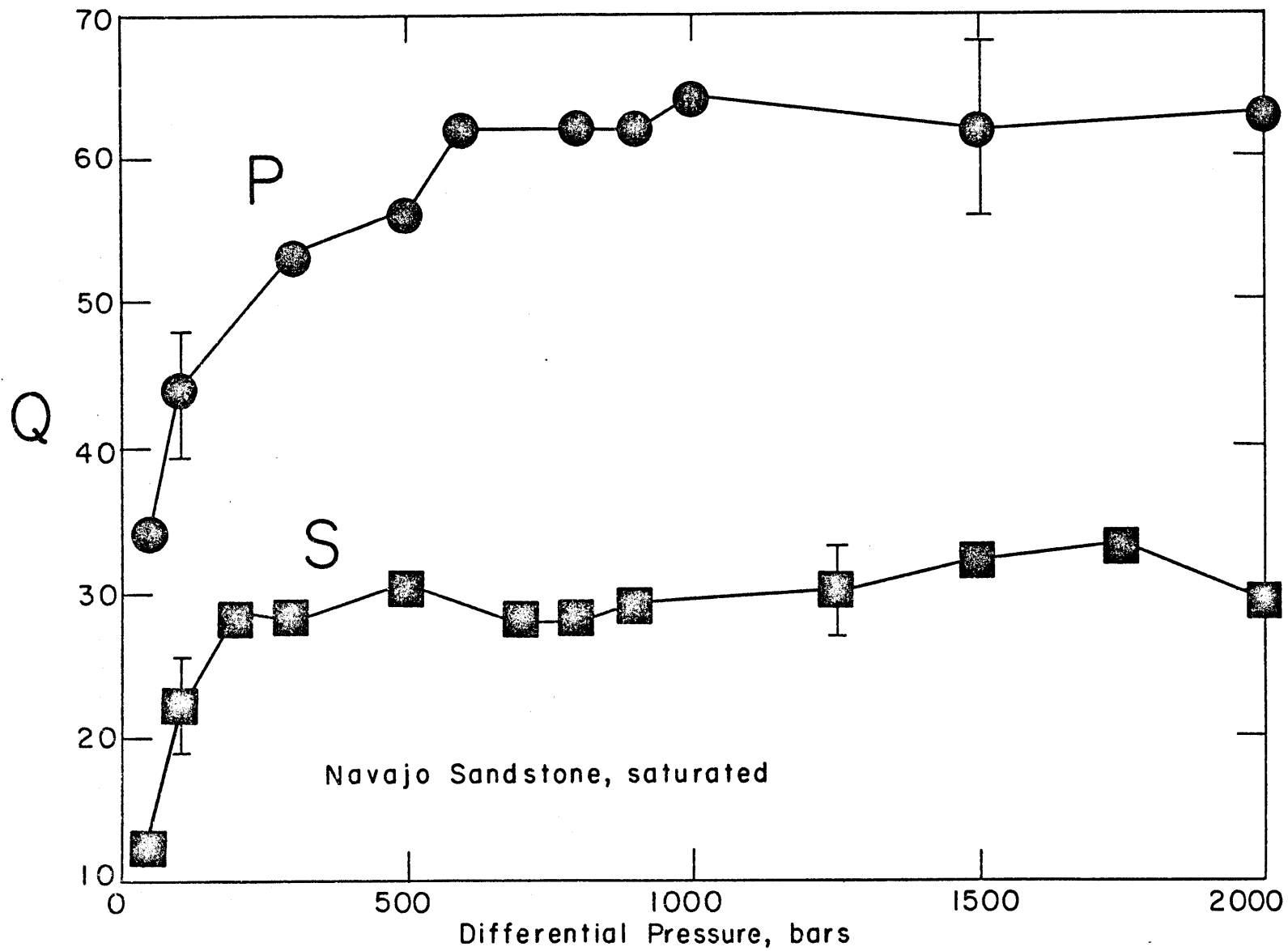


Figure 5-25

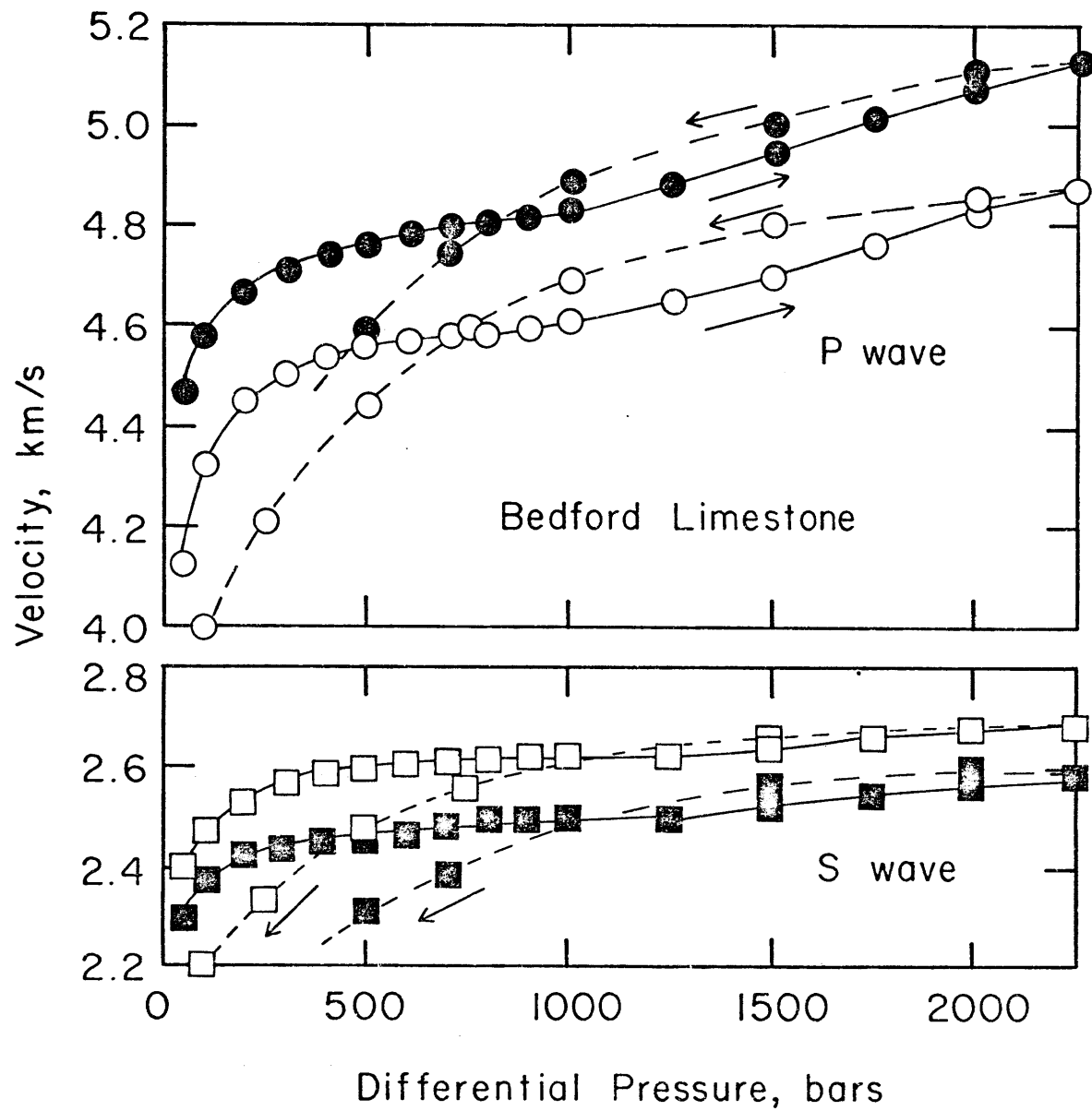


Figure 5-26

# Dry Bedford Limestone - P wave

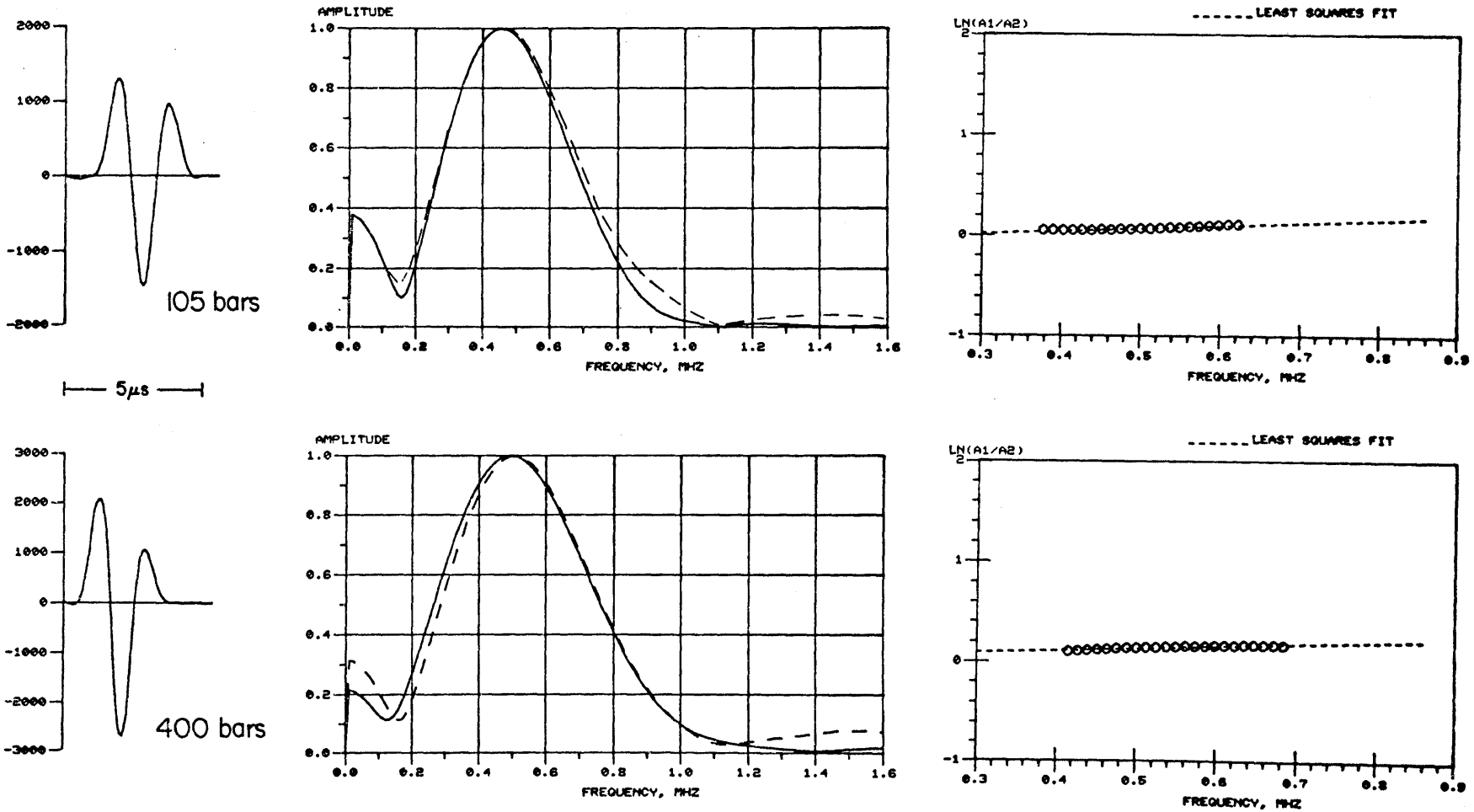


Figure 5-27

# Dry Bedford Limestone - S wave

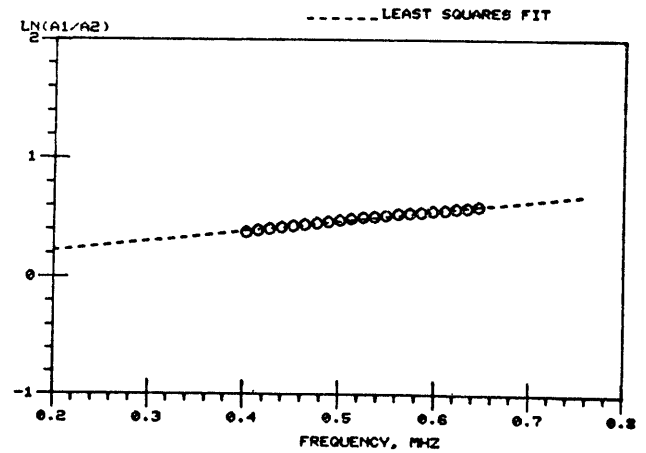
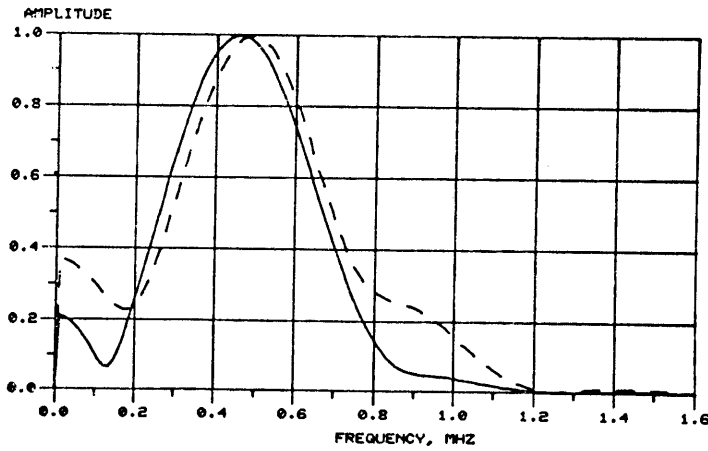
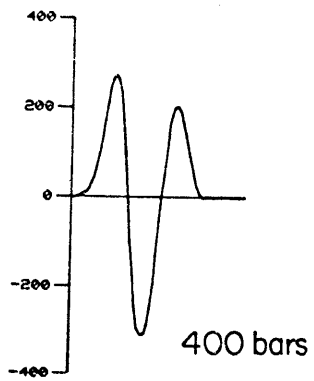
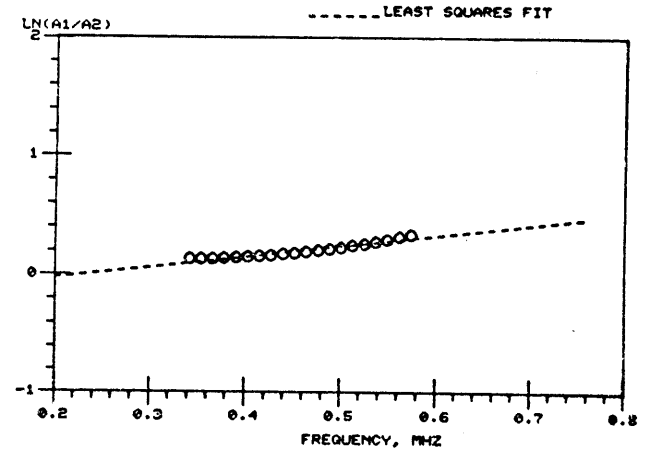
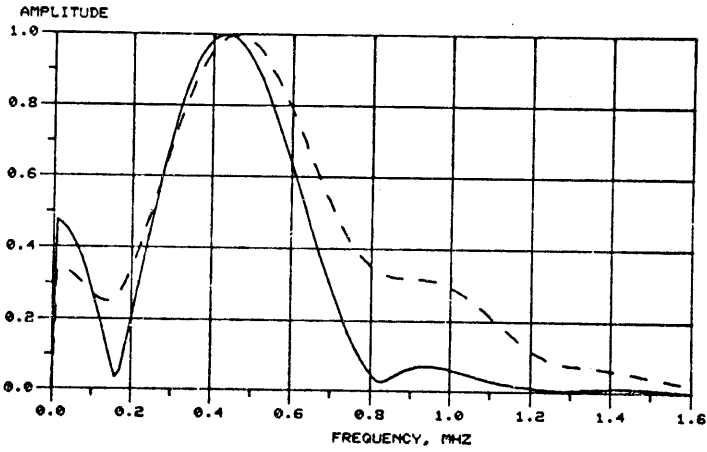
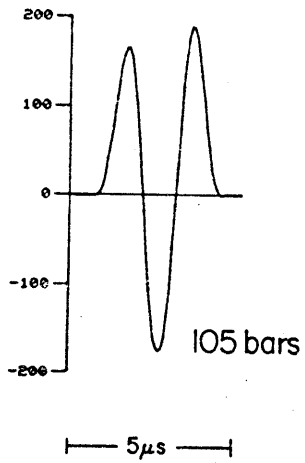


Figure 5-28

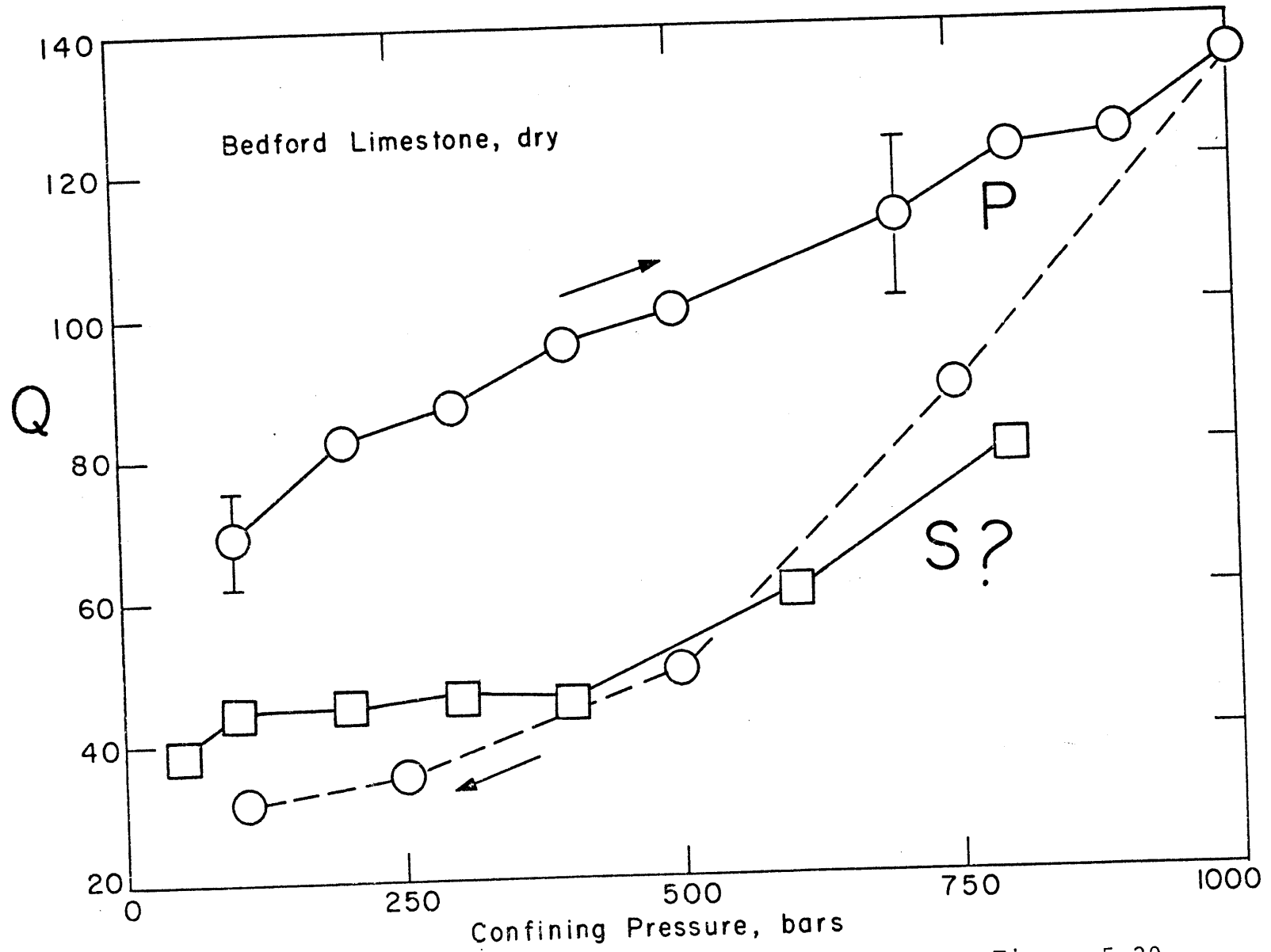


Figure 5-29

# Saturated Bedford Limestone - P wave

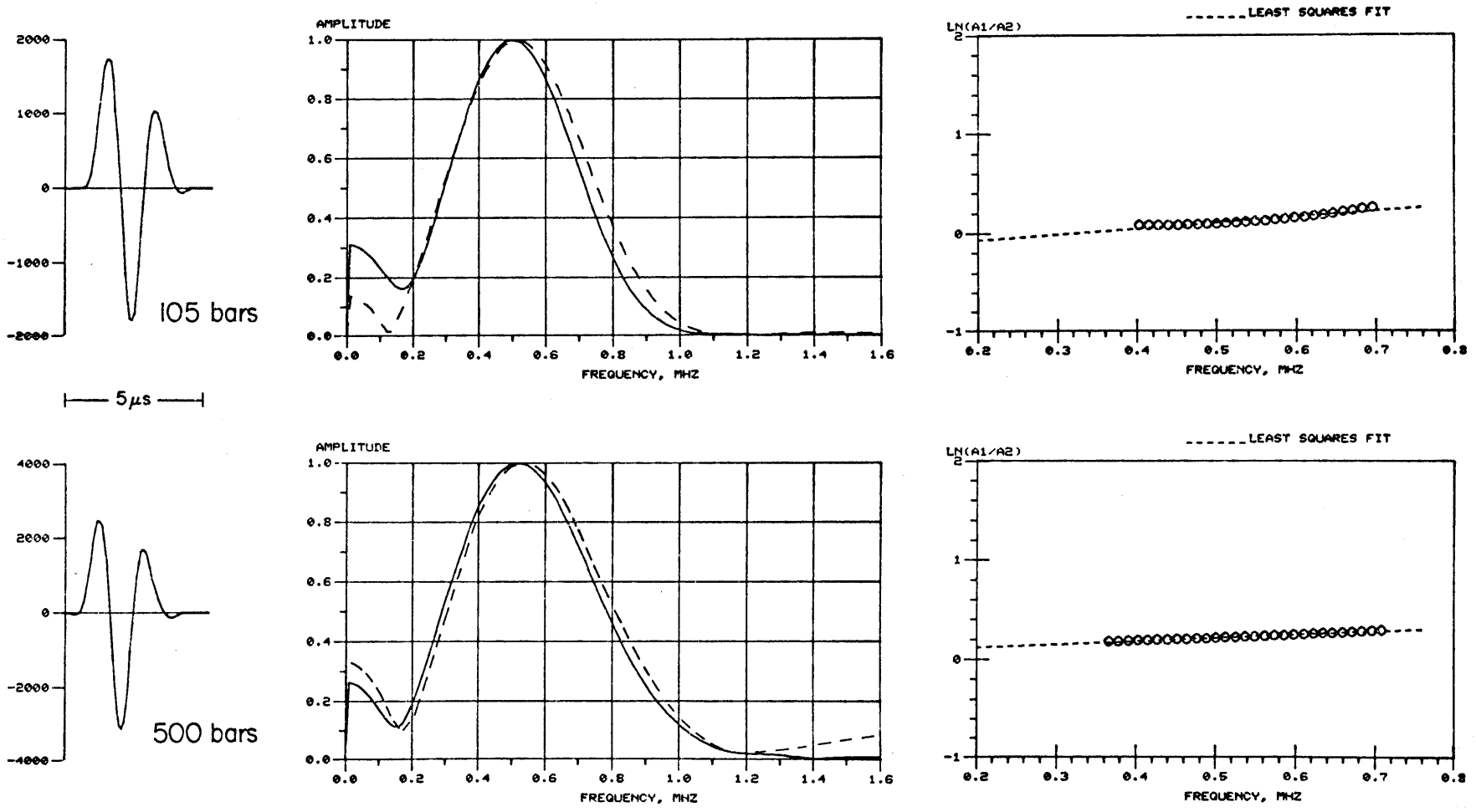


Figure 5-30

# Saturated Bedford Limestone - S wave

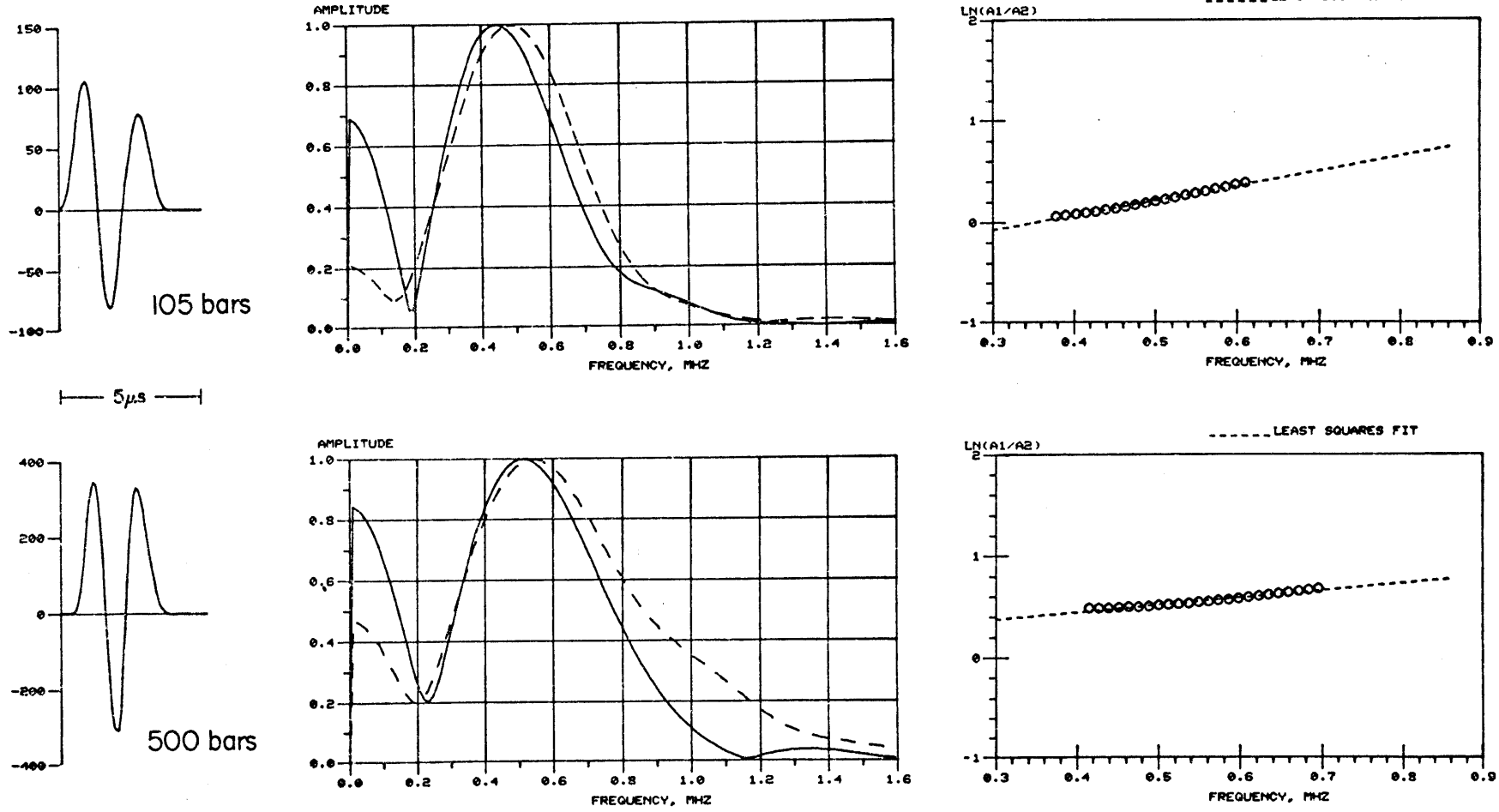


Figure 5-31

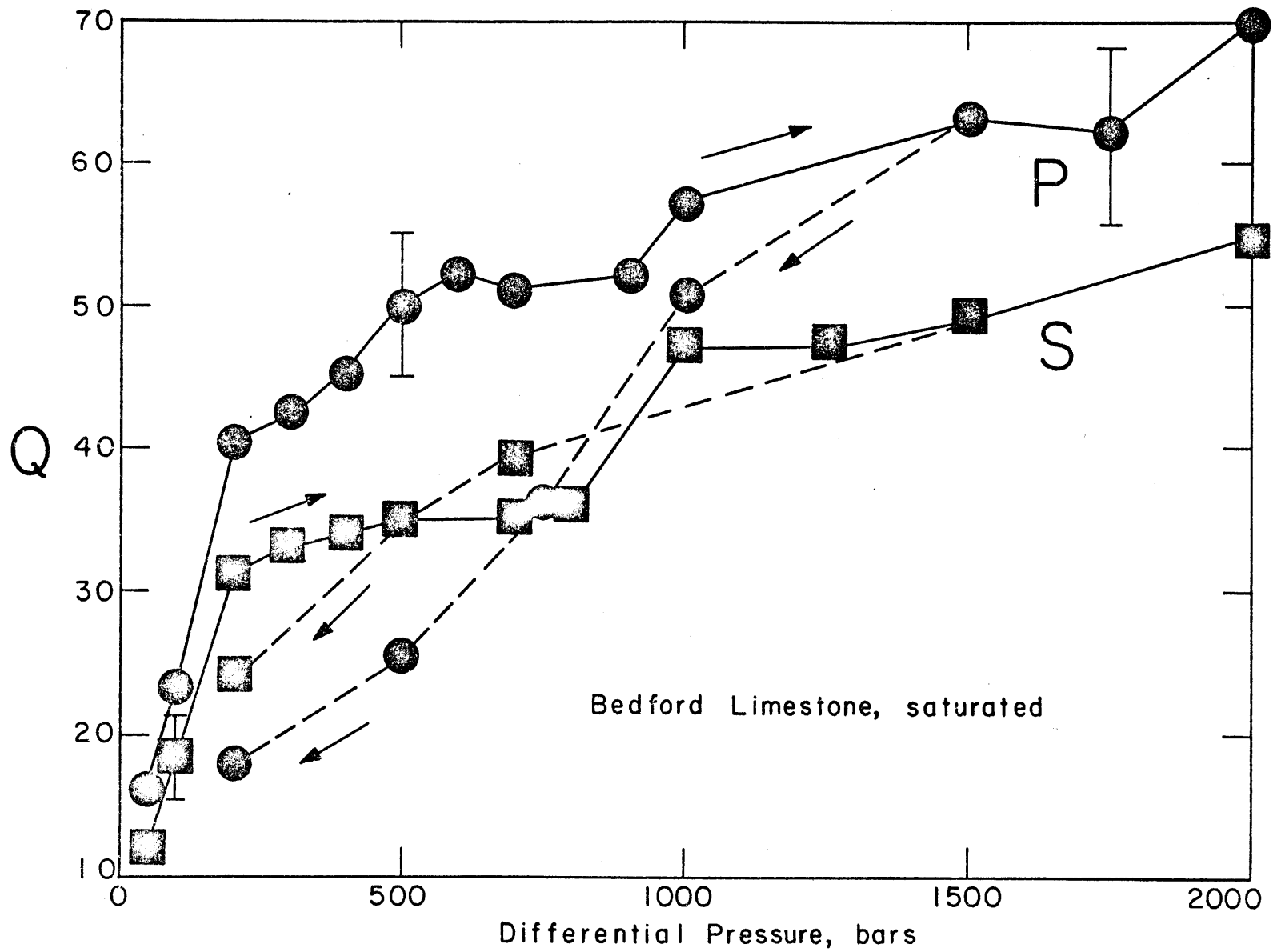


Figure 5-32



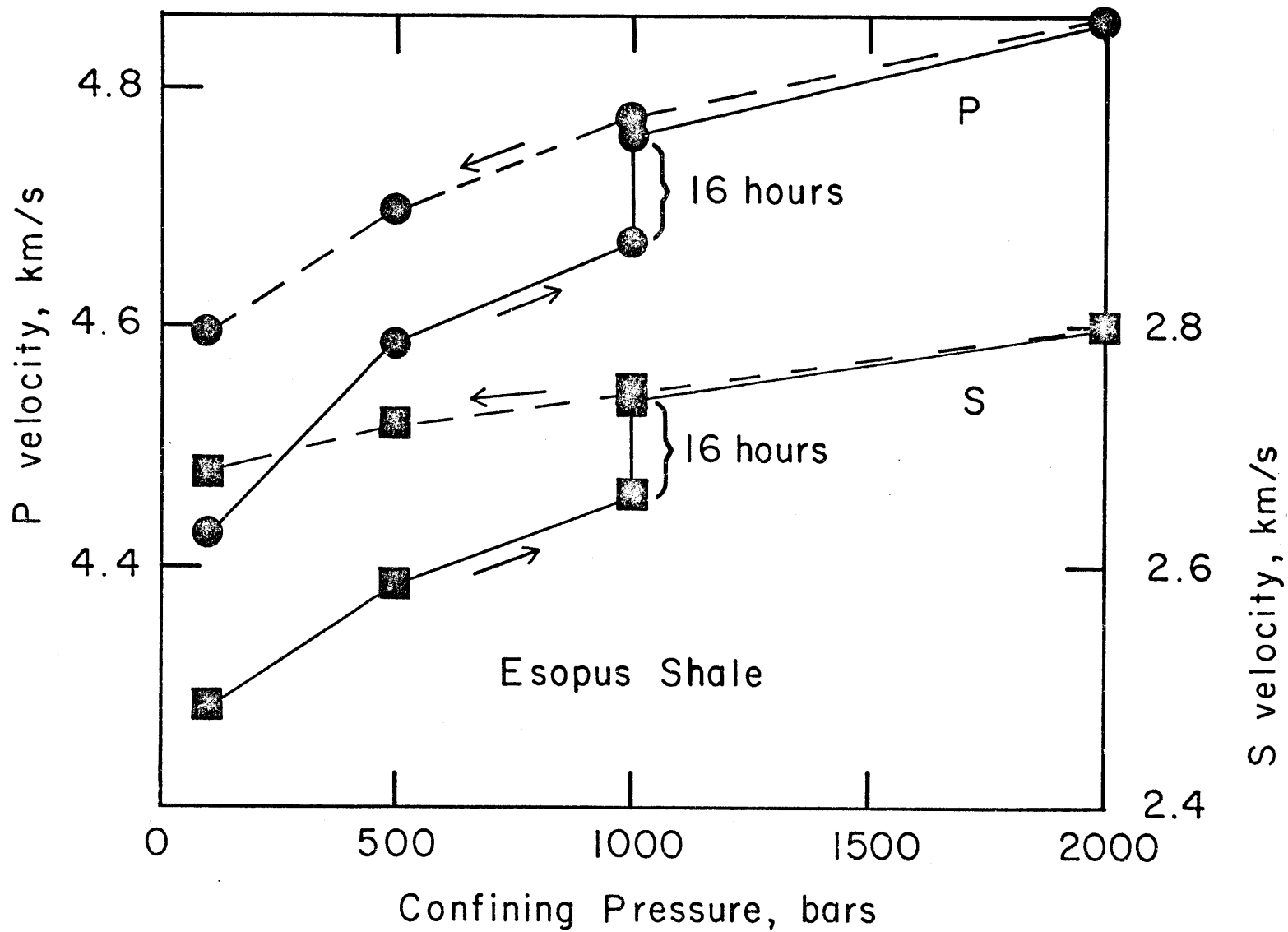


Figure 5-33

# Esopus Shale - P wave

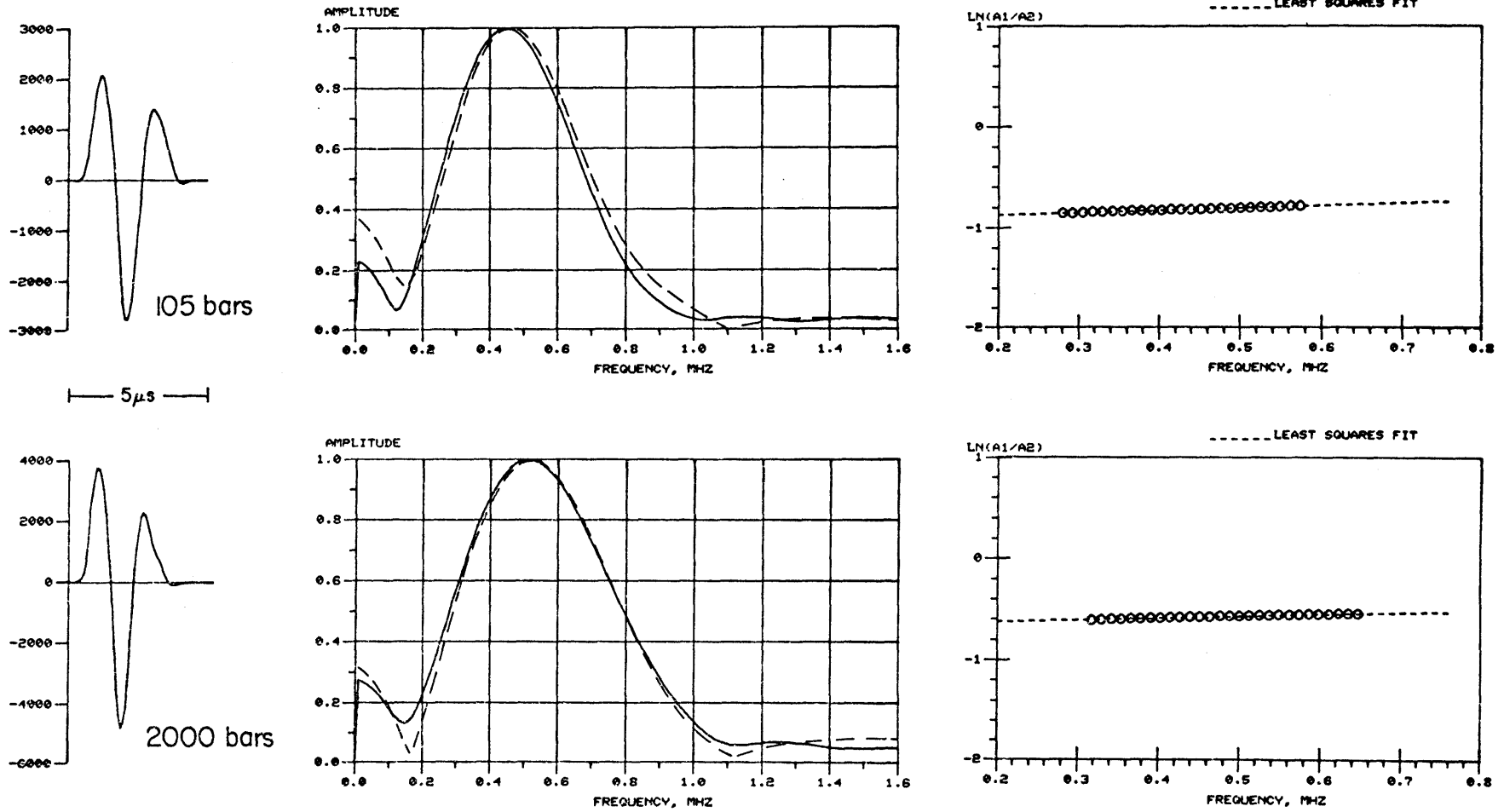


Figure 5-34

# Esopus Shale - S wave

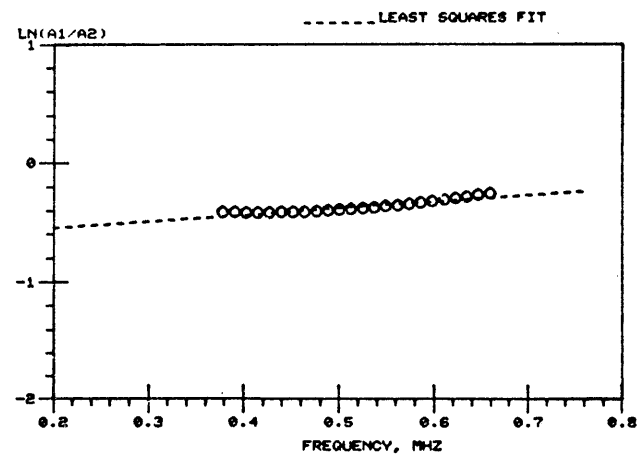
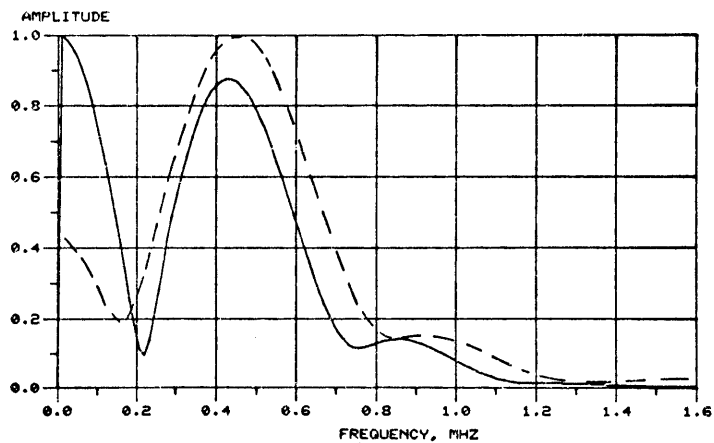
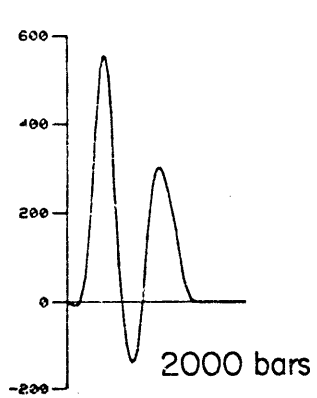
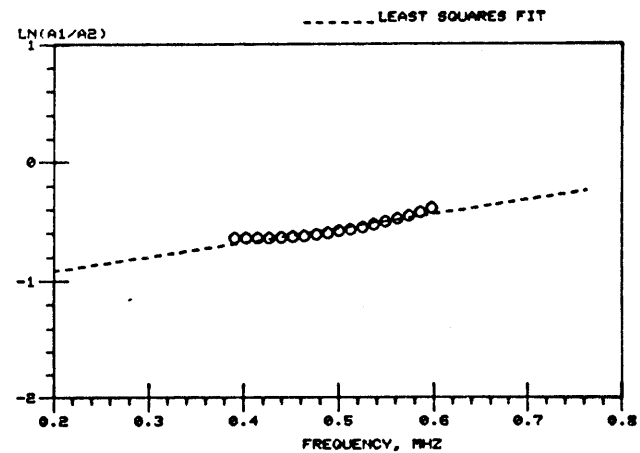
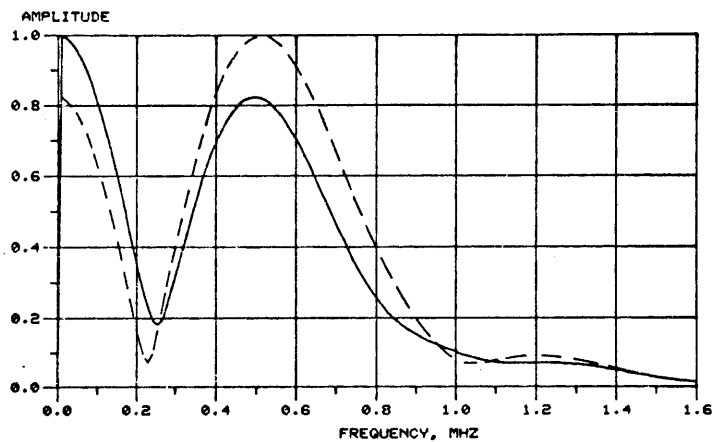
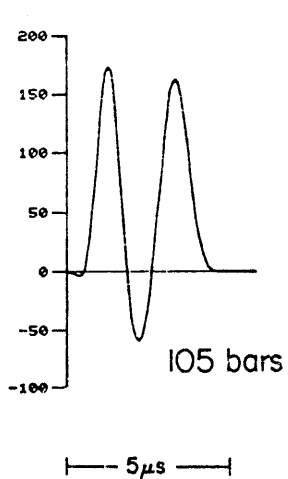


Figure 5-35

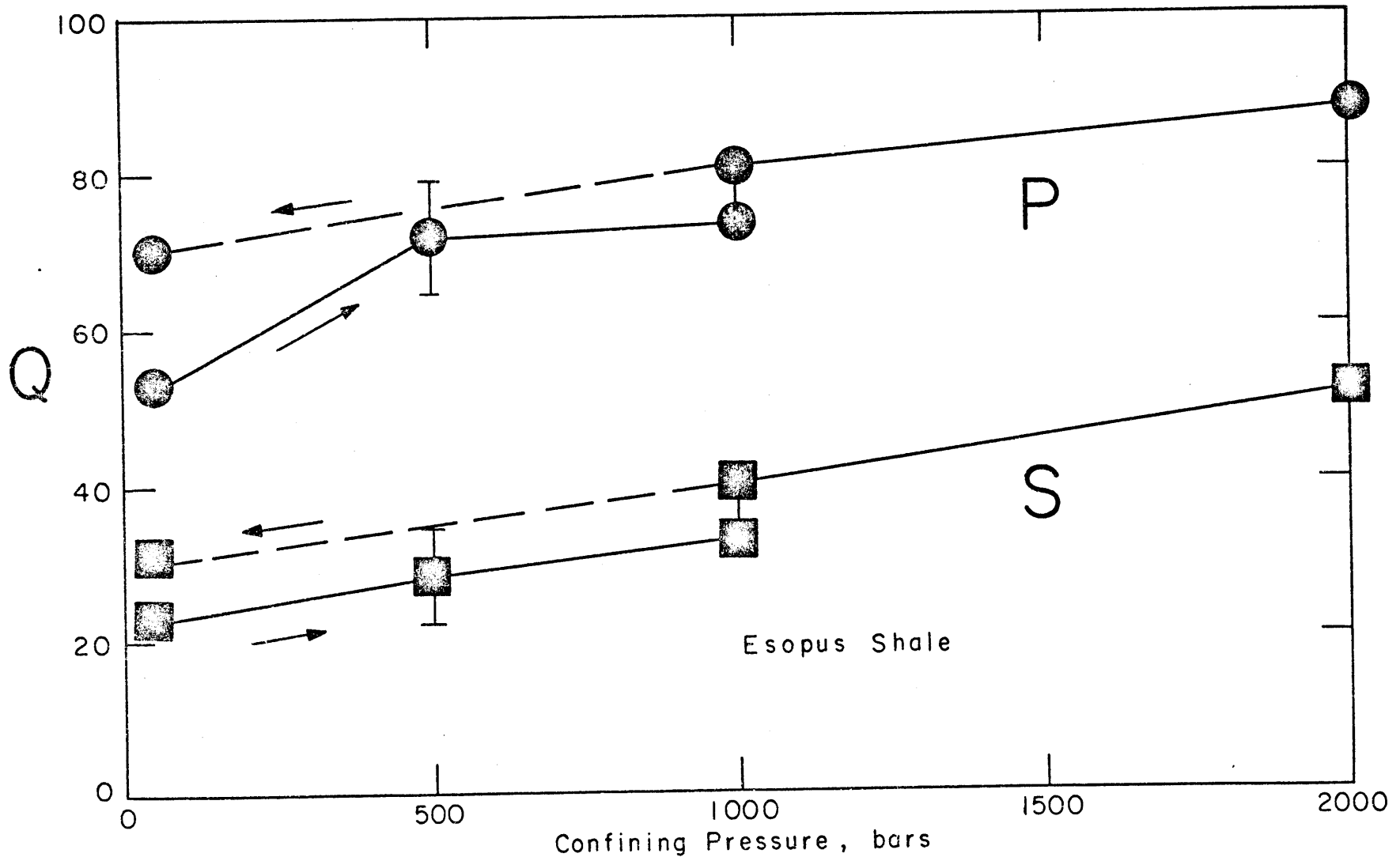


Figure 5-36

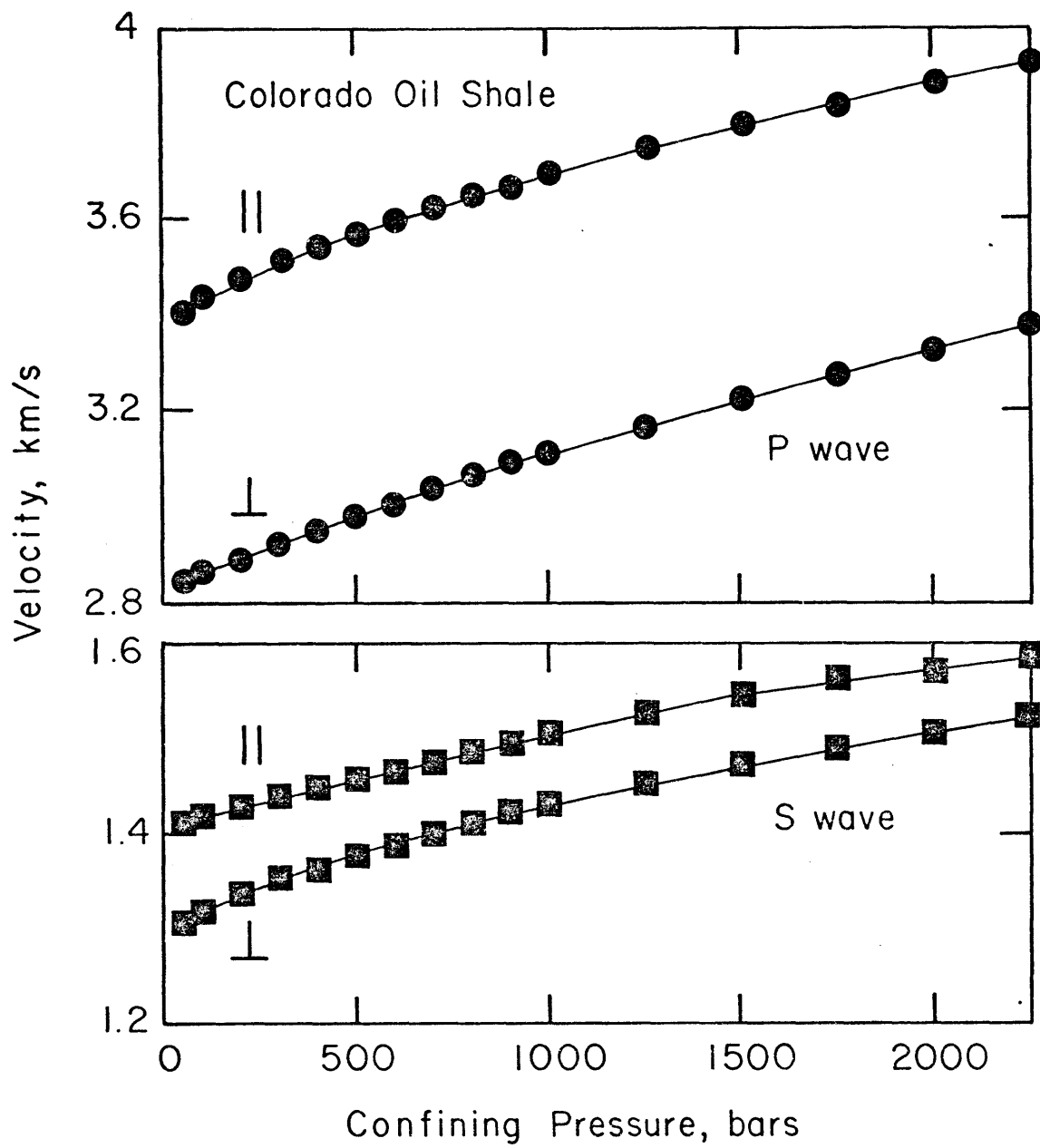


Figure 5-37

# Colorado Oil Shale - P wave

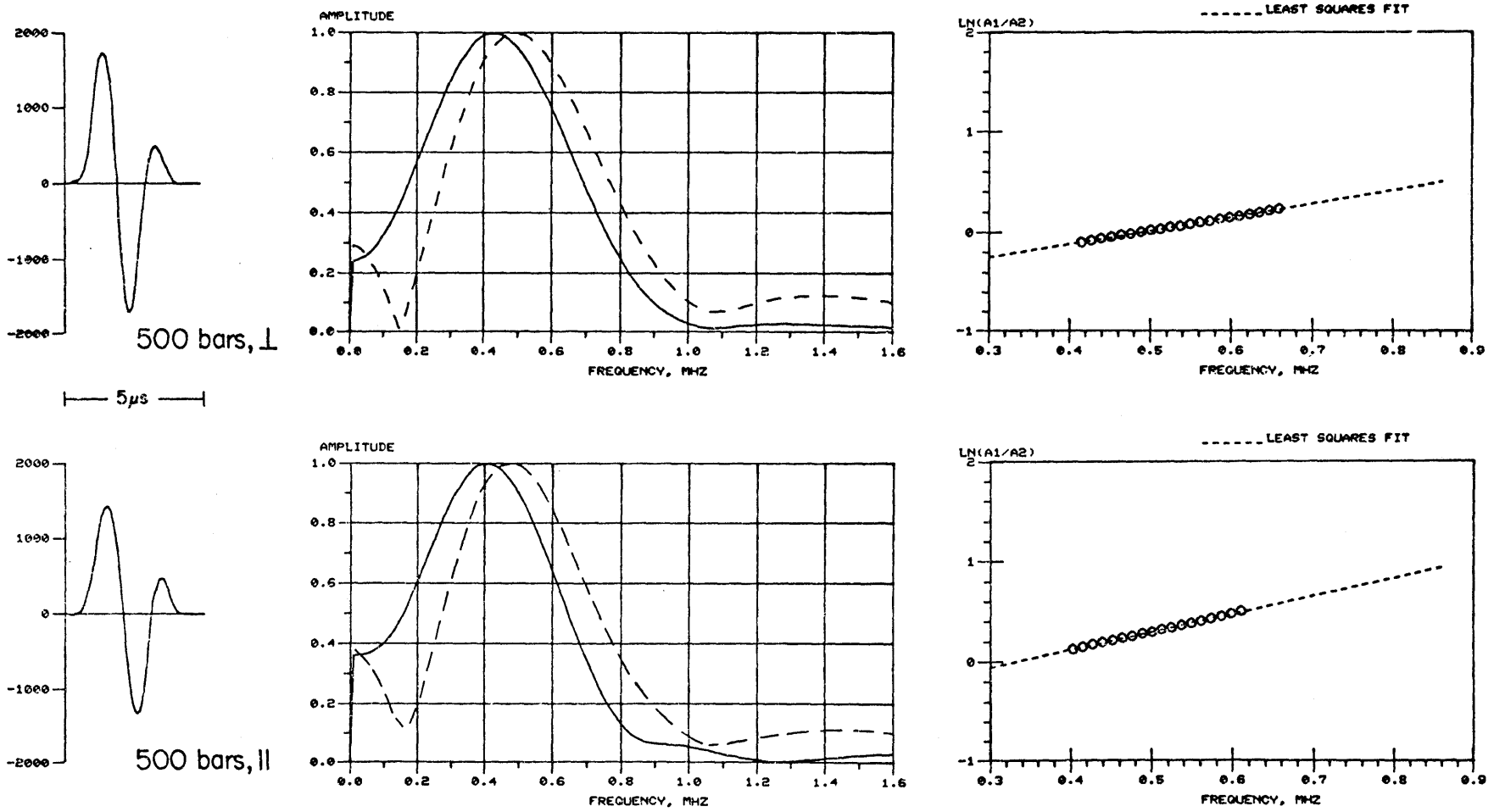


Figure 5-38

# Colorado Oil Shale - S wave

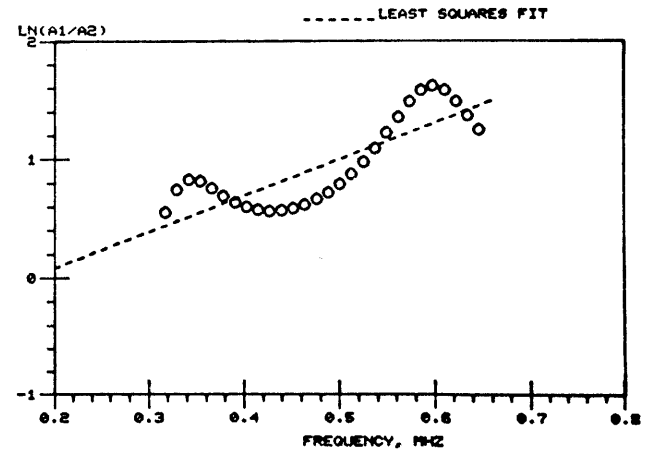
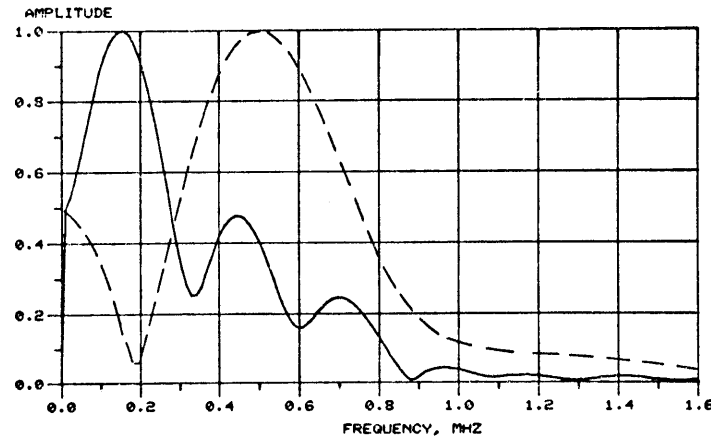
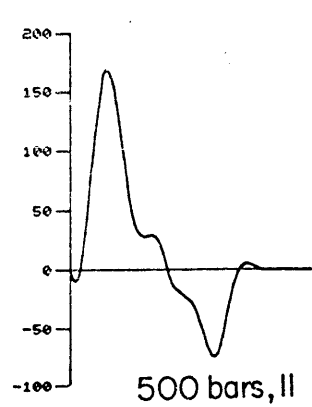
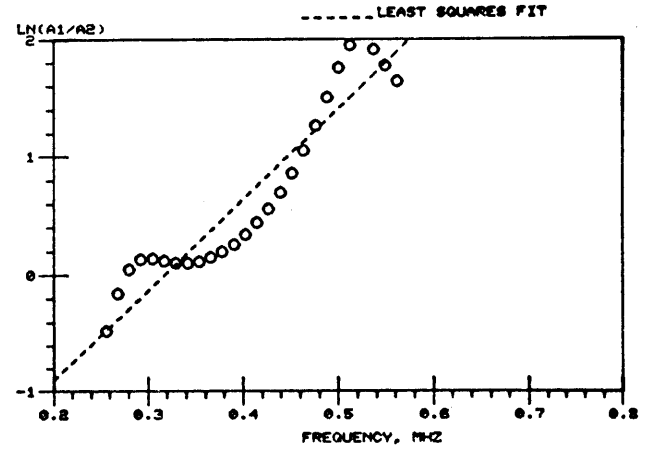
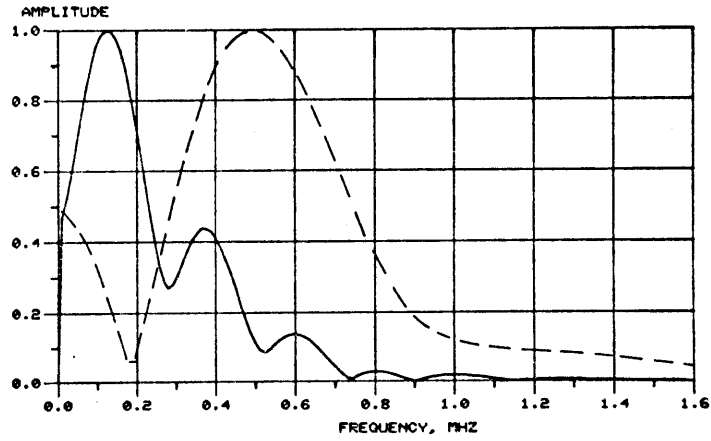
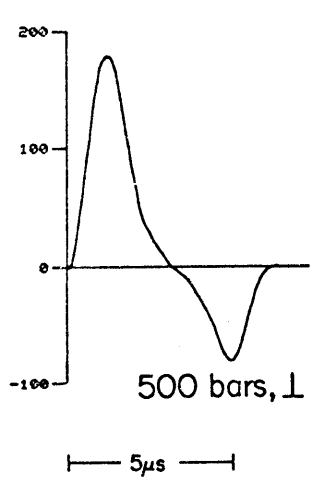


Figure 5-39

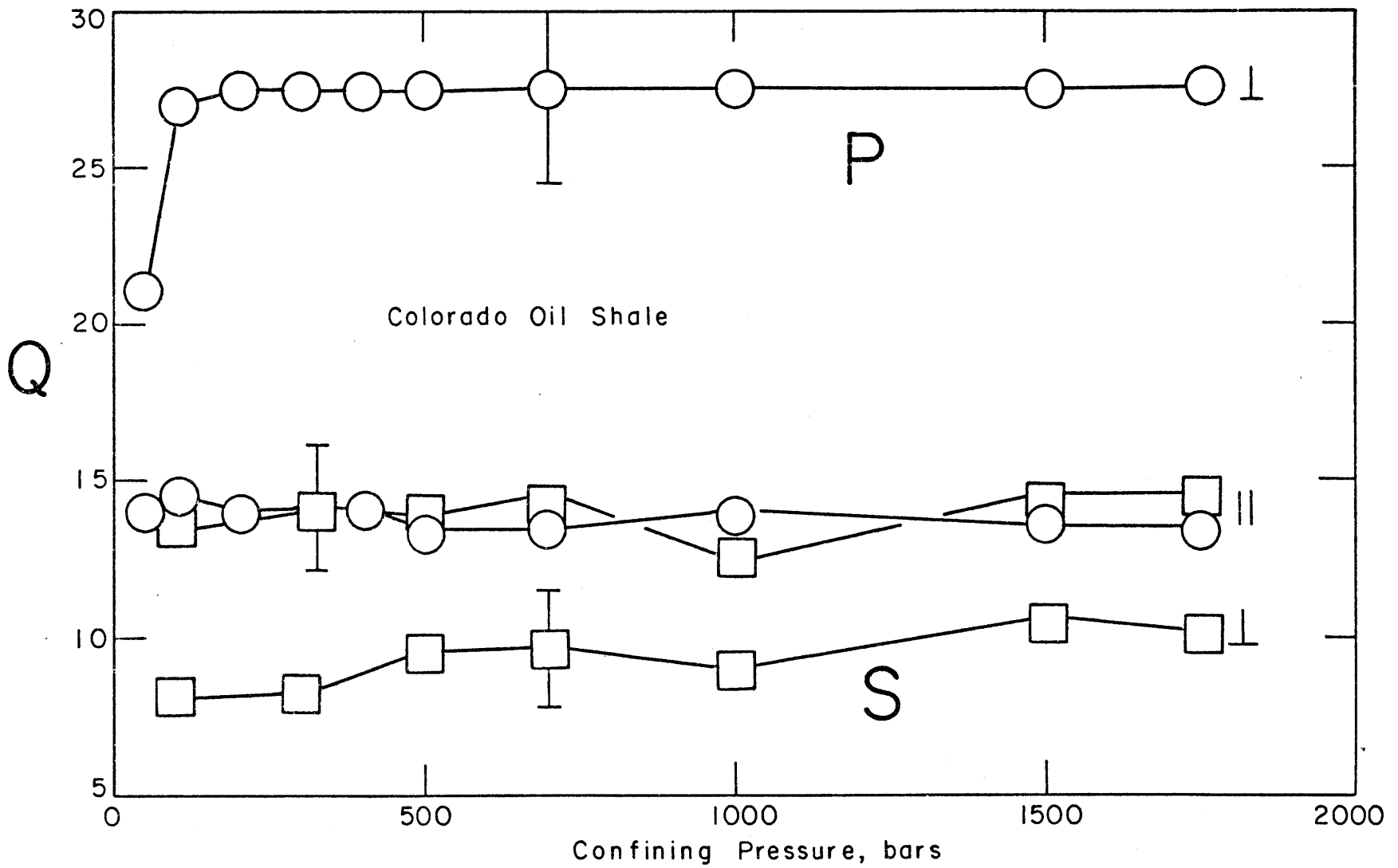


Figure 5-40



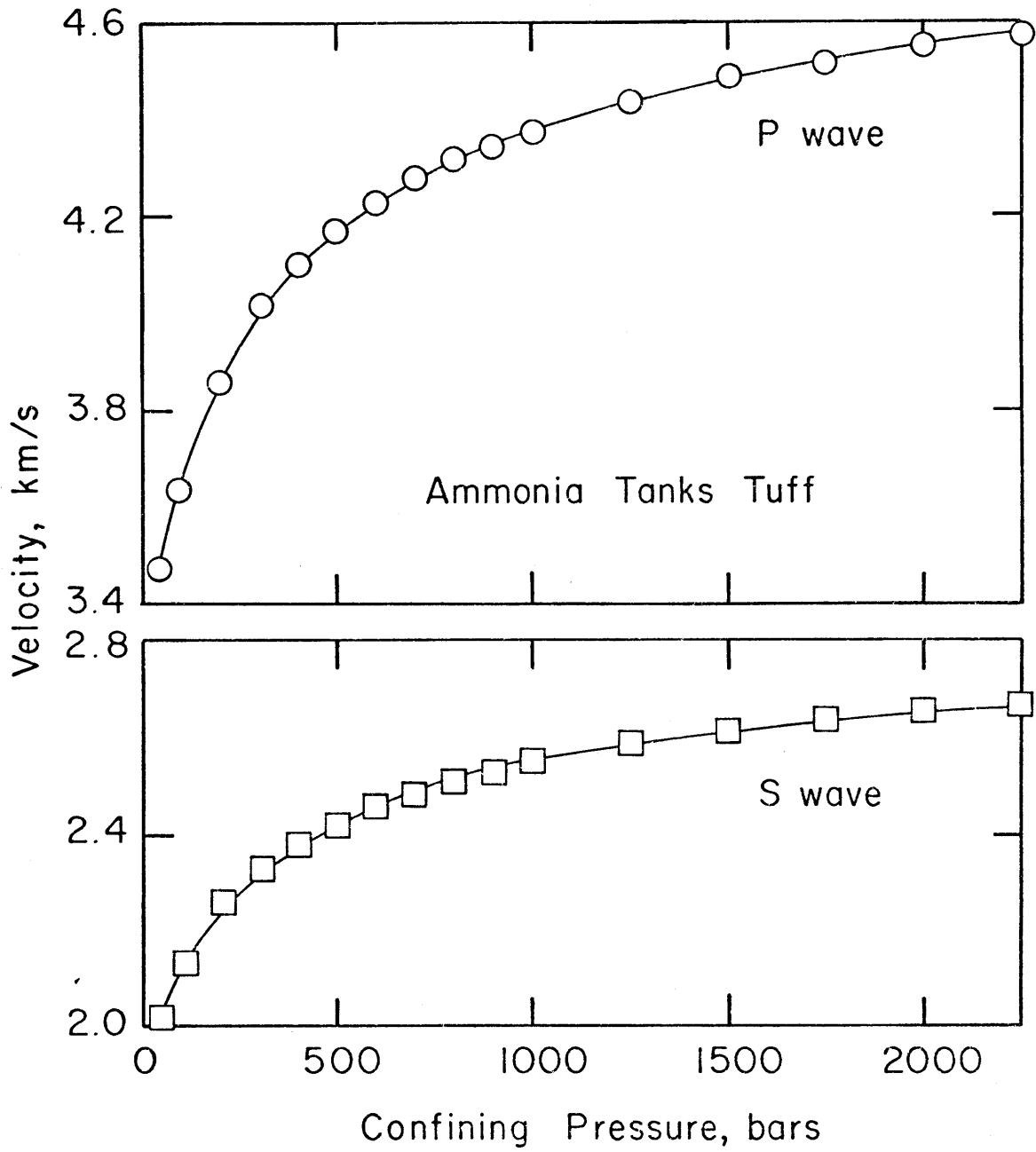


Figure 5-41

# Ammonia Tanks Tuff - P wave

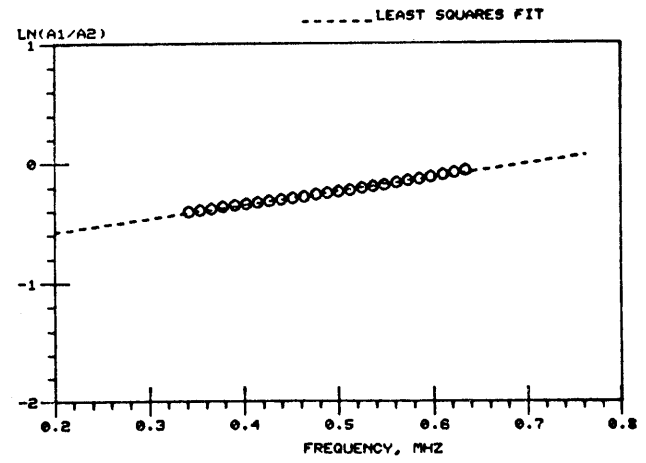
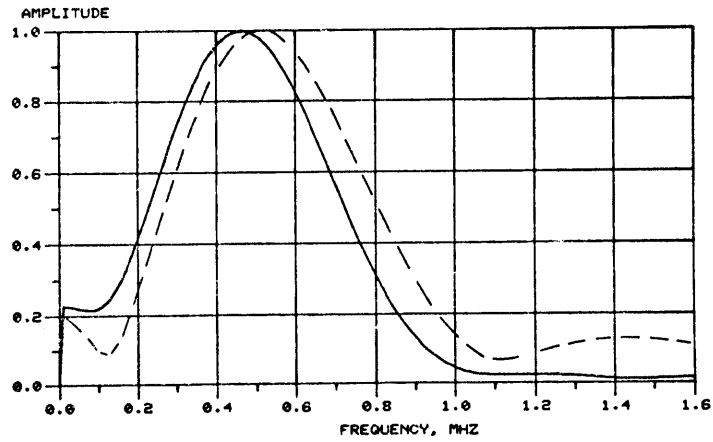
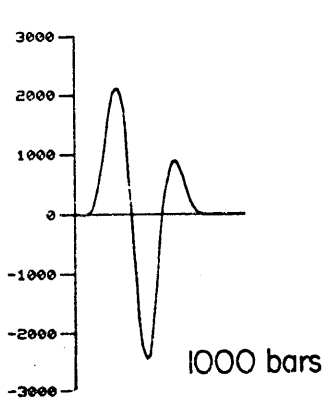
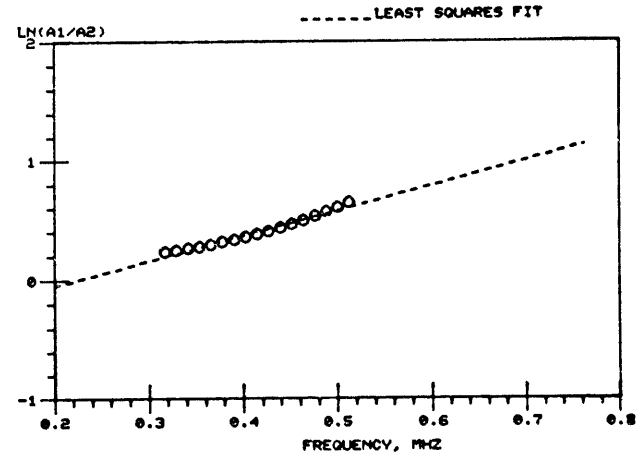
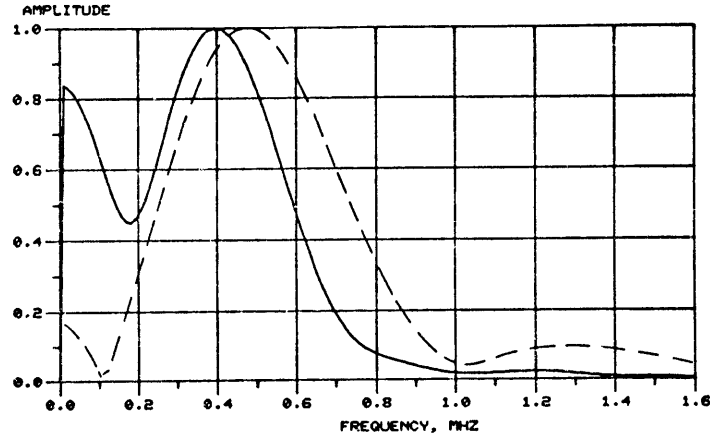
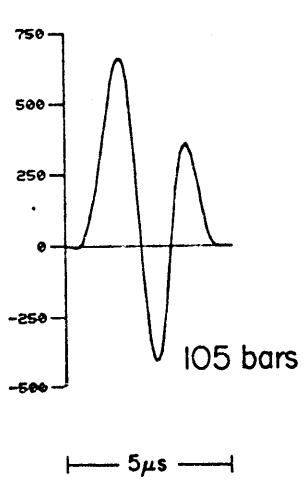


Figure 5-42

# Ammonia Tanks Tuff-S wave

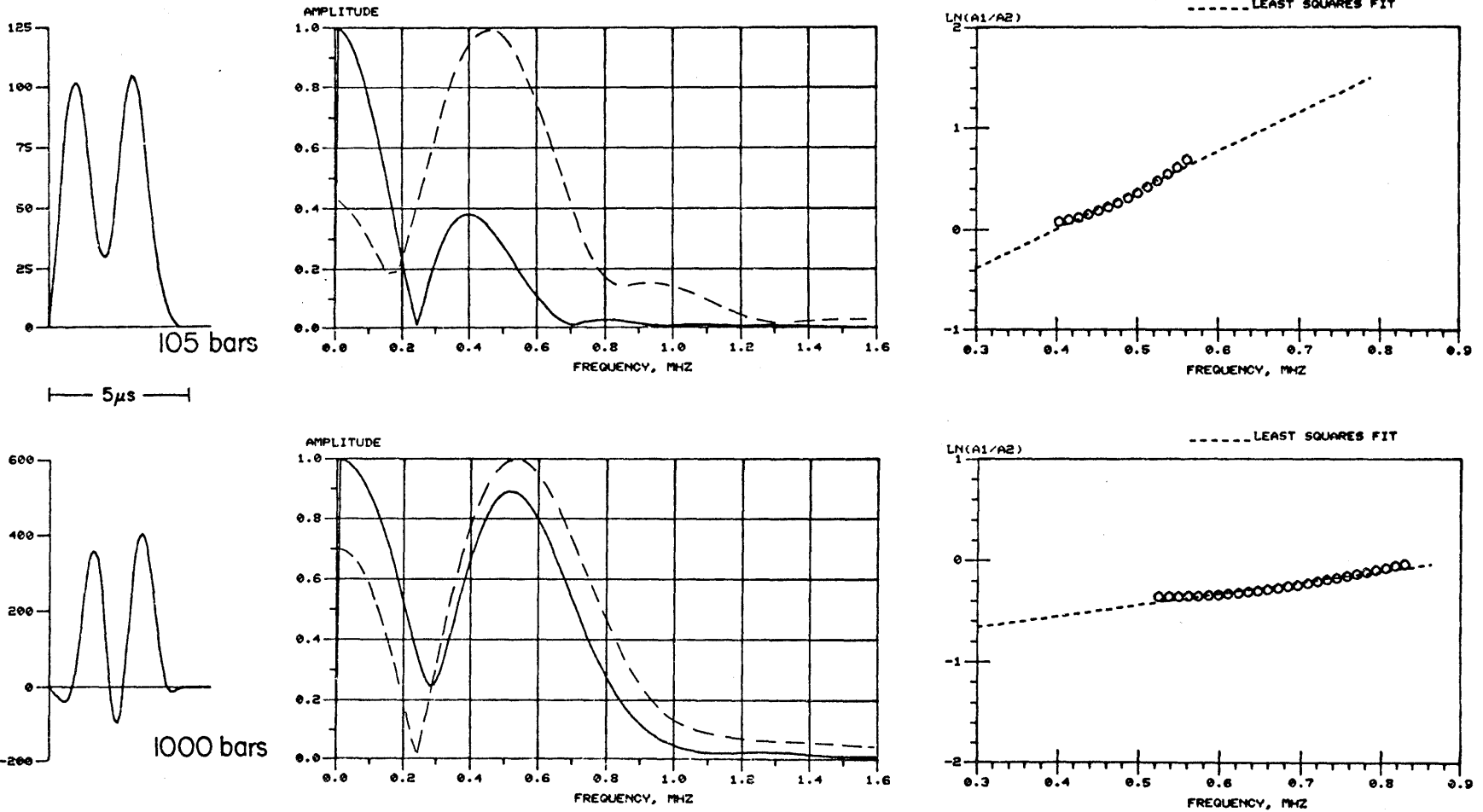


Figure 5-43

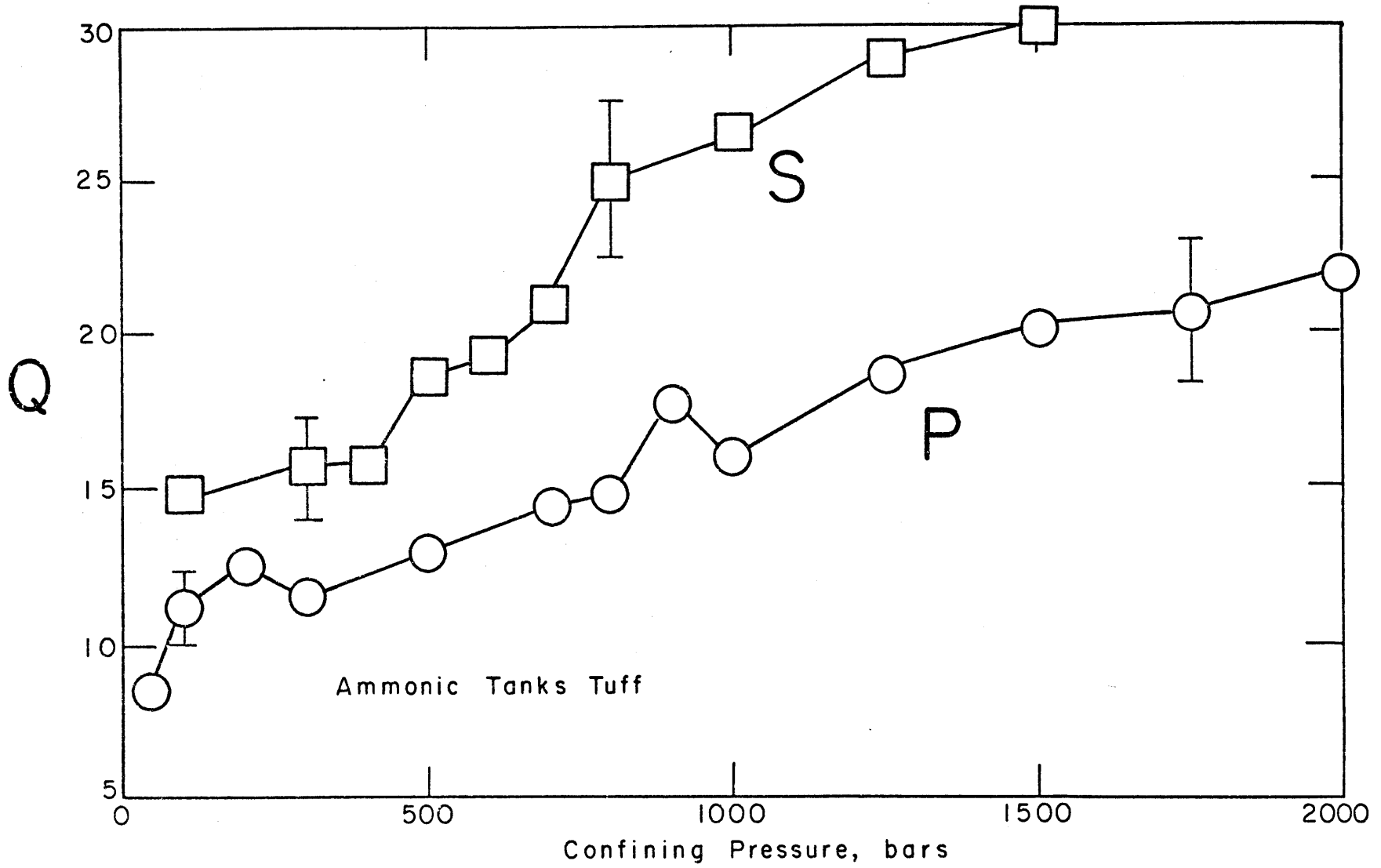


Figure 5-44

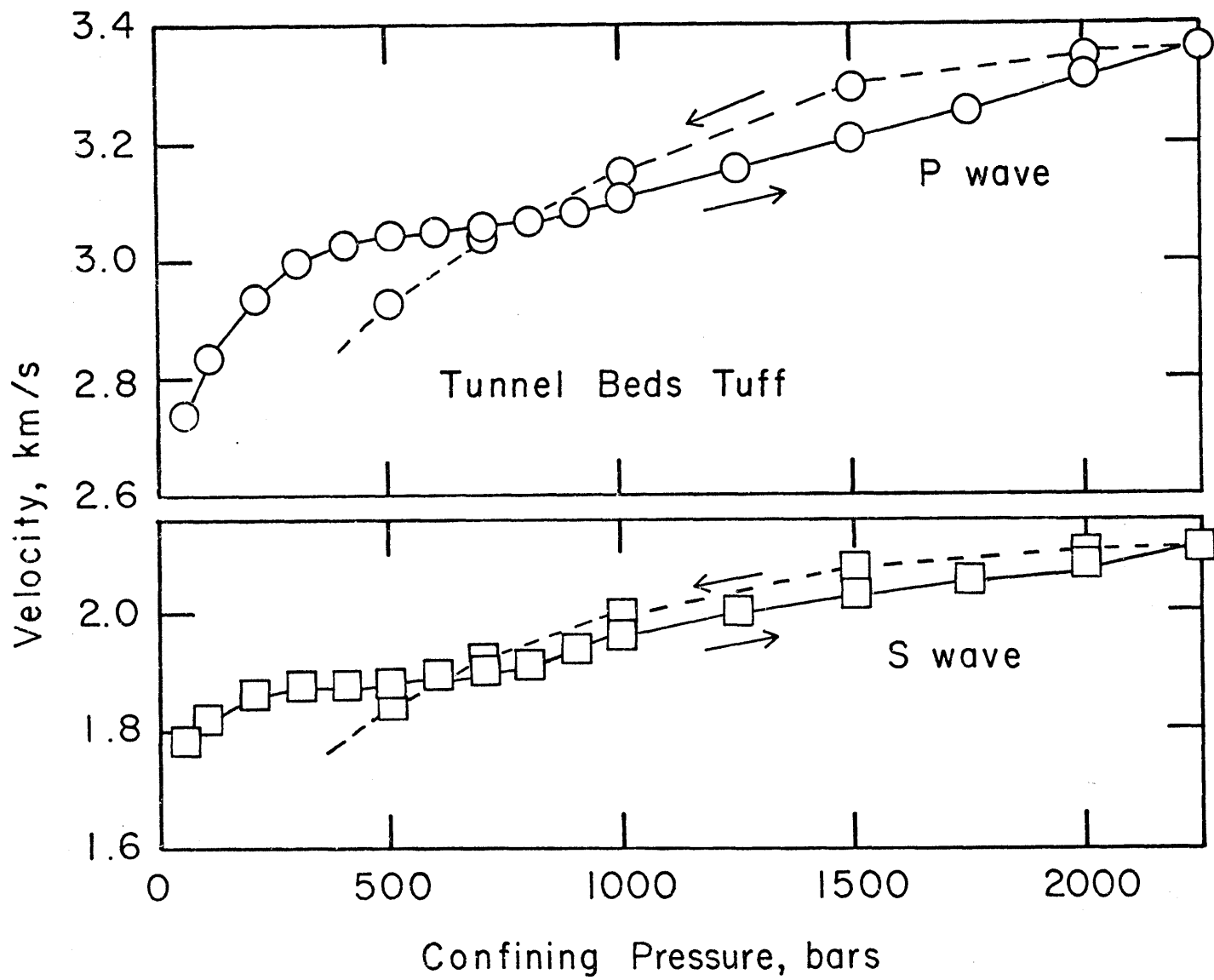


Figure 5-45

TB TUFF DRY P210

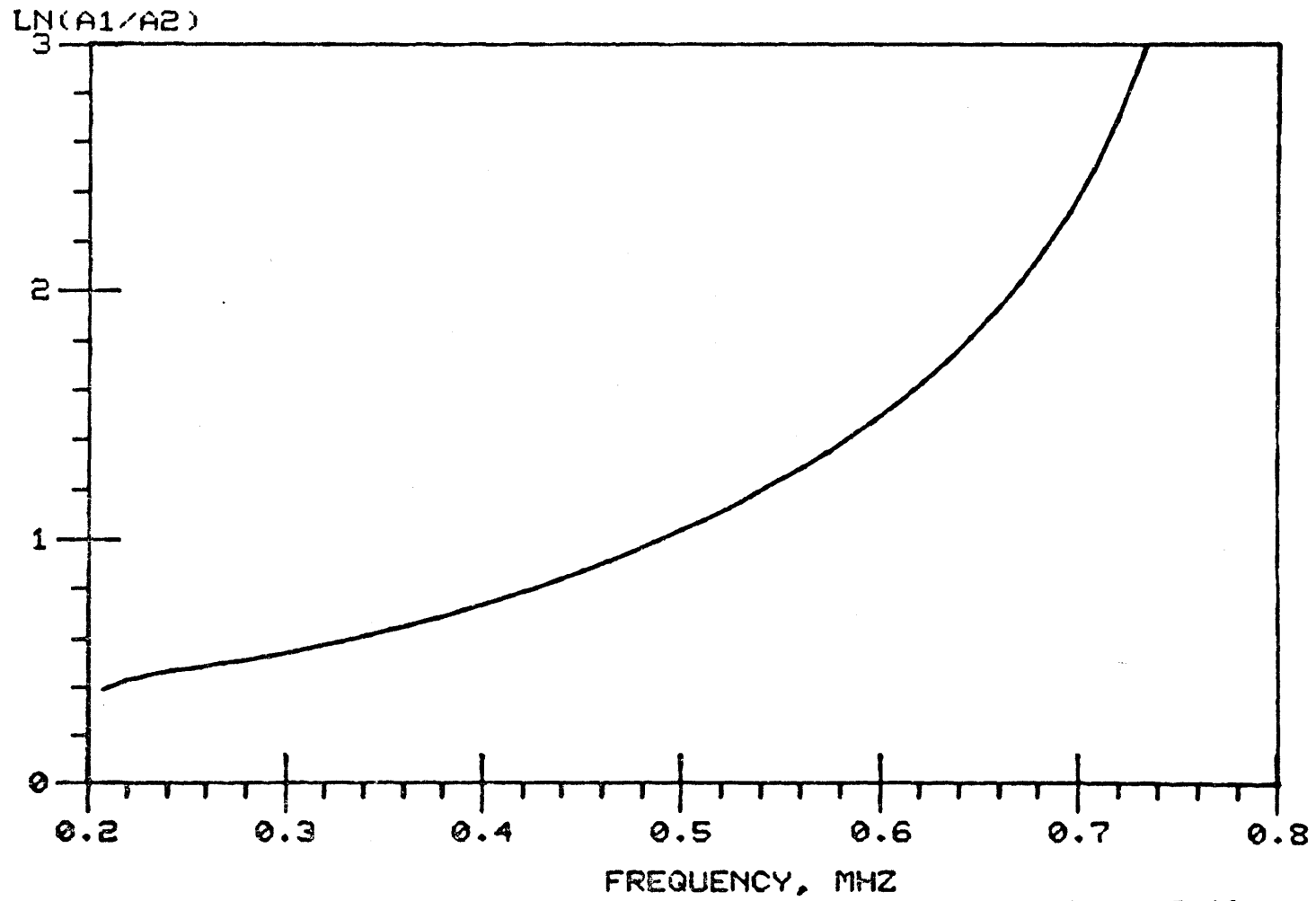


Figure 5-46

# Tunnel Beds Tuff - P and S waves

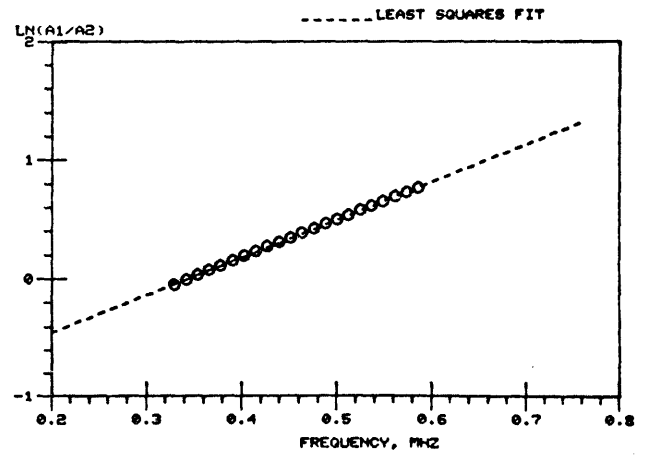
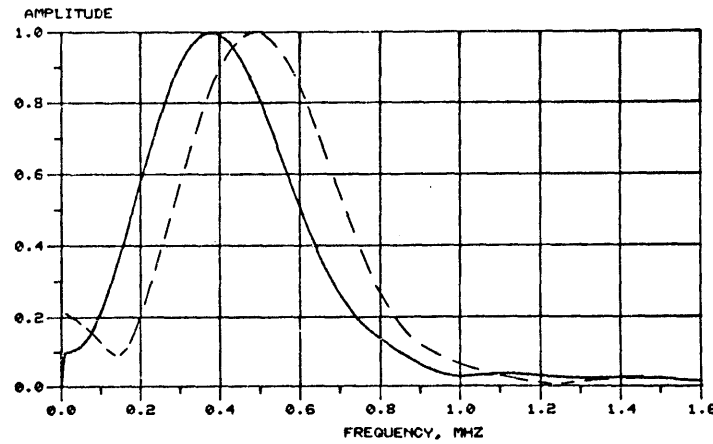
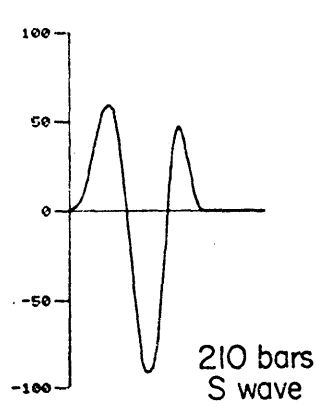
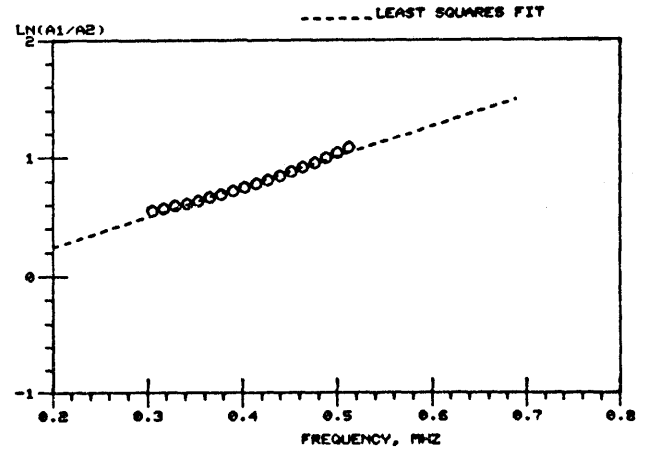
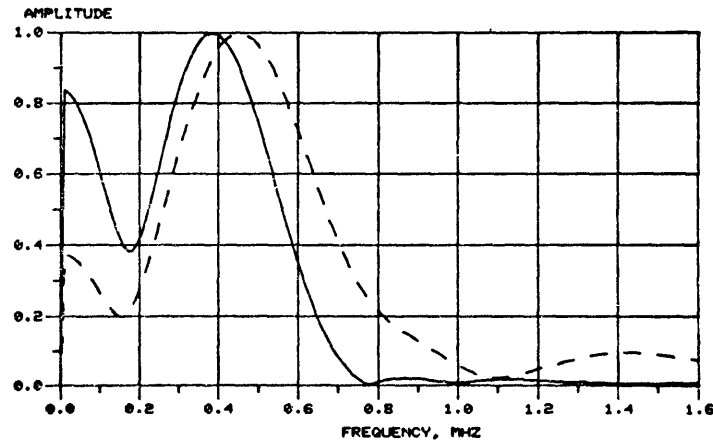
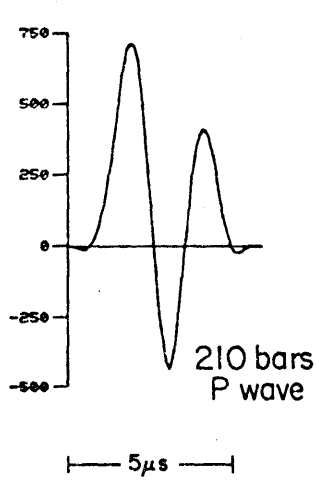


Figure 5-47

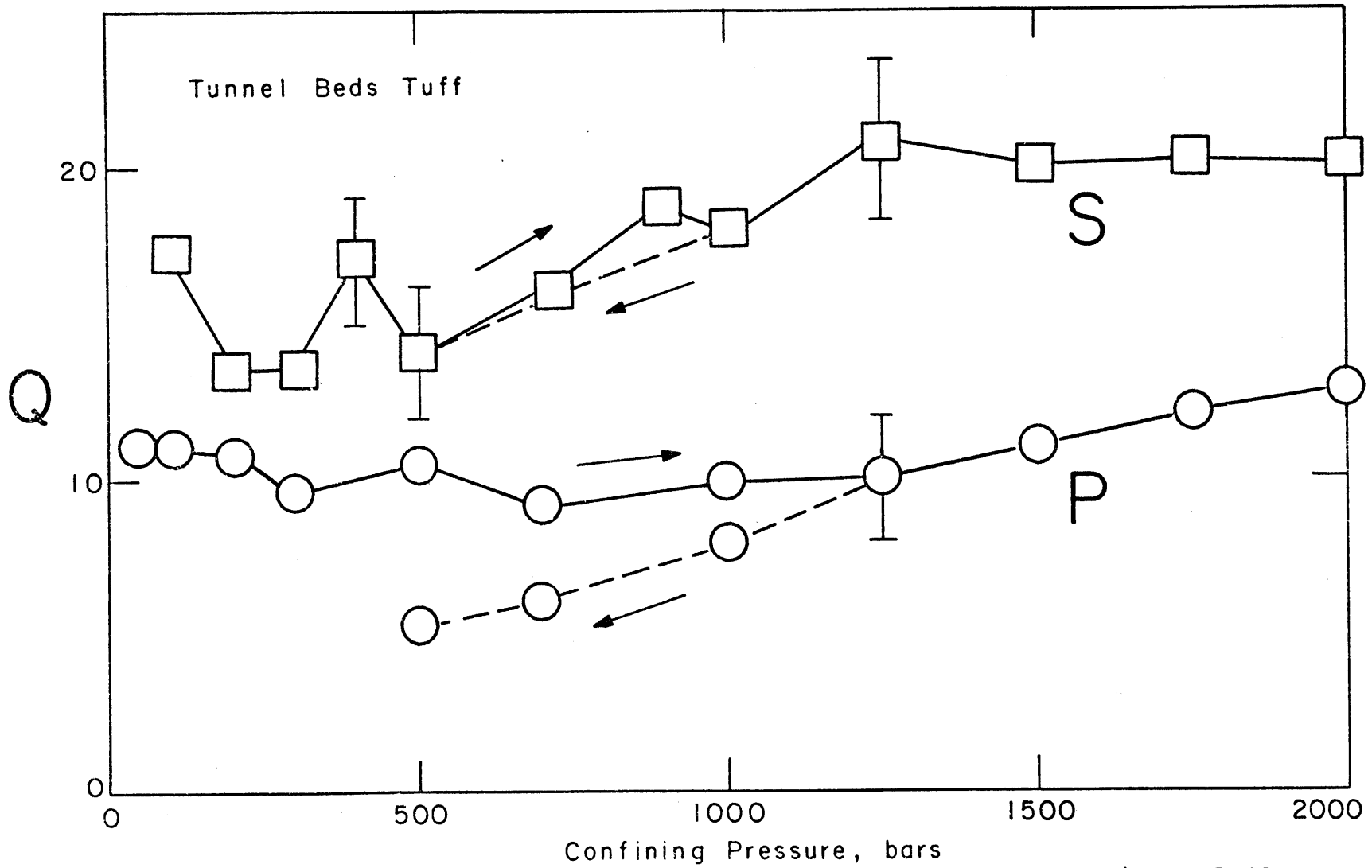


Figure 5-48



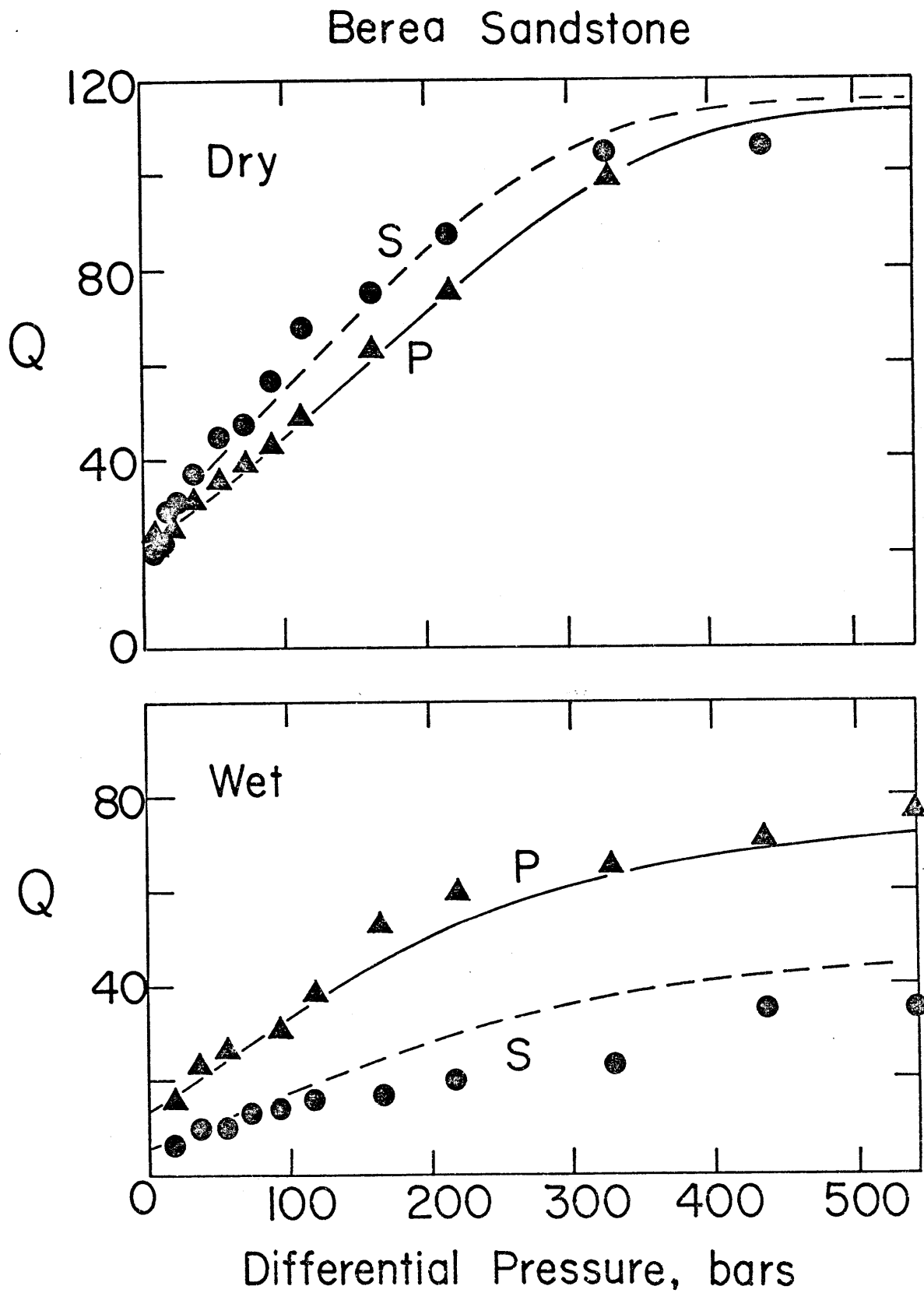


Figure 5-49

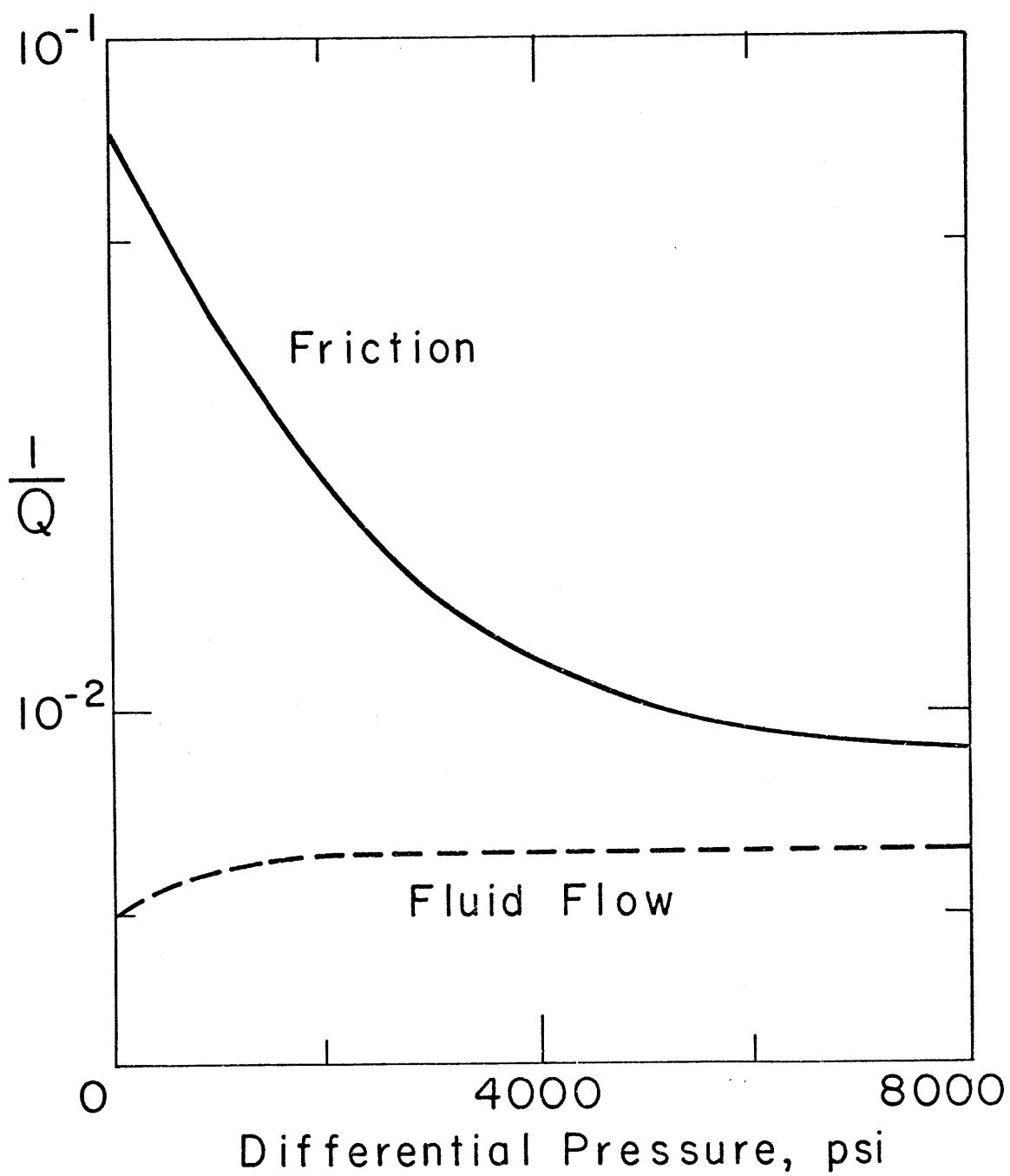


Figure 5-50

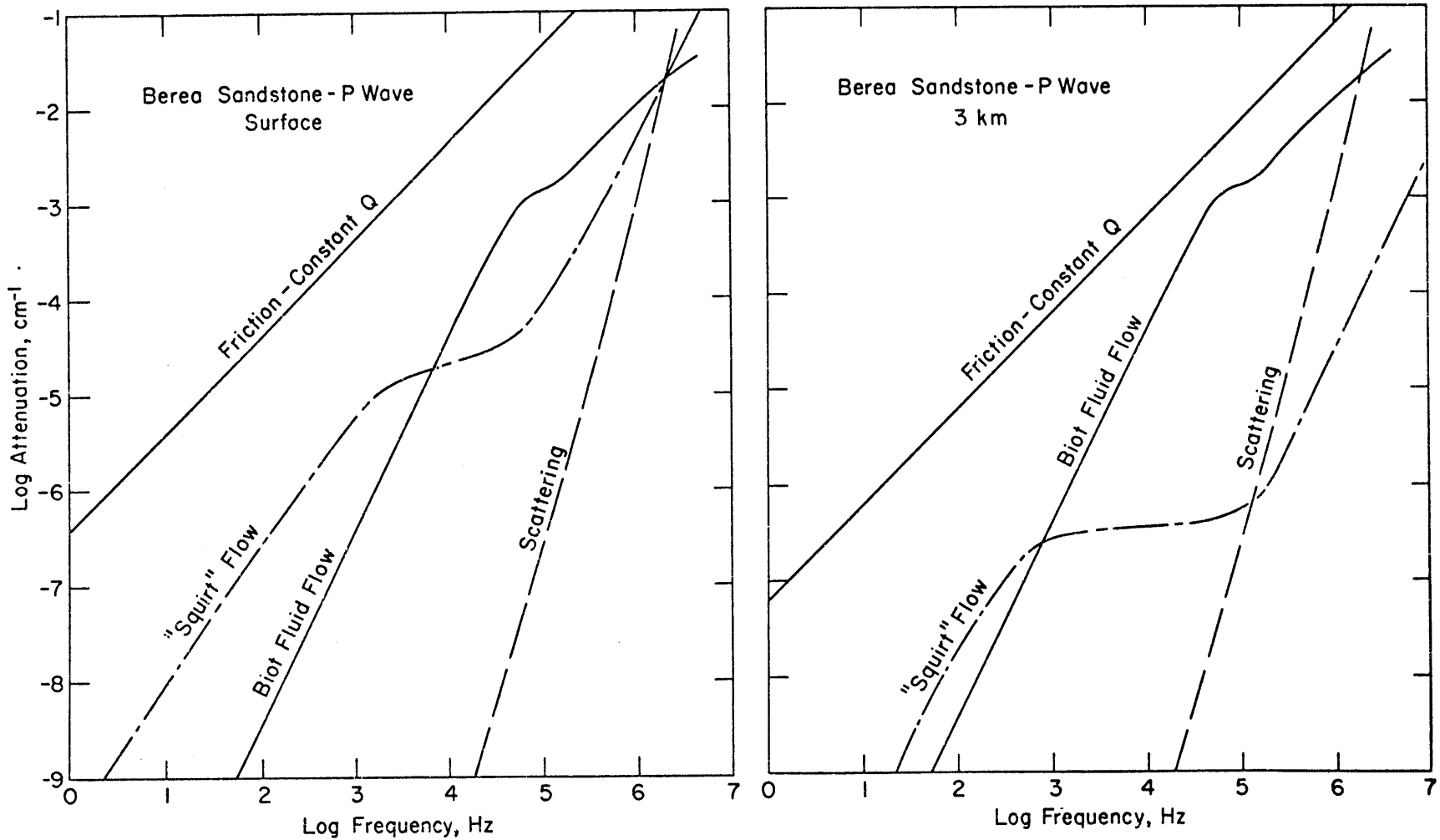


Figure 5-51

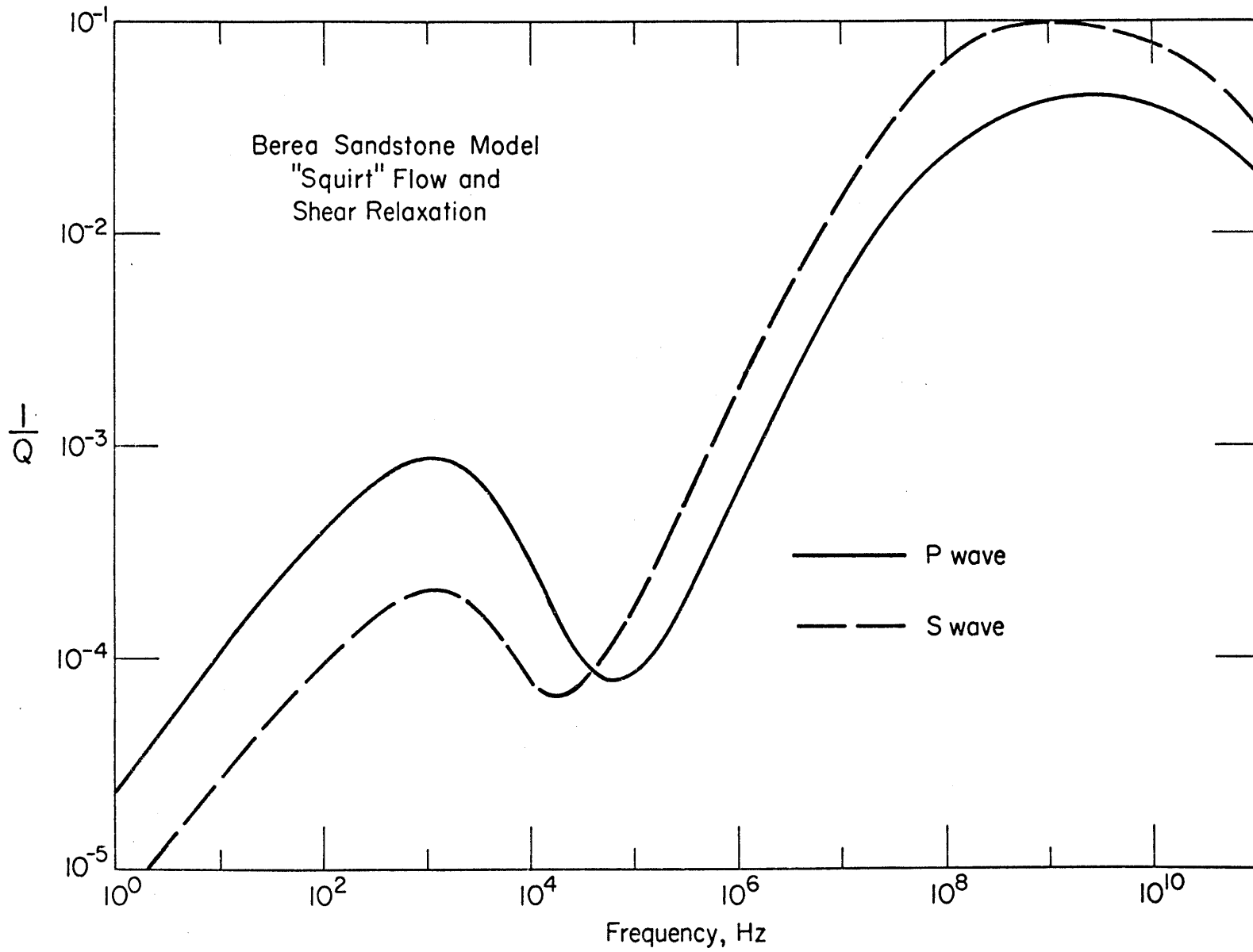


Figure 5-52

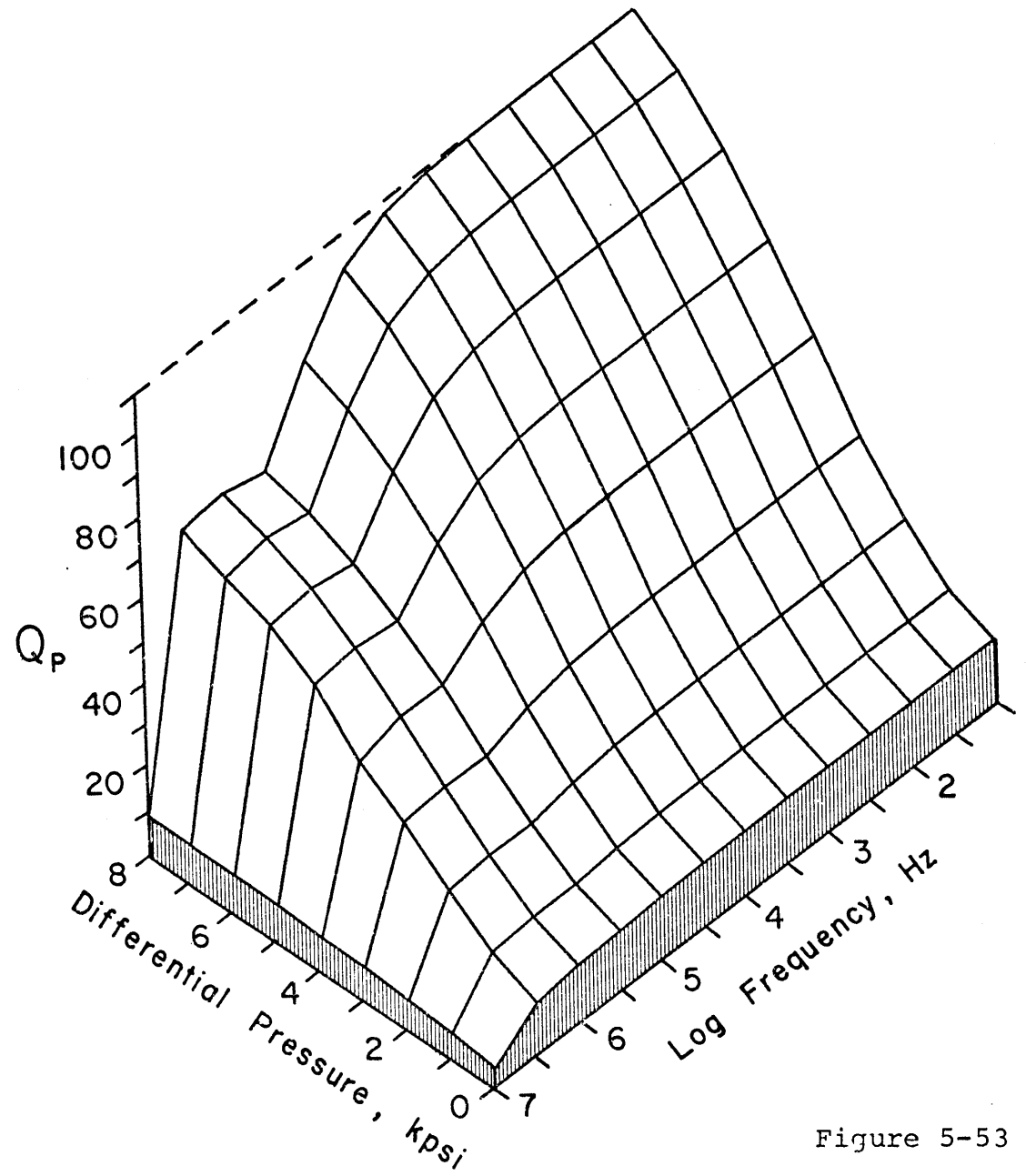


Figure 5-53

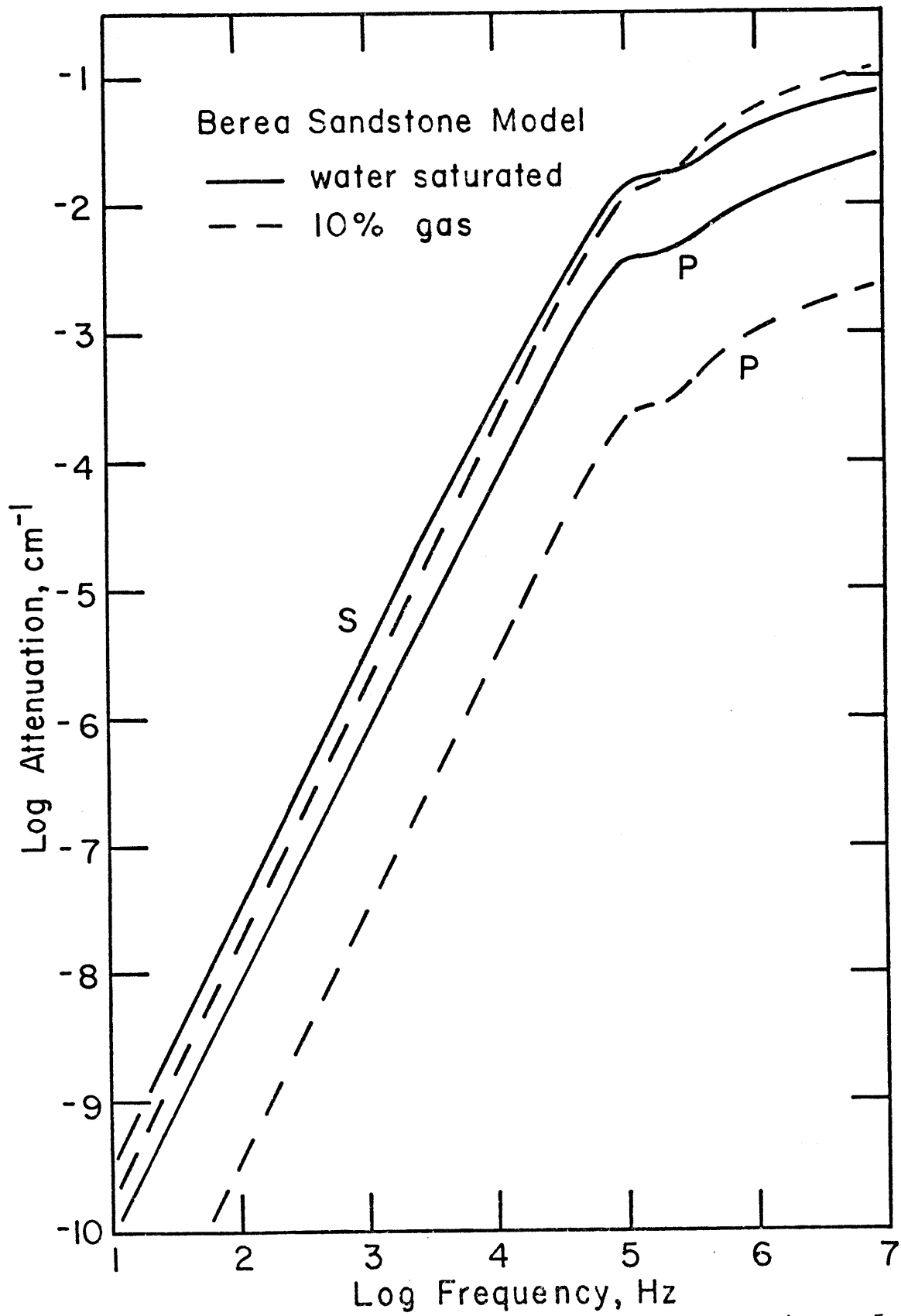


Figure 5-54

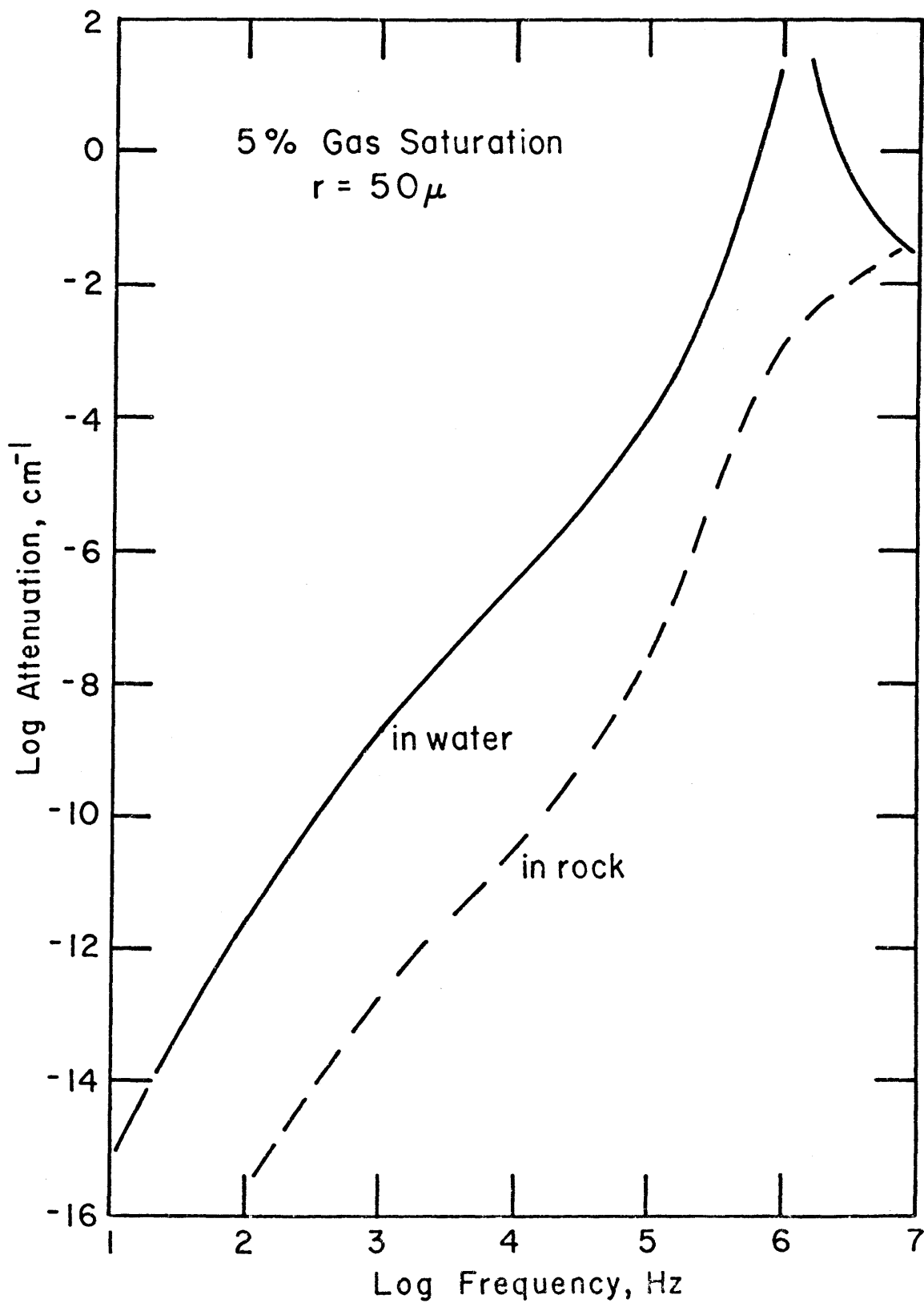


Figure 5-55

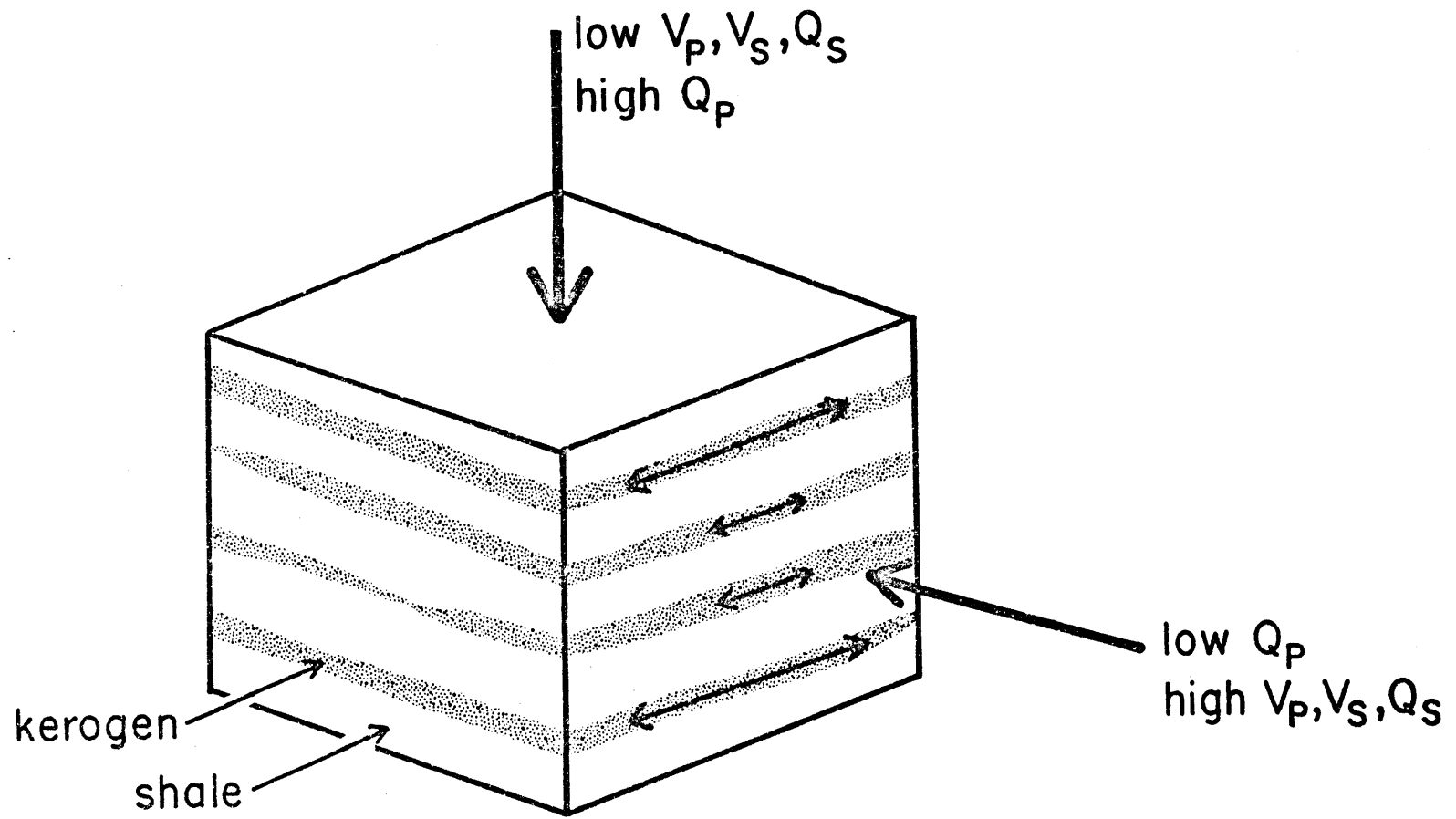


Figure 5-56



## CHAPTER 6

## CRACKS AND AMPLITUDE DEPENDENT ATTENUATION

One of the less satisfying aspects of modeling the ultrasonic data discussed in the previous chapter was the empirical nature of describing the friction mechanism. Yet, as we have seen, this mechanism is clearly dominant under most physical conditions in the upper crust. The experiments described in this chapter were designed to study the nature of crack friction in more detail.

The phenomenon of frictional attenuation is investigated along two fronts. First is the dependence of  $Q$  on strain amplitude. The careful reader has noted a rather large discrepancy between  $Q$  measurements obtained by dynamic resonance and ultrasonic pulse techniques. Either dry friction attenuation is frequency dependent or some other factor comes into play. A dependence on amplitude might explain the discrepancy in observed  $Q$  values. This possibility will be addressed.

Secondly, the effect of increasing crack density due to thermal stresses induced by temperature cycling on attenuation is studied. Since frictional attenuation depends primarily on the density of low aspect ratio cracks, it was first thought that one could obtain an independent test of the Walsh theory if the increase in

crack porosity could be determined from static stress-strain measurements. As will be seen, the thermal cycling experiments yielded results that abrogated this idea. In many cases,  $Q$  increased with thermal cracking. This will be interpreted in terms of volatile loss from sliding surfaces and increasing aspect ratios of cracks during thermal cycling. The effect of volatile loss is to increase the friction coefficient and thus prevent sliding at low strains. The widening of thin cracks, likely to contribute to attenuation due to friction, also increases  $Q$ .

It will also be seen that amplitude dependence is coupled to the effects of thermal cycling. This will provide a further means of understanding the importance of cracks in determining the overall attenuation.

### 6.1 Experimental Results

For most of the experiments described in this section  $Q$  values were obtained using the longitudinal resonant bar technique discussed in section 3.6. The samples were about 15 cm long by 0.635 cm in diameter producing fundamental mode frequencies in the 10-20 kHz range. One set of runs was done with a sample diameter of 1.27 cm.  $Q$  was obtained for maximum strain amplitudes,  $\epsilon_{\max}$ , varying from  $10^{-8}$  to  $10^{-5}$ . The samples studied include the Berea and Navajo sandstones, Plexiglas, Westerly

granite, Solenhofen limestone, and Frederick diabase. The latter two were chosen for their low crack porosity in the virgin state.

Strain amplitude may be adjusted by varying the voltage applied to the driving transducer (see Figure 4-11). Amplitude at resonance is found using continuity of stress across the transducer-sample boundary. Maximum strain in the transducer for the thickness (compressional) mode is given by:

$$\epsilon_t = \frac{t_{\max}}{t} = \frac{Vd_{33}}{t} \quad (6-1)$$

where  $t$  is the unperturbed transducer thickness,  $V$  is the peak driving voltage, and  $d_{33}$  is the piezoelectric charge coefficient perpendicular to the transducer face (3 direction). For PZT-4 transducers,  $d_{33} = 2.8 \times 10^{-10} \text{ m/V}$ . The stress,  $\sigma_t$ , is given by:

$$\sigma_t = E_{33}^D \epsilon_t$$

where  $E_{33}^D$  is the open circuit Young's modulus in the 3 direction and is equal to 1.18 Mbar. Applying continuity of stress, the maximum strain in the sample,  $\epsilon_{\max}$ , may be written as:

$$\epsilon_{\max} = \frac{\epsilon_t E_{33}^D}{2E_s} \quad (6-2)$$

where  $E_s$  is the Young's modulus of the sample. The factor of 1/2 is included since one end of the transducer is a free surface.

#### 6.1a Strain Amplitude Dependent Q

As discussed in sections 2.2a and 3.2, attenuation values for dry rocks obtained by dynamic resonance and ultrasonic techniques differ, the former yielding higher Q's. Since these measurements are generally made at different frequencies, one might possibly hypothesize a frequency dependent mechanism. However, no data support this. Q dependent on strain amplitude though, may provide an explanation. Most resonance experiments are carried out at low strains relative to those associated with ultrasonic pulses. If Q for low strains is higher than for high strains, the apparent discrepancy in the data may be resolved. This behavior is indeed observed for the dry Berea sandstone as shown in Figure 6-1 where Q and bar velocity are plotted as a function of maximum strain amplitude. Also shown for comparison is Q for amorphous Plexiglas over the same amplitude range. Behaving similarly to data reported by Winkler et al. (1977) for the Massilon sandstone, Q for the Berea rapidly decreases from a value of 75 to a value of 30 at a strain amplitude of about  $10^{-5}$ . This corresponds to a 60% decrease in Q. Velocity decreases by only 1%.

Comparison of the increasing amplitude curve versus decreasing amplitude shows nearly complete recovery of the initial  $Q$  value. As will be seen, this lack of hysteresis is observed for all the rocks studied and implies that little or no damage to the crack surfaces (assuming that attenuation is due to frictional sliding) occurs at high strains.

For the same range of strain amplitude,  $Q$  of the Plexiglas remains relatively constant and if anything, increases slightly. This fact strongly suggests that the presence of cracks in the rock is the controlling factor in producing amplitude dependent behavior.

A further experiment with the Berea sandstone was done using the ultrasonic pulse technique. The data from the resonance experiment are limited at the high amplitude range but imply that  $Q$  may approach a constant value. This was investigated by measuring  $Q$  from spectral ratios in a dry Berea at 45, 210, and 500 bars confining pressure with applied pulse voltages of 100 to 2000 volts. The results of this experiment must be interpreted with some trepidation since the acoustical properties of the transducers vary nonlinearly with applied voltage due to domain reorientation (Berlincourt et al., 1964). In particular, the mechanical  $Q$  of the transducer decreases with increasing voltage and thus the data obtained for higher amplitudes may be biased

to lower  $Q$  values.

The results of the pulse experiment are shown in Figures 6-2 and 6-3. It is difficult to directly compare these data with those of Figure 6-1 in terms of strain amplitude since equations like 6-1 strictly apply to frequencies well below the transducer resonance. It is safe to say, however, that the amplitudes one is dealing with are at least as high as the highest obtained for the resonance experiment. In any event, it is wise to use the data in Figures 6-2 and 6-3 for qualitative interpretation only.

For all three confining pressures, there is a clear decrease in  $Q$  for P waves as a function of amplitude. For S waves, however, there is no such significant change. As mentioned by Walsh (1966) it is possible that high amplitude P waves may be able to close open cracks and then cause them to slide. This process increases the number of cracks contributing to attenuation. For S waves there are fewer orientations of cracks relative to the direction of propagation that can slide, thus the amplitude effect would be smaller. Also, the efficiency of the S wave transducers is less than for P waves and for a given voltage the strain amplitude in the rock would be less. But, an arguement against amplitude dependent  $Q$  behavior in this case is that virtually no

change in velocities were observed as shown in Figure 6-4. If the resonance experiment can be taken as a guide, velocity should decrease with  $Q$ .

This takes us back to the possibility that the observed decrease in  $Q$  is due to the change in transducer properties where for HDT-31 (PZT-4) piezoelectric material,  $Q$  decreases from over 500 to well under 100 in the voltage range used. It is difficult to understand, however, why the S waves are not affected as the P waves. At best, one must say that the results of the ultrasonic work on the Berea are inconclusive as regards to the amplitude dependence of  $Q$ .

To further investigate the amplitude effect, another resonance experiment was run, this time with the Navajo sandstone. In Figure 6-5,  $Q$  is plotted as a function of strain amplitude. One sees nearly the same behavior as observed for the Berea - constant  $Q$  at low amplitudes with a sharp decrease at a strain amplitude of  $10^{-6}$ . The  $Q$  values, 60 at low amplitude and 28 at high amplitude, are lower than those observed for the Berea. This is in contradiction with the ultrasonic results presented in the last chapter where  $Q$  for the Navajo was higher than for the Berea. It may be, however, that this is an effect of air humidity, the Berea experiment being run in the winter (40% relative humidity) and the Navajo run

in the summer (75% humidity).

Does the amplitude dependence explain the difference between reported resonance and ultrasonic measurements? For the most part - yes.  $Q_p$  values at low pressure obtained in the last chapter using ultrasonic pulses are compared to the results just described for the dry Berea and Navajo sandstones in Table 6.1. Here, low and high amplitude resonant bar  $Q$  values are listed along with the ultrasonic P wave values. Clearly the high amplitude results from the resonance technique are comparable to the ultrasonic data. The data, however, are limited and it would be premature to rule out other mechanisms - even frequency dependent dry friction - as supplements to amplitude dependence in interpreting the discrepancy between the two experimental methods. It is inescapable, however, that amplitude dependence must be considered if any comparison is to be made between not only different experimental techniques but also between laboratory and field data.

#### 6.1b Thermal Cracking and Amplitude Dependent $Q$

The data in the preceding section strongly suggest that cracks in the rock are important in determining the amplitude dependent behavior of  $Q$ . Thermal cycling presents a unique opportunity to form cracks in rock. Thus, if information on the induced crack porosity is



available, the change in  $Q$  might be quantified in terms of crack density. Intuitively, one would expect that  $Q$  would decrease with increasing thermal cycling. As will be seen, this is not always the case. In fact, one of the more interesting results of this chapter is what can be said about the nature of thermal cracking mechanisms.

Samples of Frederick diabase, Solenhofen limestone, and Westerly granite, 0.635 cm in diameter, were thermally cycled up to a maximum temperature of 600°C at room pressure in order to induce cracking. Second samples of each rock were cycled in separate runs in order to check reproducibility. As discussed in section 3.8b, the heating and cooling rates were kept under 2°C/minute. The samples were exposed to the maximum temperature for at least one hour. Data from Johnson et al. (1978) suggest that this time is required for the decay of acoustic emissions (and thus cracking) in a rock at constant temperature.

Other samples of each rock were slowly cycled to maximum temperatures of 400° and 800°C. These were used for static stress-strain measurements to obtain a handle on the induced crack density. Finally, samples of Solenhofen limestone and Frederick diabase, 1.27 cm in diameter, were subjected to thermal cycling at high

heating rates of about 20°C/minute. Westerly granite did not remain coherent during these runs and was thus not used.

In both procedures, after cooling the samples were left in laboratory air for several days. All attenuation measurements were made at room temperature and pressure in air. The relative humidity in the laboratory varied during the course of the experiments from 45 to 75%. This appeared to have had no bearing on the Q measurements. In fact, several samples were saturated with water and then allowed to dry with little change in the results.

Thermally induced crack porosity may be characterized using static stress-strain analysis. Linear strain as a function of hydrostatic confining pressure is shown for virgin and thermally cycled samples of diabase, limestone, and granite in Figures 6-6 through 6-10. For Westerly granite, data is shown for two orientations: the stiff (parallel) and soft (perpendicular) directions. The induced crack porosities for cycling to 400 and 800° are found using the method described in section 4.6 and the results are listed in Table 6.2. The increase in porosity is generally proportionally greater for the samples cycled to 800° than those heated to 400°. The shapes of the thermally induced cracks seem also to depend on the temperature achieved during cycling. In the diabase, for

the 400° curve, the cracks appear to be of fairly high aspect ratio. The closure pressure is relatively high (>1000 bars) and there is little curvature at low pressures. The case for higher aspect ratio cracks in the 400° cycled Westerly samples is not nearly as clear as for the diabase. The effect is masked by preexisting low aspect ratio cracks. However, evidence to be presented later suggest relatively higher concentrations of wide cracks compared to thin ones produced by thermal cycling to temperatures no greater than 400°C. In both the diabase and granite, heat treatment to 800° not only produces a dramatic increase in crack porosity but also, these cracks seem to be of lower aspect ratio. In both cases, the curvature of the stress-strain curve at low pressures is strikingly high compared to the other runs. For the Solenhofen limestone, however, a rapid change in crack porosity is not observed after heating to 800° nor are the induced cracks of particularly low aspect ratio.

Q values at low strain amplitude and bar velocity as functions of maximum temperature obtained in slow heating and cooling cycles for the diabase and limestone are shown in Figures 6-11 and 6-12. Q and V for the two core directions of Westerly are shown in Figure 6-13. For all three rocks, two separate experiments were run to

check reproducibility (with the exception of the "stiff" core of Westerly granite). These are denoted on the figures by different symbols. While the experiments were run under different humidity conditions, there is quite satisfactory agreement between the two runs for all three rocks.

The remarkable aspect of the data is the dramatic increase in  $Q$  for all the samples at maximum temperatures of  $400^\circ$  and less. Simultaneously, velocity decreases - quite substantially for the Westerly granite which contains more cracks initially. The changes in velocity seen for the granite are nearly identical to those reported by Johnson et al. (1978) in a similar experiment on Westerly ( $Q$  values were not obtained). Anisotropy in Westerly is apparent, amounting to 10% for velocity and 25% for  $Q$ . The velocity changes in the diabase and limestone are low compared to the granite for temperatures below  $400^\circ$  followed by a rapid change above that point. This is reflected by the changes in crack porosity upon thermal cycling listed in Table 6.2. It is clear then, from all the data, that  $Q$  increases up to a point, even though crack porosity is also increasing. This change in  $Q$  is also apparently independent of orientation as shown for the Westerly granite in Figure 6-13.

Between  $400$  and  $500^\circ$ , however, the trend in  $Q$

reverses and in two of the three cases,  $Q$  decreases substantially. These data are very similar to those reported by Todd et al. (1972) for Westerly granite and Fairfax diabase. The high temperature  $Q$  values of the limestone do not follow the form of the other two rocks, showing only a slight decrease. This difference might have been expected from the static measurements where the Solenhofen was the only sample not exhibiting a large increase in low aspect ratio cracks at 800°. It should be noted that the decrease in  $Q$  above 400° observed for the diabase and granite is not initially due to the  $\alpha$ - $\beta$  transition in quartz which does not occur until 573°C.

$Q$  and bar velocity for the 1.27 cm diameter cores of rapidly heated limestone and diabase are shown in Figures 6-14 and 6-15. The behavior of  $Q$  as a function of maximum temperature for the limestone is clearly opposite that observed for low heating rates. For the diabase, there is an initial decrease in  $Q$  at 200° followed by a gradual rise to a maximum at 500° although the  $Q$  values at this point are far below those obtained by slow heating even though the sample here was kept at temperature for at least one hour as before. A sharp decrease in  $Q$  is noted between 500 and 600°C probably due to the phase transition in quartz. In cycling to

800°C, a marked change in the sample appearance was noted. This was accompanied by a further decrease in  $Q$  and a very rapid decrease in velocity.

These results imply that a different crack producing mechanism is operative for high heating rates. Compared to the slow rate, one might expect that finer (lower aspect ratio) cracks are generated. The data are more conclusive for the limestone where not only  $Q$  decreases continuously but the decrease in velocity is larger than for the slow heating rate case. For a given volume concentration, lower aspect ratio cracks produce larger changes in the elastic moduli compared to high aspect ratio cracks (Toksöz et al., 1976). Apparently in the diabase, permanent outgassing of volatiles has a compensating effect on the generation of thin cracks at temperatures between 300 and 500°C. The minor contribution of this same effect may be observed in the limestone where  $Q$  levels off between 400 and 600°C.

Amplitude dependent behavior is also coupled to the nature of thermally induced cracks.  $Q$  as a function of maximum strain amplitude is shown for several temperatures each for the three slowly cycled rocks in Figures 6-16 through 6-18. Amplitude dependence, not readily apparent in the virgin states of the diabase and limestone, appears for thermally cycled samples. The important

feature to note from the data is that while  $Q$  increases as a function of temperature for low strains, the transition from low to high strain amplitude behavior migrates to lower amplitudes. It also appears that the  $Q$  values for high strains tend to converge. Once the maximum temperature exceeds  $400^{\circ}\text{C}$  and the  $Q$ 's at low strains decrease, the amplitude transition moves back to higher strains. The exception to this is the Solenhofen limestone. Again it is apparent in this case that the nature of the cracks obtained at high temperature are different than in the granite or diabase.

Amplitude dependent behavior was also observed for the rapidly heated samples although for a given maximum obtained temperature, the transition seems to occur at a higher strain than for the slowly heated samples. This is shown in Figure 6-19 for the Frederick diabase where  $Q$  as a function of amplitude is plotted for the virgin rock and the two heat treated runs. The amplitude dependence for the  $20^{\circ}\text{C}/\text{minute}$  treated sample is not as clearly defined as for the other run. Either the transition does occur at higher strains or the amplitude dependence is smeared out or reduced somewhat.

The behavior of amplitude cycling on  $Q$  is nearly identical for all the rocks including the sandstones shown in Figures 6-1 and 6-5. Typical curves for the diabase,

limestone and granite are shown in Figures 6-20 through 6-22. Again, the lack of hysteresis implies little or no rock damage at high strain amplitudes.

## 6.2 Mechanisms of Amplitude Dependence, Volatile Loss and Thermal Cracking

The data presented in the preceding section will be interpreted in terms of sliding contact area, degassing of volatiles from the contact surfaces, and most importantly, the nature of the cracks produced by thermal cycling.

In this section first the amplitude dependence of attenuation in general is discussed. Then, volatile loss as a result of heating will be discussed particularly in terms of comparing the results of this thesis with data acquired on lunar samples and terrestrial analogs.

Mechanisms for thermal cracking and their implications in terms of crack characteristics will then be presented.

This will be followed in the next section by a discussion of the above results in relation to the Q data obtained.

### 6.2a Amplitude Dependent Attenuation

It is almost invariably assumed in the literature that attenuation is independent of strain amplitude. While this may indeed be true for strains associated with teleseismic waves ( $\epsilon < 10^{-6}$ ) numerous experimental studies, including this one, have shown amplitude dependent behavior at higher strains ( $\epsilon > 10^{-6}$ ). Gordon and Davis



(1968) examined  $Q$  as a function of amplitude ranging from  $10^{-9}$  to about  $10^{-4}$  using a resonant bar at 90 kHz. The samples studied included granite, basalt, dunite, quartzite, and others. The results obtained were similar to the data presented in the previous section.  $Q$  was observed to be constant at low strains, decreasing sharply for strain amplitudes greater than about  $10^{-6}$ . Their explanation that these features are due to rock damage is not valid since we have seen little hysteresis effect upon unloading. Other studies by Peselnick and Outerbridge (1961) on Solenhofen limestone under torsional vibrations at 1 Hz and Gordon and Rader (1971) for the Chester granite produce similar results.

The theoretical basis for amplitude dependent attenuation is not well developed. The difficulty lies in the fact that such behavior is very model dependent. The important parameter to consider in the development of models is the product of the frictional stress,  $\tau_f$ , and the contact area of sliding,  $a$ . If  $\tau_f \cdot a$  is linear with strain amplitude, then  $Q$  is independent of amplitude. If  $\tau_f \cdot a$  is parabolic with amplitude, then  $Q^{-1}$  linearly depends on strain and so on.

While not explicitly dependent on strain amplitude, Walsh (1966) admitted that his model could be considered amplitude dependent if one is willing to assume that high

amplitude waves are able to both close and then slide non zero width cracks.

A friction model producing a more explicit amplitude dependence was developed by Mindlin and Deresiewicz (1953) for elastic spheres in contact. The attenuation is given by:

$$Q^{-1} = \frac{2A\xi}{9\kappa F_n} \quad (6-3)$$

where  $A$  is the amplitude of an applied shear force (assumed  $\ll \kappa F_n$ ),  $\kappa$  is the coefficient of friction, and  $F_n$  is the normal force acting on the area of contact.  $\xi$  is a dimensionless function depending on the orientation of the contact surface relative to the propagation direction of the seismic wave. The spherical contact model, while a highly specialized geometry, has lately served as a basis for a crack friction model proposed by Mavko (1978). In his treatment, Mavko assumes a flat, two dimensional, tapered crack undergoing plane strain sliding. The result of his analysis is that  $Q^{-1}$  is linearly dependent upon strain. Again, this is a direct result of  $\tau_f \cdot a$  being parabolic with amplitude. In an attempt to explain the strain independent behavior of  $Q$  at low amplitudes, Mavko proposes that linear mechanisms such as thermoelasticity mask the attenuation due to friction. As will be shown later, the data presented in

the last section do not necessarily support or disprove this hypothesis. But, it may be that cracks and sliding friction play a role in the observed attenuation even at low strain amplitudes.

The data presented in this chapter have shown that the amplitude dependence of attenuation, while not necessarily important at seismic amplitudes, is most important for understanding the nature of the friction mechanism. Section 6.3 will come back to the basis for amplitude dependence - directed more specifically towards the data obtained for the thermally cycled rocks.

#### 6.2b Volatile Loss

It is widely accepted that small amounts of volatiles, most commonly water, produce large effects in attenuation. Since the earliest observations by Born (1941) the effect of absorbed water vapor on  $Q$  has been studied in detail. Perhaps the most exhaustive survey of the effects of volatiles has been carried out in conjunction with the study of the acoustical properties of lunar rocks (Tittmann et al., 1973, 1974, 1975, and 1976). As is discussed in Chapter 3, extremely high in-situ  $Q$  values  $>3000$  have been observed for the moon (Latham et al., 1974; Dainty et al., 1976). In their series of experiments, Tittmann et al. have shown that these high values can be duplicated in the laboratory by repeated thermal cycling

and application of hard vacuum ( $10^{-7}$  torr) for both lunar samples and terrestrial lunar analog basalts. The results of an experiment described in Tittmann et al. (1975) for which a  $Q$  of 3100 was obtained for lunar rock 70215,85 are shown in Figure 6-23. Here  $Q$  and velocity are plotted as functions of vacuum pressure in torr. The solid lines indicate runs in which the vacuum was increased while the temperature was held constant. Dashed lines show where the sample was slowly thermally cycled to  $300^{\circ}\text{C}$ . For example, on run AB, the pressure was reduced from atmospheric to  $10^{-3}$  torr while the temperature remained at room value. On path BC, however, the pressure was held constant while the rock was thermally cycled.

While the changes in velocity are small compared to changes in  $Q$ , it is important to notice that velocity decreases only when the sample is thermally cycled. Furthermore, it is apparent that the offset AF in  $Q$  at room temperature and pressure is due mostly to changes induced by thermal cycling.

Tittmann et al. have hypothesized that these effects are due almost entirely to outgassing of volatiles from the rock. To study this effect, Tittmann et al. (1976) subjected a terrestrial analog of a lunar basalt to a vacuum of  $10^{-8}$  torr and cycled to a maximum temperature of  $400^{\circ}\text{C}$  resulting in a  $Q$  (at room temperature) of 740.

The sample was then exposed for 30 minutes to saturated vapors of volatiles at ambient pressure in the absence of water. Several volatiles, free of water as an impurity, resulted in significant drop (40-50%) in  $Q$  with small (1-2%) reductions in velocity. Water vapor, though, produced the largest change, a 60% decrease in  $Q$  and a 4.4% decrease in velocity. Interestingly, the viscosity of the volatile had little effect on  $Q$ . This supports the contention made in Chapter 3 that boundary or imperfect lubrication theory is appropriate for the friction mechanism in rocks. Volatiles with different dipole moments produced similar changes in  $Q$  but ones with higher moments (e.g. water) proved more difficult to outgass.

#### 6.2c Thermal Cracking

It is possible that a large portion of the increase in  $Q$  observed in both the lunar rocks and those studied here is due not to outgassing but to changes in crack densities and shape as a result of thermal stresses during cycling. Two mechanisms for thermal cracking have been hypothesized and we will show that each one produces cracks of quite different characteristics. The first mechanism opens cracks at low pressure due to differential thermal expansion across grain boundaries and preexisting cracks. The second is the propagation of cracks induced

by thermal gradients.

Thermal expansion in rocks measured at room pressure is generally found to be irreversible in thermal cycles. Residual strains remain after a heating and cooling cycle. Much of the data can be explained by thermally induced cracks (Richter and Simmons, 1974) and it is found that thermal expansion is reversible in temperature if the measurements are made at a pressure high enough to close these cracks (Wong and Brace, 1978).

For low thermal gradients in the sample, internal stresses and cracking are induced by mismatches in thermal expansion across the grains. This will occur even in monomineralic rocks such as the Solenhofen since thermal expansion is a tensor quantity and grains of different orientations produce differential expansion coefficients. As will be seen, this mechanism is operative at the low heating and cooling rates (<2°C/min) primarily used in this work. For this case, the internal stress,  $\sigma$ , induced by a temperature change,  $\Delta T$ , is given by (Myklestad, 1942; Edwards, 1951; Eshelby, 1957):

$$\sigma \approx E\Delta\alpha\Delta T \quad (6-4)$$

where  $E$  is the Young's modulus and  $\Delta\alpha$  is the differential thermal expansion.

There is a great deal of evidence to support the hypothesis that expansion and contraction of grains at

thermal equilibrium has the effect of opening cracks. Differential strain analysis of several rock types including Westerly granite and Frederick diabase (Cooper and Simmons, 1977) show that the peak in crack porosity as a function of closure pressure shifts to higher closure pressure and thus higher aspect ratio cracks as a result of thermal cycling. Wong and Brace (1978) have shown that the pressure required to produce reversible thermal expansion also increases after cycling. These effects have been observed qualitatively in Figures 6-6 through 6-9 showing linear strain as a function of pressure. As was noted in section 6.1b, while the effect of cycling a rock to 400°C is to increase the overall crack porosity, these seem to be of high aspect ratio. This is most evident for the diabase and limestone, more or less crack free in their virgin states. Again note that further heating to 800°C produces a dramatic change in the crack porosity for the diabase and granite. It is possible that above 400°C, the rocks are unable to accommodate any more thermal expansion induced strain and low aspect ratio cracks are propagated. Thus we see a sharp increase in strain for low confining pressures. The change for the Solenhofen at 800° (Figure 6-7) is not nearly as dramatic and this is reflected in the Q values which did not suffer a dramatic decrease for maximum

temperatures above 400°C. The limestone probably deforms plastically at these temperatures and thus fine crack growth is inhibited.

Perhaps the most concrete evidence for crack widening due to thermal expansion mismatch at cycling temperatures no greater than 400°C has been obtained by direct observation using a scanning electron microscope (SEM). Sprunt and Brace (1974) used SEM photographs to determine the form and distribution of microcracks in both virgin and stressed crystalline rocks. Figure 6-24 from their paper shows graphically, the effect of thermal cycling to 400°C in Chelmsford granite. Clearly, thin preexisting cracks have been widened and new, fairly wide, cracks have been formed at the grain boundaries. Figure 6-25, also from Sprunt and Brace, shows the aspect ratio distribution of unstressed (virgin) and thermally stressed Westerly granite. There is a decrease in the number of low aspect ratio cracks ( $10^{-4}$ ) while a substantial increase in the number of cracks with aspect ratios of  $10^{-2}$  is observed.

In the second mechanism for thermal cracking, local thermal gradients in the rock may induce crack growth. These gradients occur in the transient stage before thermal equilibrium. Goodier and Florence (1964) have shown that for a Griffith crack of length  $l$ , and specific



fracture surface energy,  $S$ , crack growth is initiated if the temperature gradient,  $\tau$ , exceeds a critical gradient,  $\tau_c$ , given by:

$$\tau_c = \frac{8S}{2\pi E\alpha (\ell/2)^2} \quad (6-5)$$

$E$  is the Young's modulus,  $\alpha$  the thermal expansion coefficient and the solid material is assumed to be homogeneous and isotropic. Wong and Brace (1978) have estimated  $\tau_c$  to be  $313^\circ\text{C}/\text{mm}$  for Westerly granite.

The actual gradient achieved in the sample is a function of the heating rate, thermal properties of the solid, and the geometry. From solutions to the heat conduction equation for an infinite cylinder uniformly heated at its surface at a rate,  $\dot{\theta}$ , Russell (1936) showed that the maximum gradient (at the surface) is approximated by:

$$\frac{\partial T}{\partial r} = \frac{1}{2} \frac{\dot{\theta} r_0}{\kappa} \quad (6-6)$$

where  $\kappa$  is the thermal diffusivity and  $r_0$  is the radius. Taking the sample dimension  $r_0 = 64 \text{ mm}$  and  $\kappa = 1.2 \text{ mm}^2/\text{s}$  with  $\dot{\theta} = 2^\circ\text{C}/\text{min}$ , we find  $\partial T/\partial r = 1.8^\circ\text{C}/\text{mm}$ , far below the critical value obtained from the Goodier and Florence theory. This theory may be of little quantitative use, however. Indirect evidence of the heating rate required to induce crack growth has been obtained by Todd (1973).

For rates of 5°C/min and higher in samples of 2.5 cm radius, acoustic emissions and increasing residual strain with heating rate imply significant thermal gradient cracking. Applying equation 6-6 for  $\dot{\theta} = 5^\circ\text{C}/\text{min}$  and  $r_0 = 250 \text{ mm}$ , we find  $\partial T/\partial r = 8.68^\circ\text{C}/\text{mm}$  which may be used as a critical gradient. It is clear that if one can indeed use this value as a guide, it is difficult to induce gradient cracking in the 0.64 cm samples used in this thesis even at high heating rates. For the 1.27 cm diameter samples, however, with  $\dot{\theta} = 20^\circ\text{C}/\text{min}$ , we obtain  $\partial T/\partial r = 17.64^\circ\text{C}/\text{mm}$ .

One may assume then, for the samples of 0.64 cm diameter with a heating rate of less than 2°C/min, that the most important mechanism for thermal cracking is differential thermal expansion which has the effect of widening cracks. For larger diameter samples and faster heating rates, thermal gradient cracking predominates. Stresses due to thermal gradients exist over a volume larger than the grains, while with differential thermal expansion stresses are concentrated between grains. Thus, cracks produced by thermal gradients may propagate through the grains, providing a mechanism by which contact area is increased. Therefore, attenuation is also increased as generally observed in the data.

### 6.3 Discussion

The purpose of this section is to explain the resonance  $Q$  data in terms of both the thermal cycling and amplitude dependent behavior. The discussion will first emphasize the thermal cycling data. From the analysis, we will see that reduction of sliding contact area for thermal cracking at low heating rates is consistent with the observed data. This will be followed by several hypotheses to explain amplitude dependent  $Q$  which are also in agreement with the variations of this behavior with thermal cycling.

To summarize the data presented in section 6.1 for thermally cycled rocks, we have seen that for low heating rates ( $<2^{\circ}\text{C}/\text{min}$ ),  $Q$  increases substantially up to a maximum temperature of  $400^{\circ}$ , and velocity decreases as a function of temperature. These effects may be explained by one or both of the following mechanisms:

1. Outgassing of volatiles tied to mineral grains and sliding surfaces. This has the effect of increasing the friction coefficient as shown in section 3.2 and thus decreasing the attenuation (increasing  $Q$ )
2. Increasing aspect ratio of cracks as a result of cracking due to differential thermal expansion. The widening of thin cracks, likely to contribute to attenuation due to friction, also increases  $Q$ . Alternatively, this

mechanism may also be thought of as decreasing the sliding surface contact area.

While the data is limited, the decrease in  $Q$  observed for the rapidly cycled Solenhofen limestone and Frederick diabase is probably due to an increase in the number of thin cracks as a result of thermal gradient cracking.

Concentrating on the low heating rate data, it is important to determine, at least qualitatively, the relative contribution of each mechanism. Since the measurements were made in laboratory air, one might assume that the samples had reabsorbed water vapor. If this is true, then most of the effect in  $Q$  observed may be due to thermal cracking. However, this assumption must be justified. The diffusion time for volatile replacement may be quite long considering it may have taken 10-100 million years for them to be tied up to the mineral grains in the first place.

The question may be resolved, though, by comparing the data of this thesis with that obtained for lunar rocks and analogs. First note that permanent offsets in  $Q$  measured for lunar rocks at atmospheric conditions after heat treatment and vacuum outgassing are due mostly to thermal cycles. Next, relative changes in  $Q$  for a terrestrial lunar analog (W-8, from Tittmann et al., 1974) and the samples studied here are plotted as a function of

the maximum temperature achieved during thermal cycling in Figure 6-26. The major difference between W-8 and the others is that its Q's were measured at a vacuum of  $10^{-7}$  torr. Roughly, the effect of measuring Q under laboratory conditions is to reduce the change in Q by one half.

It appears that the presence of high vacuum is required to maintain a volatile free state. Tittmann et al. (1976) noted that exposure to ultra high vacuum alone, was sufficient to increase Q in lunar rock 70215,85 from 1871 at  $10^{-7}$  to 3330 at  $10^{-10}$  with a 0.21% increase in velocity. As noted before, vacuum outgassing not only increases Q but also increases velocity, both effects being reversible. Thermal cycling, on the other hand, irreversibly reduces velocity due to the overall increase in crack density.

For the experiments described in this thesis, the exposure to the air does seem to imply that volatiles (water vapor) have been able to reenter the rock. Also, thermally cycled samples were saturated with water and then allowed to dry. Little change in the Q values was observed. Thus, most of the increase in Q is probably due to crack widening. If volatile depletion had a major effect on the Q, then this should have been seen for the rapidly heated samples also. Rather, Q decreased or remained relatively constant with maximum

temperature. Furthermore, and most important, one would expect that outgassing would inhibit sliding and thus amplitude dependent attenuation would not be observed.

Finally, these results are consistent with data reported by Kissell (1972) in which  $Q$  was obtained as a function of temperature (ambient) from  $-200^{\circ}$  to  $600^{\circ}\text{C}$ . Kissell observed an increase in  $Q$  as a function of temperature above  $0^{\circ}\text{C}$ . For moderate temperatures, this effect was reversible and Kissell interpreted it to be associated with moisture loss. Returning the sample to room temperature resulted in the reabsorption of moisture. For temperatures above  $100^{\circ}$ , the effect was irreversible. Kissell offered no explanation but this observation is easily explained by thermal cracking.

In some respects, thermal cracking at low heating rates is similar to the effect of pressure on  $Q$ . This is schematically illustrated in Figure 6-27 where crack concentration or porosity is shown as a function of aspect ratio. From theoretical considerations described in Chapter 3 and data in Chapter 5, we have seen that the effect of pressure is to reduce the number of all cracks including the small aspect ratio ones that contribute to attenuation. Thermal cracking via thermal expansion mismatch also reduces these small aspect ratio cracks even though the total crack porosity increases as shown

by the broken line. Temperature gradient cracking, on the other hand, appears to increase the number of low aspect ratio cracks along with (perhaps) higher aspect ratio ones.

Strain amplitude effects may be incorporated into this model in several ways. First recall the Mavko (1978) model of friction for which  $Q$  is inherently amplitude dependent. It is necessary in this case to hypothesize some amplitude independent linear mechanism that masks attenuation due to friction at low strains. If the effect of low heating rate thermal cycling is to decrease the attenuation due to this linear mechanism, then the total effect on  $Q$  is as observed for maximum temperatures up to 400°C as illustrated in Figure 6-28. The transition from low to high amplitude  $Q$  behavior would migrate to lower strains as the rock was thermally cycled. The  $Q$  values at high strains would be equivalent regardless of the temperature history. This explanation is appealing except for the fact that the linear mechanism is undefined and that cracks seem to be important even at low strains. This is borne out by  $Q$  versus pressure measurements made at low amplitudes (Gardner et al., 1964) where attenuation decreases with pressure just as in the case of the higher amplitude ultrasonic measurements. Furthermore, the decreases in

$Q$  at low amplitudes upon heat treating above  $400^\circ$  and also at high heating rates at all temperatures, strongly suggest the presence of cracks and frictional sliding of some kind.

An alternative explanation may be found in terms of contact area in cracks available for sliding. Consider a crack with a distribution of contact areas as illustrated in Figure 6-29a. For a given normal stress acting on the contacts, those with smaller area will slide at lower amplitudes. When the wave amplitude exceeds the frictional stress,  $\tau_f$ , on the larger surface areas, they too will slide and attenuation increases. The widening of cracks due to differential thermal expansion will decrease the area of contacts as shown in Figure 6-29b. Thus  $Q$  increases and sliding on the once larger area surfaces is induced at lower amplitudes. Once low aspect ratio cracks are propagated (above  $400^\circ\text{C}$  or by thermal gradients) the contact area increases,  $Q$  is lowered, and the amplitude dependent behavior shifts back to higher strains.

A similar crack model which holds great promise to quantitatively explain these effects has been recently proposed by Walsh and Grosenbough (1978). Cracks are modeled as cavities formed by contact of two bumpy surfaces. The bumps, or asperities, are considered round and thus Hertzian contact theory is assumed. The



distribution of asperity heights and therefore contact area or normal stress is taken to be nearly Gaussian in nature. While the exact form of this distribution is critical in terms of Walsh and Grosenbaugh's elastic model, it is sufficient for this discussion that there is merely a peak in the distribution. A Gaussian profile, however, is observed for slightly polished steel and bead blasted gold surfaces (Greenwood and Williamson, 1966).

Now consider the effect of this model in terms of general amplitude dependence of attenuation. For low strains, sliding is induced on the low contact area tail end of the distribution. Since the distribution here is relatively flat,  $Q$  would appear independent of amplitude. As strain amplitude increases, sliding of contact areas near the peak of the distribution occurs and  $Q$  decreases. At very high amplitudes, this theory would predict a leveling off of  $Q$  as sliding passes the peak. The model is illustrated in Figure 6-30a where  $Q$  as a function of amplitude is superimposed on the distribution of contact area or normal stress.

This same model predicts the behavior of amplitude effects for thermally cycled rocks. Thermal cracking that widens cracks will shift the peak in the distribution of contact area to lower values. This is shown in Figure 6-30b for normalized distributions. Thus while

the actual density of contacts may decrease and  $Q$  increases, the peak occurs at lower areas and the drop in  $Q$  due to amplitude effects happens at lower strains.

The two contact models just presented are closely related. Their essential feature, quite different from the Mavko model, is that cracks play a role at all strain amplitudes investigated in this thesis. This is more consistent with our notion that the increase in  $Q$  as a function of pressure measured at low amplitudes by resonance techniques is due to crack closing just as interpreted for the ultrasonic data. All of the amplitude dependent models, however, require further development. For the Mavko model, the low amplitude linear mechanism must be identified and its properties understood before any judgement can be made in terms of its acceptability in explaining the data. Clearly the contact models need much mathematical development to justify the qualitative arguments made in this thesis. This is beyond the scope of the present work but is obviously the next step to take in order to fully understand the nature of frictional attenuation.

Table 6.1

Comparison of Resonance and Ultrasonic Q Data

	<u>Berea</u>	<u>Navajo</u>
Resonance, low amplitude	75	60
Resonance, high amplitude	30	28
Ultrasonic P wave	20	30

Table 6.2

Crack Porosity (%) From Thermal Cycling

	<u>virgin</u>	<u>400°C</u>	<u>800°C</u>
Frederick Diabase	--	0.05	0.20
Solenhofen Limestone	--	0.09	0.18
Westerly Granite			
perpendicular	0.30	0.54	2.70
parallel	0.12	0.34	2.07

## FIGURE CAPTIONS

Figure 6-1.  $Q$  and bar velocity as a function of strain amplitude for longitudinal waves in the dry Berea sandstone. Also shown is  $Q$  as a function of strain amplitude for plexiglass. In this and later figures, representative error bars are shown.

Figure 6-2.  $Q$  values for P waves in the dry Berea sandstone as a function of peak voltage applied to the transducers. Data obtained at 45, 210 and 500 bars confining pressure ( $P_f = 0$ ).

Figure 6-3.  $Q$  values for S waves in the dry Berea sandstone as a function of applied voltage.

Figure 6-4. P and S wave velocities as a function of applied voltage in the dry Berea sandstone.

Figure 6-5.  $Q$  as a function of strain amplitude for longitudinal waves in the dry Navajo sandstone.

Figure 6-6. Linear strain as a function of confining pressure in Frederick diabase for a virgin sample and samples thermally cycled to 400 and 800°C.

Figure 6-7. Linear strain as a function of confining pressure in Solenhofen limestone for virgin and thermally cycled samples.

Figure 6-8. Linear strain as a function of confining pressure in Westerly granite for the "soft"

direction. Curves for the virgin and 400°C cycled samples are shown.

Figure 6-9. Linear strain as a function of confining pressure in Westerly granite for the "stiff" direction.

Figure 6-10. Linear strain as a function of confining pressure in Westerly granite for both directions for samples thermally cycled to 800°C.

Figure 6-11.  $Q$  (solid symbols) and bar velocity (open symbols) as a function of maximum temperature achieved in slow thermal cycling in the Frederick diabase. Two separate experiments were run and the results are denoted by the different symbols. Representative error bars are also shown.

Figure 6-12.  $Q$  and bar velocity as a function of maximum temperature in Solenhofen limestone. See Figure 6-11 for explanations.

Figure 6-13.  $Q$  and bar velocity as a function of maximum temperature in Westerly granite for both directions. See Figure 6-11 for explanations.

Figure 6-14.  $Q$  (solid symbols) and bar velocity (open symbols) as a function of maximum temperature achieved in fast thermal cycling in Solenhofen limestone.

- Figure 6-15.  $Q$  and bar velocity as a function of maximum temperature (fast cycling) in Frederick diabase.
- Figure 6-16.  $Q$  as a function of strain amplitude in Frederick diabase for virgin and several slow thermally cycled samples.
- Figure 6-17.  $Q$  as a function of strain amplitude in Solenhofen limestone for virgin and several slow thermally cycled samples.
- Figure 6-18.  $Q$  as a function of strain amplitude in Westerly granite (soft direction) for virgin and several slow thermally cycled samples.
- Figure 6-19. Comparison of amplitude dependent  $Q$  behavior for slow and fast cycled samples of Frederick diabase.
- Figure 6-20. Typical strain amplitude- $Q$  hysteresis in Frederick diabase.
- Figure 6-21. Typical strain amplitude- $Q$  hysteresis in Solenhofen limestone.
- Figure 6-22. Typical strain amplitude- $Q$  hysteresis in Westerly granite.
- Figure 6-23.  $Q$  and bar velocity as a function of

vacuum pressure from results of an experiment described in Tittmann et al. (1975) for lunar rock 70215, 85. Solid lines indicate isothermal runs and dashed lines thermally cycled runs.

Figure 6-24. Photomicrographs of the same field in virgin (a) and thermally cycled to 400°C (b) Chelmsford granite. From Sprunt and Brace (1974).

Figure 6-25. Frequency distribution of crack aspect ratio in virgin (unstressed) and thermally cycled (stressed) Westerly granite. In each a random sample of 80 cracks was compared. From Sprunt and Brace (1974).

Figure 6-26. Increase in  $Q$  as a function of maximum temperatures achieved during slow thermal cycling for the three rocks studied in this thesis, measured under atmospheric conditions and a terrestrial lunar analog (W-8) measured at  $10^{-7}$  torr vacuum (Tittmann et al., 1973).

Figure 6-27. The effect of increasing pressure and slow thermal cycling on the distribution of crack aspect ratios.

Figure 6-28. A model to explain the strain amplitude effects of attenuation in rock proposed by Mavko (1978). Here, the effect of thermal cycling is assumed to decrease the attenuation (increase  $Q$ ) due to a linear mechanism.

Figure 6-29. Schematic illustration of a crack and sliding surfaces in a virgin (a) and thermally cycled (b) rock.  $\tau_f$  is the frictional stress that must be overcome to induce sliding on each surface. The effect of thermal cycling is to widen the cracks and reduce the sliding contact area.

Figure 6-30. Possible extension of the Walsh and Grosenbaugh (1978) crack model to attenuation. A normal distribution of contact area (or normal stress) is assumed. a) The effect of the contact area distribution on the amplitude dependence of  $Q$ . b) The effect of thermal cycling on the contact distribution and the resulting changes in  $Q$  as a function of strain amplitude. The curves have been normalized.



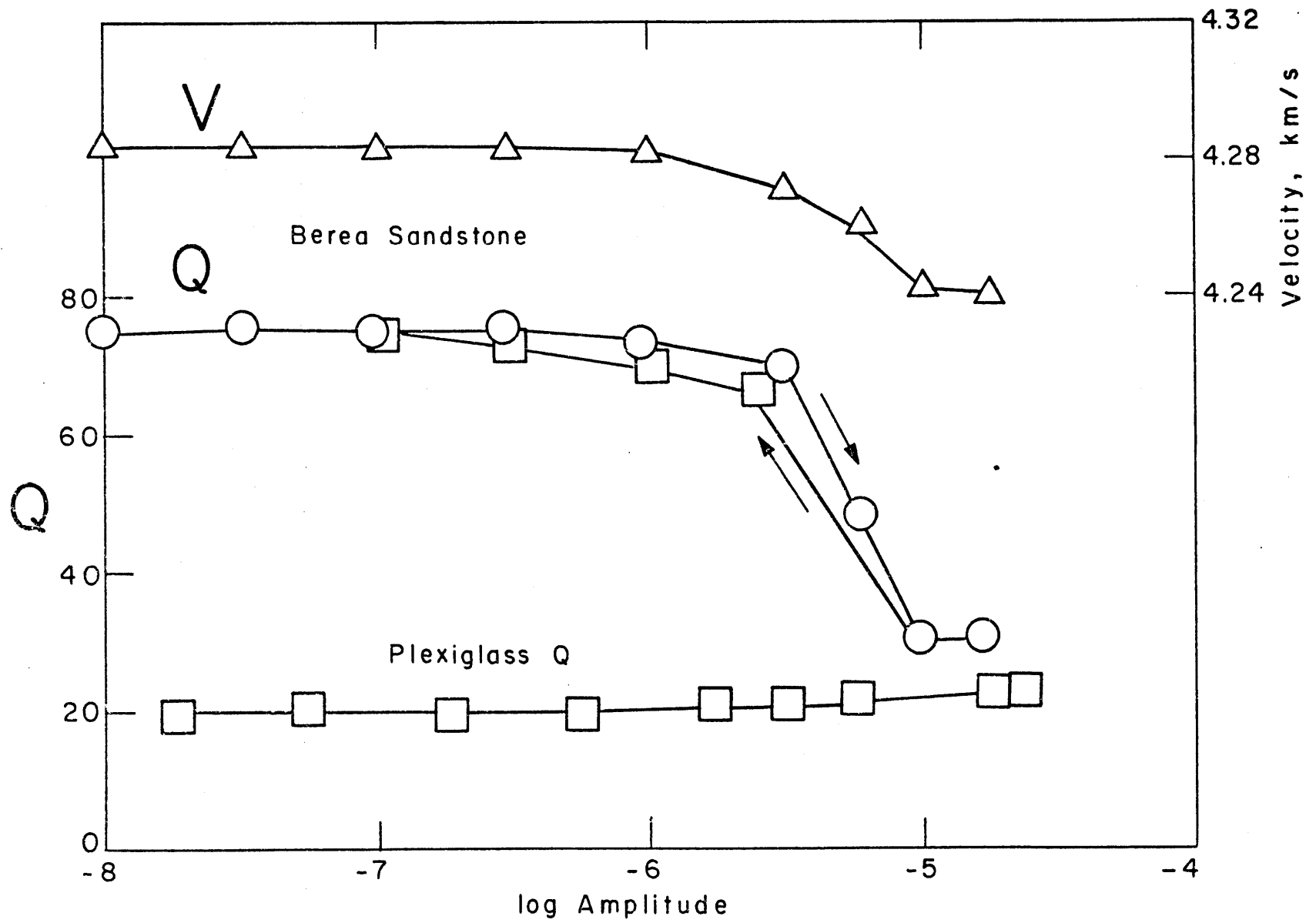


Figure 6-1

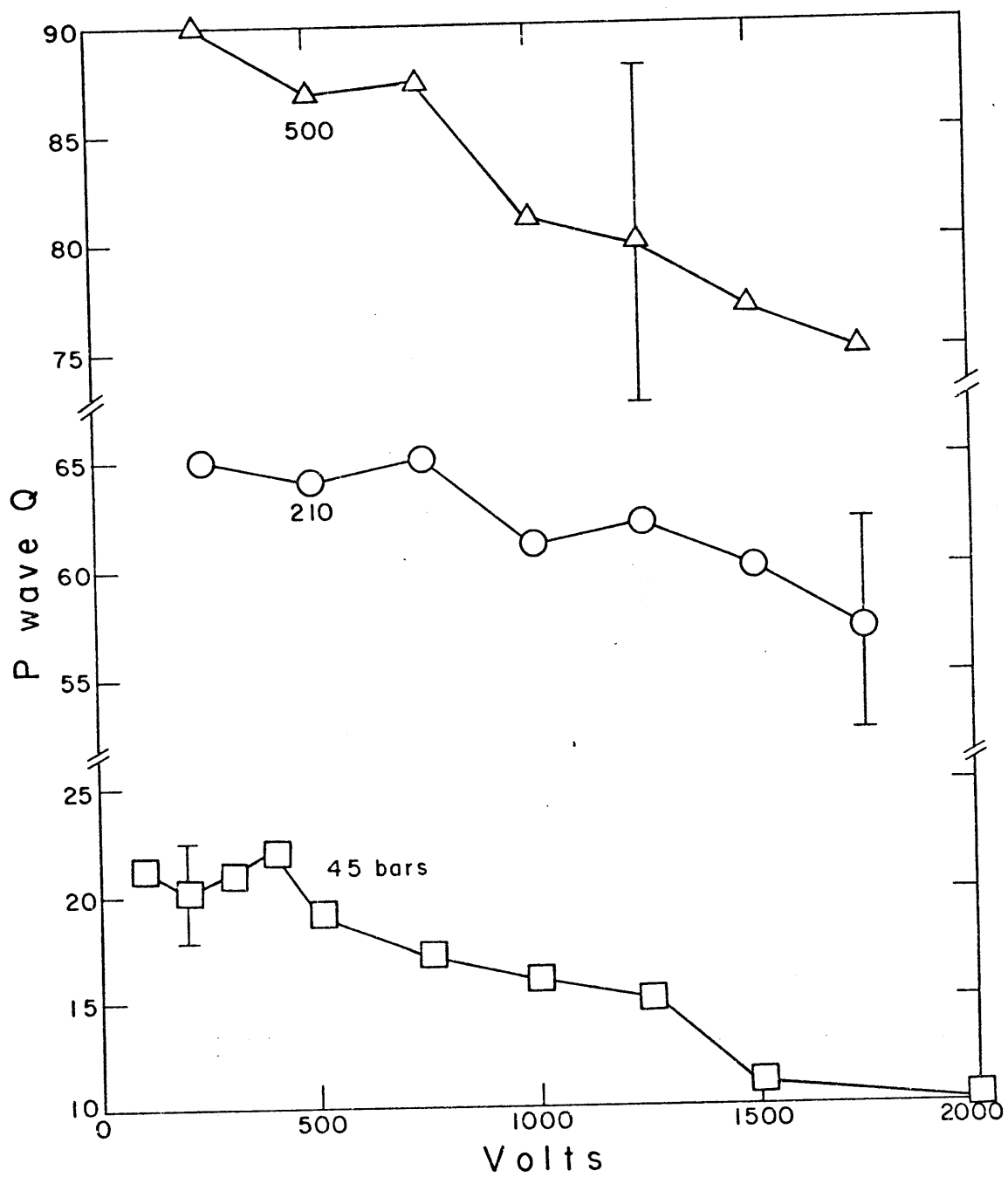


Figure 6-2

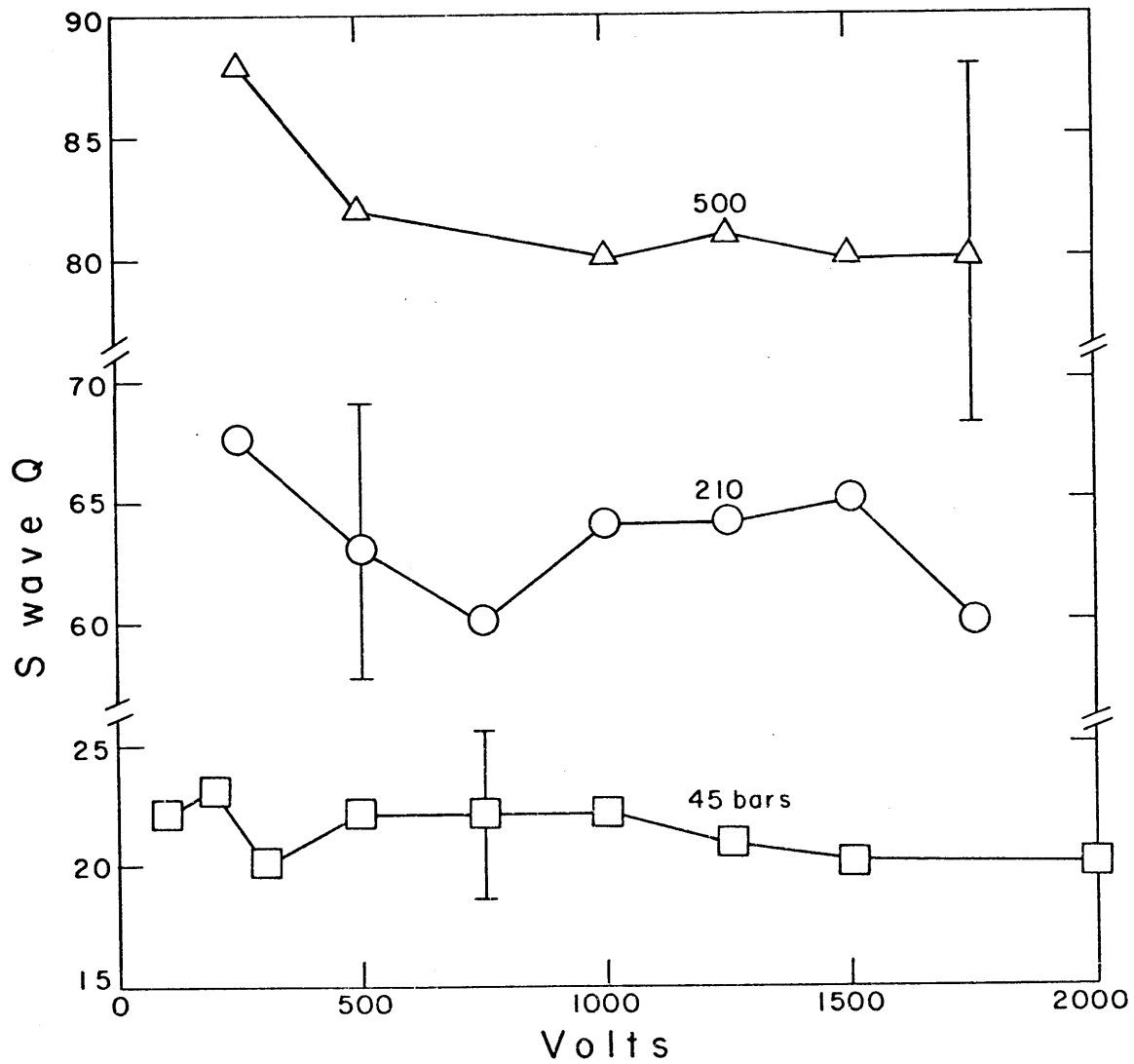


Figure 6-3

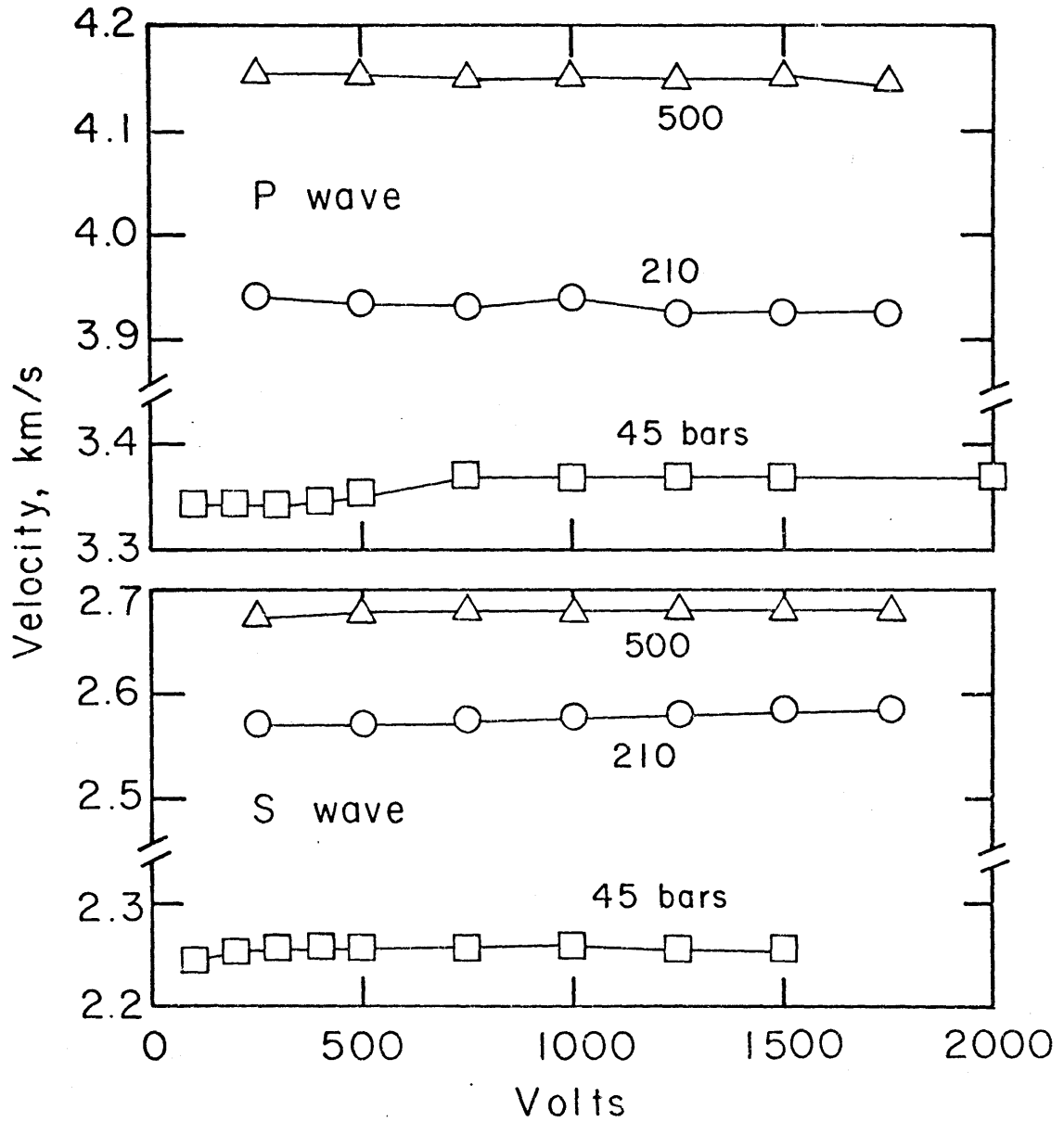


Figure 6-4

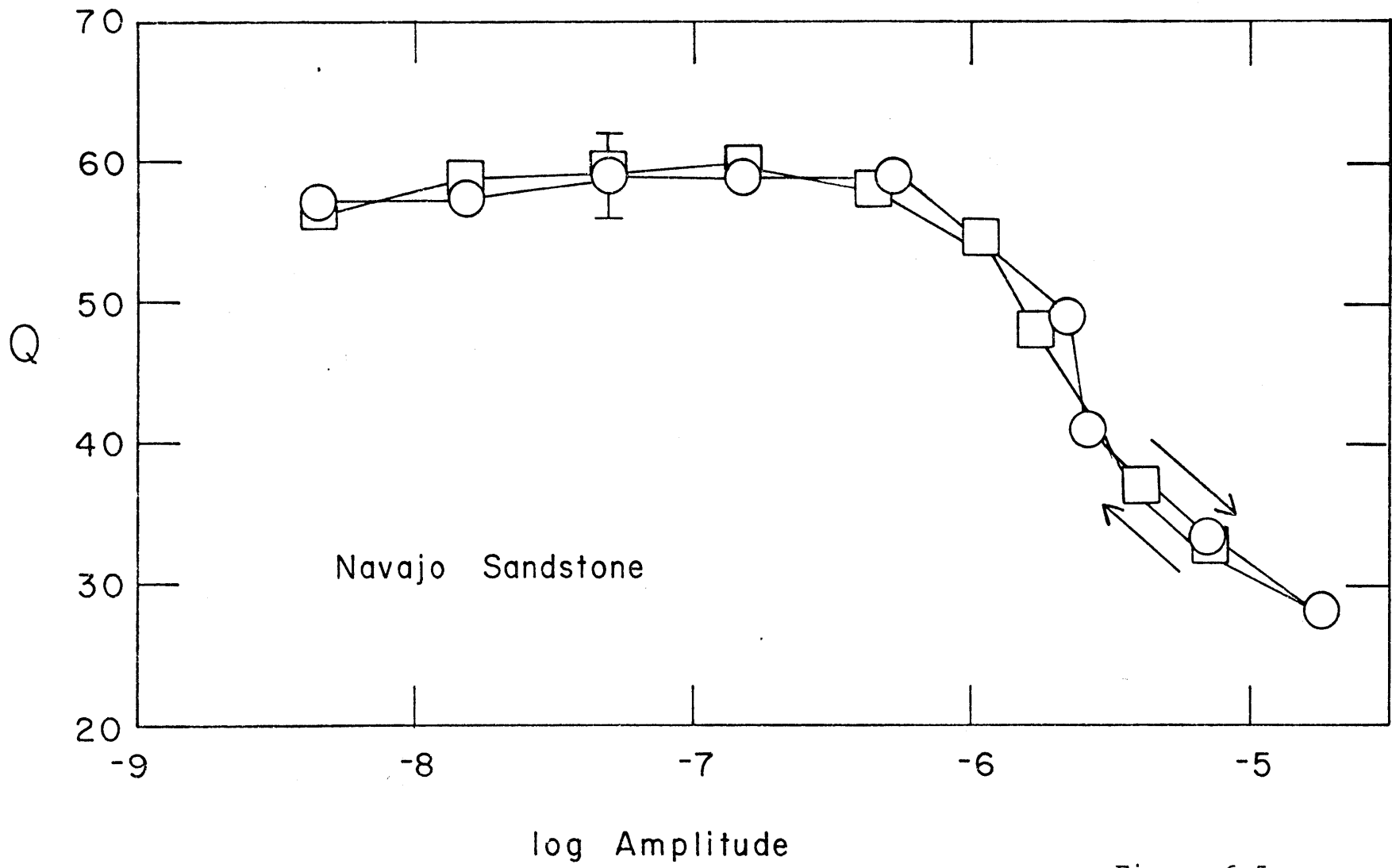


Figure 6-5

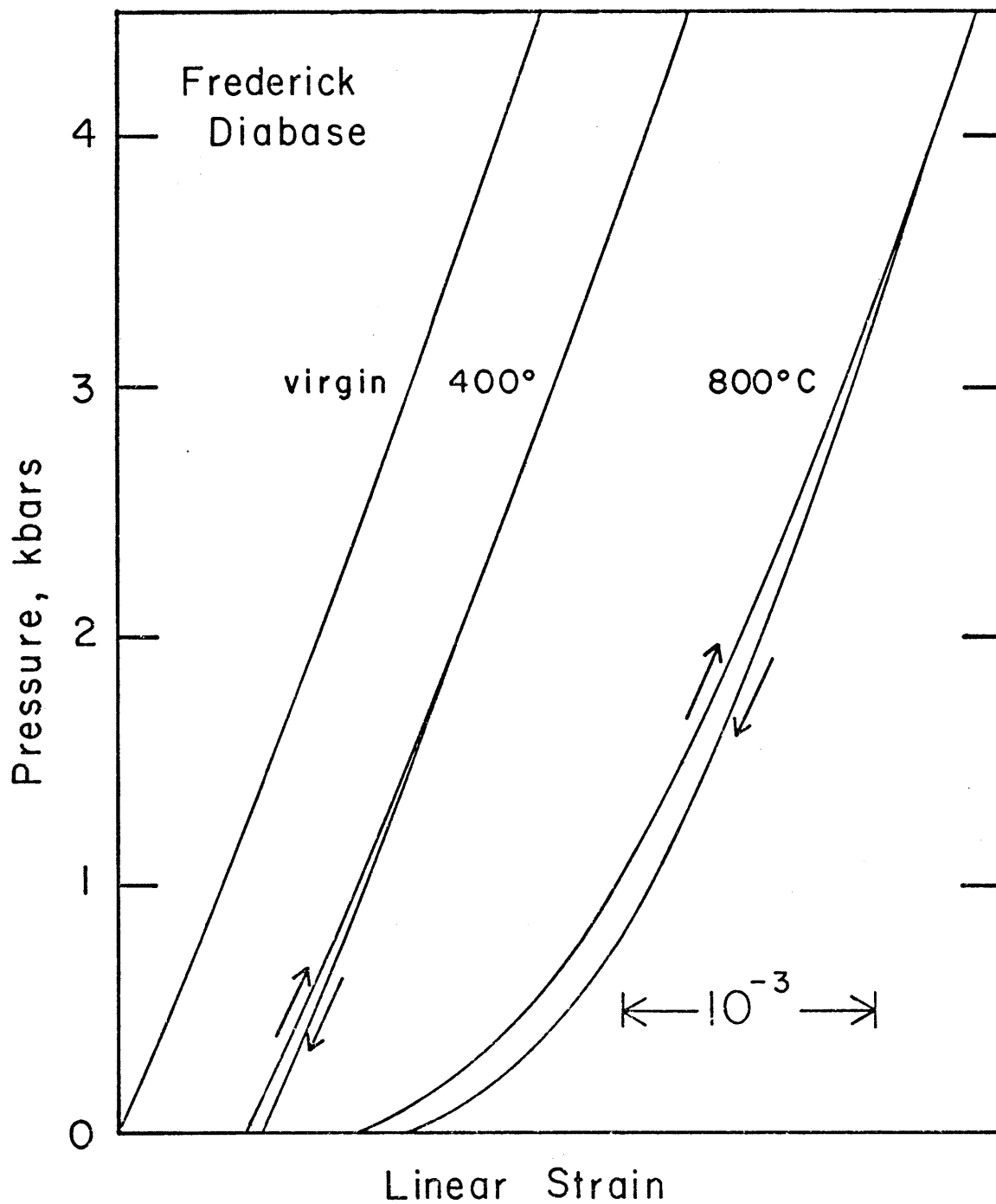


Figure 6-6

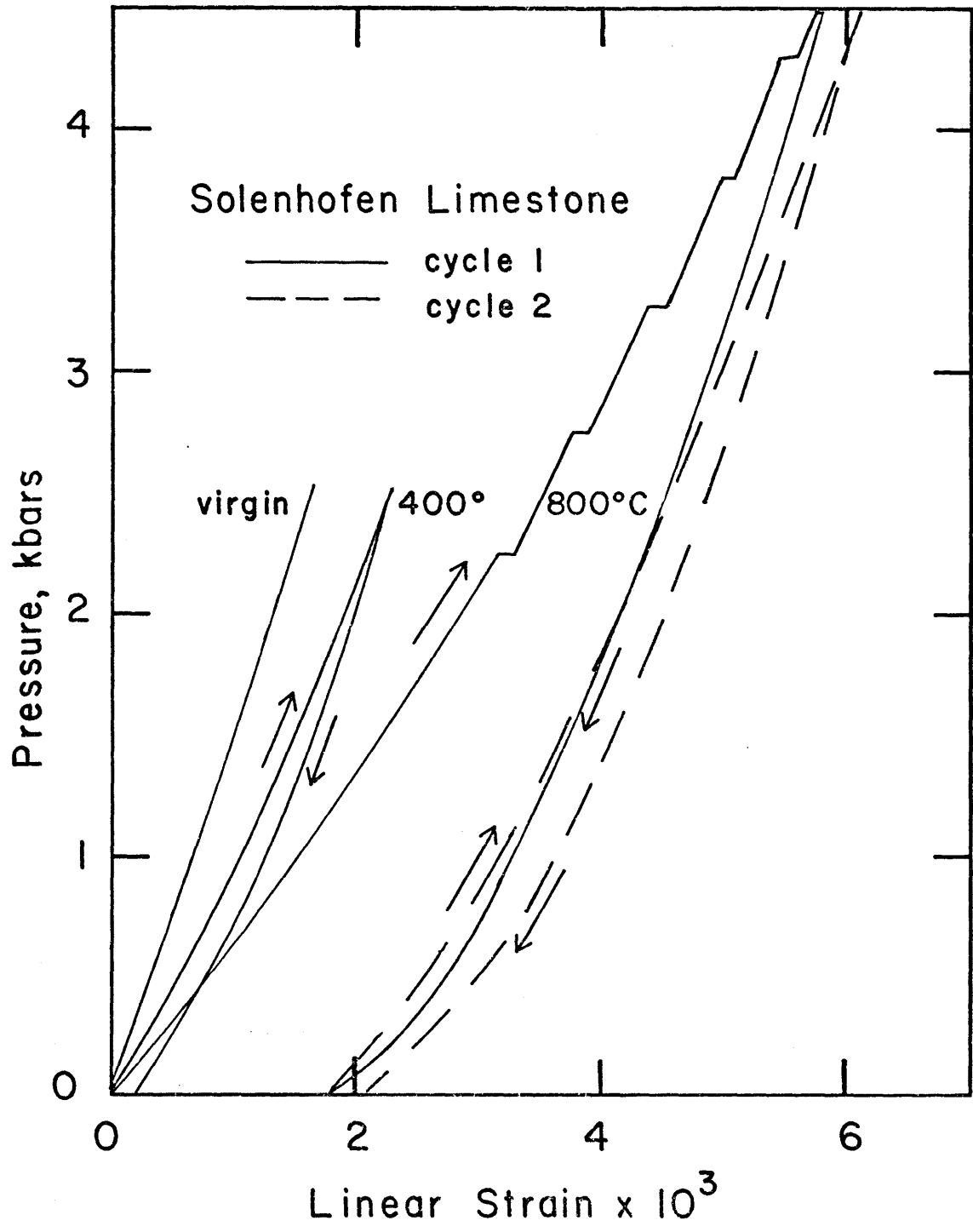


Figure 6-7

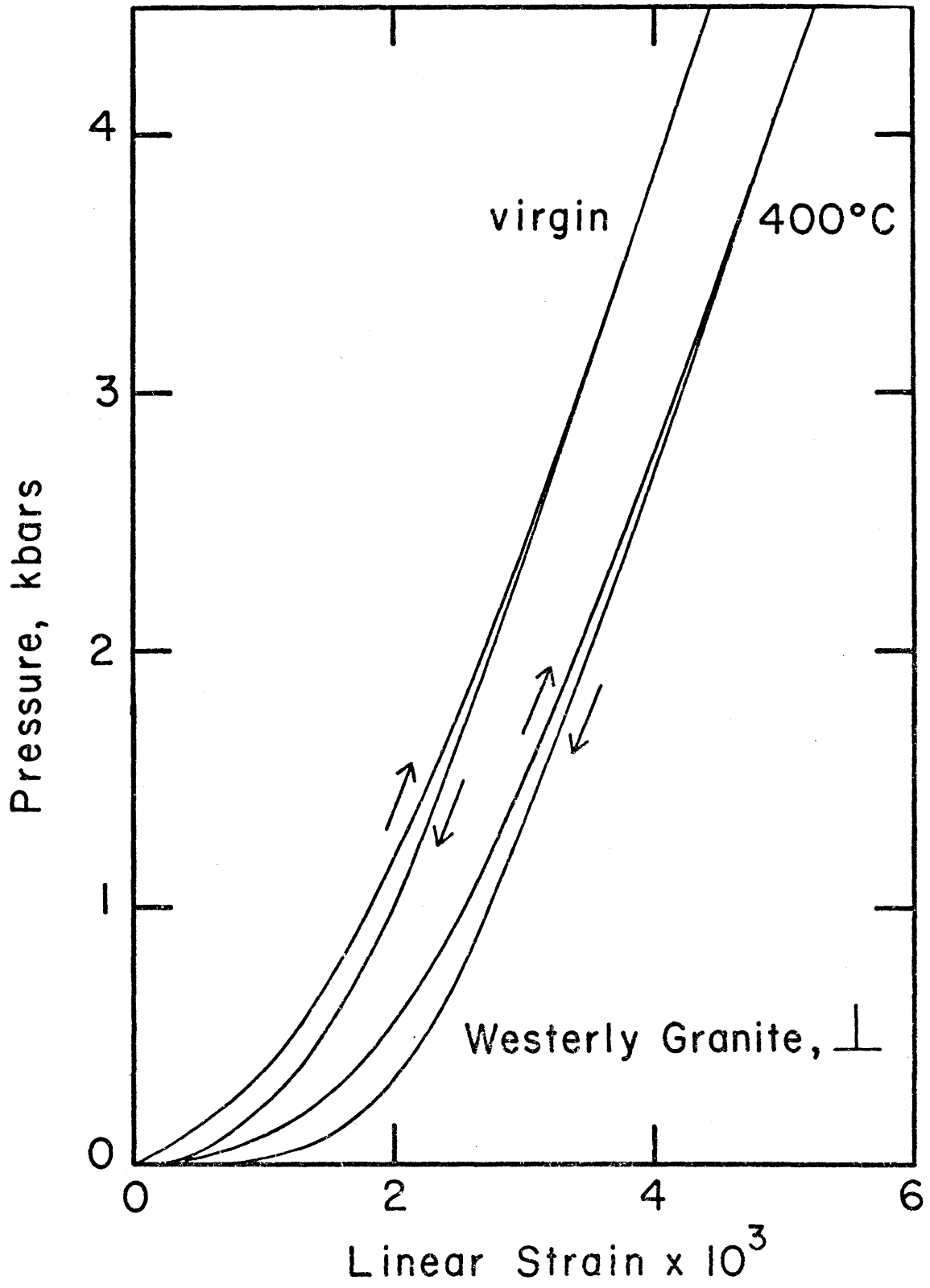


Figure 6-8



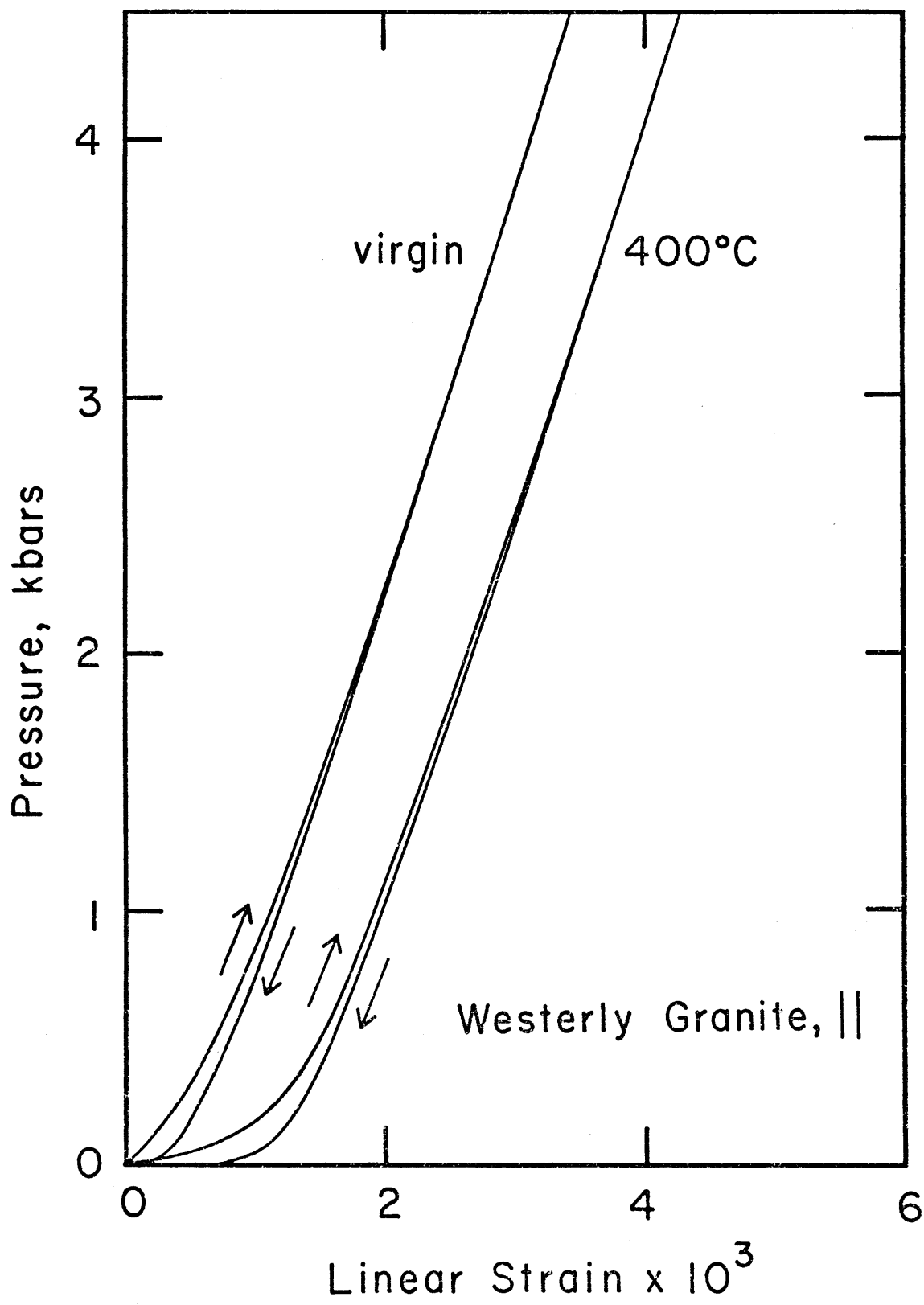


Figure 6-9

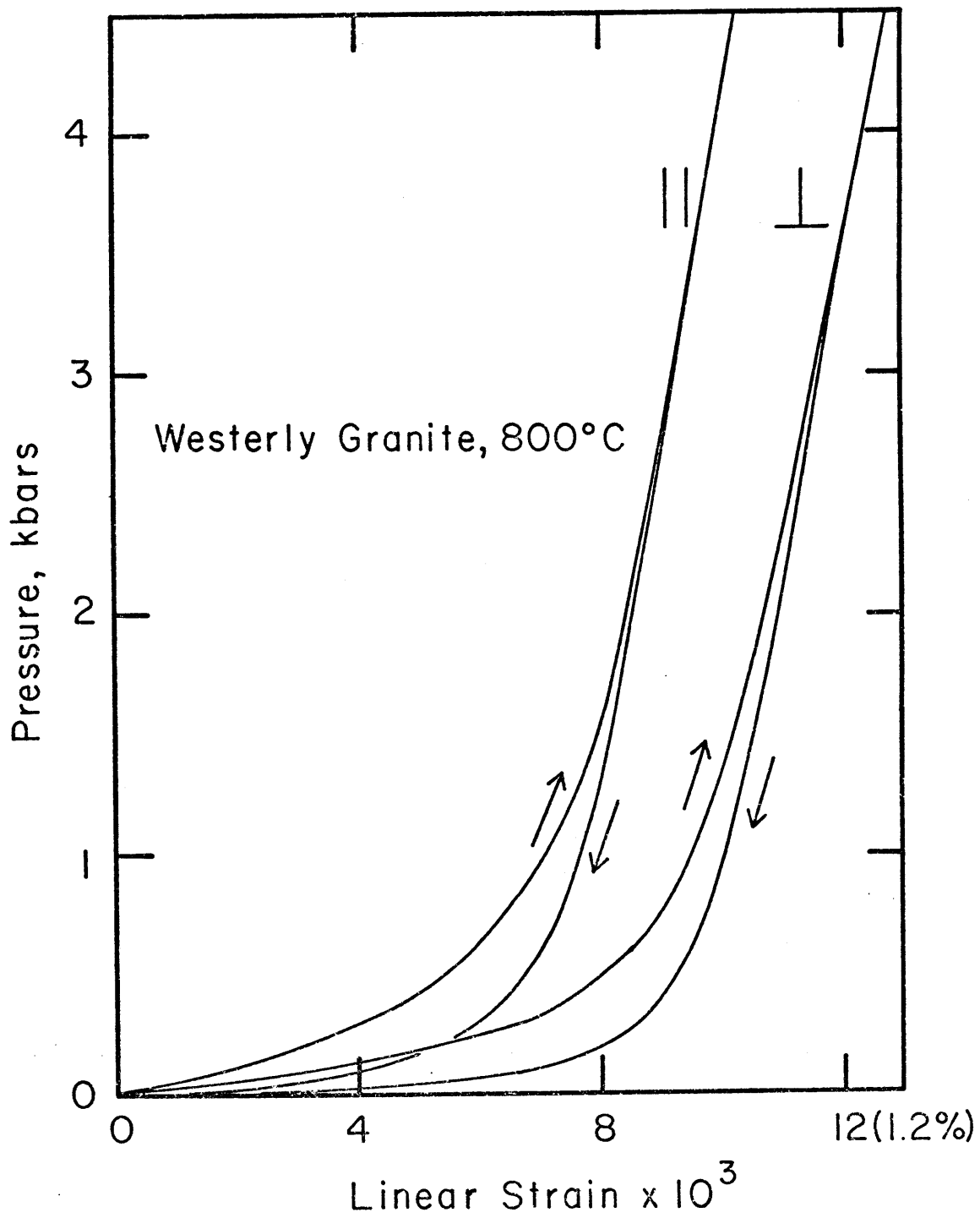


Figure 6-10

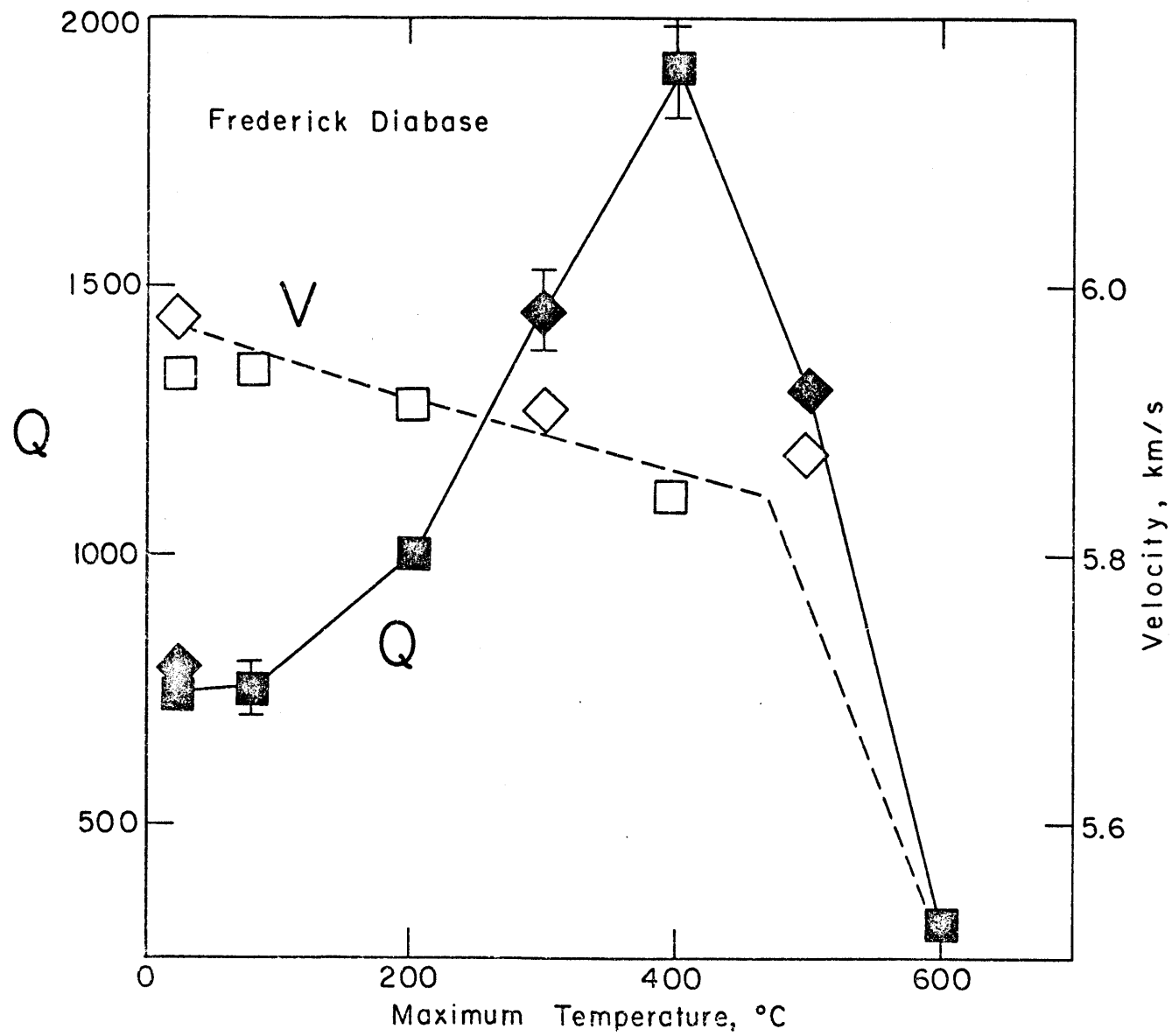


Figure 6-11

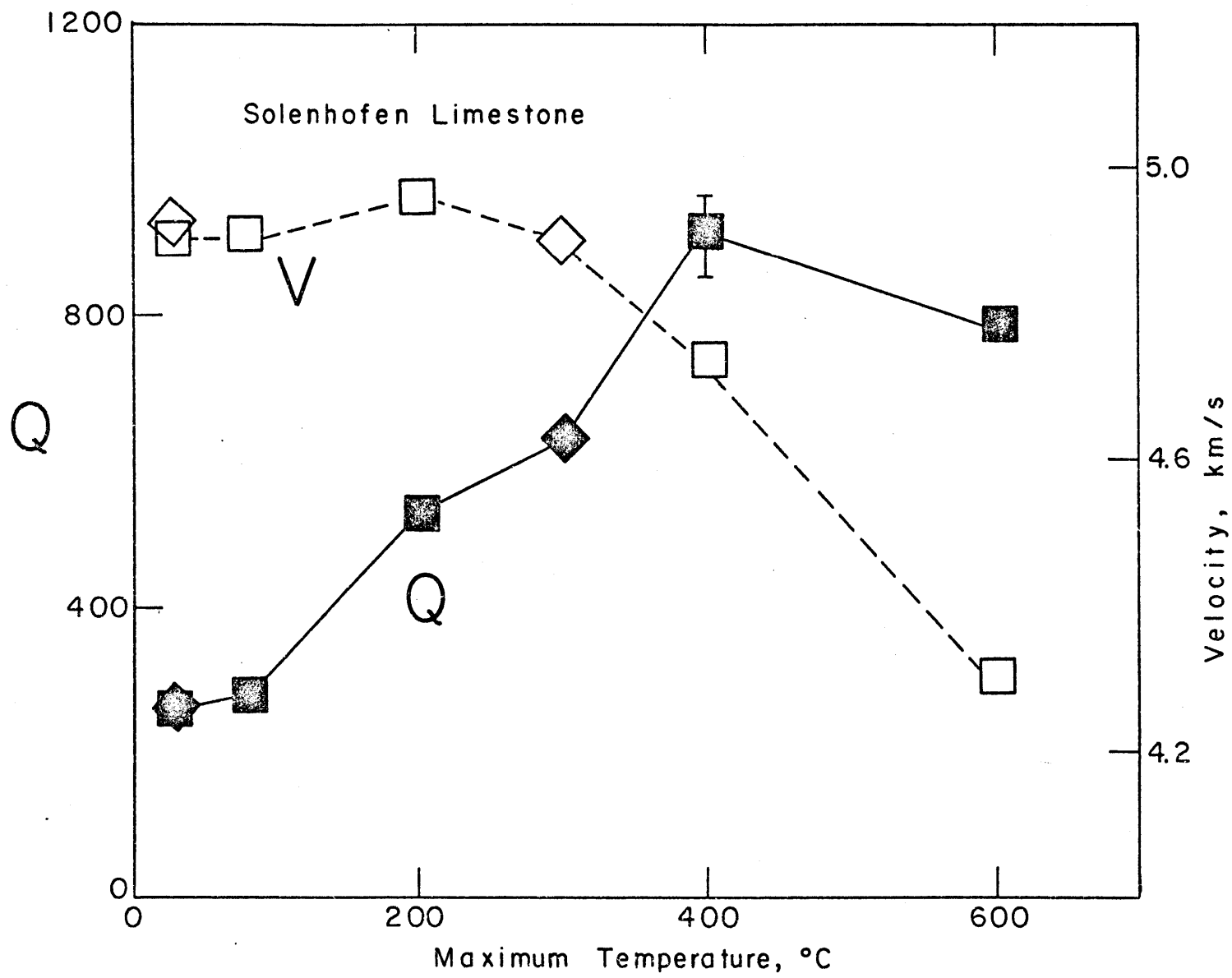


Figure 6-12

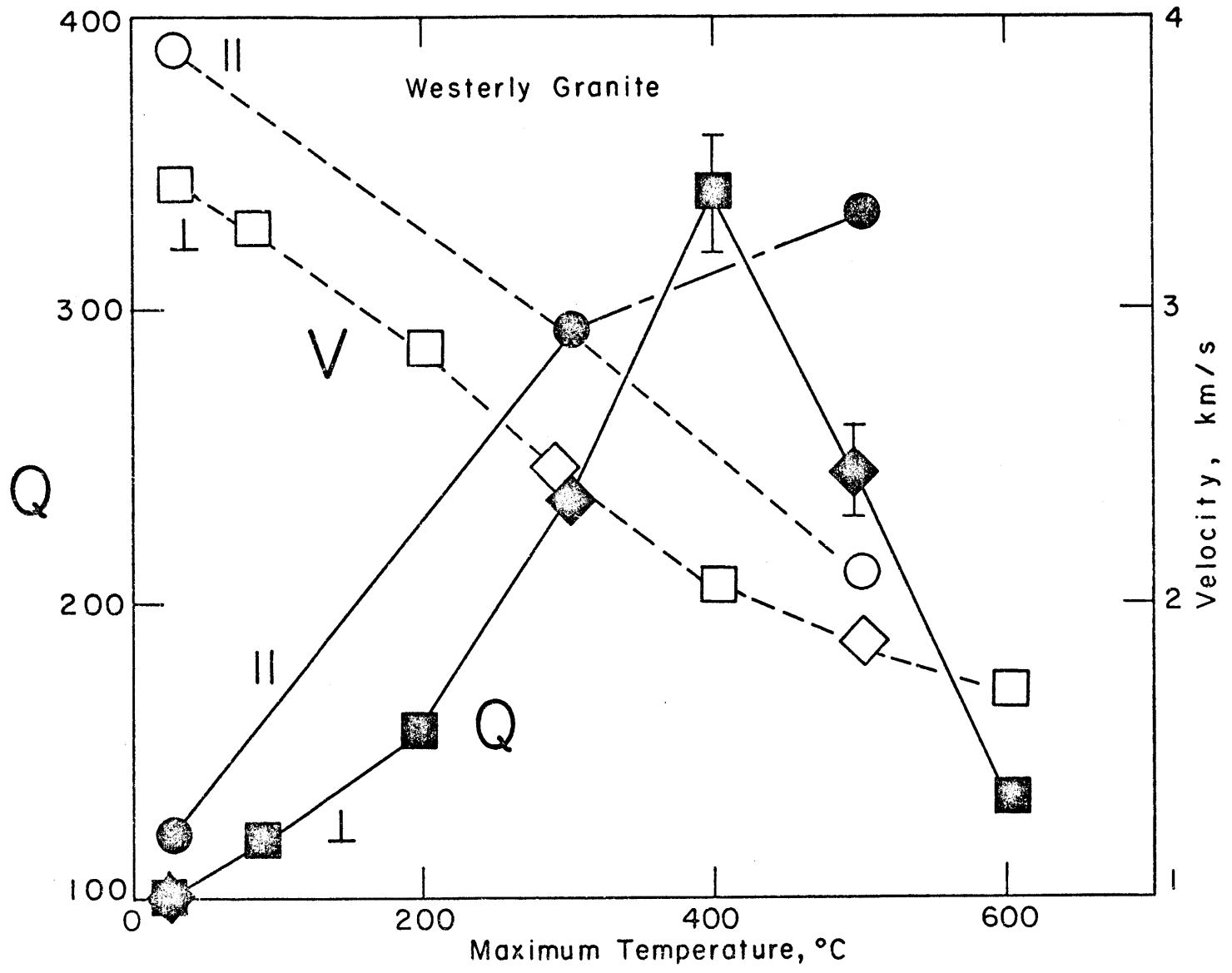


Figure 6-13

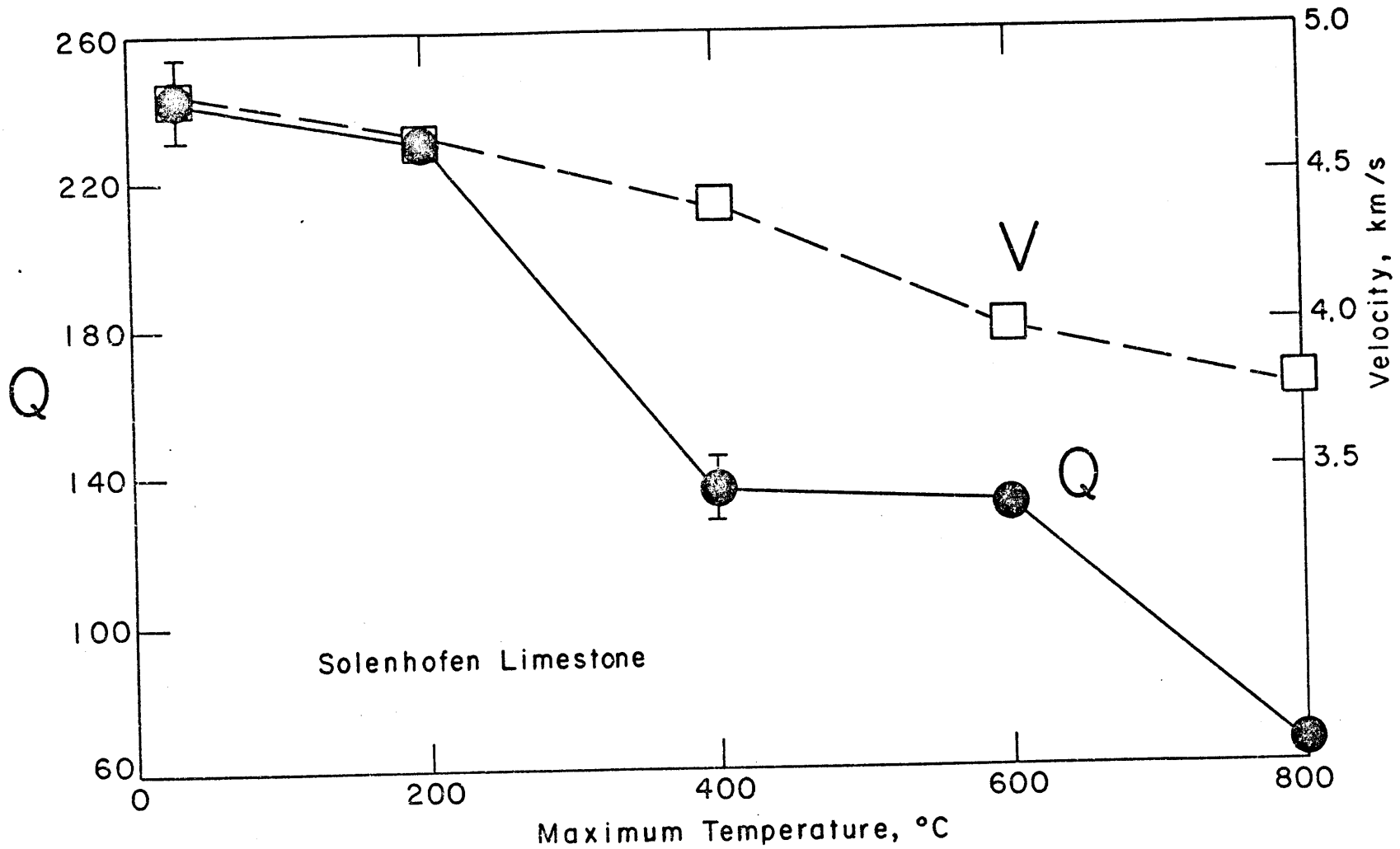


Figure 6-14

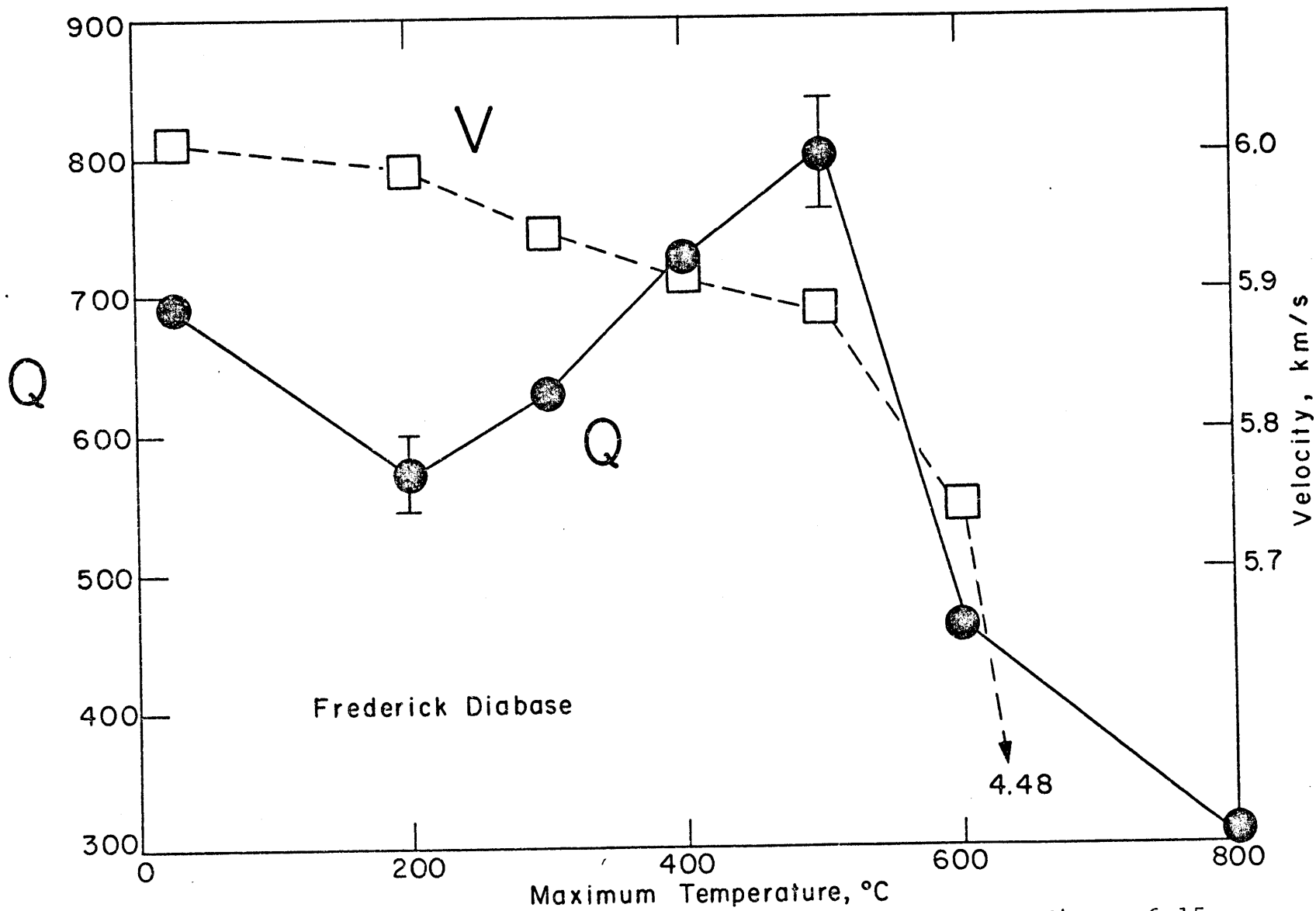


Figure 6-15

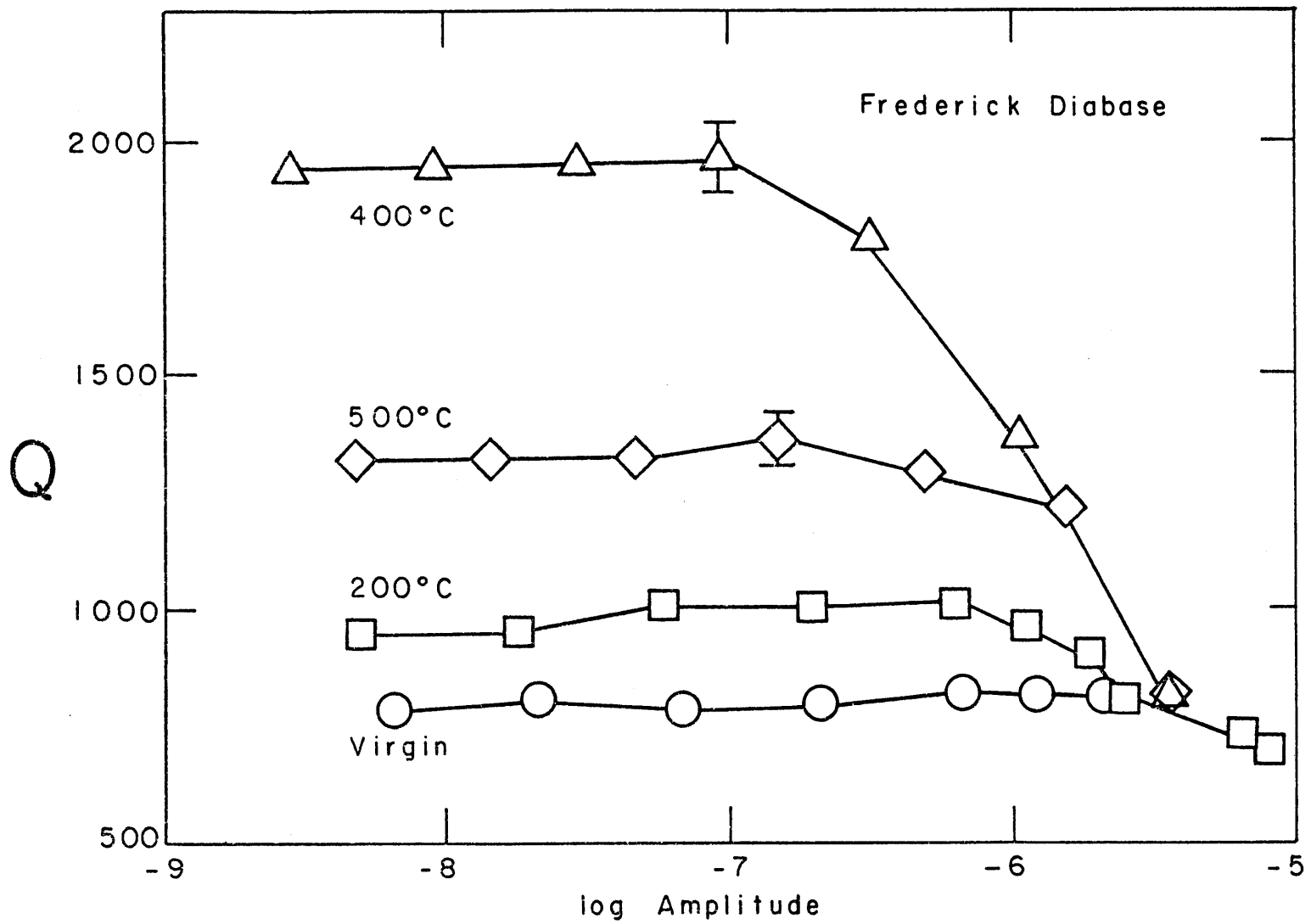


Figure 6-16



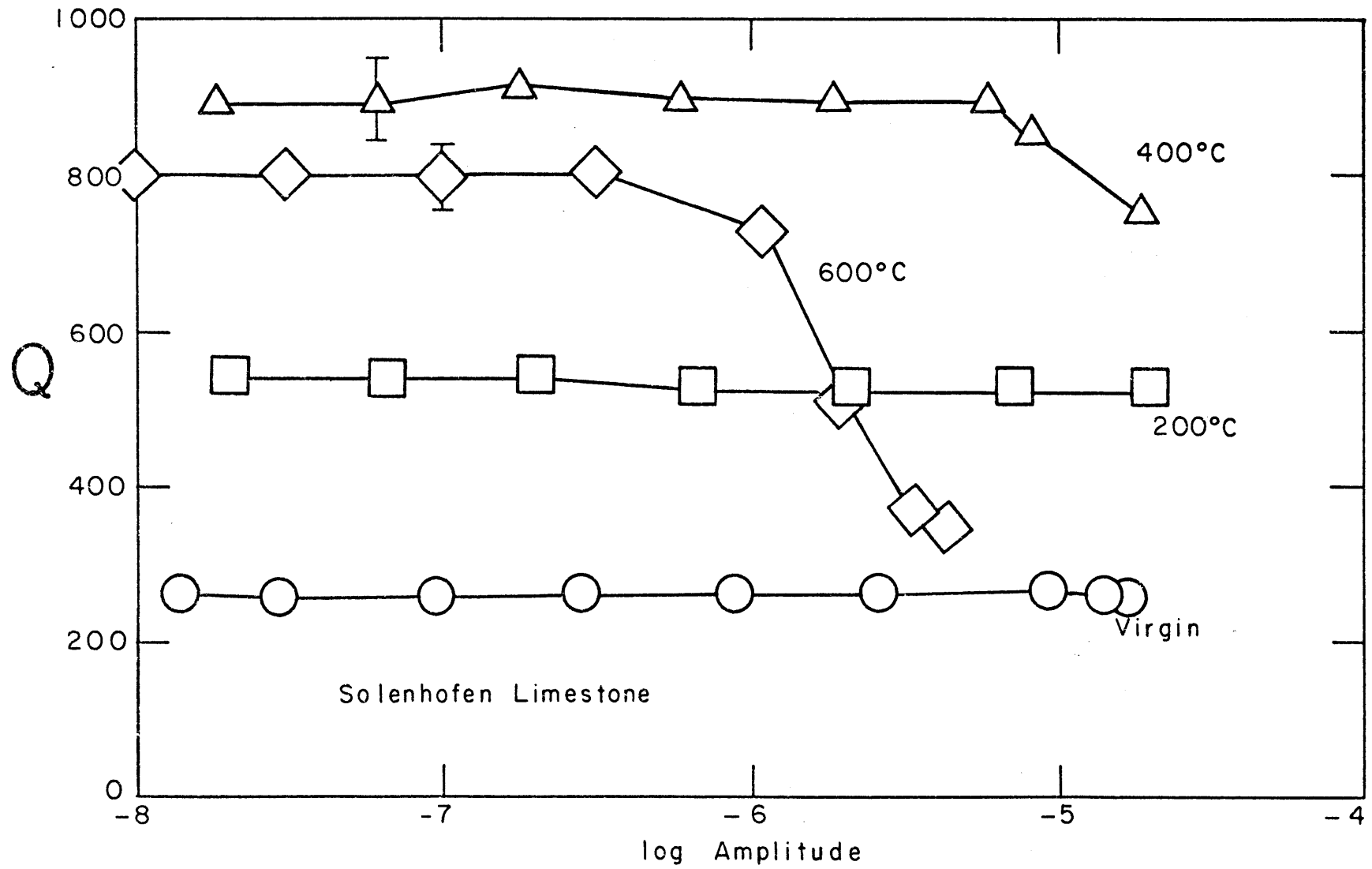


Figure 6-17

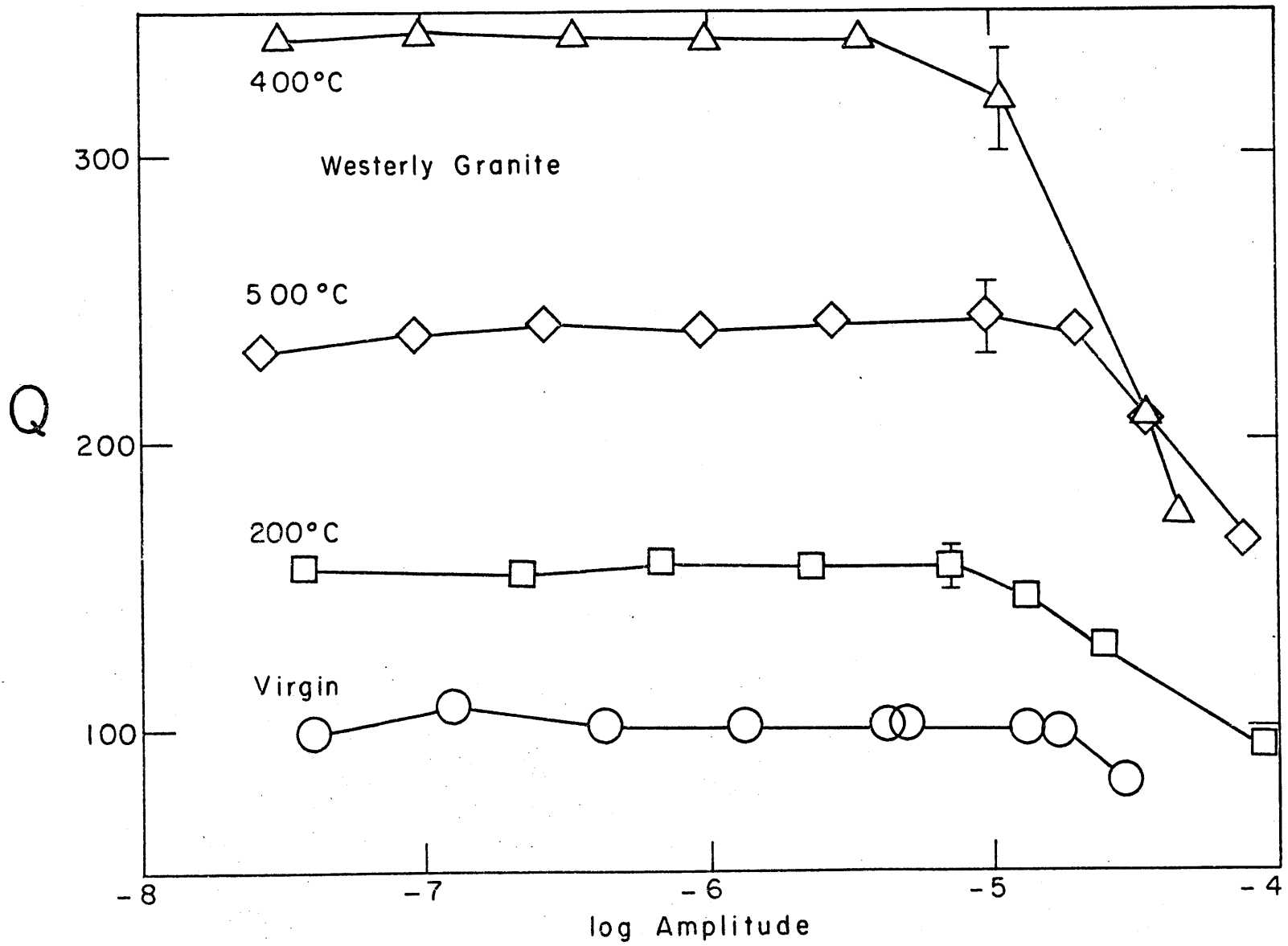


Figure 6-18

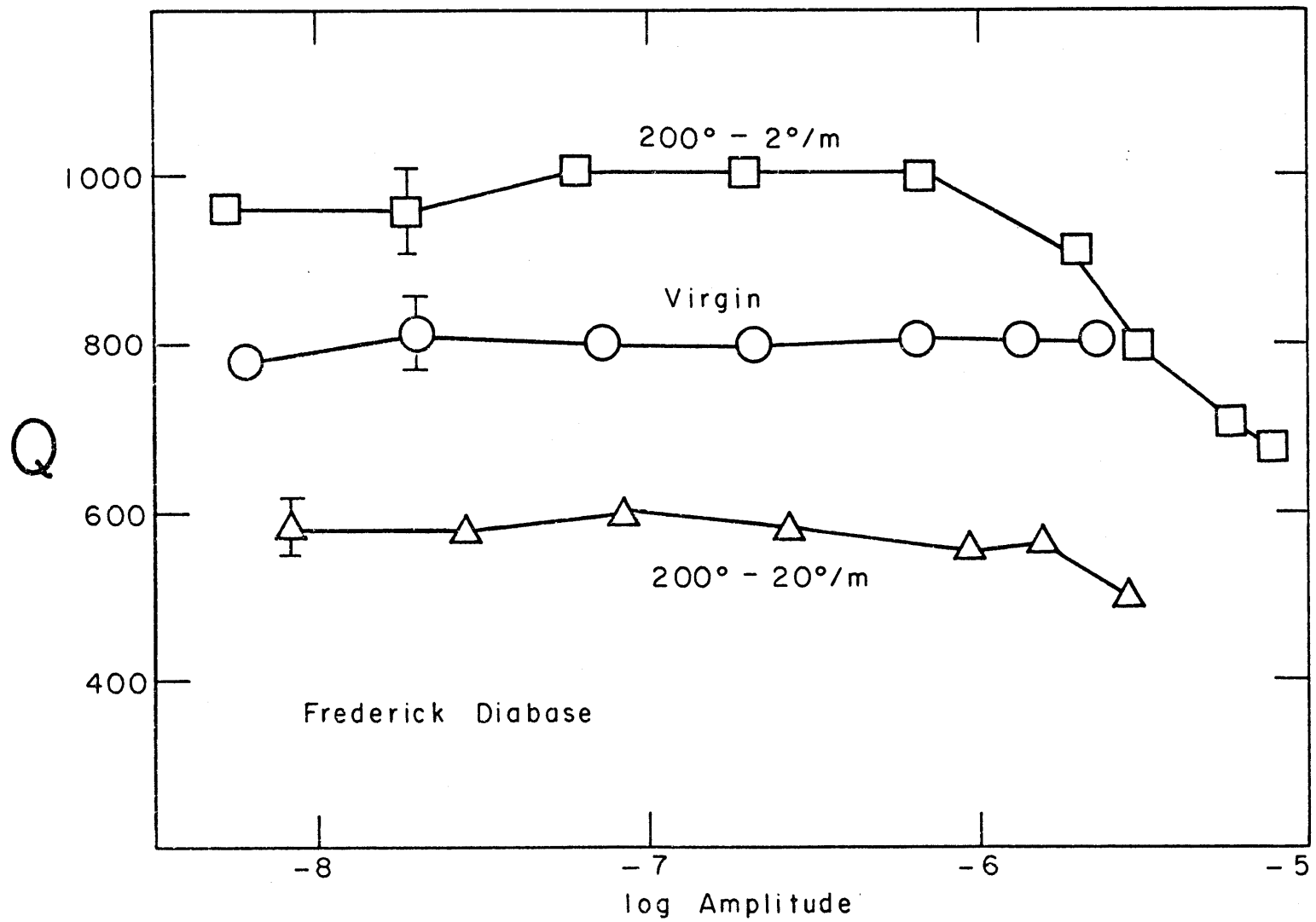


Figure 6-19

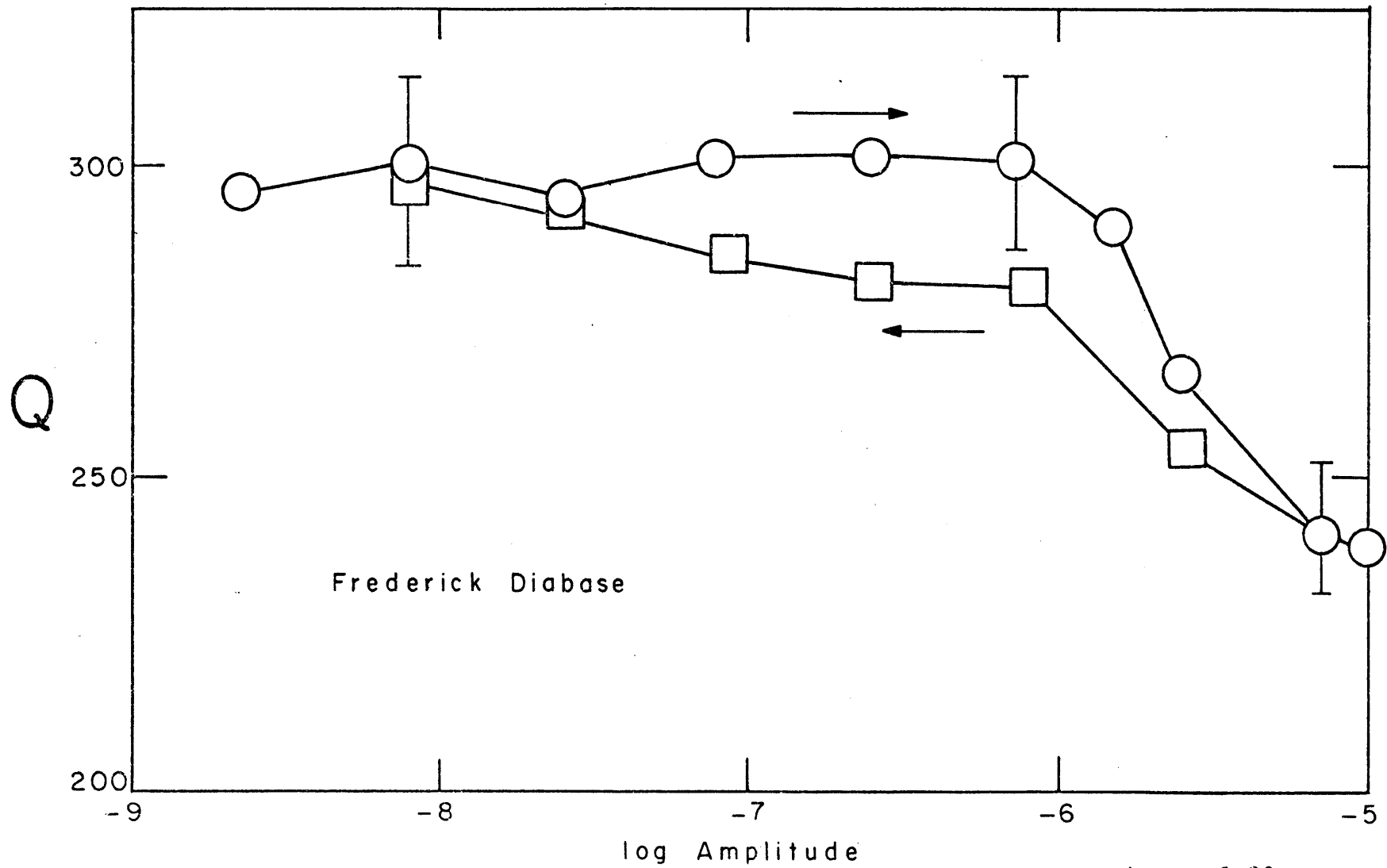


Figure 6-20

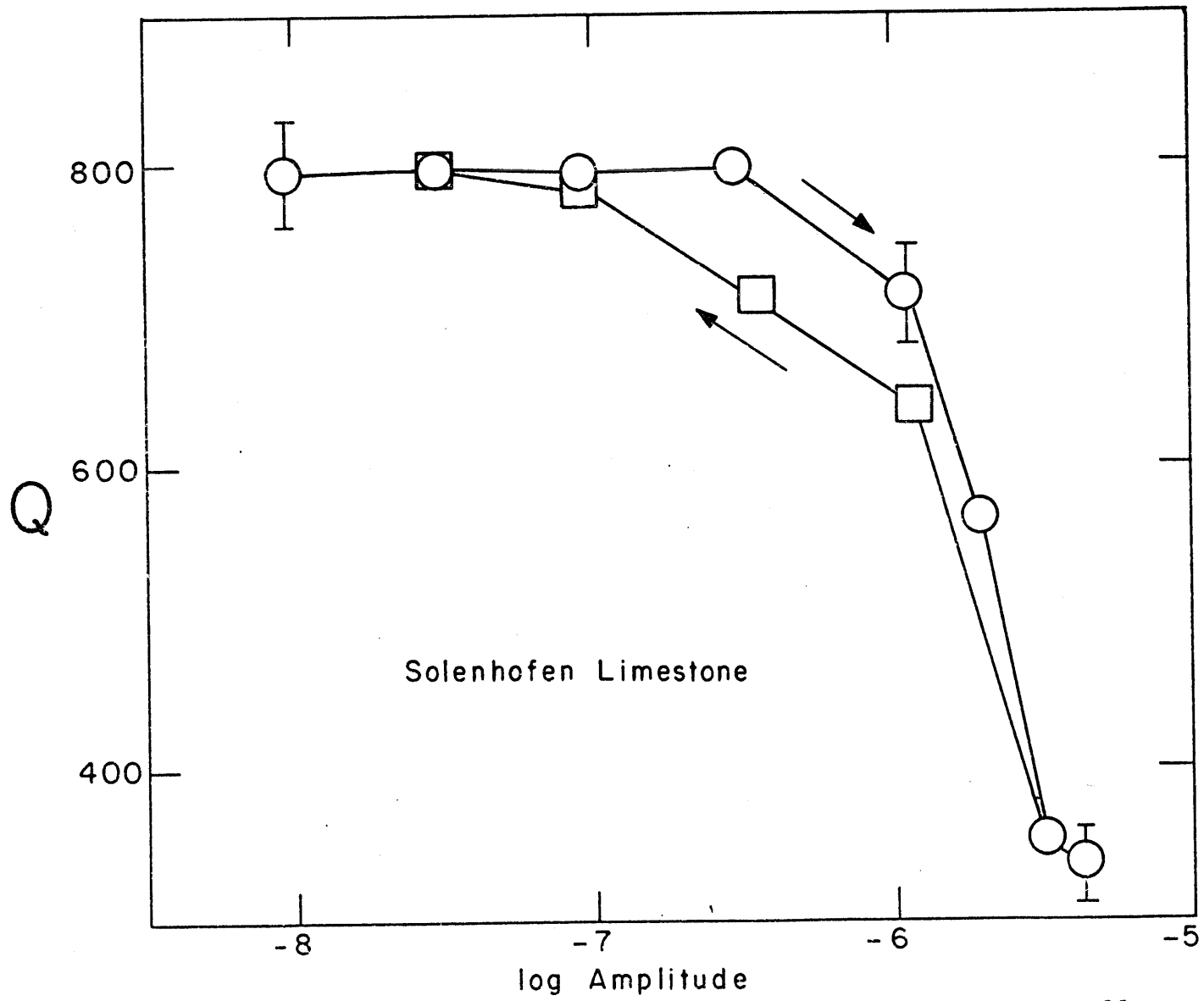


Figure 6-21

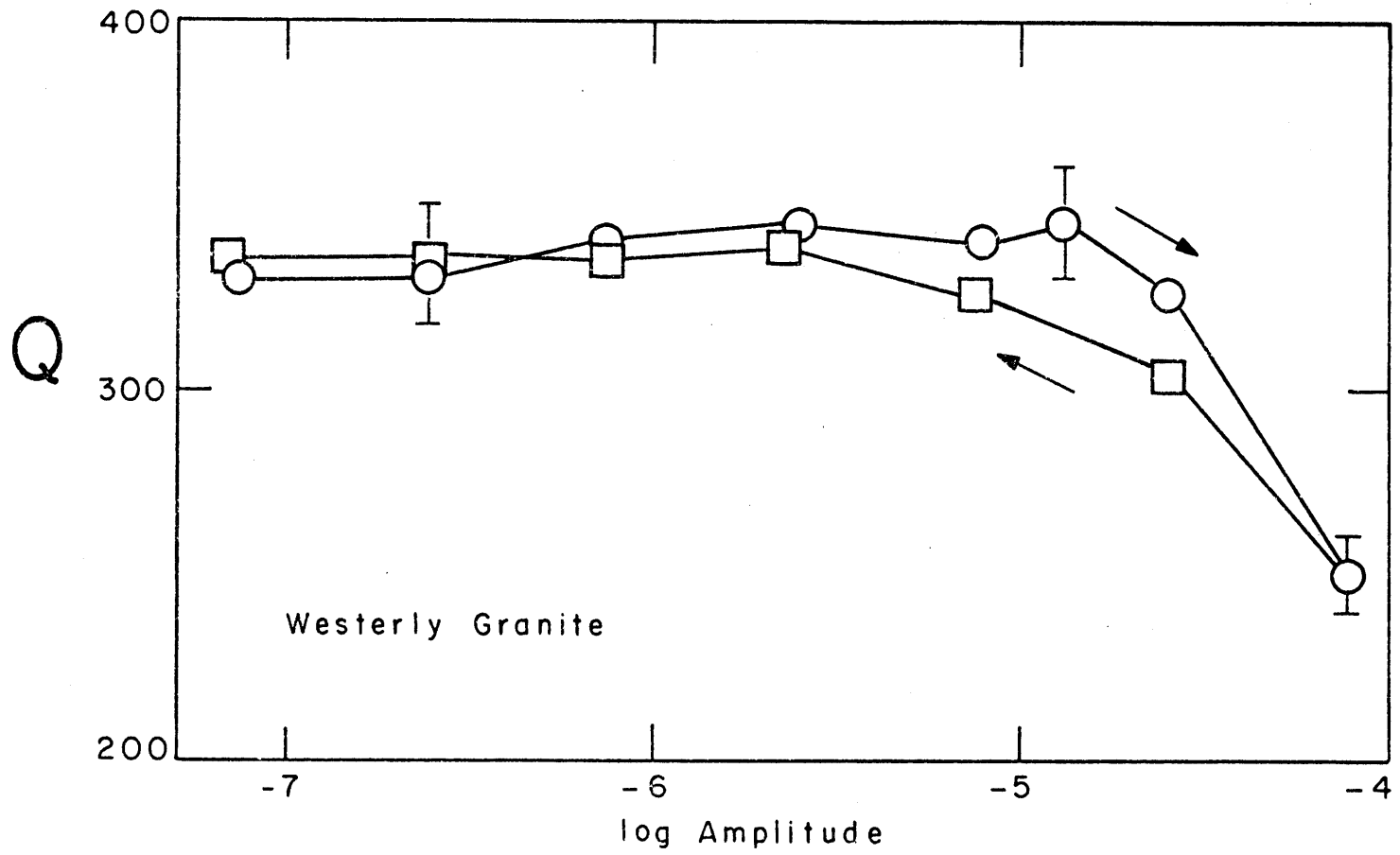


Figure 6-22

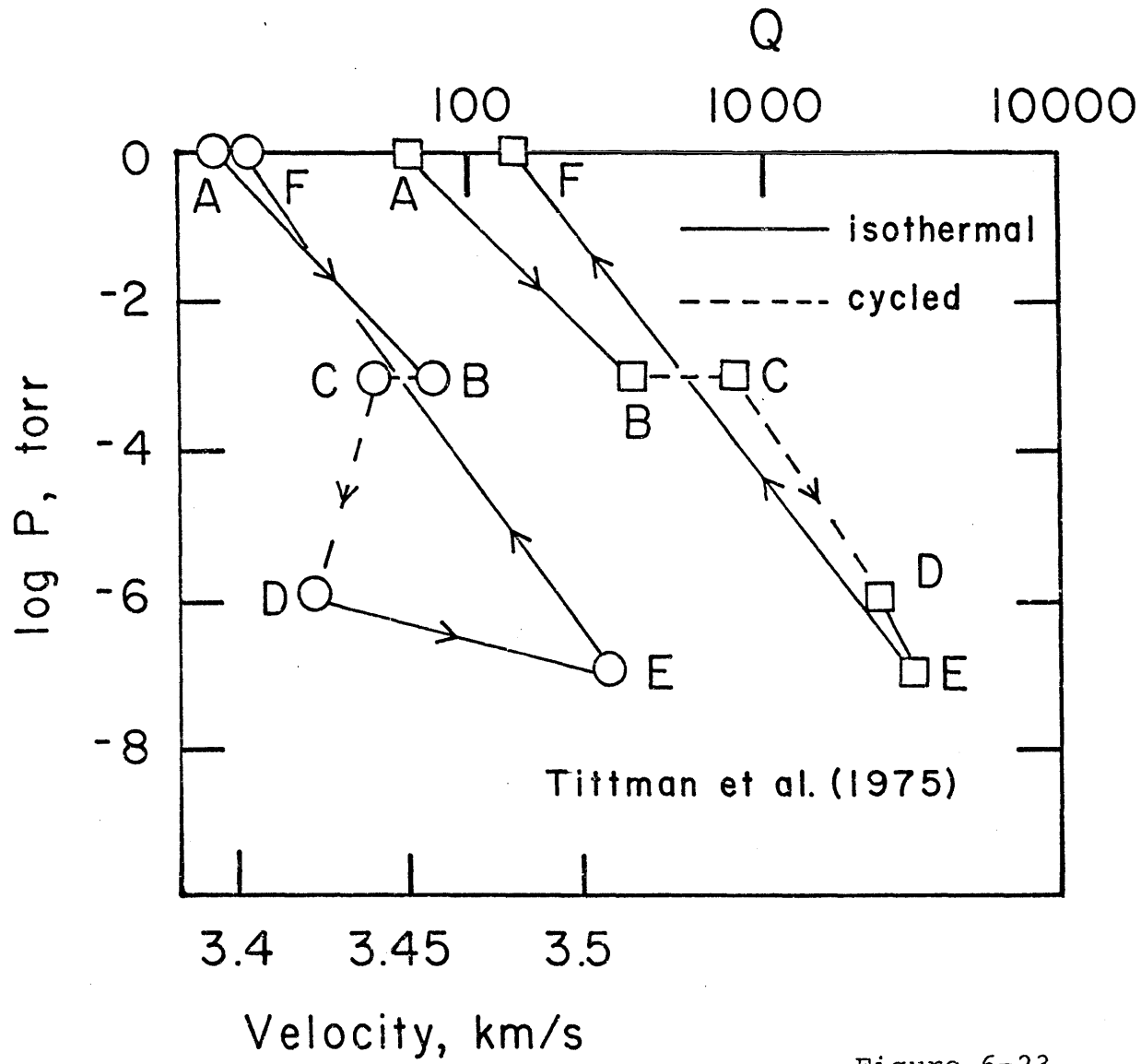
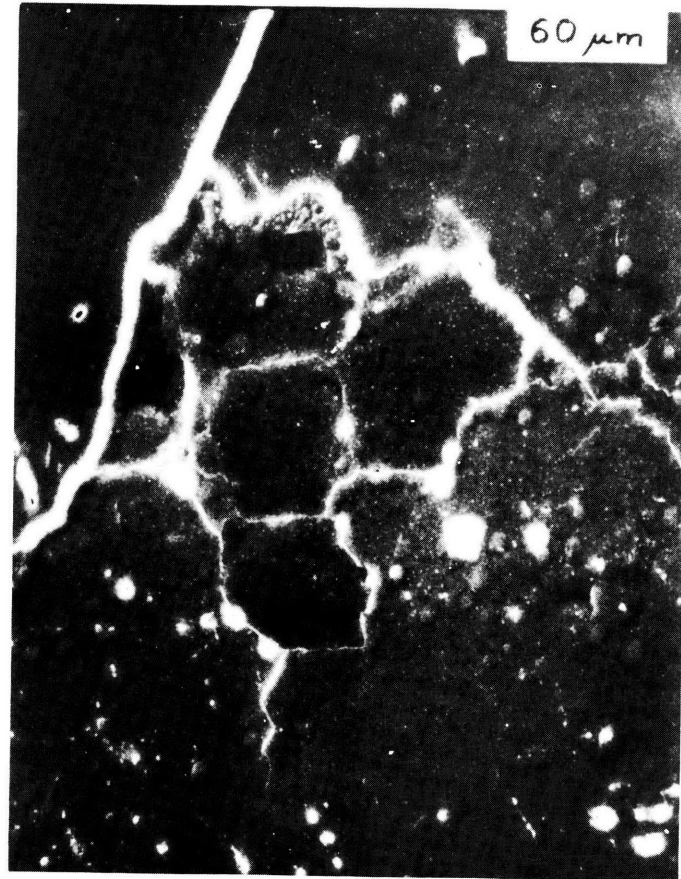


Figure 6-23



(a)



(b)

Figure 6-24



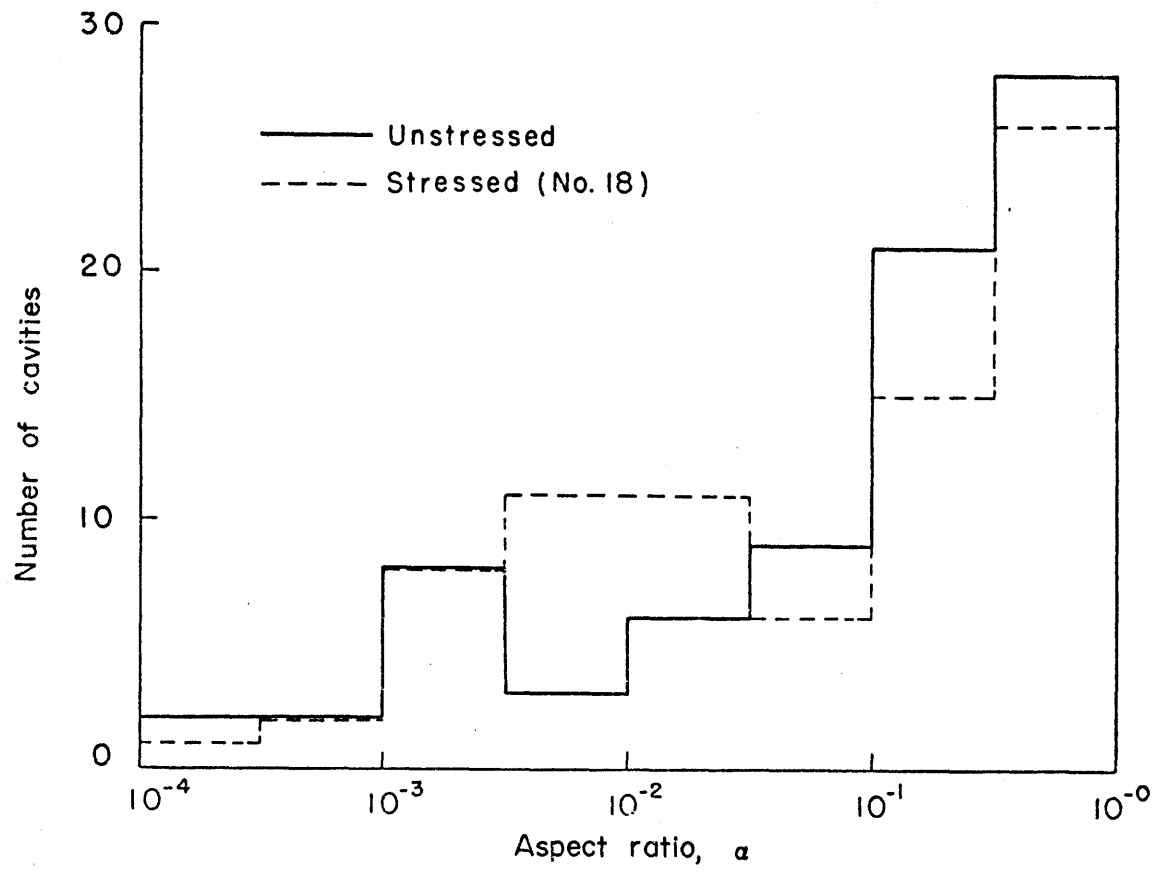


Figure 6-25

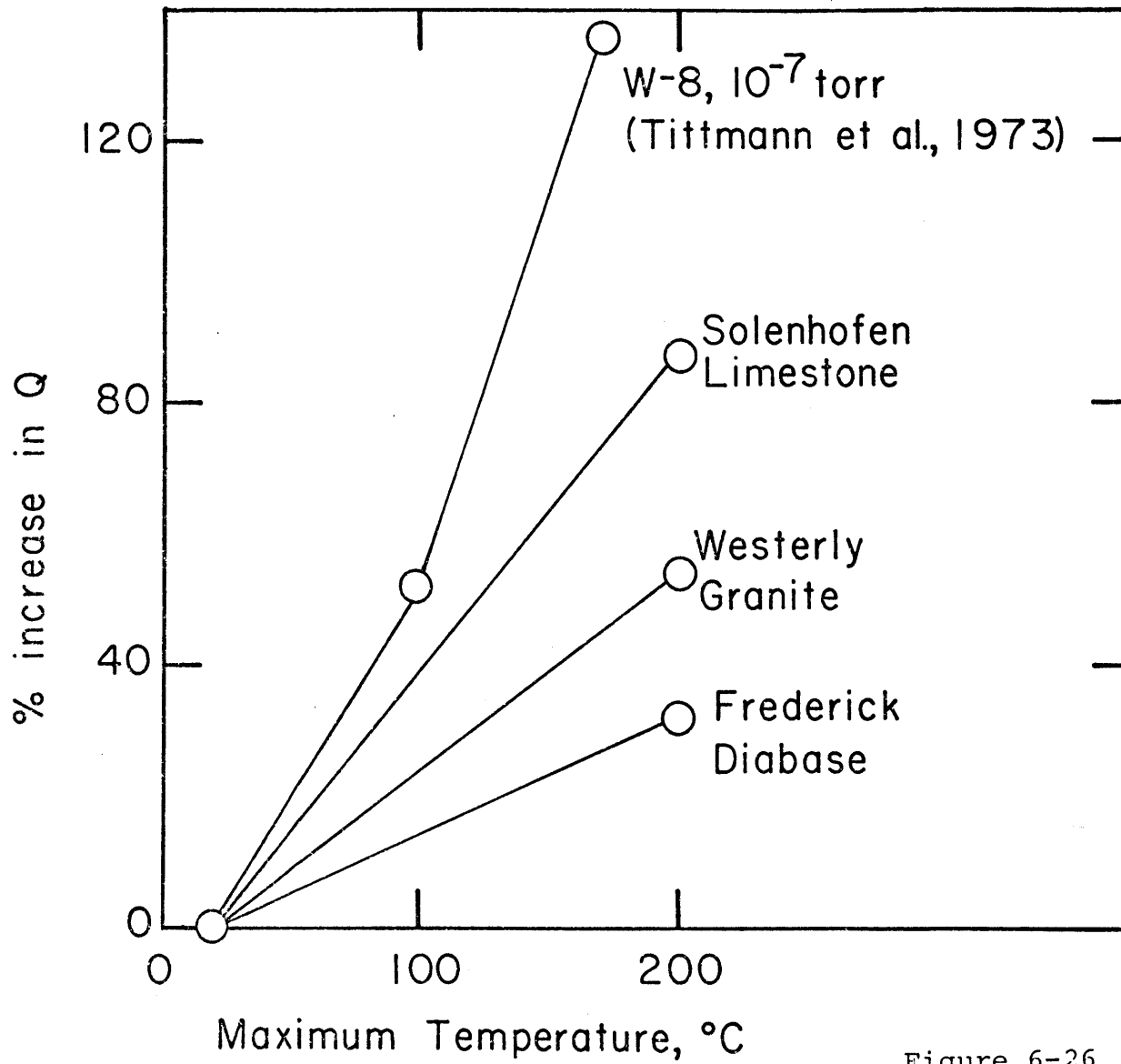


Figure 6-26

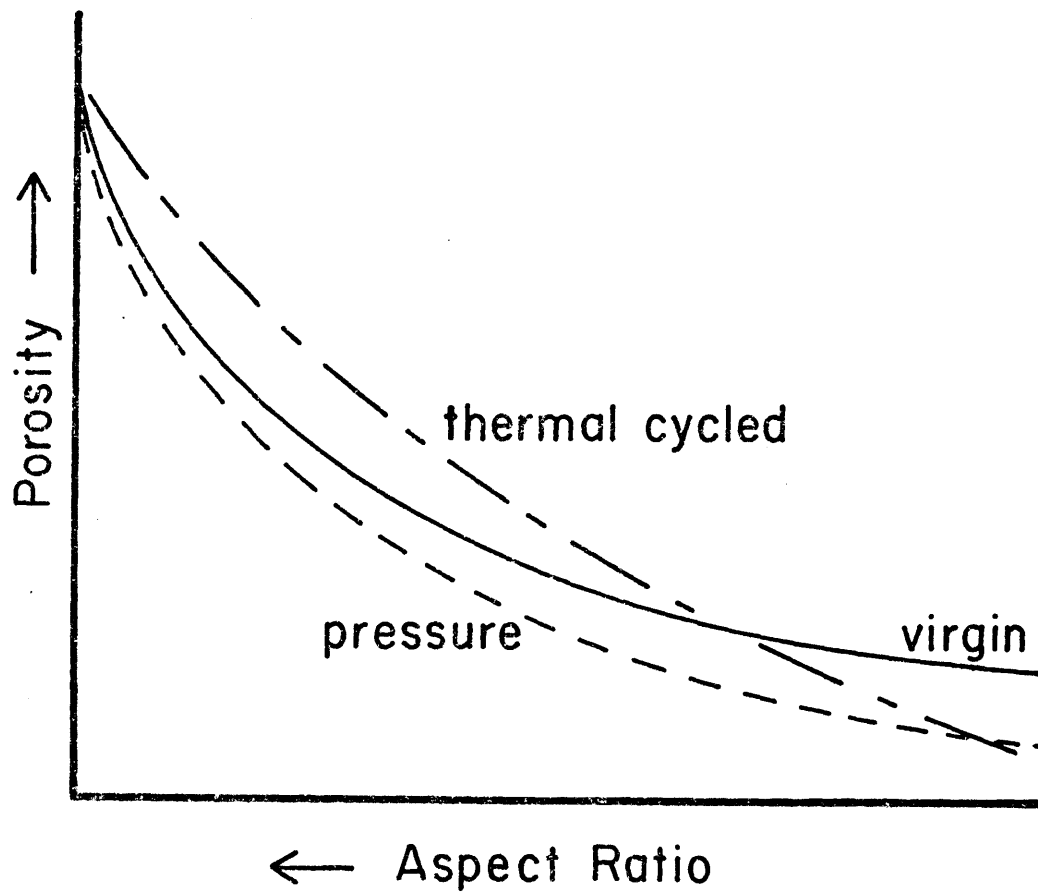


Figure 6-27

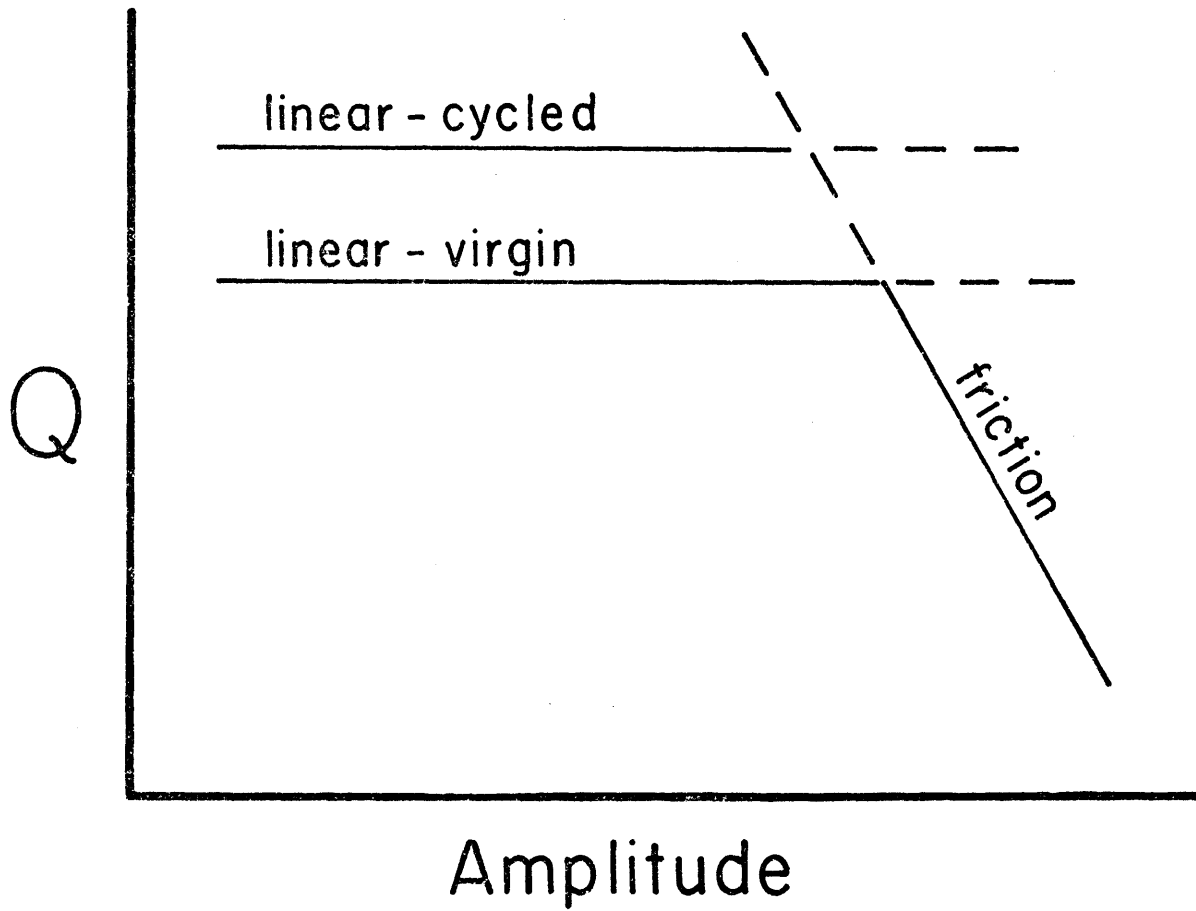
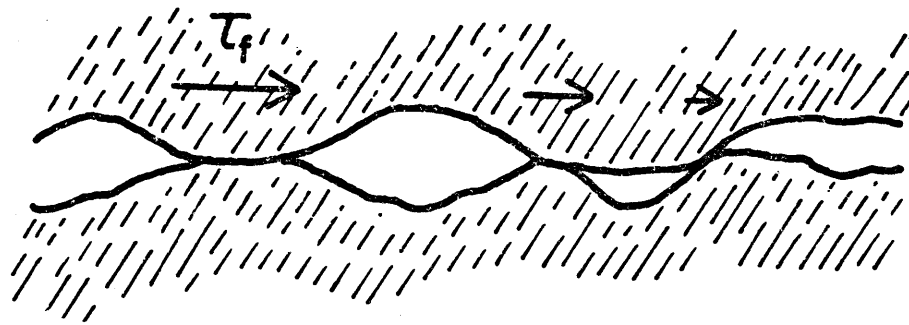
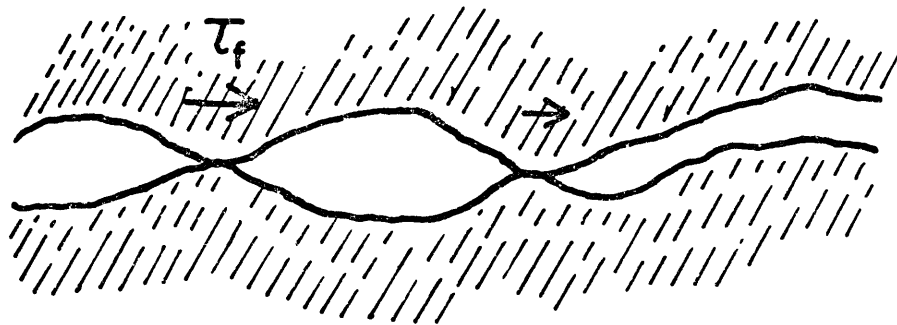


Figure 6-28



(a)



(b)

Figure 6-29

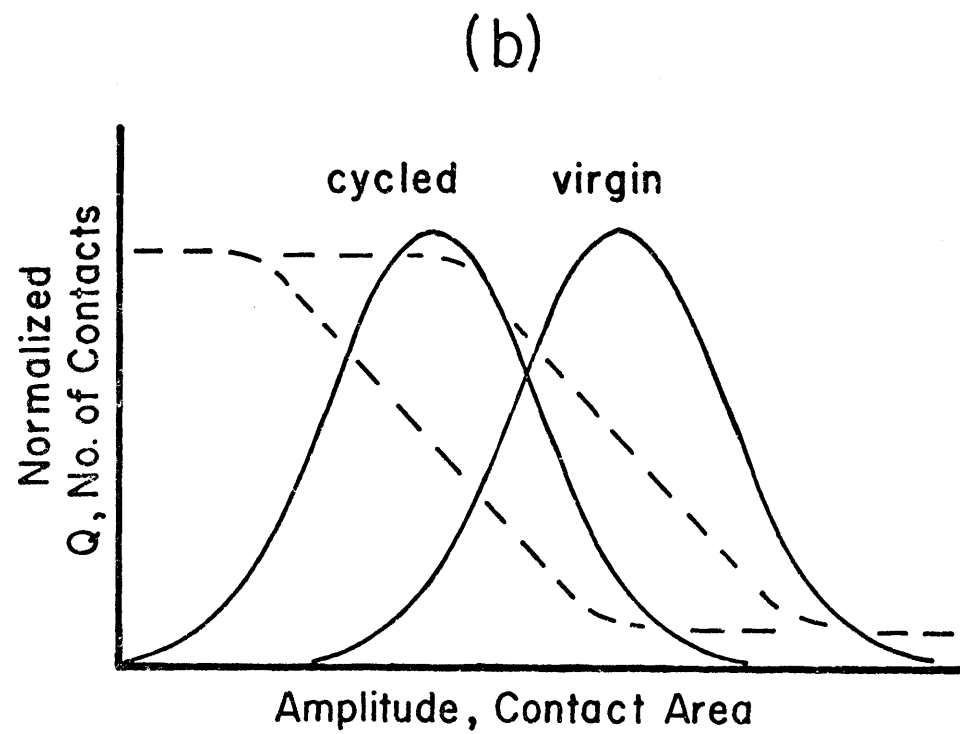
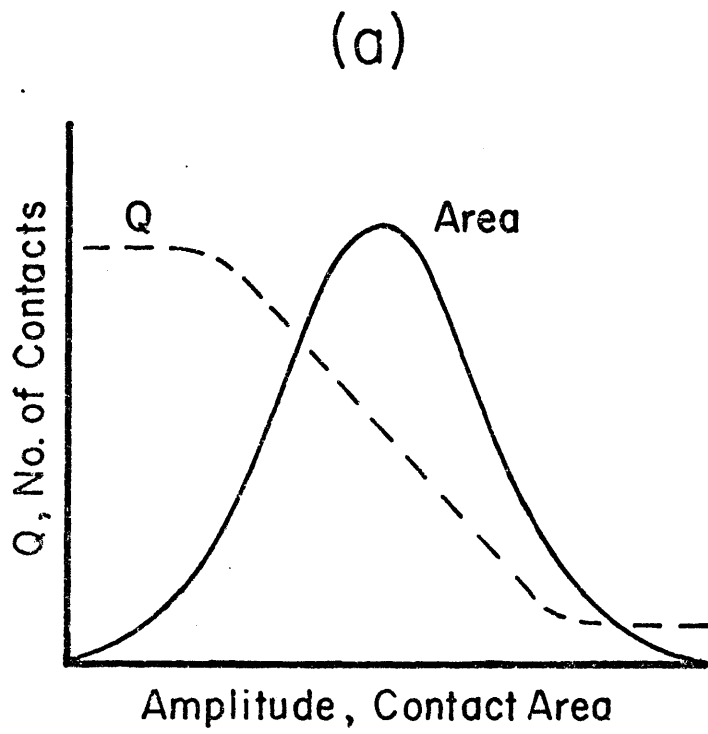


Figure 6-30

## CHAPTER 7

## SUMMARY AND CONCLUSIONS

This thesis has attempted to cover, from both experimental and theoretical points of view, the nature of seismic wave attenuation in dry and saturated upper crustal rocks. The investigation of both published and new data on the attenuation in rocks has shown that many of the same properties and processes that affect velocity also affect attenuation, many times to a greater extent. These properties include the number and distribution of cracks, the type and amount of fluid saturation, and the mechanical properties of the rock matrix.

Data obtained for this thesis, using both ultrasonic pulse transmission and resonant bar methods, have shown for a limited number of samples the following:

1. There are wide variations in  $Q$  (10-1000) for typical crustal rocks under varying conditions.
2. For rocks with cracks, attenuation decreases ( $Q$  increases) with increasing differential pressure both for P and S waves in all cases of saturation. The rate of increase is high at low pressures and levels off at higher pressures. For rocks undergoing pore collapse,  $Q$  increases during the loading cycle (increasing pressure). During unloading, at pressures less than the point of

initial collapse, both  $Q_p$  and  $Q_s$  are lower than the values attained while loading. The difference appears to be larger for P waves.

3. The major exception to the above result was for the oil shale. In this case the attenuation appears not to be controlled by cracks.  $Q$  did not increase rapidly for the tuffs either. Here, that effect was masked by scattering.

4. Attenuation in brine and water saturated rocks is greater (lower  $Q$ ) than in dry or methane saturated rocks. There was no significant difference between the  $Q$  values obtained for a partially saturated Berea sandstone and those found for the completely saturated sample. However, a hint of increased bulk attenuation (opposed to shear) was observed for the Berea with gas saturations of 5% and less.

5. In water saturated rocks,  $Q_p$  is higher than  $Q_s$  at both high and low pressures. In dry or methane saturated rocks,  $Q_s$  is generally slightly higher than or equal to  $Q_p$ .

6. The  $Q$  value is critically dependent not only on the number of cracks in the rock but also their shapes or widths. Rock samples thermally cycled at low heating and cooling rates up to 400°C show a marked increase in  $Q$  that cannot be entirely explained by outgassing of



volatiles. Such cycling also widens thin cracks thus reducing the numbers that contribute to attenuation due to friction. Fast thermal cycling propagates thin cracks and  $Q$  decreases.

7.  $Q$  is dependent on strain amplitude. Above a certain amplitude,  $10^{-6}$  to  $10^{-5}$  for the rocks studied,  $Q$  decreases rapidly. The behavior of amplitude dependent  $Q$  is also a function of the crack distribution in the rock. Thermally cycled samples experience the transition from high to low  $Q$  at lower amplitudes than untreated rocks. The lack of hysteresis in  $Q$  versus amplitude implies that little or no damage to the crack surfaces occurs at high strains.

The strain amplitude dependence of  $Q$  could have major implications. For example, to increase the high frequency content of seismic pulses, one may need to transmit the energy with relatively low near-source strain amplitudes.

8. Rocks anisotropic in velocity are also anisotropic in attenuation. For Westerly granite the anisotropy is apparently controlled by crack orientations. The  $Q$  anisotropy in oil shale is complicated and not easily explained by cracks

One procedure by which laboratory data may be compared to in-situ data is through the use of theoretical models.

Results obtained at high frequency then, in principle, may be extrapolated to seismic frequencies. This problem has been approached by examining a number of hypothesized attenuation mechanisms for which numerical models may be applied. The formulation of the pressure dependences of these models allows a reasonable fit to the ultrasonic  $Q_p$  and  $Q_s$  data obtained for the Berea sandstone. Such modeling provides a basis for the understanding of the mechanisms of attenuation in other rocks as well. However, the models require the specification of several free parameters thus limiting their predictive abilities. Furthermore, assumptions involving the amplitude behavior must also be considered. Given the limitations of the models, several specific conclusions regarding the attenuation mechanisms of seismic waves in porous rocks may be made.

1. At relatively shallow depths under normal hydrostatic pore pressures in the earth's crust, the primary mechanism for attenuation in rocks is motion and friction across grain boundaries and thin cracks. This is evident from the  $Q_p/Q_s$  ratios and the pressure, frequency, and amplitude dependencies in dry rocks. It has been said that  $Q$  is critically dependent on the geometry of the contact surfaces. In fact, the amplitude behavior of attenuation may be explained by assuming one of several possible sliding surface

configurations, most likely a peaked distribution of contact area.

2. Increasing differential pressure decreases the number of surfaces contributing to attenuation by friction. Since frictional loss depends on the number of cracks or sliding surfaces, the attenuation decreases ( $Q$  increases) with increasing pressure.

3. The introduction of fluid into a dry rock will wet crack surfaces and grain boundaries. By this crack lubrication, frictional sliding is facilitated and the attenuation increases. The amount of increase in attenuation is probably determined by several complex factors including the amount of clay in the rock and the wetting properties of the fluid relative to the solid rock matrix.

4. In a saturated porous rock, attenuation due to fluid flow plays a secondary role relative to friction. At low frequencies, squirting flow may be a viable mechanism, especially in the case of partial saturation. At ultrasonic frequencies, the Biot type fluid flow mechanism, while not necessarily dominating, plays an important role in the overall attenuation at moderately high pressures.

5. Losses associated with gas bubble resonances may result in an increase in P wave attenuation but only

for high frequencies (MHz range) and low gas saturations (<5%). The conditions for which this might be an important mechanism are extremely limited.

6. In rocks with large grains or pores, such as the tuffs, the dominant mechanism for attenuation at ultrasonic frequencies is scattering.

7. Attenuation in shales is in large part not due to crack friction. It is postulated in this thesis that the mechanism involved in oil shale is relative shear motion between the stiff shale component and the soft kerogen. For other shales, clay may play the role of kerogen in this model.

The most important and immediate application of the work done in this thesis, as has been mentioned many times throughout the text, is the use of laboratory measurements to infer rock properties from seismic data obtained in the field. While the ultrasonic data may be understood and modeled by several mechanisms, some problems still exist in the extrapolation of these data to other conditions. Such extrapolations are not only required in frequency, as has been done here, but also in strain amplitude. Amplitudes at seismic exploration frequencies may not be the same as those used in ultrasonic measurements, thus invalidating the absolute estimates of  $Q$ . It is clear that in order to utilize

laboratory data, it is most important to critically evaluate all the conditions of the measurements. Many of the discrepancies, even between separate laboratory measurements on the same rock, may be due to factors such as amplitude. However, given all that has been said about the frequency independence of  $Q$  in rocks, it may be that amplitude dependence cannot explain all the differences observed between  $Q$  values obtained with different experimental techniques. It may be that there is a frequency dependent component to friction or some other unaccounted for mechanism.

Even so, theoretical models provide the best method at the present time of comparing laboratory data taken under controlled conditions with in-situ data. One has to be aware, however, that the contributions of mechanisms that may be important at low frequencies are difficult to establish from ultrasonic data unless supplementary information is available. This may be in the form of certain low frequency resonance experiments performed at surface conditions. Furthermore, one must address the question of scaling. At best, models and data in this thesis represent only a point property of the rock. Factors which affect the amplitude of seismic waves in the real earth include such things as source strength and coupling, geometrical spreading, reflection

coefficients at interfaces, noise interference, interference of different waves, multiple reflections from thin beds, scattering and diffraction from large joints, faults, and other inhomogeneities, and even recording instrument response. Hidden under all of these is the intrinsic rock attenuation which must be isolated before any meaningful comparisons with laboratory data can be made.

As has been alluded to several times in the preceding chapters, a great deal of work is left to be done in the field of attenuation. This is especially true for amplitude dependence which has been seriously studied for only a very short time. In the future, experiments must be carefully designed and controlled to isolate important effects. Researchers using high frequency, high amplitude methods should consider simultaneous use of low frequency, low amplitude techniques on the same sample.

Other than amplitude effects, future experimental work should perhaps concentrate on the effects of acoustic anisotropy, considering the interesting results obtained for the oil shale. Also the effects of partial saturation should be studied in more detail. In particular, it is very important to understand the crack lubrication process for small fluid saturations. The influence of the wetting properties of the fluid on the behavior of  $Q$

with saturation should prove to be a useful experiment along these lines. In an effort to better simulate in-situ conditions, attenuation should be measured in saturated rock at relatively high ambient temperatures (up to 200°C) and pressures. Finally, experimental and field measurement techniques must be improved. It is meaningless to say that attenuation varies so much more than velocity if these changes cannot be detected with better precision.

From a theoretical point of view, the details of the friction mechanism are not much better understood now than 10 to 15 years ago. The extension of the contact model of cracks to attenuation, however, holds great promise to quantitatively explain many of the phenomena associated with the frictional mechanism observed in this thesis.

The development of new theory and its application to in-situ data should depend strongly on the direction taken in the experimental laboratories. Not enough systematic or appropriate data have been obtained in the past to justify much of the theoretical work done. It is not sufficient just to propose new mechanisms with no data to support them. The challenge will be to merge a growing set of controlled experimental and field data with new theoretical developments.

## REFERENCES

- Adam, N.K., 1938: "The Physics and Chemistry of Surfaces", Clarendon Press, Oxford.
- Adams, L.H., 1931, Equilibrium in binary systems under pressure: I - An experimental and thermodynamic investigation of the system, NaCl-H<sub>2</sub>O at 20°: Am. Chem. Soc. J., 53, pt. 3, 2769-3785.
- Al-Sinawi, S., 1968, An investigation of body wave velocities, attenuation and elastic parameters of rocks subjected to pressure at room temperature: Ph.D. Thesis, St. Louis University, Geophysics.
- Anderson, A.L., 1974: "Acoustics of gas-bearing sediments", Appl. Res. Lab., Univ. of Texas at Austin, ARL-TR-74-19.
- Anderson, D.L., Ben-Menahem, A., and Archambeau, C.B., 1965, Attenuation of seismic energy in the upper mantle: J. Geophys. Res., 70, 1441-1448.
- Anderson, O.L. and Liebermann, R.C., 1966: "Sound Velocities in Rocks and Minerals", VESIAC Report 7885-4-X, Willow Run Laboratories, Ann Arbor, MI.
- Andreeva, I.B., 1964, Scattering of sound by air bladders of fish in deep sound-scattering ocean layers: Sov. Phys. Acoust., 10, 17-20.
- Attewell, P.B., Ramana, Y.V., 1966, Wave attenuation and internal friction as functions of frequency in rocks:



Geophysics, 31, 1049-1056.

- Berlincourt, D.A., Curran, D.R. and Jaffe, H., 1964, Piezoelectric and piezomagnetic materials: in "Physical Acoustics, vol. 1A", Academic Press, New York, 169-270.
- Biot, M.A., 1956a, Theory of propagation of elastic waves in a fluid-saturated porous solid. I. Low frequency range: J. Acoust. Soc. Am., 28, 168-178.
- Biot, M.A., 1956b, Theory of propagation of elastic waves in a fluid-saturated porous solid. II. High frequency range: J. Acoust. Soc. Am., 28, 179-191.
- Biot, M.A., 1962a, Mechanics of deformation, and acoustic propagation in porous media: J. Appl. Phys., 33, 1482-1498.
- Biot, M.A., 1962b, Generalized theory of acoustic propagation in porous dissipative media: J. Acoust. Soc. Am., 34, 1254-1264.
- Birch, F., 1960, The velocity of compressional waves in rocks to 10 kilobars: J. Geophys. Res., 65, 1083-1102.
- Birch, F., and Bancroft, D., 1938, Elasticity and internal friction in a long column of granite: Bull. Seis. Soc. Am., 28, 243-254.

- Bland, D.R., 1960: "The Theory of Linear Viscoelasticity",  
New York, Pergamon Press.
- Boltzmann, L., 1876, Zur Theorie der elastischen  
Nachwirkung: Ann. Phys. Chem. (Poggendorff), Erg.-Bd.,  
7, 624-654.
- Born, W.T., 1941, Attenuation constant of earth materials:  
Geophysics, 6, 132-148.
- Bozorth, R.M., Mason, W.P., and McSkimin, H.J. 1951,  
Frequency dependence of elastic constants and losses  
in nickel: Bell System Tech. J., 30, 970-989.
- Brace, W.F., 1965, Some new measurements of linear  
compressibility of rocks: J. Geophys. Res., 70 (2),  
391-398.
- Bradley, J.J. and Ford, A.N., Jr., 1966, Internal friction  
in rocks: in "Handbook of Physical Constants",  
S.P. Clark, Jr., ed., Geol. Soc. Am. Publication,  
175-193.
- Briggs, H.B., Johnson, J.B., and Mason, W.P., 1947,  
Properties of liquids at high sound pressure: J.  
Acoust. Soc. Am., 19, 664-677.
- Browne, M.T. and Pattison, J.R., 1957, The damping effect  
of surrounding gases on a cylinder in longitudinal  
oscillations: Brit. Jour. Appl. Phys., 8, 452-456.

- Bruckshaw, J. McG., and Mahanta, P.C., 1954, The variation of elastic constants of rocks with frequency: Petroleum, 17, 14-18.
- Byers, F.M., Carr, W.J., Orkild, P.T., Quinlivan, W.D. and Sargent, K.A., 1976, Volcanic suites and related cauldrons of Timber Mountain - Oasis Valley caldera complex, southern Nevada: U.S.G.S. Prof. Paper 919.
- Collins, F. and Lee, C.C., 1956, Seismic wave attenuation characteristics from pulse experiments: Geophysics, 21, 16-40.
- Cooper, H.W. and Simmons, G., 1977, Thermal cycling cracks in three igneous rocks: submitted to Int. J. Rock Mech. Min. Sci. and Geomech. Abstr.
- Crawford, F.S., 1968: "Waves, Berkeley Physics Course, v. 3", McGraw-Hill, New York, 102-108.
- Dainty, A.M., Goins, N.R., and Toksöz, M.N., 1976, Seismic investigation of the lunar interior: in "Lunar Science VII", Lunar Science Institute, Houston, TX, 181-183.
- Devin, C., Jr., 1959, Survey of thermal, radiation and viscous damping of pulsating air bubbles in water: J. Acoust. Soc. Am., 31, 1654-1667.
- Donnell, J.R., 1964, Geology and oil shale resources of the Green River Formation: in "Proc. of First Five Symposia on Oil Shale", Colo. School of Mines, 153-163.

- Duncan, D.C. and Denson, N.M., 1949, Geology of Naval Oil Shale Reserves 1 and 3, Garfield County, CO: U.S. Geol. Sur. Map OM-94.
- Edwards, R.H., 1951, Stress concentrations around spheroidal inclusions and cavities: J. Applied Mech. 19-30.
- Eller, A.I., 1970, Damping constant of pulsating bubbles: J. Acoust. Soc. Am., 47, 1469-1470.
- Eshelby, J.D., 1957, The determination of the elastic field of an ellipsoidal inclusion, and related problems: Proc. Roy. Soc. (London), 241(A), 376-396.
- Fatt, I. and Davis, D.H., 1952, Reduction in permeability with overburden pressure: Trans. AIME, Pet. Branch, 195, 329.
- Fortsch, O., 1956, Die Ursachen der Absorption elastischer Wellen: Ann. Geofis., 9, 469-524.
- Frangos, W.T., 1967, The effect of confining pressure on the permeability of Westerly granite: B.S. Thesis, Dept. Earth and Planet. Sci., M.I.T.
- Futterman, W.I., 1962, Dispersive body waves: J. Geophys. Res., 67 (13), 5257-5291.
- Gardner, G.H.F., Wyllie, M.R.J., Droschak, D.M., 1964;

- Effects of pressure and fluid saturation on the attenuation of elastic waves in sands: J. Petroleum Tech., 189-198.
- Gemant, A., 1950: "Frictional Phenomena", Chemical Pub. Co., New York.
- Goodier, J.N. and Florence, A.L., 1964, Localized thermal stress at holes, cavities, and inclusions disturbing uniform heat flow. Thermal crack propagation: Proc., 11th Int. Cong. of Applied Mech., Munich.
- Gordon, R.B., 1974, Mechanical relaxation spectrum of crystalline rock containing water: J. Geophys. Res., 79, 2129-2131.
- Gordon, R.B., and Davis, L.A., 1968, Velocity and attenuation of seismic waves in imperfectly elastic rock: J. Geophys. Res., 73, 3917-3935.
- Gordon, R.B. and Rader, D., 1971, Imperfect elasticity of rock: its influence on the velocity of stress waves: "Geophysical Monograph Series, Vol. 14", J.G. Heacock ed., Am. Geophys. Union, Washington.
- Greenwood, J.A. and Williamson, J.B.P., 1966, Contact of nominally flat surfaces: Proc. Roy. Soc. London, 295(A), 300.
- Hamilton, E.L., 1972a, Compressional wave attenuation in marine sediments: Geophysics, 37, 620-646.

- Hamilton, E.L., 1972b, Correlation between  $Q_S$  of shear waves and rigidity: Mar. Geol., 13, M27-M30.
- Houghton, G., 1963, Theory of bubble pulsation and cavitation: J. Acoust. Soc. Am., 35, 1387-1393.
- Jackson, D.D., 1969, Grain boundary relaxations and the attenuation of seismic waves: Ph.D. Thesis, M.I.T., Dept. of Earth and Planet. Sci.
- Jackson, D.D., and Anderson, D.L., 1970, Physical mechanisms of seismic wave attenuation: Rev. Geophys. Space Phys., 8, 1-63.
- Johnson, B., Gangi, A.F., and Handin, J., 1978, Thermal cracking of rock subjected to slow, uniform temperature changes: in "19th U.S. Rock Mechanics Symposium", Univ. of Nevada, Reno, 259-267.
- Ke, T.S., 1947, Experimental evidence on the viscoelastic behavior of grain boundaries in metals: Phys. Rev., 25, 533.
- Kelvin, Lord, 1878, Elasticity: in "Encyclopedia Britannica, 9th ed.", also, "Collected Works, 3" Cambridge University Press, London, 1890, 1-112.
- Kingery, W.D., 1959: "Property Measurements at High Temperature", Wiley, New York.

- Kissell, F.N., 1972, Effect of temperature on internal friction in rocks: J. Geophys. Res., 77, 1420-1423.
- Klima, K., Vanck, J., and Pros, Z., 1964, The attenuation of longitudinal waves in diabase and greywacke under pressures up to 4 kilobars: Studia Geophy. et Geod., 8, 247-254.
- Knopoff, L., 1964, Q: Rev. Geophys., 2, 625-660.
- Knopoff, L., and MacDonald, J.F., 1960, Attenuation of small amplitude stress waves in solids: Rev. Mod. Phys., 30, 1178-1192.
- Kolsky, H., 1953, "Stress Waves in Solids", Oxford University Press, London; also 1963, Dover Publications, New York.
- Krech, W.W., Henderson, F.A., and Hjelmstad, E., 1974, A standard rock suite for rapid excavation research: U.S. Bureau of Mines, RI 7865.
- Kuster, G.T. and Toksöz, M.N., 1974, Velocity and attenuation of seismic waves in two-phase media: Part I - Theoretical formulations: Geophysics, 39, 587-606.
- Latham, G.V., Nakamura, Y., Lammlein, D., Dorman, J., and Duennebier, F., 1974, Structure and state of the lunar interior based upon seismic data (abst.): in "Lunar Science V", Lunar Science Institute, Houston, TX, 434.

- Levykin, A.I., 1965, Longitudinal and transverse wave absorption and velocity in rock specimens at multi-lateral pressures up to  $4000 \text{ kg/cm}^2$ : No. 1, 94-98, Physics of the Solid Earth.
- Lockner, D., Walsh, J.B., and Byerlee, J., 1977, Changes in seismic velocity and attenuation during deformation of granite: J. Geophys. Res., 82, 5374-5378.
- Loeb, J., 1961, Attenuation des ondes sismiques dans les solides: Geophys. Prospecting, 9, 370-381.
- Lomnitz, C., 1957, Linear dispersion in solids: J. Appl. Phys., 28, 201-205.
- Long, G., and Chierici, G., 1961, Salt content changes compressibility of reservoir brines: Petroleum Engineer, July, p. B-25, B-26, and B-31.
- Low, P.H., 1959, Viscosity of water in clay systems: in "Eighth national conference on clays and clay minerals", Pergamon Press Inc., New York, 170-182.
- Marx, J.W., 1951, Use of the piezoelectric gauge for internal friction measurements: Rev. Sci. Instr., 22, 503-509.



- Mason, W.P., 1958: "Physical acoustics and the properties of solids", Van Nostrand Co., Princeton, NJ.
- Mason, W.P., and McSkimin, H.J., 1947, Attenuation and scattering of high frequency sound waves in metals and glasses: J. Acoust. Soc. Am., 19, 464-473.
- Mavko, G., 1978, A more general description of frictional attenuation, abst: Trans. Am. Geophys. Union (EOS), 59, 376.
- Mavko, G. and Nur, A., 1975, Melt squirt in the aesthenosphere: J. Geophys. Res., 80, 1444-1448.
- Mayer-Gürr, A., 1976: "Petroleum Engineering", Halstad Press, John Wiley and Sons, New York, p. 40.
- McDonal, F.J., Angona, F.A., Mills, R.L., Sengbush, R.L., Van Nostrand, R.G., and White, J.E., 1958, Attenuation of shear and compressional waves in Pierre Shale: Geophysics, 23, 421-439.
- McSkimin, H.J., 1956, Propagation of longitudinal waves and shear waves in cylindrical rods at high frequencies: J. Acoust. Soc. Am., 28, 484-494.
- McSkimin, H.J., 1964, Ultrasonic methods for measuring the mechanical properties of liquids and solids: in "Physical Acoustics, Vol. I", W.P. Mason, ed., Academic Press, New York, 271-334.

- Merkulova, V.M., Pigulevskiy, E.D. and Tsaplev, V.M.,  
1972, Sound absorption measurements in uniaxially  
compressed rocks: Physics of the Solid Earth, no. 3,  
166-167.
- Meyer, O., 1874, Zur Theorie der inner Reibung: J. Reine  
Angew. Math., 58, 130.
- Millahn, K.O. and Jurczyk, D., 1977, Measurement of  
attenuation in reflection seismograms: presented at  
the 47th meeting, Soc. Expl. Geophys., Calgary, Alberta.
- Mindlin, R.D. and Deresiewicz, H., 1953, Elastic spheres  
in contact under varying oblique forces: J. Appl. Mech.,  
20, 327-344.
- Minnaert, M., 1933, On musical air bubbles and the sounds  
of running water: Phil. Mag., 10, 235-248.
- Morrow, C., Brace, W.F., and Carter, E., 1977, Dramatic  
electrical changes in porous rocks at low stress, abst.:  
Trans. Am. Geophys. Union (EOS), 58, 1235.
- Munson, D.E. and Young, E.G., 1977, Dynamic modeling of  
rock springs oil shale using a homogeneous equivalent  
Maxwell model: Int. J. Rock Mech. Min. Sci. and  
Geomech., 14, 283-287.

- Myklestad, N.O., 1942, Two problems of thermal stress in the infinite solid: J. Applied Mech., 136-143.
- Nakamura, Y., Dorman, J., Duennebier, F., Ewing, M., Lammlein, D., and Latham, G., 1974, High frequency lunar teleseismic events: Geochim. Cosmochim. Acta, Suppl. 5, 2883-2890.
- Nur, A., 1969, Effect of stress and fluid inclusions on wave propagation in rock: Ph.D. Thesis, M.I.T., Dept. Earth Planet. Sci.
- Nur, A., and Simmons, G., 1969a, The effect of viscosity of a fluid phase on velocity in low porosity rocks: Earth Planet. Sci. Lett., 7, 99-108.
- Nur, A.M., and Simmons, G., 1969b, The effect of saturation on velocity in low porosity rocks: Earth Planet. Sci. Lett., 7, 183-193.
- N.Y. State Dept. of Commerce, 1951: "The Clays and Shales of New York State", p. 196-198 and p. 345.
- Obert, L., Windes, S.L. and Duvall, W.I., 1946, Standardized tests for determining the physical properties of mine rock: U.S. Bur. Mines R.I. 3891.
- O'Connell, R.J. and Budiansky, B., 1977, Viscoelastic properties of fluid saturated cracked solids: J. Geophys. Res., 82, 5719-5736.

- O'Doherty, R.F. and Anstey, N.A., 1971, Reflections on amplitudes: Geophysical Prospecting, 19, 430-485.
- Oppenheim, A.V. and Schafer, R.W., 1975, "Digital Signal Processing", Prentice Hall, Englewood Cliffs, NJ, 480-531.
- Pandit, B.I. and Tozer, D.C., 1970, Anomalous propagation of elastic energy within the Moon: Nature, 226, 335.
- Pandit, B.I., and Savage, J.C., 1973, An experimental test of Lomnitz's theory of internal friction in rocks: J. Geophys. Res., 78, 6097-6099.
- Peselnick, L. and Zietz, J., 1959, Internal friction of fine-grained limestones at ultrasonic frequencies: Geophysics, 24, 285-296.
- Peselnick, L. and Outerbridge, W.F., 1961, Internal friction and rigidity modulus of Solenhofen limestone over a wide frequency range: U.S. Geol. Survey, Prof. Paper No. 400B.
- Pinkerton, J.M.M., 1947, A pulse method for the measurement of ultrasonic absorption in liquids: Results for water: Nature, 160, 128-129.
- Pros, Z., Vanek, J., and Klima, K., 1962, The velocity of elastic waves in diabase and greywacke under pressures up to 4 kilobars: Studia Geoph. et Geod., 6, 347-367.

- Quimby, S.L., 1925, On the experimental determination of the viscosity of vibrating solids: Phys. Rev., 25, 558-573.
- Rayleigh, Lord, 1945, "The Theory of Sound", v. 1, Dover Publications, New York, 252.
- Richter, D. and Simmons, G., 1974, Thermal expansion behavior of igneous rocks: Int. J. Rock Mech. Min. Sci. and Geomech. Abstr., 11, 403-411.
- Robertson, E.C., 1955, Experimental study of the strength of rocks: Bull. Geol. Soc. Am., 66, 1275-1314.
- Russell, T.F., 1936, Some mathematical considerations on the heating and cooling of steel: Iron and Steel Institute Spec., Report 14.
- Schafer, R.W., 1968, Echo removal by discrete generalized linear filtering: Ph.D. Thesis, M.I.T., Dept. of Elec. Eng.
- Schoenberger, M. and Levin, F.K., 1974, Apparent attenuation due to intrabed multiples: Geophysics, 39, 278-291.
- Schreiber, E., Anderson, O.L., Soga, N., 1973, "Elastic Constants and Their Measurements", McGraw-Hill, NY.
- Shima, A., 1970, The natural frequency of a bubble oscillating in a viscous compressible liquid: J. Basic Eng. (Trans. ASME), 555-562.

- Silberman, E., 1957, Sound velocity and attenuation in bubbly mixtures measured in standing wave tubes: J. Acoust. Soc. Am., 29, 925-933.
- Simmons, G., Siegfried, R.W., II and Feves, M., 1974, Differential strain analysis: a new method for examining cracks in rocks: J. Geophys. Res., 79, 4383-4385.
- Smith, F.D., 1935, On the destructive mechanical effects of the gas bubbles liberated by the passage of intense sound through a liquid: Phil. Mag., 1147-1151.
- Solomon, S.C., 1973, Shear wave attenuation and melting beneath the mid-Atlantic Ridge: J. Geophys. Res., 78, 6044-6059.
- Spencer, T.W., Edwards, C.M., and Sonnad, J.R., 1977, Seismic wave attenuation in non-resolvable cyclic stratification: Geophysics, 42, 939-949.
- Spetzler, H. and Anderson, D.L., 1968, The effect of temperature and partial melting on velocity and attenuation in a simple binary system: J. Geophys. Res., 73, 6051-6060.
- Spinner, S. and Tefft, W.E., 1961, Method for determining mechanical resonance frequencies and for calculating elastic moduli from these frequencies: Am. Soc.

- Test. Mater. Proc., 61, 1221-1238.
- Spitzer, L., Jr., 1943, Acoustic properties of gas bubbles in a liquid: OSRD 1705, Division of War Research, Columbia University.
- Sprunt, E.S. and Brace, W.F., 1974, Direct observation of microcavities in crystalline rocks: Rock Mech. Mining Sci. Geomech., 11, 139-150.
- Stephen, T. and Stephen, H. (ed.), 1963, "Solubilities of Inorganic and Organic Compounds, Vol. I, Part I", MacMillan and Co., New York, p. 83.
- Stoll, R.D., 1974, Acoustic waves in saturated sediments: in "Physics of Sound in Marine Sediments", L. Hampton, ed., Plenum, New York.
- Stoll, R.D., 1977, Acoustic waves in ocean sediments: Geophysics: 42, 715-725.
- Stoll, R.D. and Bryan, G.M., 1970, Wave attenuation in saturated sediments: J. Acous. Soc. Am., 47, 1440-1447.
- Terry, N.B., 1957, Some considerations of the magnetostrictive composite oscillator method for the measurement of elastic moduli: Br. J. Appl. Phys., 8, 270.

- Timur, A., 1968, Velocity of compressional waves in porous media at permafrost temperatures: Geophysics, 33, 584-596.
- Timur, A., 1977, Temperature dependence of compressional and shear wave velocities in rocks: Geophysics, 42, 950-956.
- Tittmann, B.R., Abdel-Gawad, M., and Housley, R.M., 1972, Elastic velocity and Q factor measurements on Apollo 12, 14, and 15 rocks: in Lunar Science Conf. 3rd Proc., Geochim. Cosmochim. Acta, Suppl. 3, v. 3, 2565-2575.
- Tittmann, B.R., Housley, R.M. and Cirilin, E.H., 1973, Internal friction of rocks and volatiles on the moon: in Lunar Science Conf., 4th Proc. Geochim. Cosmochim. Acta, Suppl. 4, v. 3, 2631-2637.
- Tittmann, B.R., Housley, R.M., Alers, G.A., and Cirilin, E.H., 1974, Internal friction in rocks and its relationship to volatiles on the moon: in Lunar Science Conf., 5th Proc., Geochim. Cosmochim. Acta, Suppl. 5, v. 3, 2913-2918.
- Tittmann, B.R., Curnow, J.M., and Housley, R.M., 1975, Internal friction quality factor  $Q \geq 3100$  achieved in lunar rock 70215, 85: in Lunar Science Conf., 6th Proc. Geochim. Cosmochim. Acta, Suppl. 6, v. 3, 3217-3226.



- Tittmann, B.R., Ahlberg, L., and Curnow, J., 1976,  
Internal friction and velocity measurements: in  
Lunar Science Conf., 7th Proc., Geochim. Cosmochim.  
Acta, Suppl. 4, v. 3, 3123-3132.
- Todd, P.T., 1973, Effect of cracks on elastic properties  
of low porosity rocks: Ph.D. Thesis, M.I.T., Dept.  
Earth and Planet. Sci.
- Todd, P.T., Wang, H., Baldrige, W.S., and Simmons, G.,  
1972, Elastic properties of Apollo 14 and 15 rocks:  
in Proc. Third Lunar Sci. Conf., Geochim. Cosmochim.  
Acta, v. 3, M.I.T. Press, 2577-2586.
- Toksöz, M.N., Dainty, A.M., Solomon, S.C., and Anderson,  
K.R., 1974, Structure of the moon: Rev. Geophys. Space  
Phys., 12, 539-567.
- Toksöz, M.N., Cheng, C.H., and Timur, A., 1976, Velocities  
of seismic waves in porous rocks: Geophysics, 41,  
621-645.
- Toksöz, M.N., Johnston, D.H. and Timur, A., 1978, Attenuation  
of seismic waves in dry and saturated rocks: I.  
Laboratory measurements: in press, Geophysics.
- Tribolet, J.M., 1977a, A new phase unwrapping algorithm:  
IEEE Trans. Acoust., Speech, Signal Proc., v. ASSP-25,  
170-177.

- Tribolet, J.M., 1977b, Seismic applications of homomorphic signal processing: Sc.D. Thesis, M.I.T., Res. Lab. of Elec.
- Truell, R., and Oates, W., 1963, Effect of lack of parallelism in sample faces on measurement on ultrasonic attenuation: J. Acoust. Soc. Am., 35, 1382.
- Truell, R., Elbaum, C., and Chick, B., 1969, "Ultrasonic Methods in Solid State Physics", Academic Press, NY.
- Tu, L.Y., Brennan, J.N., and Saver, J.A., 1955: Dispersion of ultrasonic pulse velocity in cylindrical rods: J. Acoust. Soc. Am., 27, 550-555.
- Ulrych, T.J., 1971, Application of homomorphic deconvolution to seismology: Geophysics, 36, 650-660.
- Voigt, W., 1892, "Über Innere Reibung fester Körper, Insbesondere der Metalle: Ann. d. Phys., 47, 671-693.
- Volarovich, M.P. and Gurevich, G.I., 1957, Investigation of dynamic moduli of elasticity for rocks in relation to temperature: Bull. Acad. Sci. USSR, Geophys., no. 4, 1-9.
- Walsh, J.B., 1965, The effect of cracks on the compressibility of rock: J. Geophys. Res., 70, 381-389.
- Walsh, J.B., 1966, Seismic wave attenuation in rock due to friction: J. Geophys. Res., 71, 2591-2599.

- Walsh, J.B., 1968, Attenuation in partially melted material:  
J. Geophys. Res., 73, 2209-2216.
- Walsh, J.B., 1969, New analysis of attenuation in partially  
melted rock: J. Geophys. Res., 74, 4333-4337.
- Walsh, J.B., Brace, W.F. and Wawersik, W.R., 1970,  
Attenuation of stress waves in Cedar City quartz  
diorite: Air Force Weapons Laboratory Tech. Rep. No.  
AFWL-TR-70-8.
- Walsh, J.B. and Grosenbaugh, M.A., 1978, A new model for  
analyzing the effect of fractures on compressibility:  
submitted to J. Geophys. Res.
- Wang, C. and Meltzer, M., 1972, Propagation of elastic  
waves in a rock undergoing phase transitions: in  
Cordilleran Section, 68th Annual Meeting, Geol. Soc.  
Am. Abst., 4, no. 3, 256-257.
- Ward, R.W. and Toksöz, M.N., 1971, Causes of regional  
variation of magnitude: Bull. Seis. Soc. Am., 61,  
649-670.
- Warren, N., Trice, R., and Stephens, J., 1974, Ultrasonic  
attenuation: Q measurements on 70215, 29: Geochim.  
Cosmochim. Acta, Suppl. 5, 2927-2938.
- Watson, T.H. and Wuenschel, P.C., 1973, An experimental  
study of attenuation in fluid saturated porous media

compressional waves and interfacial waves: Presented at the 43 Annual Meeting of the Society of Exploration Geophysicists.

- Weston, D.E., 1967, Sound propagation in the presence of bladderfish: in "Underwater Acoustics", Vol. II, V.M., Albers, ed., Plenum Press, NY.
- White, J.E., 1965, "Seismic waves, radiation, transmission, and attenuation", McGraw-Hill, NY.
- White, J.E., 1975, Computed seismic speeds and attenuation in rocks with partial gas saturation: Geophysics, 40, 224-232.
- Winkler, K., Gladwin, M., and Nur, A., 1977, The dependence of seismic attenuation on effective stress (abst.): Trans. Am. Geophys. Union (EOS), 58, 1183.
- Wong, T.F. and Brace, W.F., 1978, Thermal expansion of rocks: some measurements at high pressure: submitted to Tectonophysics.
- Wood, A.B., 1955, "A Textbook of Sound (third edition)", McGraw-Hill, NY, 1930.
- Wyllie, M.R.J., 1962, Relative permeability: in "Petroleum Production Handbook, Vol. 2", T.C. Frick, ed., AIME, Dallas, TX, Chapter 25.

- Wyllie, M.R.J., Gregory, A.R., and Gardner, G.H.F., 1958, An experimental investigation of factors affecting elastic wave velocities in porous media: Geophysics, 23, 459-493.
- Wyllie, M.R.J., Gardner, G.H.F., and Gregory, A.R., 1962, Studies of elastic wave attenuation in porous media: Geophysics, 27, 569-589.
- Yamakawa, N., 1962, Scattering and attenuation of elastic waves: Geophysical Magazine (Tokyo), 31, 63-103.
- Zamanek, J., Jr. and Rudnick, I., 1961, Attenuation and dispersion of elastic waves in a cylindrical bar: J. Acoust. Soc. Am., 33, 1283-1288.
- Zener, C., 1948, "Elasticity and Anelasticity of Metals", The University of Chicago Press, Chicago.
- Zoback, M.D. and Byerlee, J.D., 1976, Effect of high pressure deformation on permeability of Ottawa sand: Am. Assoc. Pet. Geol. Bull., 60, 1531-1542.

APPENDIX A  
DEFINITIONS

For plane waves propagating in a homogeneous medium the amplitude is given by:

$$A(x,t) = A_0 e^{i(kx - \omega t)} \quad (A-1)$$

where  $\omega$  is the angular frequency and  $k$  is the wave number. Attenuation may be introduced by allowing either complex velocity or wavenumber. In the latter case:

$$k = k_R + i\alpha \quad (A-2)$$

so that

$$A(x,t) = A_0 e^{-\alpha x} e^{i(k_R x - \omega t)}$$

$\alpha$  is the attenuation coefficient in units of inverse length and the phase velocity is:

$$v = \frac{\omega}{k_R} \quad (A-3)$$

Attenuation may also be defined in terms of inverse time by allowing  $\omega$  to be complex.

Letting the attenuation be determined by

$$A(x) = A_0 e^{-\alpha x} \quad (A-4)$$

$\alpha$  may be written as

$$\alpha = -\frac{1}{A(x)} \frac{dA(x)}{dx} = -\frac{d}{dx} \ln A(x)$$

For two different positions,  $x_1$  and  $x_2$  with respective amplitudes  $A(x_1)$  and  $A(x_2)$  then

$$\alpha = \frac{1}{x_2 - x_1} \ln \left( \frac{A(x_1)}{A(x_2)} \right) \quad (\text{A-5})$$

for  $x_1 < x_2$  in units of nepers/unit length. Alternatively:

$$\alpha = \frac{1}{x_2 - x_1} \cdot 20 \log \left( \frac{A(x_1)}{A(x_2)} \right)$$

in units of db/unit length.

For an oscillating system in free decay, the definition of the logarithmic decrement,  $\delta$ , immediately follows:

$$\delta = \ln \left( \frac{A_1}{A_2} \right) = \alpha \lambda = \frac{\alpha v}{f} \quad (\text{A-6})$$

where  $A_1$  and  $A_2$  are the amplitudes of two consecutive cycles,  $v$  is the velocity,  $f$  the frequency, and  $\lambda$  is the wavelength.

Attenuation may also be considered as the phase lag of strain behind stress or in terms of the energy dissipated per cycle. We define the "quality factor",  $Q$ , to be:

$$Q = \frac{\omega E}{-dE/dt} = \frac{2\pi W}{\Delta W} \quad (\text{A-7})$$

where  $E$  is the instantaneous energy in the system,  $dE/dt$  is the energy loss per second,  $W$  is the elastic energy stored at maximum strain and stress,  $\Delta W$  is the energy loss per cycle of a harmonic excitation. An alternative definition is in terms of the resonance peak bandwidth for an oscillating system:

$$Q = \frac{f_r}{\Delta f} \quad (\text{A-8})$$

where  $\Delta f$  is the frequency between half power points about a resonant peak at  $f_r$  on a power-frequency plot. These two definitions are equivalent as we will now show.

We first consider the transient decay of the oscillations. The equation of motion including a damping term is:

$$\ddot{x}(t) + \Gamma \dot{x}(t) + \omega_0^2 x(t) = 0 \quad (\text{A-9})$$

where  $\omega_0$  is the natural frequency of the undamped system and is equal to  $(K/M)^{1/2}$  where  $K$  is the restoring force and  $M$  is the mass.  $\Gamma$  is the damping constant per unit mass. This equation has a solution of the form:

$$x(t) = e^{-t/2\tau} \cos(\omega_1 t + \theta) \quad (\text{A-10})$$

where  $\tau = 1/\Gamma$  and  $\omega_1^2 = \omega_0^2 - (\frac{\Gamma}{2})^2$ . Of course a more general solution is the superposition of linearly independent solutions. For weakly damped systems we may assume  $e^{-t/2\tau} =$



$e^{-\Gamma t/2}$  to be relatively constant during one cycle of oscillation. We may then write:

$$\dot{x}(t) = -\omega_1 e^{-\Gamma t/2} \sin(\omega_1 t + \theta) \quad (\text{A-11})$$

The total kinetic plus potential energy is

$$E = \frac{1}{2}M\dot{x}^2 + \frac{1}{2}M\omega_0^2 x^2 \quad (\text{A-12})$$

This can be shown from (A-11) to be

$$E = E_0 e^{-\Gamma t} \quad (\text{A-13})$$

where  $E_0 = \frac{M}{2}(\omega_1^2 + \omega_0^2)$ . If we identify  $\Gamma = \omega_1/Q$  then (A-13) is a solution to:

$$\frac{dE}{dt} = \frac{-\omega_1 E}{Q}$$

or

$$Q = \frac{\omega_1 E}{-dE/dt} \quad (\text{A-14})$$

which is the definition given for  $Q$  in (A-7).

We now consider steady state oscillation under a harmonic driving force of the form:

$$F(t) = F_0 \cos(\omega t)$$

The equation of motion is:

$$\ddot{x}(t) + \Gamma \dot{x}(t) + \omega_0^2 x(t) = \frac{F_0}{M} \cos \omega t \quad (\text{A-15})$$

The steady state solution is:

$$x(t) = A \sin \omega t + B \cos \omega t \quad (\text{A-16})$$

where (Crawford, 1968):

$$A = \frac{F_0}{M} \frac{\Gamma \omega}{[(\omega_0^2 - \omega^2)^2 + \Gamma^2 \omega^2]} \quad (\text{A-17})$$

and

$$B = \frac{F_0}{M} \frac{(\omega_0^2 - \omega^2)}{[(\omega_0^2 - \omega^2)^2 + \Gamma^2 \omega^2]} \quad (\text{A-18})$$

The instantaneous power delivered to the system by the driving force is  $F_0 \cos \omega t \cdot \dot{x}(t)$  or:

$$P(t) = F_0 \cos \omega t (\omega A \cos \omega t - \omega B \sin \omega t) \quad (\text{A-19})$$

The time average input power is found by the average over one cycle:

$$\begin{aligned} \bar{P} &= F_0 A \langle \cos^2 \omega t \rangle - F_0 \omega B \langle \cos \omega t \sin \omega t \rangle \\ &= \frac{1}{2} F_0 \omega A \end{aligned} \quad (\text{A-20})$$

We see from equation (A-20) that only the velocity component

of  $x$  that is in phase with the driving force (displacement  $90^\circ$  out of phase) contributes to the average input power. For steady state oscillations the time average input power is equal to the power dissipated by attenuation. It can be shown that the average power loss is

$$\begin{aligned} P_\ell &= M\Gamma \langle \dot{x}^2 \rangle \\ &= \frac{1}{2} M\Gamma \omega^2 [A^2 + B^2] \end{aligned} \quad (\text{A-21})$$

and is in fact equal to (A-20). This is not to say that the instantaneous power input and loss are equal, only the time average over a cycle.

We shall now derive the frequency bandwidth definition of  $Q$ . From (A-20) and (A-17):

$$P = \frac{1}{2} \frac{F_0^2}{M} \frac{\Gamma \omega^2}{(\omega_0^2 - \omega^2)^2 + \Gamma^2 \omega^2} \quad (\text{A-22})$$

The maximum average power will occur at the minimum of the denominator of (A-22). This resonance occurs when  $\omega = \omega_0$  so that  $P_{\max} = F_0^2 / 2M\Gamma$ . Then:

$$P = P_{\max} \frac{\Gamma^2 \omega^2}{(\omega_0^2 - \omega^2)^2 + \Gamma^2 \omega^2} \quad (\text{A-23})$$

Values of  $\omega$  for which the power is one-half maximum are

given by  $\omega^2 = \omega_0^2 \pm \Gamma\omega$  with the two possible (out of four) solutions giving:

$$\omega = \sqrt{\omega_0^2 + \frac{1}{4}\Gamma^2} \pm \frac{\Gamma}{2} \quad (\text{A-24})$$

The full frequency width of the half power units is simply

$$\Delta\omega = \Gamma \quad (\text{A-25})$$

If  $\Gamma = \omega_1/Q$  as defined before then:

$$\frac{\Delta\omega}{\omega_1} = \frac{\Delta f}{f_1} = \frac{1}{Q} \quad (\text{A-26})$$

In the above analysis we have assumed that the rapid variation in the denominator of (A-23) is due to the  $(\omega_0^2 - \omega^2)$  term and have neglected the  $\Gamma^2\omega^2$  term. This is valid for the weak damping case where  $\omega_1 \approx \omega_0$ . In actuality the undamped resonance frequency,  $\omega_0$ , is pulled towards the free decay frequency  $\omega_1$  by the damping term. For most rocks, however, the assumption of low loss is appropriate.

Furthermore, the same analysis and result obtained in (A-26) also holds for half energy units. From (A-12):

$$E = E_0 \frac{\frac{1}{2}\Gamma^2(\omega^2 + \omega_0^2)}{(\omega_0^2 - \omega^2)^2 + \Gamma^2\omega^2}$$

Again it may be shown that the values of  $\omega$  for which  $E = 1/2 E_0$  are:

$$\omega^2 = \omega_0^2 \pm \Gamma\omega$$

or

$$\omega = \sqrt{\omega_0^2 + \frac{1}{2}\Gamma^2} \pm \frac{\Gamma}{2} .$$

## APPENDIX B

## ELASTIC MODULI FOR CALCULATING ATTENUATION

The calculation of attenuation requires the knowledge of several elastic moduli and their pressure dependence. Given the matrix or grain moduli and density,  $K$ ,  $\mu$ , and  $\rho$ , and the inclusion properties  $K'$ ,  $\mu'$  and  $\rho'$ , the effective properties of a composite medium may be found following the treatment of Kuster and Toksöz (1974). Cracks and large pores in the rock are represented by a discrete spectrum of various aspect ratio spheroids. Letting  $c(\alpha_m)$  be the concentration of pores and cracks with aspect ratio  $\alpha_m = \text{thickness/diameter}$ , the effective moduli are given by (Kuster and Toksöz, 1974):

$$\frac{K^*-K}{3K^*+4\mu} = \frac{1}{3} \frac{K'-K}{3K+4\mu} \sum_{m=1}^M c(\alpha_m) T_{iijj}(\alpha_m) \quad (\text{B-1})$$

$$\frac{\mu^*-\mu}{6\mu^*(K+2\mu)+\mu(9K+8\mu)} = \frac{\mu'-\mu}{25\mu(3K+4\mu)} \sum_{m=1}^M c(\alpha_m) \cdot [T_{ijij}(\alpha_m) - \frac{1}{3}T_{iijj}(\alpha_m)] \quad (\text{B-2})$$

where '\*' denotes effective properties, primed quantities refer to fluid properties and unprimed quantities are matrix properties.  $K$  and  $\mu$  represent bulk and shear moduli and  $T_{iijj}$  and  $T_{ijij}$  are scalar quantities. The total porosity is:

$$\phi = \sum_{m=1}^M c(\alpha_m)$$

and the density is:

$$\rho^* = \rho(1-\phi) + \rho'\phi$$

The effect of pressure on the crack and pore distributions and thus the effective moduli and velocities of rocks has been studied by Toksöz et al. (1976). The strain field around an ellipsoidal cavity is calculated as a function of the elastic moduli of the matrix and an applied strain field at infinity. The dilatation of the applied field is  $-P/K_A^*$  where  $P$  is the applied hydrostatic differential pressure and  $K_A^*$  is the effective static bulk modulus or frame bulk modulus. From this, the fractional change in pore volume,  $dc/c$  may be found. For the particular case of very thin cracks (i.e.  $\alpha_m \rightarrow 0$ ),

$$\frac{dc}{c} = - \frac{P}{K_A^*} \left\{ \frac{4}{3\pi\alpha_m} \frac{(1-\sigma)^2}{(1-2\alpha)} \right\} \quad (\text{B-3})$$

where  $\sigma$  = matrix Poisson's ratio. This relationship also provides the basis for calculating the change in attenuation due to friction under increasing hydrostatic or differential pressure.

Anelasticity may be introduced into the effective moduli formulations by employing the concept of complex

moduli (Anderson et al., 1965 and Bland, 1960). This method is particularly useful in dealing with frequency independent  $Q$  mechanisms such as grain boundary and crack friction. Let the complex bulk and shear moduli be expressed as

$$K = K_R + iK_I \quad (\text{B-4})$$

$$\mu = \mu_R + i\mu_I$$

where subscripts R and I refer to real and imaginary parts. If the attenuation is small, then the velocities and attenuation coefficients can be expressed conveniently. For compressional waves,

$$v_p = \left( \frac{K_R + \frac{4}{3}\mu_R}{\rho} \right)^{1/2} \quad (\text{B-5})$$

$$Q_p^{-1} = \frac{K_I + \frac{4}{3}\mu_I}{K_R + \frac{4}{3}\mu_R}$$

For shear waves,

$$v_s = \left( \frac{\mu_R}{\rho} \right)^{1/2} \quad (\text{B-6})$$

$$Q_s^{-1} = \frac{\mu_I}{\mu_R}$$

To determine the imaginary part of the moduli it is necessary to rely on observation and to follow an empirical



approach. The magnitudes of  $K_I$  and  $\mu_I$  should be chosen in each case to match observed  $Q$  values at appropriate conditions.

## APPENDIX C

## FLUID FLOW FROM CRACKS

## FORMULATION AND ESTIMATION OF THE RELAXATION TIME

Flow will take place between thin cracks with aspect ratio  $\alpha_m \approx 0$  and pores with  $\alpha_m \approx 1$  due to a differential volume change induced by the stress wave. The fluid pressures and volume changes are given by:

$$P_0 = -K'\theta_0 \quad \text{and} \quad dC_0 = C_0\theta_0, \quad \alpha_m \approx 0 \quad (\text{C-1})$$

$$P_1 = -K'\theta_1 \quad \text{and} \quad dC_1 = C_1\theta_1, \quad \alpha_m \approx 1$$

where  $C$  is the volume concentration of cracks or pores and  $\theta$  is the dilatation. The pressure difference is  $\Delta P = P_0 - P_1$ . Letting the equalized pressure after flow be  $\bar{P}$ , then the corresponding dilatation in both the crack and pore is  $\bar{\theta} = -\bar{P}/K'$ . The total liquid volume displaced in order to equalize the pressure is given by:

$$q_T = d\bar{C}_0 - dC_0 = dC_1 - d\bar{C}_1 \quad (\text{C-2})$$

where  $d\bar{C}_0 = C_0\bar{\theta}$  and  $d\bar{C}_1 = C_1\bar{\theta}$ . Solving for  $\bar{\theta}$  we obtain:

$$\bar{\theta} = \frac{\varepsilon\theta_0 + \theta_1}{1 + \varepsilon} \quad (\text{C-3})$$

where  $\varepsilon = C_0/C_1$ , or the volumetric ratio of connected cracks to pores. Furthermore:

$$q_T = C_0 \left( \frac{\theta_1 - \theta_0}{1 + \epsilon} \right) \quad (C-4)$$

The instantaneous flow between two parallel plates (crack surfaces) separated by distance  $h$  is given by

$$q = \frac{h^2 A}{3\eta} \frac{dP}{dx} \quad (C-5)$$

where  $A$  now becomes the cross sectional area of the crack and is equal to  $\pi h^2 / \alpha_m$  or  $\pi h \ell$ . If we let  $dx = 2\ell$  (crack length) then from equation (C-1) and (C-5):

$$q = \frac{\pi h^3}{6} K' (\theta_1 - \theta_0) \quad (C-6)$$

Assuming a relaxation of the form:

$$q_T = q \int_0^{\infty} e^{-t/\tau} dt = q\tau \quad (C-7)$$

where  $\tau$  is the relaxation time, we obtain

$$\tau = \frac{C_0 (\theta_1 - \theta_0) / (1 + \epsilon)}{\pi h^3 K' (\theta_1 - \theta_0) / 6\eta} \quad (C-8)$$

Since the volume of the crack,  $C_0 = 4\pi h^3 / 3\alpha_m^2$ :

$$\tau = 8\eta / \alpha_m^2 K' (1 + \epsilon) \quad (C-9)$$

Viscoelastic Formulation:

We will now show that by using the correspondence principle for both the shear and bulk moduli of the fluid phase that the equations for the effective moduli may be written in terms of real and imaginary parts and two characteristic frequencies. Rewriting equations (B-1) for the effective bulk modulus by letting  $\delta'' = (K'/K - 1)T_{ijjj}/3$  (dropping the summation over aspect ratios we obtain:

$$K^* = \frac{K + \frac{4CK\mu\delta''}{3K+4\mu}}{1 - \frac{3CK\delta''}{3K+4\mu}} = K \left( \frac{1+4\mu C\delta'}{1-3KC\delta'} \right) \quad (C-10)$$

where  $\delta' = \delta''/(3K+4\mu)$ . Letting  $\delta'$  be complex, i.e.  $\delta' = a+ib$ , then:

$$K^* = K \left( \frac{1+4\mu C(a+ib)}{1-3KC(a+ib)} \right) = K_R^* + K_I^*$$

where

$$K_R^* = K \left( \frac{(1+4\mu Ca)(1-3KCa) - 12K\mu C^2 b^2}{(1-3KCa)^2 + (3KCb)^2} \right) \quad (C-11)$$

and

$$K_I^* = bK \left( \frac{4\mu C(1-3KCa) + 3KC(1+4\mu Ca)}{(1-3KCa)^2 + (3KCb)^2} \right)$$

Applying the correspondence principle we let  $K' = K_R' + i\omega g$  and  $\mu' = i\omega\eta$  where  $\eta$  is the viscosity and  $g$  is con-

sidered an unknown to be determined from the relaxation time for flow. We now show that the equations for the effective moduli can be written in terms of two characteristic frequencies and that the real and imaginary parts of  $\delta'$  are uniquely determined. For small aspect ratios:

$$\delta' = \frac{1}{3K+4\mu} \left( \frac{K'}{K} - 1 \right) \frac{3K+4\mu'}{3K'+4\mu'+K_1} \quad (\text{C-12})$$

(Toksöz et al., 1976, equation (C-4)) where  $K_1 = 3\pi\alpha_m \mu(3K+4\mu)/(3K+4\mu)$ . Substituting the complex  $K'$  and  $\mu'$  we obtain after some algebra:

$$\delta' = \frac{1}{3K+4\mu} \left( K'' - 1 + \frac{i\omega}{\omega_c} \right) \frac{1 + \frac{i\omega}{\omega_d}}{(K''+K_2) + i\omega \left( \frac{1}{\omega_c} + \frac{1}{\omega_d} \right)}$$

where  $K'' = K'_R/K$ ,  $K_2 = K_1/3K$  with  $\omega_c = K/g$  and  $\omega_d = 3K/4\eta$ .  $\omega_d$  is recognized as the characteristic frequency for viscous relaxation in isolated cracks (Walsh, 1969) and  $\omega_c$  is the characteristic frequency for fluid flow from cracks. Finally, it can be shown that the real and imaginary parts of  $\delta' = a+ib$  can be written as:

$$a = \frac{1}{A} \left[ (K''-1) (K'' + K_2 + \frac{\omega^2}{\omega_d} (\frac{1}{\omega_c} + \frac{1}{\omega_d})) - \frac{\omega^2}{\omega_c} (\frac{K''+K_2}{\omega_d} - \frac{1}{\omega_c} - \frac{1}{\omega_d}) \right] \quad (C-14)$$

$$b = \frac{1}{A} \left[ \omega (\frac{K''+K_2}{\omega_d} - \frac{1}{\omega_c} - \frac{1}{\omega_d}) (K''-1) + \frac{\omega}{\omega_c} (K''+K_2) + \frac{\omega^3}{\omega_c \omega_d} (\frac{1}{\omega_c} + \frac{1}{\omega_d}) \right]$$

where  $A = \left[ (K''+K_2)^2 + \omega^2 (\frac{1}{\omega_c} + \frac{1}{\omega_d})^2 \right] / (3K+4\mu)$ . The equivalent result is obtained for the effective shear modulus.

From equation (C-9) we have

$$\frac{1}{\omega_c} = \frac{8\eta}{\alpha_m^2 K'_R (1+\epsilon)} \quad (C-15)$$

so that

$$g = \frac{8\eta}{\alpha_m^2 (1+\epsilon)} \frac{K}{K'_R} \quad (C-16)$$

## APPENDIX D

## HOMOMORPHIC DECONVOLUTION

A homomorphic system is one that obeys a generalized principle of superposition. That is, let  $\square$  denote a rule for combining inputs (e.g. addition, multiplication or convolution) and  $:$  a rule for combining scalars with inputs. Also allow  $\circ$  to represent the rule for combining outputs and  $\uparrow$  for combining scalars with outputs. Then:

$$H[x_1(n) \square x_2(n)] = H[x_1(n)] \circ H[x_2(n)]$$

and

(D-1)

$$H[c : x_1(n)] = c \uparrow H[x_1(n)]$$

where  $x_1(n)$  and  $x_2(n)$  are input sequences,  $c$  is a scalar and  $H$  is the system transformation (Oppenheim and Schaffer, 1975). The particular homomorphic system that is useful for seismic deconvolution is when the input rule is convolution and the output rule, addition. This is suited for our purposes since the input sequence may be considered to be the convolution of a wavelet with the impulse response of the medium. While linear inverse filtering can be used to separate the components of such signals, this would require detailed knowledge of one of its components.

We define then, the characteristic homomorphic system

$D_*$  (\* refers to the convolution rule) by:

$$\begin{aligned} D_*[x_1(n) * x_2(n)] &= D_*[x_1(n)] + D_*[x_2(n)] \\ &= x_1(n) + x_2(n) \end{aligned} \quad (D-2)$$

$$D_*[c : x_1(n)] = cD_*[x_1(n)] = cx_1(n)$$

If  $L$  is a linear system and  $D_*^{-1}$  is the inverse of  $D_*$ , then the homomorphic filter can be represented in canonical form as shown in Figure D-1a.

The characteristic system  $D_*$  is found by considering the properties of the  $z$  transform. The input sequence  $x(n)$  can be represented by its  $z$  transform  $X(z)$ . Then, if

$$x(n) = x_1(n) * x_2(n)$$

it follows that

$$X(z) = X_1(z) \cdot X_2(z) \quad (D-3)$$

It is apparent that the system,  $D_*$ , can be realized in terms of the  $z$  transform, by the complex logarithm,  $\log [X(z)]$ , defined so that if

$$X(z) = X_1(z) \cdot X_2(z)$$

then



$$\begin{aligned}\hat{X}(z) &= \log [X_1(z) \cdot X_2(z)] \\ &= \log [X_1(z)] + \log [X_2(z)] \quad (D-4)\end{aligned}$$

The canonical form of  $D_*$  is given in Figure D-1b where  $Z[ ]$  represents the  $z$  transform and  $Z^{-1}[ ]$  the inverse transform.  $\hat{x}(n)$  is known as the complex cepstrum since the complex logarithm and transforms are commonly used.  $\hat{x}(n)$ , however, is real for purely real input sequences.

If the input sequence is minimum phase, then the homomorphic system of Figure D-1b may be realized with the Fourier transform. In general, however, signals to be processed are of mixed phase. To remedy this situation exponential weighting of the form

$$x(n) = \alpha^n x(n) \quad \alpha < 1 \quad (D-5)$$

may be used (Schafer, 1968; Ulrych, 1971).  $\alpha$  is chosen so that all zeros of  $Z[x(n)]$  lying outside the unit circle are moved inside. Of course, the output of  $D_*^{-1}$ ,  $y(n)$ , must be scaled by  $\alpha^{-n}$ .

The implementation of  $D_*$  requires the use of the complex logarithm which must be carefully defined. If  $X(e^{i\omega})$  is the Fourier transform of  $x(n)$ ,

$$\begin{aligned} X(e^{i\omega}) &= X_R(e^{i\omega}) + iX(e^{i\omega}) \\ &= |X(e^{i\omega})| \exp\{i \arg X(e^{i\omega})\} \end{aligned} \quad (D-6)$$

where  $X(e^{i\omega})$  is the magnitude and  $\arg X(e^{i\omega})$  is the phase of the transform. The Fourier transform of the complex cepstrum is then:

$$\hat{X}(e^{i\omega}) = \log X(e^{i\omega}) = \log |X(e^{i\omega})| + i \arg X(e^{i\omega}) \quad (D-7)$$

The complex logarithm, and thus the cepstrum is uniquely defined if  $\hat{X}(z)$  is a valid transform and if it is analytic on the unit circle. This implies that  $\hat{X}(e^{i\omega})$  must be a continuous function of  $\omega$ . However, we note that:

$$e^{i \arg\{X(z)\}} = e^{i \text{ARG}\{X(z)\}} \quad (D-8)$$

where  $\text{ARG}[X(z)]$  is the phase principle value.

$\text{ARG}[X(z)]$  is clearly discontinuous in  $\omega$  and does not satisfy the requirement of analyticity on the unit circle. But, the principle value is what is determined from the Fourier transform. In order to remove the ambiguity in the complex logarithm implied by equation D-8, the phase principle value must be "unwrapped" to obtain a continuous phase function. That is, at any frequency  $\omega_1$ :

$$\arg[X(e^{i\omega_1})] = \text{ARG}[X(e^{i\omega_1})] + 2\pi\ell(\omega_1) \quad (D-9)$$

where  $\ell(\omega_1)$  is an integer. A phase unwrapping algorithm

using an adaptive numerical integration scheme has been published by Tribolet (1977b) and is used in this study.

The canonical representation of  $D_*^{-1}$  defined by:

$$D_*^{-1}[D_*[x(n)]] = x(n)$$

is shown in Figure D-1c. There is no uniqueness problem for the complex exponential so that if  $Y(z)$  is analytic on the unit circle, so is  $\exp[Y(z)]$ .

The separation of the direct pulse from the reflection components is achieved by applying a frequency invariant linear filter to the complex cepstrum as shown in Figure D-1a. For the linear filter,  $L$ :

$$\hat{Y}(e^{i\omega}) = \frac{1}{2\pi} \int_{-\pi}^{\pi} X(e^{i\theta}) L[e^{i(\omega-\theta)}] d\theta \quad (D-10)$$

where

$$X(e^{i\omega}) = \log[X(e^{i\omega})]$$

may be written in the time domain as:

$$\hat{y}(n) = \ell(n) \hat{x}(n) \quad (D-11)$$

where  $\ell(n)$  is the inverse transform of  $L(e^{i\omega})$

(Oppenheim and Schaffer, 1975). Since  $x(n)$ ,  $\hat{x}(n)$ ,  $y(n)$ , and  $\hat{y}(n)$  are real sequences, so is  $\ell(n)$ .

The reflection component of the waveform is removed by retaining only the low time portion of the cepstrum. That is,  $\ell(n)$  is of the form:

$$\begin{aligned} \ell(n) &= 1 & n < n_1 \\ \ell(n) &= 0 & n \geq n_1 \end{aligned} \quad (D-12)$$

where  $n_1$  is the filter cut-off position. To show that the high time portion of the cepstrum does indeed correspond to the reflection components, consider a simple case of one reflection delayed by  $n_t$ :

$$x(n) = s(n) + \beta s(n-n_t)$$

or

$$x(n) = s(n) * p(n) \quad (D-13)$$

where

$$p(n) = \delta(n) + \beta \delta(n-n_t)$$

where  $\beta$  is a scale factor and  $s(n)$  is the signal to be recovered. The Fourier transform of D-13 is:

$$X(e^{i\omega}) = S(e^{i\omega}) (1 + \beta e^{-i\omega n_t}) \quad (D-14)$$

The contribution to the complex logarithm due to  $p(n)$  is:

$$\hat{p}(e^{i\omega}) = \log (1 + \beta e^{i\omega n_t}) \quad (D-15)$$

Then for  $|\beta| < 1$ ,

$$\hat{p}(n) = \sum_{k=1}^{\infty} (-1)^{k+1} \frac{\beta^k}{k} \delta(n-kn_t) \quad (D-16)$$

(Oppenheim and Schaffer, 1975). Thus,  $\hat{p}(n)$  is nonzero only for integer multiples of  $n_t$ . If  $S(e^{i\omega})$  is slowly varying relative to the variations in  $P(e^{i\omega})$  then these components may be separated with the frequency invariant filter  $L(e^{i\omega})$ . In reality, reflections are not equally spaced. However, for minimum phase sequences,

$\hat{p}(n) = 0$  for  $n < 0$  and  $p(n) = 0$  for  $n < n_t$  where  $n_t$  is the shortest delay (Schafer, 1968).

In summary, the input waveform is processed to remove the reflection components by the following steps:

1. Exponential weighting of the waveform,  $x(n)$ , to force it to minimum phase.

2. Fourier transform to give  $X(e^{i\omega})$ . Unwrap the phase principle value to obtain a continuous phase function.

3. Take the complex logarithm of  $X(e^{i\omega})$  to find the transform,  $\hat{X}(e^{i\omega})$ , of the complex cepstrum.

4. Inverse Fourier transform  $\hat{X}(e^{i\omega})$  to obtain the complex cepstrum,  $\hat{x}(n)$ .

5. Apply a frequency invariant filter,  $l(n)$  to  $\hat{x}(n)$  obtaining  $\hat{y}(n)$  and eliminating the reflection components of the cepstrum.

6. Fourier transform  $\hat{y}(n)$  to give  $\hat{Y}(e^{i\omega})$ . Taking the complex exponential of  $\hat{Y}(e^{i\omega})$  gives  $Y(e^{i\omega})$ . Inverse Fourier transform to get  $y(n)$ .

7. De-exponentiate  $y(n)$  to obtain the resulting deconvolved direct waveform.

An example of this method is shown in Figures D-2 and D-3. The original unweighted waveform is shown in Figure D-2a. Following exponential weighting with  $\alpha = 0.965$ , the log magnitude and the phase principle value are shown in Figures D-2b and c respectively.

A 4096 point FFT was used (padding the initial waveform with zeros) and the abscissa of Figures D-2b and c is plotted in terms of  $n$ . The phase is then unwrapped and a linear trend removed (resulting in a time shift of the deconvolved waveform that must be corrected for), the results being displayed in Figure D-3a. The complete complex cepstrum is shown in Figure D-3b with an enlargement of the low time (low  $n$ ) portion shown in Figure D-3c. The cepstrum was then filtered according to equation D-12 with  $n_1 = 25$  and the recovered waveform after de-exponentiation is shown in Figure D-3d.

As stated in Chapter 4, homomorphic deconvolution turned out to be an expensive and cumbersome method to apply to large quantities of data. It was, however, useful as a guide to time windowing. As an example, the low time portion of the cepstrum, windowed (solid lines) and deconvolved (dashed lines) waveforms and spectra are shown for P and S waves in dry Berea sandstone at 300 bars in Figure D-4. The major difference between the windowed and deconvolved results is the hole in the windowed spectra near 0.2 MHz due to the approximately  $5\mu\text{s}$  window used. The deconvolution also seems to result in slightly higher amplitude at the high frequencies. However, in the peak portion of the spectra, the two methods produce nearly identical results.

## FIGURE CAPTIONS

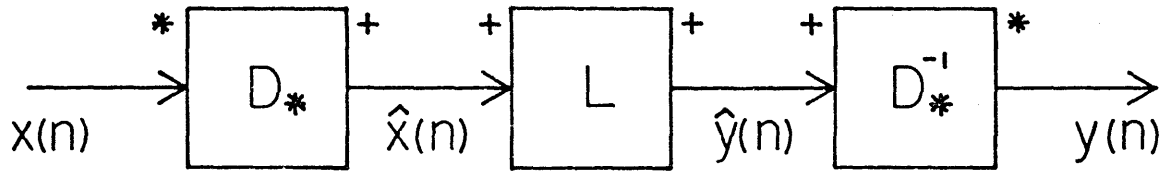
Figure D-1. a) Canonic form of the homomorphic system in which convolution is the input operation. b) The realization of  $D_*$  by means of the Z transform and complex logarithm. c) The realization of  $D_*^{-1}$ .

Figure D-2. An example of homomorphic deconvolution: the initial waveform (a) with log amplitude (b) and phase principle value (c) as functions of n for a 4096 point FFT.

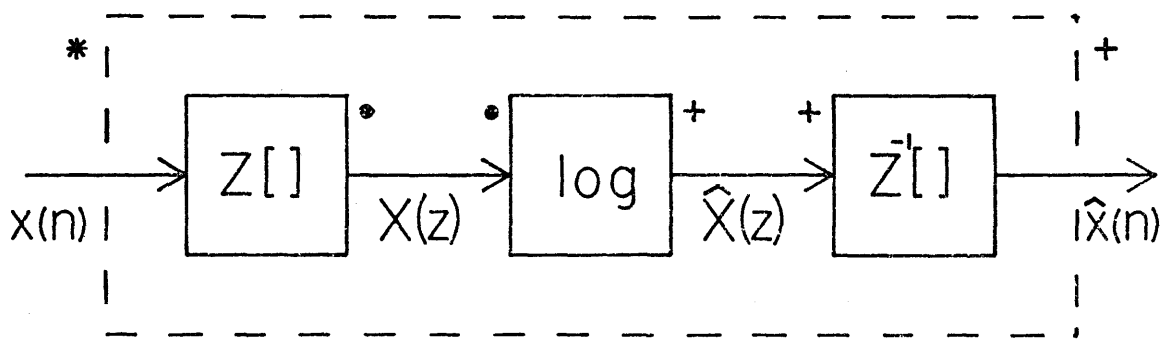
Figure D-3. An example of homomorphic deconvolution: a) Unwrapped phase of figure D-2c with the linear trend removed. b) Complete complex cepstrum of the waveform shown in figure D-2a. c) Enlargement of the low time portion of the cepstrum. d) The deconvolved waveform after filtering the cepstrum to remove the high time (n) portion.

Figure D-4. Typical low time portions of the complex cepstrum for P and S waves (top). Comparison of deconvolved (dashed lines) and time windowed (solid lines) waveforms (middle) and spectra (bottom).

(a) Canonic Form



(b) Realization of  $D_*$



(c) Realization of  $D_*^{-1}$

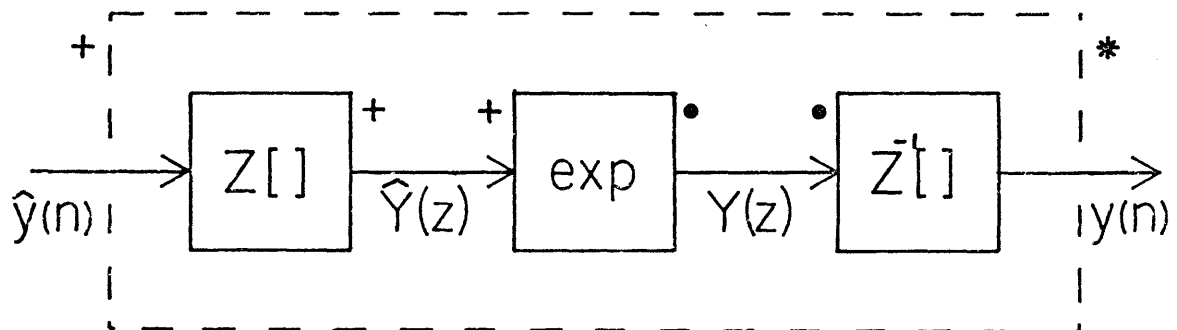


Figure D-1



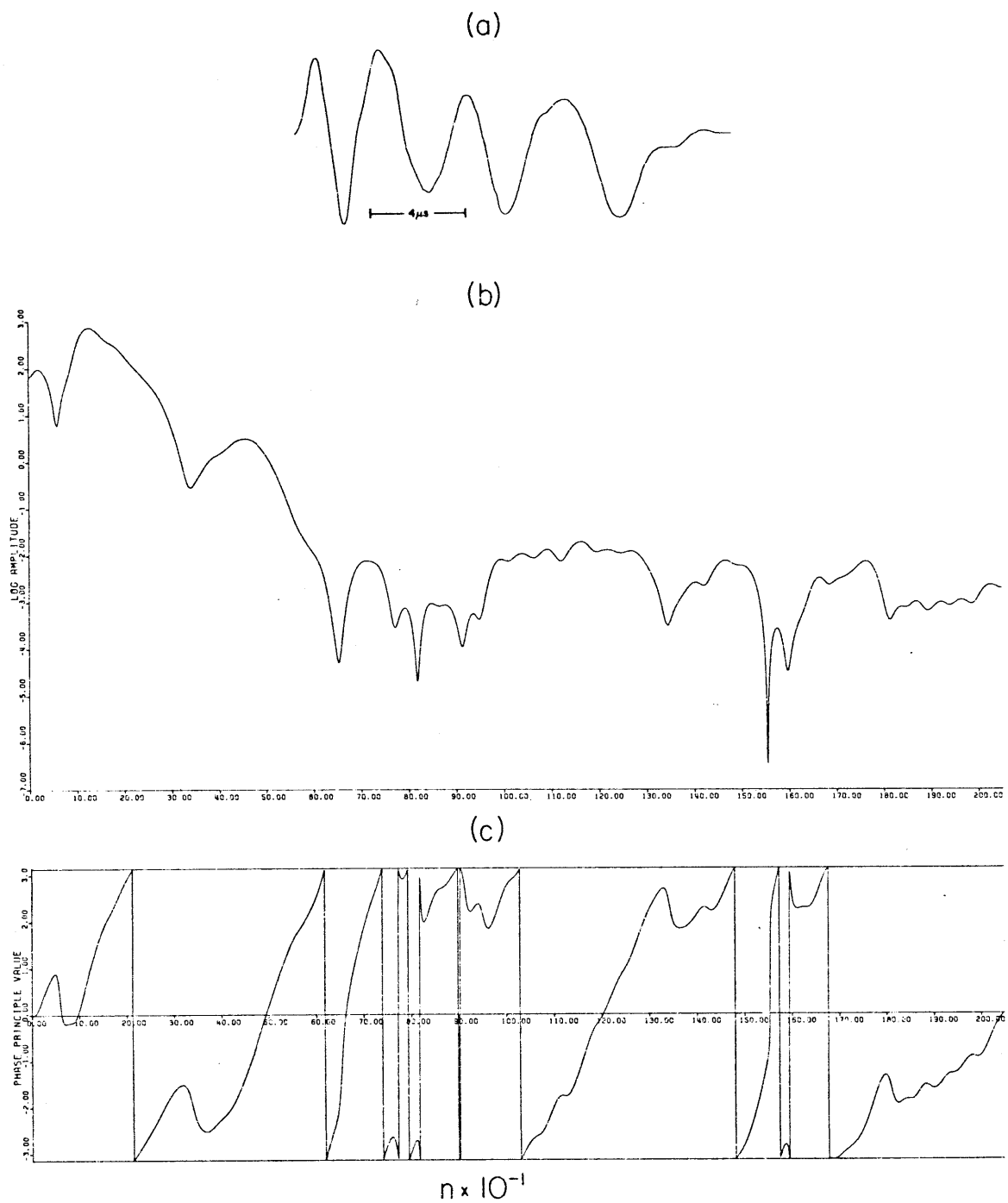


Figure D-2

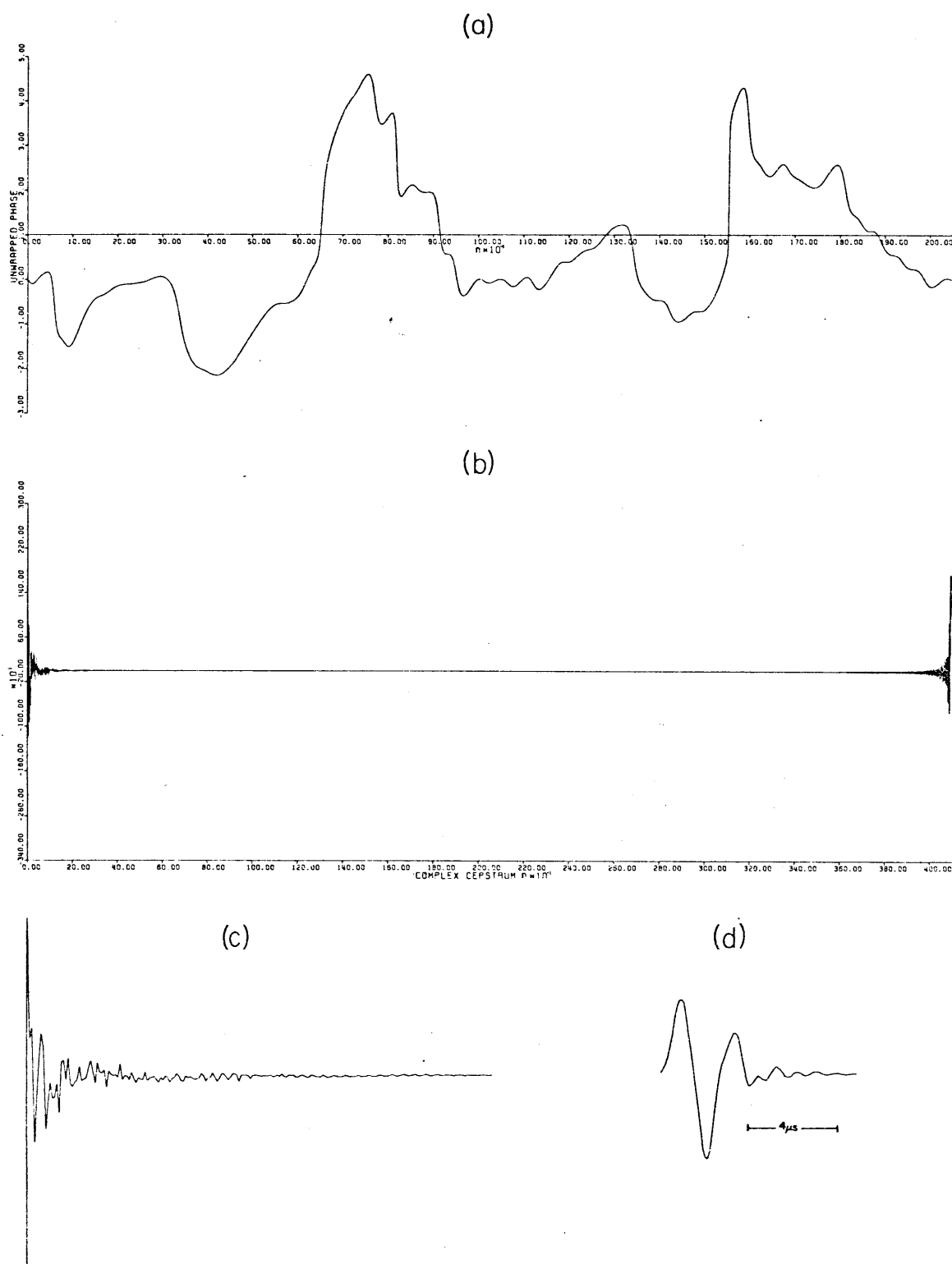
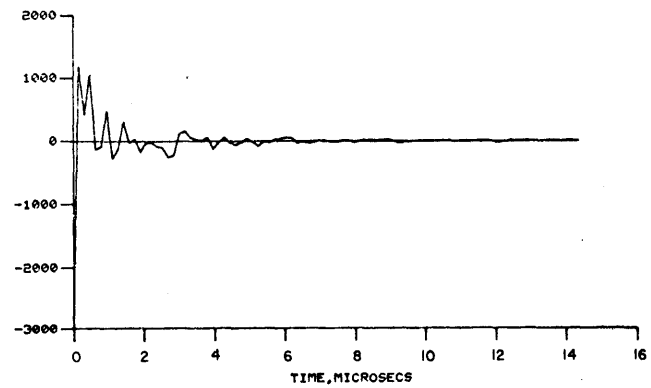
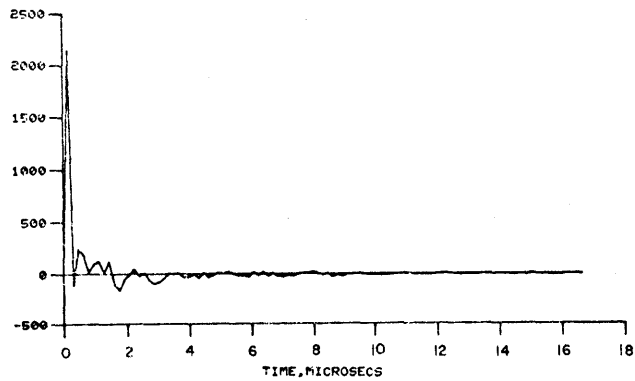
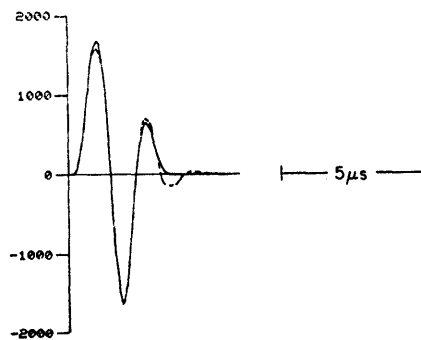


Figure D-3



P wave



S wave

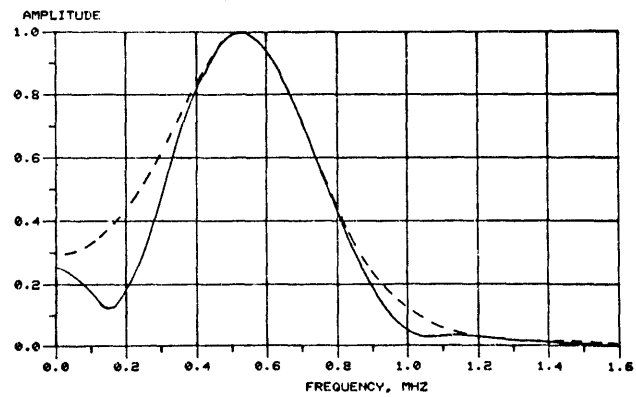
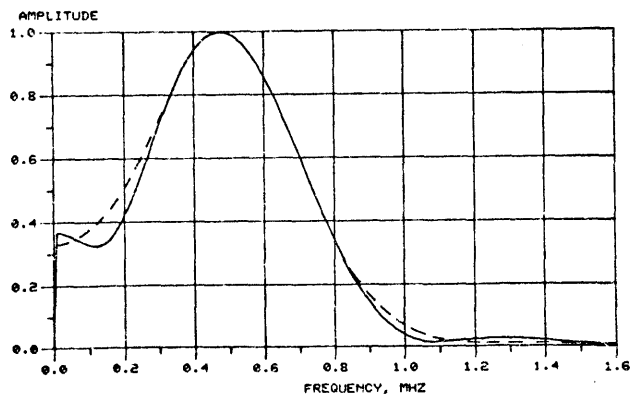
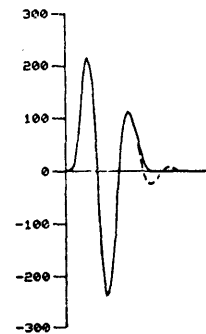


Figure D-4

## BIOGRAPHY

David H. Johnston, Mary and Phil's little boy, was born in Syracuse, NY on August 25, 1951. His first recollections were of the booming metropolis of Albany, NY. In the quest of the American Dream, his family then moved to Delmar, NY. Here he grew up in the suburban bliss of paper routes, Boy Scouts, proms, and the like, graduating from the Bethlehem Central High School in 1969.

Rumor has it that as a young boy on a visit to Boston, he caught a glimpse of some strange Roman revival buildings stretched out along the Charles River and decided that institution was for him. Little did he know...

So, in the fall of 1969 he entered MIT and quickly got swept up by the rising tide of anti-Vietnam demonstrations. If nothing else, these political activities were the catalyst for his meeting Linda Kaznova, who barged her way into his heart.

In the sophomore year he declared Earth and Planetary Sciences as a major. He immediately began to work for Nafi Toksöz on several projects (how little time changes) and settled down on the study of planetary interiors, a field with practically no data but a lot of speculation, enabling one to publish many papers on the same topic as the reference list illustrates.

In the fall of 1972, Linda and Dave were married. And yes, all of you statistics fans, Linda was a Simmons College graduate.

After four years of MIT, he graduated in June of 1973. If that weren't enough, he decided to stay at MIT for graduate school because he thought there would be a good chance to get out with a PhD earlier. He quickly came down to earth in more ways than one. Power hungry, he procured the services of several undergraduates and set up the MIT seismic network, declaring himself to be Deputy Director of the Wallace Geophysical Observatory (Director Toksöz gave mixed blessings).

The summer of 74 was spent in California working for Chevron, which is how he got started in that "new, exciting, and challenging" field of rock physics. Four years later, after several false starts, blood (as the scar on his right arm testifies to), sweat, tears, nail biting, swearing at equipment, and writer's cramp, this thesis was finished.

## PUBLICATIONS

- Toksöz, M.N., S.C. Solomon, J.W. Minear and D.H. Johnston, Thermal evolution of the moon, The Moon, 4, 190-213, 1972.
- Toksöz, M.N., A.M. Dainty and D.H. Johnston, Structural constraints and the evolution of the moon, Abst. with Programs, GSA, 5, 843, 1975.
- Toksöz, M.N. and D.H. Johnston, The evolution of the moon, Icarus, 21, 389-414, 1974.
- Johnston, D.H., T.R. McGetchin and M.N. Toksöz, The thermal state and internal structure of Mars, J. Geophys. Res., 79, 3959-3971, 1974.
- Johnston, D.H., Earthquakes of New England, New England Outdoors, November, 1976.
- Toksöz, M.N. and D.H. Johnston, The evolution of the moon and terrestrial planets, in Proc. Soviet-American Conference on the Cosmochemistry of the Moon and Planets, J.H. Pomeroy and N.J. Hubbard, ed., NASA Pub., 295-328, 1977.
- Johnston, D.H. and M.N. Toksöz, Internal structure and properties of Mars, Icarus, 32, 73-84, 1977.
- Toksöz, M.N., A.T. Hsui and D.H. Johnston, Thermal evolutions of the terrestrial planets, The Moon and the Planets, 18, 281-320, 1978.
- Toksöz, M.N., D.H. Johnston and A. Timur, Attenuation of seismic waves in dry and saturated rocks: I. Laboratory measurements, in press, Geophysics, 1978.
- Johnston, D.H., M.N. Toksöz and A. Timur, Attenuation of seismic waves in dry and saturated rocks: II. Mechanisms, in press, Geophysics, 1978.